



EVIDENCE OF TRANSVERSE MOMENTUM DEPENDENT FLOW ANGLE AND MAGNITUDE FLUCTUATIONS AT THE LHC WITH ALICE

MASTER'S THESIS

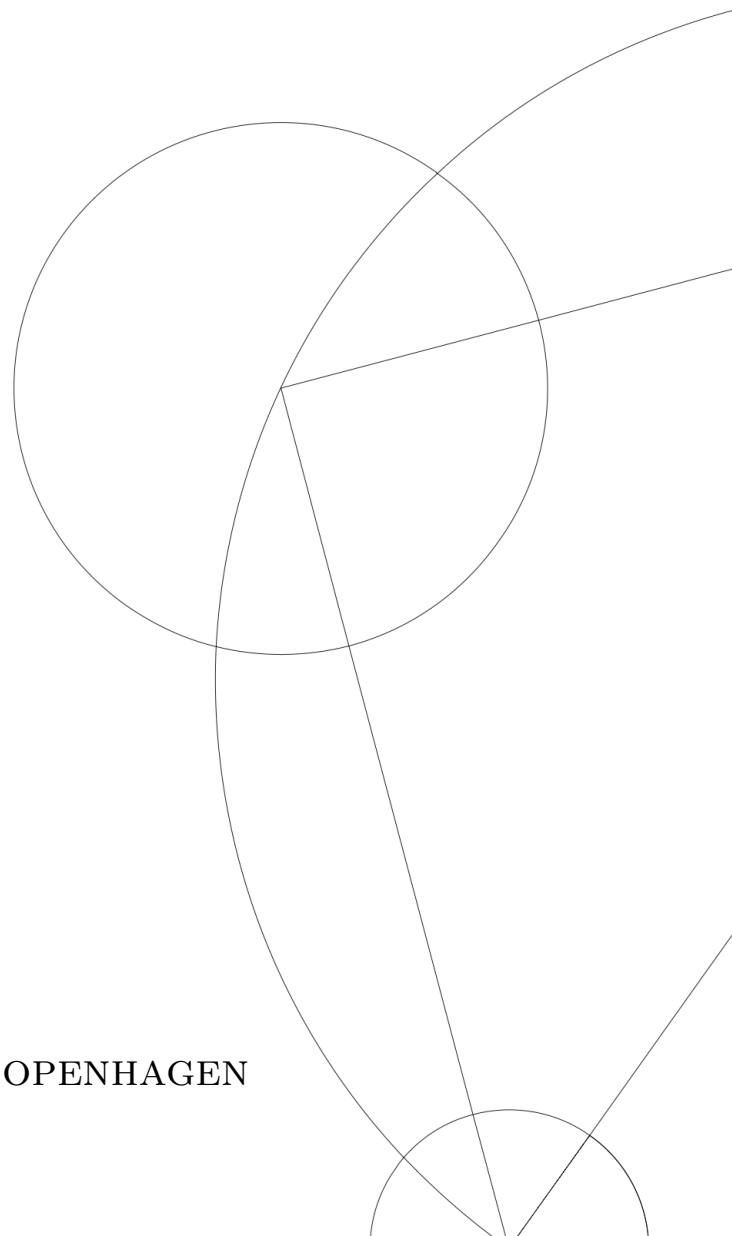
Written by *Emil Gorm Nielsen*

September 30, 2020

Supervised by

Lektor You Zhou

UNIVERSITY OF COPENHAGEN






UNIVERSITY OF
COPENHAGEN

NAME OF INSTITUTE: Niels Bohr Institute
NAME OF DEPARTMENT: High Energy Heavy Ion Group (HEHI)
AUTHOR: Emil Gorm Nielsen
EMAIL: emil.gorm.nielsen@cern.ch
TITLE: Evidence of transverse momentum dependent flow angle
and magnitude fluctuations at the LHC with ALICE
-
SUPERVISOR: Lektor You Zhou
HANDED IN: September 30, 2020
DEFENDED: October 9, 2020

NAME Emil Gorm Nielsen

SIGNATURE 

DATE 30-09-2020

Abstract

One of the main goals of ultra-relativistic nuclear collisions at the LHC is to create a new state of matter called quark-gluon plasma (QGP) and study its properties under controlled conditions. One of the experimental observables is the anisotropic flow v_n , defined as correlation of azimuthal angle of each particle with respect to a common symmetry plane Ψ_n . The v_n and Ψ_n represent the magnitude and the phase of a complex flow vector V_n , respectively. Azimuthal anisotropies are traditionally measured using 2- and/or multi-particle correlations over a large range in p_T and η . However, hydrodynamic calculations show that the event-by-event fluctuations in the initial conditions and the dynamics during the system expansion lead to additional flow vector fluctuation in p_T and/or η (also called de-correlations of flow vector), including flow magnitude and flow angle fluctuations. Understanding these effects can help us improve theoretical models and constrain initial conditions and properties of the QGP.

In this thesis, we present precise measurements of p_T -dependent flow vector fluctuations in Pb–Pb collisions at $\sqrt{s_{NN}} = 5.02$ TeV with ALICE, using particle azimuthal correlations. We find significant evidence of p_T -dependent flow vector fluctuations in Pb–Pb collisions up to $\sim 15\%$. In addition, newly proposed four-particle correlations are used to study the contributions of flow magnitude and flow angle fluctuations separately. Evidence of both flow angle fluctuation and flow magnitude fluctuations are observed in the measurements, although the flow magnitude fluctuations dominate in central collisions. The observation of both flow angle and flow magnitude fluctuations in Pb–Pb collisions provide a new flow picture, which gives us a new way to examine theoretical models and improve our understanding of initial conditions and QGP properties.

Resumé

Et af de primære mål med ultra-relativistiske kernekollisioner ved LHC er at skabe en ny tilstandsform kaldet Kvarke-Gluon Plasma (QGP), og studere dets egenskaber under kontrollerede forhold. En af de eksperimentelle observabel er det anisotropiske *flow* v_n defineret som en korrelation af den azimuthale vinkel af hver partikel i forhold til et fælles symmetriplan Ψ_n . Her repræsenterer v_n og Ψ_n henholdsvis størrelsen og vinklen på den komplekse flow-vektor V_n . Den azimuthale anisotropi bliver traditionelt målt med to- og/eller multi-partikel korrelationer over et stort p_T eller η interval. Hydrodynamiske beregninger viser dog, at fluktuationer fra begivenhed til begivenhed i begyndelsestilstandene og dynamikken i løbet af udvidelsen af systemet fører til fluktuationer i flow-vektoren i p_T og η (også kaldet dekorrelation af flow-vektoren), som inkluderer fluktuationer i både størrelsen og fasen. Forståelse af disse effekter kan hjælpe os med at forbedre teoretiske modeller, og indsnævre begyndelsestilstande og egenskaberne af QGP.

I denne afhandling præsenteres præcisionsmålinger af p_T -afhængige flow-vektor fluktuationer i Pb–Pb kollisioner ved $\sqrt{s_{NN}} = 5.02$ TeV med ALICE ved hjælp af azimuthale korrelationer. Vi finder signifikante beviser for flow-vektor fluktuationer i Pb–Pb kollisioner op til $\sim 15\%$. Derudover bliver en helt ny observabel brugt til at studere bidragene fra flow-størrelsen og flow-vinklen hver for sig. Beviser for både flow-vinkel fluktuationer og flow-størrelse fluktuationer er observeret i målingerne, selvom flow-størrelse fluktuationerne dominerer i centrale kollisioner. Observationen af både flow-vinkel og flow-størrelse fluktuationer i Pb–Pb kollisioner tegner et nyt billede af flow, som giver en ny måde at undersøge teoretiske modeller, og forbedrer vores forståelse af begyndelsestilstande og QGP egenskaber.

Acknowledgements

When I started my Master's project, I had no idea which topic to choose. Initially, I thought I would study neutrino physics with the IceCube experiment, or continue the topic from my Bachelor's thesis regarding New Physics at the energy frontier. So while I clearly had a strong interest in particle physics, the subject of heavy-physics was foreign to me. However, it did not take more than a brief discussion with my now supervisor Dr. You Zhou before I chose the subject of my thesis. His enthusiasm and passion for the field immediately convinced me that heavy-ion physics was the right fit for me. Therefore, I want to give extra thanks to You, whose advice and constant motivation kept me in high spirit when going through the tough preliminary approval period and throughout the project. He has helped me grow immensely as a physicist, and I could not have asked for a better supervisor. I look forward to working with him for the next three years. Thank you!

I would also like to thank the people around me in the office, who made it a joy to come in and work on the project. My thanks goes out to Zlatko, Zuzana, Vytautas, Freja, Ya, Jean-Loup and Joachim. Special shout-out to Joachim, my long-time friend, whose support has been invaluable during this year-long project when the work became overwhelming. Thanks to all the senior staff of the HEHI group at NBI: Jens Jørgen, Ian, Børge, Christian H. C., Hans, Christian B. and Kristjan. You have made me feel very welcome in the group.

I want to give thanks to my family: My mom, my dad and my brother for supporting me and my choice to pursue an education in physics. For shaping me into the man I am today, and for always being there. I could not have come so far without them. A final thanks goes to my girlfriend Julie. The last months of the thesis should have been the hardest but your support has made them easy.

Contents

1	Introduction	1
1.1	The Standard Model	1
1.2	Heavy-ion collisions	2
1.2.1	Theoretical description of heavy-ion collisions	5
1.3	Anisotropic flow in heavy-ion collisions	6
1.3.1	Measurements of anisotropic flow	7
2	Analysis methods	11
2.1	Standard methods of azimuthal correlations	11
2.1.1	Multi-particle azimuthal correlations	11
2.1.2	Q-cumulant method	12
2.1.3	Generic framework	14
2.2	Subevent method	16
2.2.1	Implementation of the subevent method in the Generic Framework	17
2.3	From correlations to flow observables	19
3	Experimental setup	22
3.1	The Large Hadron Collider	22
3.2	A Large Ion Collider Experiment (ALICE)	23
3.2.1	Inner Tracking System (ITS)	23
3.2.2	Time Projection Chamber (TPC)	24
3.2.3	VZERO (V0) system	26
3.2.4	Track Reconstruction	27
3.2.5	Triggering	28
4	Analysis Details	30
4.1	Data processing	30
4.2	Event Selection	31
4.3	Track Selection	34
4.4	Non-uniform Acceptance Correction	35
4.5	Systematic uncertainties	37
5	Results & Discussion	41
5.1	Flow vector fluctuations	42
5.1.1	$v_n\{2\}/v_n[2]$	42
5.1.2	Factorization ratio r_n	50
5.1.3	Angle decorrelation $C(\Psi_n)$	57
5.1.4	Outlook - Flow vector fluctuations in small systems	68
5.2	Correlations of flow	70
6	Conclusion	75
A	Run lists	83

B	Systematics	84
B.1	$v_n\{2\}/v_n[2]$	84
B.2	Factorization ratio r_n	87
B.3	Angle decorrelation	89
B.4	p_T -differential normalized symmetric cumulant	90
C	2018 data measurements	94
C.1	$v_n\{2\}/v_n[2]$	94
C.2	Factorization ratio r_n	98
C.3	Angle Decorrelation $C(\Psi_n)$	100
C.4	p_T -differential normalized symmetric cumulant	101
	List of Figures	103
	List of Tables	109

1 Introduction

This section presents the current theoretical understanding of heavy-ion physics relevant to this thesis. First, an overview of the Standard Model (SM) focusing on the theory of Quantum Chromodynamics (QCD) is given. Then, the theory of heavy-ion collisions and the concept of Quark-Gluon Plasma (QGP), and how it relates to hydrodynamics, is discussed. Finally, the core concept of anisotropic flow and collective behaviour as a probe of QGP in heavy-ion collisions is described, and relevant measurements from previous works are discussed.

1.1 The Standard Model

The Standard Model (SM) is a theory describing fundamental particles and their interactions. The particles in the Standard Model are divided into two types: fermions and bosons. The fermions are particles with half-integer spin and are further divided into *quarks* and *leptons*. Within the SM, these particles interact via three fundamental forces. These forces, or interactions, are mediated by the integer spin bosons. The massless *photon* is responsible for the electromagnetic interactions. The weak interactions are mediated by the massive W^\pm and Z bosons, and finally, the massless *gluons* carry the strong interactions. Aside from being divided into six leptons and six quarks, the fermions are also divided into three generations with the mass increasing as you go further up the generations. The six quarks are identified by their flavour: *up*, *down*, *charm*, *strange*, *top* and *bottom*. The six leptons are paired in each generation: *electron* and *electron neutrino*, *muon* and *muon neutrino*, and *tauon* and *tauon neutrino*. Finally, the Standard Model also includes the spin-0 Higgs boson, which is responsible for giving the other particles their mass through the Higgs mechanism [1, 2, 3]. All the particles of the Standard Model, along with their mass, electric charge, and spin, are summarized in figure 1.1. Each particle also has a corresponding anti-particle, which is identical but carries opposite physical charges (such as electric charge). Some particles are their own anti-particles, e.g., the photon, gluons, and the Higgs.

The particles of the Standard Model interact through the different forces based on the properties of the particle. Particles carrying electric charge can interact via the electromagnetic force, which is the most well known of the fundamental forces. The weak interaction allows for the quarks and leptons to change their flavour. This phenomenon can be seen in nuclear β -decay, where a down-quark is converted into an up-quark by emission of a W^- , which subsequently decays into an electron and electron neutrino. Finally, the strong interaction occurs between particles that carry *colour charge*, which are the quarks and gluons. This also allows for self-interactions between the mediating gluons, since they themselves carry a colour charge.

The theory that describes the strong interaction is Quantum Chromodynamics (QCD), which is a local quantum field theory based on the $SU(3)$ gauge group [5, 6]. The name of QCD refers to the fact that the particles interacting through the strong force carry a charge called "colour" [7]. Since QCD is based on a 3-dimensional symmetry group, there are three colour charges: red, green, and blue, as well as the corresponding anti-colours. The quarks carry one colour each, and the gluons carry one colour and one anti-colour. The strength of the strong interaction is determined by the coupling constant α_s . This is a running coupling constant, which means that the strength of the strong interaction depends on the length (or energy) scale. At long distances (or low

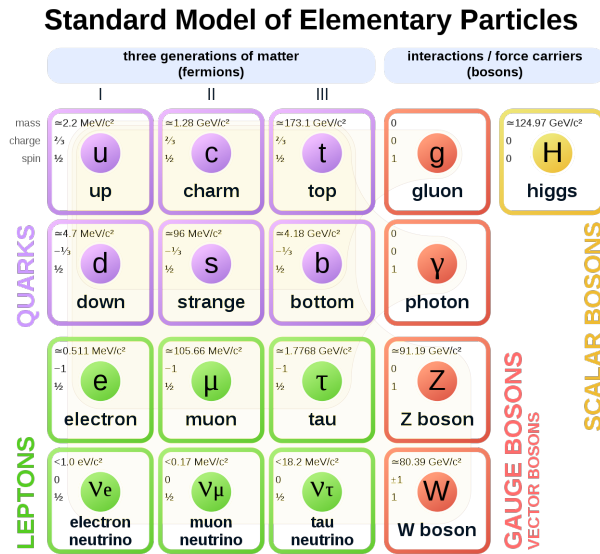


Figure 1.1: The particles of the standard model with their mass, charge, and spin. Figure from [4]

energies), α_s increases, while at short distances, it decreases. These properties of the QCD coupling constant give rise to two critical features of the strong interaction: *colour confinement* and *asymptotic freedom* [8, 9].

Colour confinement refers to the phenomenon that colour-charged particles cannot be isolated. Since α_s increases with the distance, there comes a point, when separating two quarks, where the energy is high enough that it becomes energetically favourable to create a new quark-antiquark pair from the vacuum. This means that it is not possible to observe free quarks under normal conditions. The quarks are confined in colour neutral objects called *hadrons*. In processes where quarks are produced, they will move away from each other, and new quark-antiquark pairs are created along the way, forming into a multitude of hadrons. This process is called *hadronization*, and the hadrons will form 'jets' originating from the initial quarks.

Asymptotic freedom is observed at short distances (or large energies) when α_s decreases, and the strong interaction becomes weak. This leads to deconfinement of the quarks and gluons since they are no longer bound in the hadrons. This allows for a new state of matter of free quarks and gluons called Quark-Gluon Plasma (QGP). It is believed that the universe was composed of such a matter microseconds after Big Bang, and the purpose of high-energy heavy-ion experiments is to study the properties and dynamics of this matter.

1.2 Heavy-ion collisions

High-energy heavy-ion collisions are conducted at the Large Hadron Collider, where lead nuclei are accelerated to close to the speed of light and brought to a collision at interaction points around the accelerator ring. The high velocities result in a Lorentz contraction of the nuclei into thin, narrow discs. These discs will be brought into collision with some impact parameter b , describing the geometrical overlap of the two nuclei. Depending on the impact parameter, not all of the nucleons will interact. The interacting nucleons are called participants, and the rest are called spectators. Figure

1.2 shows a simplified picture of a heavy-ion collision. The high energy density in the central region of the collision results in a new system, which rapidly expands and cools down. The space-time evolution of a collision can be described in terms of the light

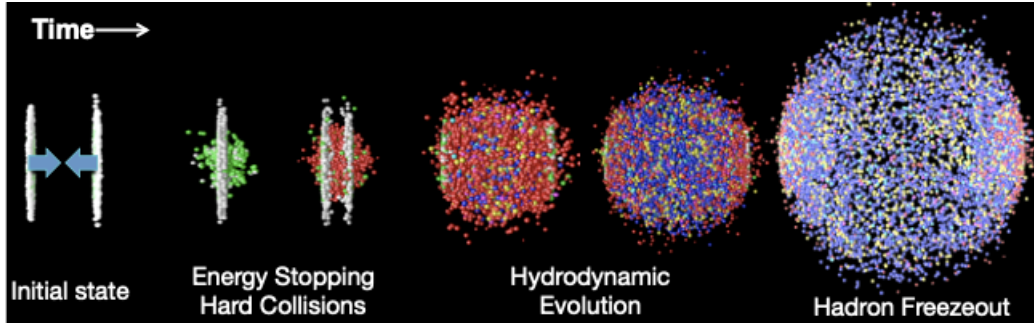


Figure 1.2: Sketch of a central collision of two high energy nuclei in the center-of-mass frame [10].

cone variables: time, t , and longitudinal direction, z . Figure 1.3 shows the evolution of the collision system. The proper time $\tau = \sqrt{t^2 - z^2}$ is constant along the hyperbola separating the different phases. The evolution of the system created in heavy-ion col-

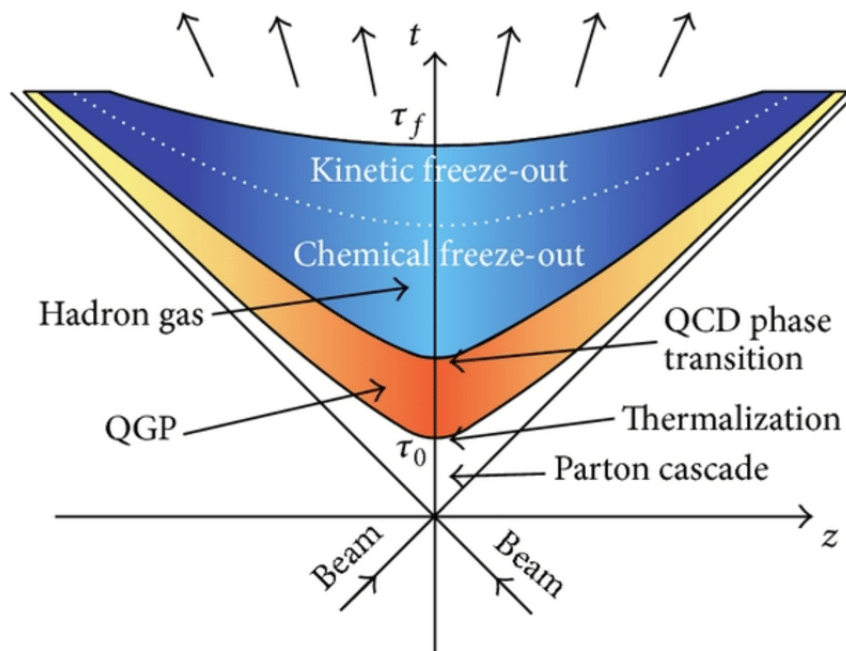


Figure 1.3: Space-time evolution of a heavy-ion collision [11].

lisions can be described in the following stages [12]:

1. The nuclei collide at a time $\tau = 0$, and the first interactions to start are those of the *hard processes*, which involve large transferred momenta. These processes are responsible for producing 'hard particles' such as hadronic jets, direct photons, dilepton pairs, heavy quarks, or vector bosons. The final state is often characterized by the hard processes, e.g., 'a dijet event'.

2. Shortly after in time, $\tau = 0.2 \text{ fm}/c$, the system enters a *pre-equilibrium* state, where the bulk of gluons are liberated by the collision. Most of the final state partons are created in this phase via fragmentation and hadronization of the liberated initial state gluons. Just after being liberated, the partons form into a dense medium called *glasma* with a high energy density.
3. The partons liberated by the collision interact strongly with each other, which is manifested as a collective behaviour in the evolution of the partons. If there were no interactions, the partons would evolve independently towards the final state hadrons. The partonic matter quickly approaches a local *thermal equilibrium* with thermalization time of order $\tau \sim 1 \text{ fm}/c$. The thermalization process leads to the high-temperature phase of QCD known as Quark-Gluon Plasma (QGP) [13, 14, 15]. The QGP is a strongly coupled so-called 'perfect fluid' due to its extremely low viscosity and can be described by hydrodynamics.
4. As the QGP cools down and expands the system undergoes a *phase transition* as it reaches the critical temperature T_c at around $\tau \sim 10 \text{ fm}/c$. The partonic matter now hadronizes as the coloured quarks and gluons become trapped in colourless hadrons. The hadrons continue to interact with each other as the hadron gas cools down and expands. The *chemical freeze-out* is reached when the inelastic processes stop, and the chemical composition of the hadrons are frozen.
5. In the end, at around $\tau = 20 \text{ fm}/c$, the density of the system has become so low that the elastic processes cease and the hadrons no longer interact with each other. After this *kinetic freeze-out*, the particles free-stream through the vacuum into the detector.

The transition from the hot and dense matter to the hadron gas can be visualized with a phase diagram, as in figure 1.4. The phase diagram is drawn with the temperature, T , on the y-axis, and the baryon chemical potential, μ_B , on the x-axis. The μ_B is connected to the net baryon density: when $\mu_B = 0$, there are equal amounts of baryons and anti-baryons. Values of $\mu_B > 0$ indicate that baryons dominate over anti-baryons. The LHC experiments provide high-energy heavy-ion collisions that can probe the high-temperature regime of the QCD phase diagram with low values of μ_B since the amount of newly created particles (which are equal amounts of baryons and anti-baryons) will heavily outnumber the constituent baryons of the nuclei. Collisions with lower energies can probe the QCD phase diagram at higher values of μ_B since the baryons of the colliding nuclei will become significant. The transition from the colour confined hadron gas to the QGP is a heavily studied subject. At lower temperatures and higher values of μ_B , the transition is of first order, while at higher temperatures and low μ_B , the transition is believed to be a cross-over. The critical temperature, T_c and energy density, ϵ_c , required for the QCD matter to undergo phase transition from hadron gas to QGP is estimated with lattice QCD to be $145\text{MeV} \leq T_c \leq 163\text{MeV}$ [16] and $0.18 \leq \epsilon_c \leq 0.5 \text{ GeV}/\text{fm}^3$ [16]. The point where the cross-over becomes a first-order phase transition is called the critical point and is studied at the Relativistic Heavy Ion Collider (RHIC) with the Beam Energy Scan (BES) [17].

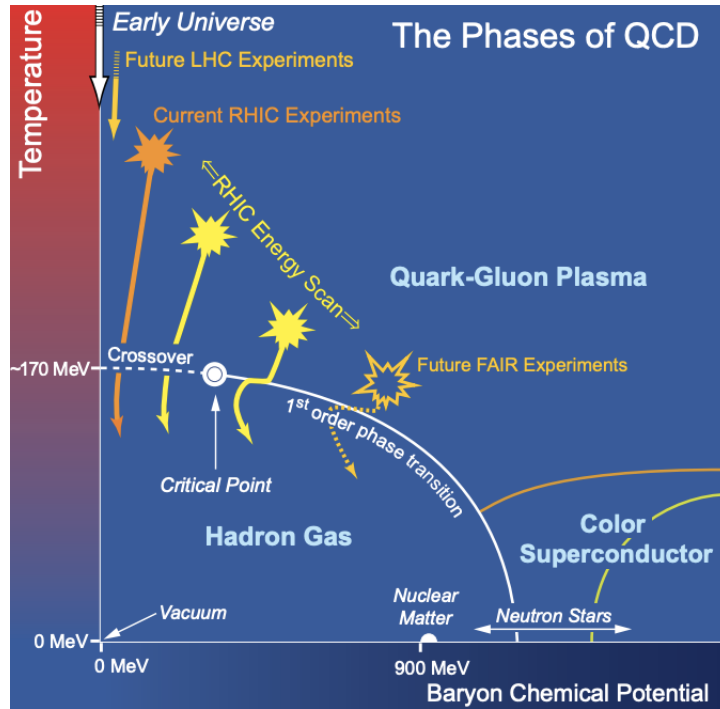


Figure 1.4: Diagram showing the QCD phase space. Figure is taken from [18].

1.2.1 Theoretical description of heavy-ion collisions

The current technological level of measuring capabilities does not allow for direct measurements of the QGP phase. Instead, the final distribution of particles is used as a probe of the earlier stages of the collision. To understand how these early stages affect the final particle distribution, the entire evolution of the heavy-ion collision needs to be understood. Inaccuracies in any stage can propagate to adjacent stages and lead to wrong predictions and data comparisons.

Hydrodynamics

The system created after the thermalization time $\tau \sim 1 \text{ fm}/c$ can be described with relativistic hydrodynamics [19, 20]. Hydrodynamics only relies on one assumption, i.e., local thermal equilibrium, which requires that the mean free path of the particles is smaller than the size of the system. The local thermal equilibrium is reached in heavy-ion collisions at $\tau \sim 1 \text{ fm}/c$. Initial conditions are necessary to describe the state of the system as it transitions to hydrodynamics. One general feature of the initial conditions is that transverse momentum averaged over a fluid element is zero since there is no preferred direction in a parton-parton collision. Any transverse collective motion observed in data must therefore be due to an intermediate hydrodynamic stage.

Hydrodynamic equation derived under the assumption of local thermal equilibrium are called ideal-fluid equations. These involve the local conservation of energy and momentum:

$$\partial_\mu T^{\mu\nu} = 0, \quad (1.1)$$

and local charge conservation:

$$\partial_\mu J_i^\mu(x) = 0, \quad i = 1, \dots, M \quad (1.2)$$

where J_i^μ is the charge current density of charges such as net baryon density or electric charge.

In heavy-ion collisions, the assumption of local thermal equilibrium is only an approximation, and the ideal-fluid equations do not hold for the expanding system. Relativistic viscous hydrodynamics study the deviations from local thermal equilibrium and involve the parameters *shear viscosity* η and the *bulk viscosity* ζ . The shear viscosity describes the friction between the fluid elements. Low values of shear viscosity indicate a strongly interacting fluid. In contrast, large values will smooth out the initial anisotropy, and therefore reduce the observed final anisotropic momentum distribution in terms of the flow coefficients v_n (see section 1.3). In heavy-ion collisions the ratio of the shear viscosity to entropy density η/s can be extracted, and has experimentally been constrained to values of $\eta/s \approx 0.08 - 0.20$, when using fixed values of η/s , which are close to the lower boundary $\eta/s \geq \hbar/4\pi k_B$ predicted with string theory [21]. However, it is also possible to let the transport coefficient evolve with the temperature of the system $\eta/s(T)$, $\zeta/s(T)$, in which case the values of η/s can exceed 0.2. The bulk viscosity describes the fluid's resistance to expansion and affects radial flow. The effect of the bulk viscosity on the development of anisotropic flow is negligible compared to the shear viscosity [22], however, there is some argument for the inclusion of a non-zero ζ/s [23].

In this thesis, the iEBE-VISHNU model [24] is used for comparison with data. The model is based on (2+1)-dimensional viscous hydrodynamics coupled to a hadronic cascade model. Initial conditions from A Multi-Phase Transport (AMPT) model [25, 26, 27, 28], and the TRENTo model [29] are used as input in the iEBE-VISHNU hydrodynamic model. The AMPT initial conditions include fluctuations of the initial state at nucleonic and subnucleonic levels and consider the partonic matter's pre-equilibrium dynamics [26]. The hydrodynamic model with the AMPT initial conditions use a constant value of shear viscosity over entropy density $\eta/s = 0.08$ and $\zeta/s = 0$. The TRENTo initial condition model does not assume any specific physical mechanism for entropy production, pre-equilibrium dynamics, or thermalization. In the hydrodynamic model with TRENTo initial conditions, the transport coefficients are temperature-dependent $\eta/s(T)$ and $\zeta/s(T)$, and are extracted using Bayesian analysis [30] from a fit to the final multiplicities of the charged hadron spectra in Pb–Pb collisions at $\sqrt{s_{NN}} = 5.02$ TeV.

1.3 Anisotropic flow in heavy-ion collisions

The heavy ions can collide with different geometrical overlaps. This can be characterized by the impact parameter b , which denotes the distance between the two centers of the nuclei in the transverse plane. A central collisions refers to $b \approx 0$, a semi-central collision has $b > 0$ and a peripheral collision has $b \gg 0$. The different types of heavy-ion collisions imply different geometries of the overlapping area between the two nuclei. A central collision will involve almost all the nucleons in the collisions and thus have a circular geometry. A peripheral collision only collides a fraction of the nucleons and will have an 'almond'-shaped overlap, as shown in figure 1.5. Anisotropies in the initial geometry lead to different pressure gradients. The geometry shown in figure 1.5 will lead to larger pressure gradients along the x-axis than along the y-axis. Strong interactions between the partons in the QGP will then transmit the initial anisotropies into the final anisotropic particle distributions. The properties of the QGP created in

high-energy heavy-ion collisions can thus be probed by observing the azimuthal distribution of particles. However, the initial geometry is highly irregular and should be viewed as a superposition of simpler geometries.

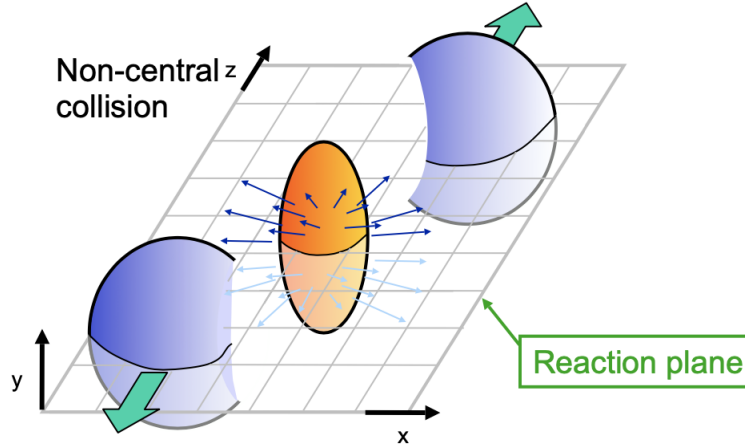


Figure 1.5: Sketch of the geometry of a peripheral heavy-ion collision. The interaction region is marked by the cut-out almond shape and is horizontally cut by the reaction plane. Figure taken from [12].

The traditional way of measuring anisotropic flow is with a Fourier expansion of the azimuthal dependence of the distribution of particles relative to some common symmetry planes [31]:

$$\frac{dN}{d\varphi} = 1 + 2 \sum_{n=1}^{\infty} V_n e^{in\varphi}, \quad (1.3)$$

where φ is the azimuthal angle of particles and $V_n = v_n e^{in\Psi_n}$ is the flow vector with magnitude v_n and phase Ψ_n . The v_n flow coefficients corresponding to the harmonic n is given by:

$$v_n = \langle \cos[n(\varphi - \Psi_n)] \rangle, \quad (1.4)$$

where brackets $\langle \rangle$ refer to an average over a sample of collisions. The v_n coefficient can be understood as the correlation of particles with respect to the common symmetry planes.

1.3.1 Measurements of anisotropic flow

In this section, measurements of anisotropic flow in heavy-ion collisions are summarized. The focus of this section will be on the general anisotropic flow measurements obtained with the ALICE experiment. The more niche measurements pertaining to this thesis will be discussed in section 5, where measurements of p_T -dependent flow vector fluctuations are presented.

Measurements of the flow coefficients v_n are shown in figure 1.6 as function of centrality in Pb–Pb collisions at $\sqrt{s_{NN}} = 5.02$ TeV. The anisotropic flow coefficient v_n quantifies the anisotropic flow as moments of the azimuthal particle distribution. The methods for extracting the flow coefficients from particle correlations are described in section 2. The elliptic flow v_2 dominates and increases as the collisions become more peripheral. This is consistent with the picture from figure 1.5, where the ‘almond’-shaped

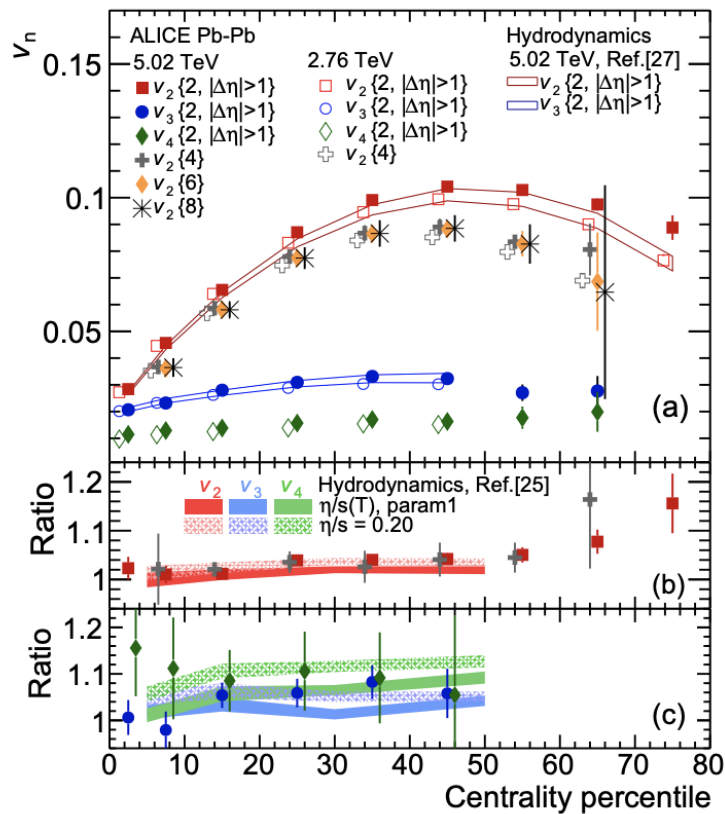


Figure 1.6: Measurements of the anisotropic flow coefficient v_n as a function of centrality. The measurements are compared to hydrodynamic calculations. Figure from [32].

geometry gives rise to high anisotropic flow compared to central collisions, where the geometry is almost circular. Measurements of v_2 from two-particle correlations $v_2\{2\}$ are larger than v_2 measured from higher-order particle correlations $v_2\{m\}$ with $m > 2$. This is due to fluctuations of the v_n distributions, which affect cumulants differently. In two-particle cumulants, the contribution of flow fluctuations is positive, while in higher-order cumulants, the contribution is negative. The non-zero values of the higher-order harmonics v_3 and v_4 show that more complex geometries, i.e., triangular and quadrangular, are also present in the system but at much lower magnitudes than the elliptic flow v_2 . It has been found that the higher-order flow is more sensitive to η/s , and can thus be a better way to constrain hydrodynamic models [33]. The comparison of the v_n coefficients to the hydrodynamic models allows the initial conditions of the heavy-ion collisions and the transport properties of the QGP to be extracted, and supports the idea of a 'perfect fluid' QGP phase of the system.

Differential measurements of the flow coefficient v_n regarding properties such as transverse momentum (p_T) or pseudorapidity (η) can help further constrain the hydrodynamic models. Measurements of v_n as a function of p_T can help constrain the equations of state in the hydrodynamic equations. The pseudorapidity-dependence of the flow harmonics plays a key role in understanding the temperature dependence of η/s , since the average temperature drops at forward rapidities, which implies η/s will also change [34]. The measurements of v_n as function of p_T and η are shown in figure 1.7.

It is observed that v_2 increases as function of p_T and reaches a peak at ~ 3 GeV/ c . As a function of η , the flow coefficients v_2 , v_3 and v_4 peak around $\eta \approx 0$ and drops off as $|\eta|$ increases.

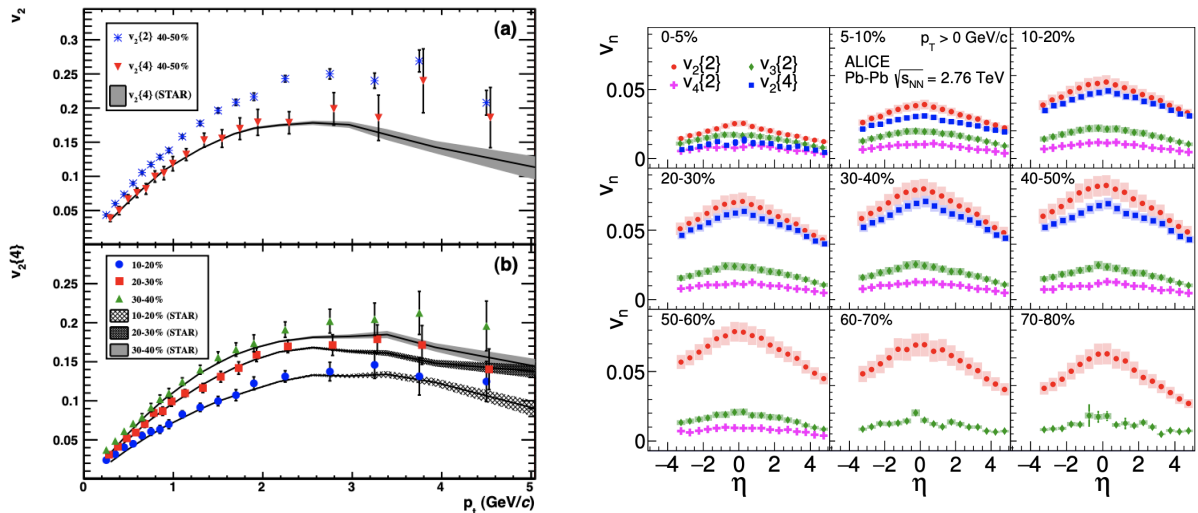


Figure 1.7: Measurements of the flow coefficient v_n as function of p_T (left) and η (right) in Pb-Pb collisions at $\sqrt{s_{NN}} = 2.76$ TeV. The left figure is taken from [35] and the right from [34].

A better method of extracting QGP properties from data was developed in [36] by applying Bayesian parameter estimation methods to a dynamical collision model (TRENTo) and a variety of experimental data. The method uses the likelihood, which quantifies how well the desired model parameters describe the experimental data, and a prior, which contains the initial knowledge of the parameters. The posterior distribution can then be obtained via Bayes' Theorem, and the model parameters can be extracted. Through this method, values of η/s and ζ/s are estimated as functions of temperature as shown in figure 1.8. The results show a slight preference for a positive slope of η/s , but cannot fully exclude a zero slope (constant value of η/s). Additionally, it is suggested that it is the integral of ζ/s that matters not its specific form. The validity of the posterior distribution and parameter estimates are evaluated by comparison with the experimental data, as shown in figure 1.9. This method provides strong constraints on the initial conditions of heavy-ion collisions and transport coefficients of the QGP. It can be further refined by including more experimental data or improving the collisions model. The methodology can also be used to extract other physical properties of heavy-ion collisions such as the heavy-quark diffusion coefficient [37] or the nucleon substructure [38].

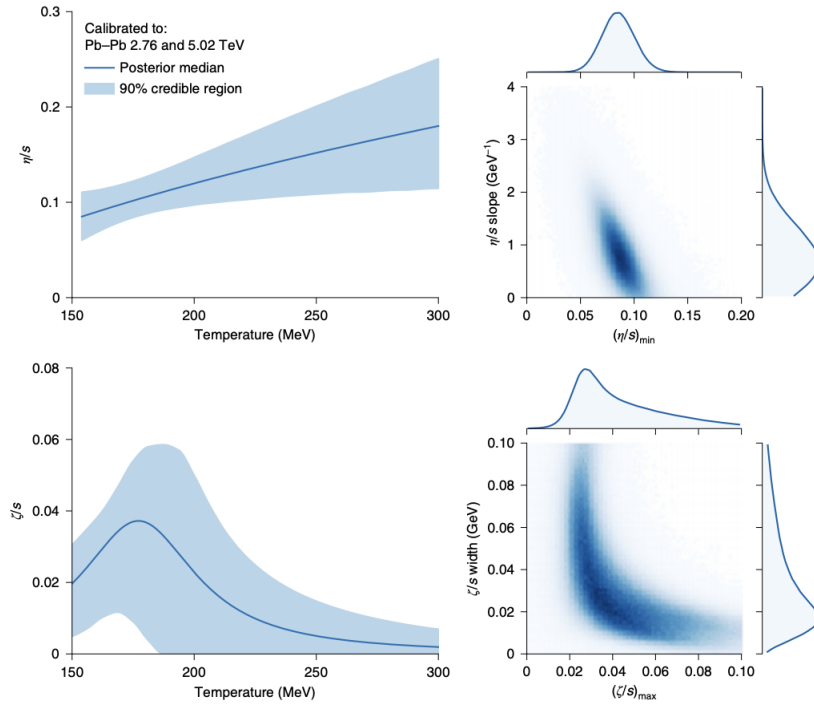


Figure 1.8: Estimated temperature dependence of shear viscosity η/s and bulk viscosity ζ/s using Bayesian parameter estimation method. Figure taken from [36].

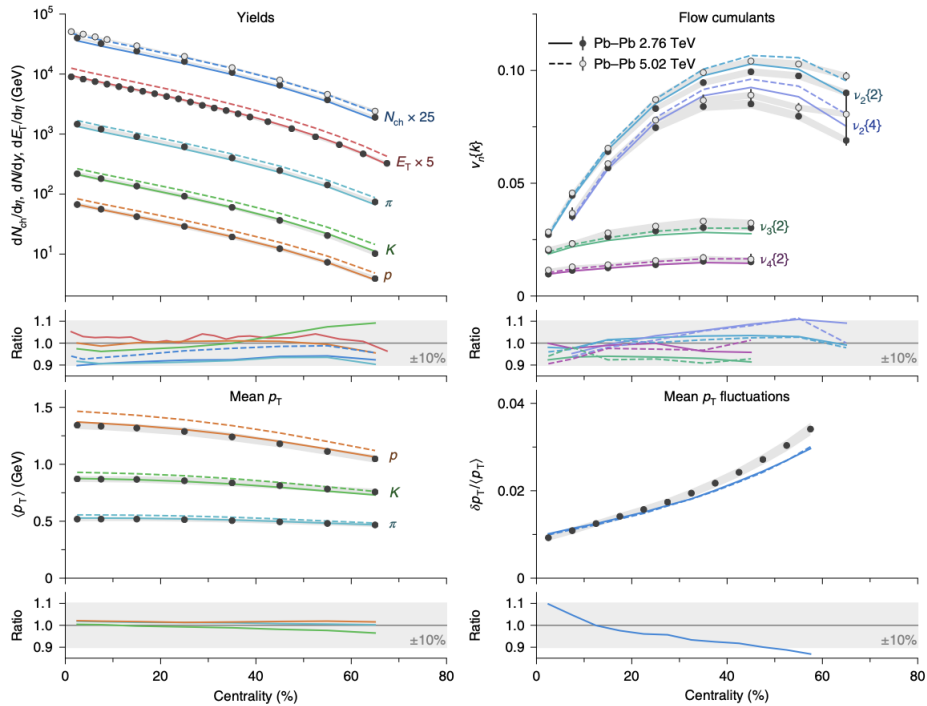


Figure 1.9: Comparison of model calculations using best-fit *maximum a posteriori* (MAP) parameters to experimental data for different observables as a function of centrality. Upper left: yields of charged particles, transverse energy, and identified particles. Lower left: mean transverse momenta $\langle p_T \rangle$. Upper right: Anisotropic flow cumulants $v_n\{k\}$. Lower right: mean transverse momentum fluctuations $\delta p_T / \langle p_T \rangle$.

2 Analysis methods

In this section, the methods of extracting flow-related measurements from data are presented. First, the standard methods of calculating azimuthal correlations are presented in section 2.1: Multi-particle azimuthal correlations, Q-cumulant method, and the Generic Framework. The subevent method is then presented for the Q-cumulant method and the Generic Framework in section 2.2. Finally, how the physical observables, which probe p_T -dependent flow vector fluctuations, are obtained from azimuthal correlations using the subevent method in the Generic Framework is shown.

2.1 Standard methods of azimuthal correlations

2.1.1 Multi-particle azimuthal correlations

The correlation between m -particles in harmonics n_1, n_2, \dots, n_m is given by:

$$\langle m \rangle_{n_1, n_2, \dots, n_m} = \langle e^{i(n_1\varphi_1 + n_2\varphi_2 + \dots + n_m\varphi_m)} \rangle \quad (2.1)$$

Here the $\langle \rangle$ represents the average over all the combinations of correlation between all M particles. An event-averaged correlation is then obtained, which is denoted as:

$$\langle \langle m \rangle \rangle_{n_1, n_2, \dots, n_m} = \langle \langle e^{i(n_1\varphi_1 + n_2\varphi_2 + \dots + n_m\varphi_m)} \rangle \rangle \quad (2.2)$$

The double brackets $\langle \langle \rangle \rangle$ represents the weighted average over many events. This thesis only uses two- and four-particle correlations, so higher-order particle correlations will not be discussed. In particular, eq. (2.1) gives the single-event average two- and four-particle correlations as:

$$\langle 2 \rangle \equiv \langle e^{in(\varphi_1 - \varphi_2)} \rangle \equiv \frac{1}{P_{M,2}} \sum'_{i,j} e^{in(\varphi_i - \varphi_j)} \quad (2.3)$$

$$\langle 4 \rangle \equiv \langle e^{in(\varphi_1 + \varphi_2 - \varphi_3 - \varphi_4)} \rangle \equiv \frac{1}{P_{M,4}} \sum'_{i,j,k,l} e^{in(\varphi_i + \varphi_j - \varphi_k - \varphi_l)} \quad (2.4)$$

Here $P_{n,m} = n!/(n-m)!$ and the prime in the sum means taking all indices to be different in order to avoid self-correlations (also called auto-correlations). The event-averaged two- and four-particle correlations are then obtained via

$$\langle \langle 2 \rangle \rangle = \frac{\sum_{events} (W_{\langle 2 \rangle})_i \langle 2 \rangle_i}{\sum_{events} (W_{\langle 2 \rangle})_i} \quad (2.5)$$

$$\langle \langle 4 \rangle \rangle = \frac{\sum_{events} (W_{\langle 4 \rangle})_i \langle 4 \rangle_i}{\sum_{events} (W_{\langle 4 \rangle})_i} \quad (2.6)$$

Here $W_{\langle n \rangle}$ is an event weight, which minimizes the effect of multiplicity variations in the event sample and the optimal choice for the event weights is:

$$W_{\langle 2 \rangle} \equiv M(M-1) \quad (2.7)$$

$$W_{\langle 4 \rangle} \equiv M(M-1)(M-2)(M-3) \quad (2.8)$$

The most straightforward way of calculating the correlations between the particles is through nested loops. For a m -particle correlation with M total particles in an event, the number of times the m loops are executed is:

$$N_{\text{loop}} = \prod_{i=0}^{m-1} (M - i) \quad (2.9)$$

This quickly becomes an extremely CPU intensive calculation for multi-particle correlations in high multiplicity events. This method also does not allow for corrections of detector inefficiencies, so the measurements will be biased by non-uniform acceptances and efficiencies (see section 4.4). Obviously, better methods are required.

2.1.2 Q-cumulant method

A better method for measuring the azimuthal correlations between particles, called the Q-cumulant method, was proposed in [39]. The multi-particle cumulants can be calculated via the multi-particle correlations, using the Q-vector Q_n for harmonic n , which is defined as the complex vector:

$$Q_n = \sum_{k=1}^M e^{in\phi_k}, \quad (2.10)$$

where ϕ is the azimuthal angle and M is the number of correlated particles within a certain phase space of the detector. This allows the m -particle correlation of any order to be obtained in a single loop over the particles in the event. A more thorough description of how the reference flow and differential flow are measured in the Q-cumulant method follows.

Reference Flow

The reference flow is the average flow in some wide window of transverse momentum. The total two-particle correlation of the reference flow is obtained by separating diagonal and off-diagonal terms in $|Q_n|^2$:

$$|Q_n|^2 = \sum_{i,j=1}^M e^{in(\varphi_i - \varphi_j)} = M + \sum_{i,j} ' e^{in(\varphi_i - \varphi_j)}. \quad (2.11)$$

Here Q_n is the event-flow vector from (2.10), and M is the number of reference particles. The total number of particle pairs is $M(M-1)$ so the two-particle correlation averaged over the number of particles is:

$$\langle 2 \rangle = \frac{|Q_n|^2 - M}{M(M-1)}. \quad (2.12)$$

In a similar manner, the single-event averaged four-particle correlation is obtained from the decomposition of $|Q_n|^4$:

$$|Q_n|^4 = Q_n Q_n Q_n^* Q_n^* = \sum_{i,j,k,l} e^{in(\varphi_i + \varphi_j - \varphi_k - \varphi_l)}. \quad (2.13)$$

When all the self-correlating terms have been corrected for, the following analytical expression is obtained:

$$\langle 4 \rangle = \frac{|Q_n|^4 + |Q_{2n}|^2 - 2 \cdot \text{Re}[Q_{2n} Q_n^* Q_n^*]}{M(M-1)(M-2)(M-3)} - 2 \frac{2(M-2) \cdot |Q_n|^2 - M(M-3)}{M(M-1)(M-2)(M-3)}. \quad (2.14)$$

The final event-averaged two- and four-particle correlations can then be obtained using Eq. (2.5) and Eq. (2.6) with the weights from Eq. (2.7) and Eq. (2.8).

Differential Flow

The reference flow from the previous section enables the calculation of the differential flow. The differential flow looks at particles in some region of interest in η or p_T relative to the reference flow. The particles used in the analysis are labeled as either *reference flow particle* (RP) and/or *particle of interest* (POI). The POIs are particles from the specific η/p_T region that is of interest to measure.

The differential flow is calculated with the p_n and q_n vectors. The former is built out of all POIs, and the latter one only from POIs labeled also as RFPs. They are calculated via:

$$p_n = \sum_{k=1}^{m_p} e^{in\phi_k} \quad (2.15)$$

$$q_n = \sum_{k=1}^{m_q} e^{in\phi_k}, \quad (2.16)$$

where m_p is the total number of particles labeled as POIs, m_q is the total number of particles tagged both as RFP and POI. Using the p_n and q_n vectors, the following equations for the single-event average two- and four-particle correlations are obtained:

$$\langle 2' \rangle = \frac{p_n Q_n^* - m_q}{m_p M - m_q} \quad (2.17)$$

$$\begin{aligned} \langle 4' \rangle = & [p_n Q_n Q_n^* Q_n^* - q_{2n} Q_n^* Q_n^* - p_n Q_n Q_{2n}^* - 2 \cdot M p_n Q_n^* - 2 \cdot m_q |Q_n|^2 \\ & + 7 \cdot q_n Q_n^* - Q_n q_n^* + q_{2n} Q_{2n}^* + 2 \cdot p_n Q_n^* + 2 \cdot m_q M - 6 \cdot m_q] \\ & / [(m_p M - 3m_q)(M - 1)(M - 2)]. \end{aligned} \quad (2.18)$$

The event-average differential two- and four-particle azimuthal correlations are then calculated analogue to Eq. (2.5) and Eq. (2.6) with $\langle 2' \rangle$ replacing $\langle 2 \rangle$, and $\langle 4' \rangle$ replacing $\langle 4 \rangle$. Similarly, the weights are modified and now read:

$$W_{\langle 2' \rangle} \equiv m_p M - m_q \quad (2.19)$$

$$W_{\langle 4' \rangle} \equiv (m_p M - 3m_q)(M - 1)(M - 2). \quad (2.20)$$

Issues with the Q-cumulant method

The Q-cumulant method removes the bias that existed in the original cumulant analysis [40], which did not account for the interference of different order harmonics, since the original method neglected terms evaluated in the different order harmonics (such as $|Q_{2n}|^2$ and $\text{Re}[Q_{2n} Q_n Q_n^*]$). These terms cancel out the higher-order contributions picked up by $|Q_n|^4$, when such a higher-order harmonic is present. However, the method presented here assumes full uniform azimuthal coverage in the detector. In circumstances, where this is not the case (which is unfortunately the reality for all experiments) the cumulants will pick up additional terms and have contributions from different order flow harmonics. This will affect the extracted flow values [41, 42]. It is possible to correct for these effects with additional terms. These terms will not be explained here, however, as this thesis uses the Generic Framework [43], which improves upon the Q-cumulant method in numerous ways, in order to calculate the genuine azimuthal correlations.

2.1.3 Generic framework

The Generic Framework [43] was introduced as an improved method of calculating any generic multi-particle correlation in an exact and fast fashion. It has the capability of correcting for systematic biases due to various detector inefficiencies by introducing a weight w on the Q-vector:

$$Q_{n,p} = \sum_{k=1}^M w_k^p e^{in\varphi_k}, \quad Q_{-n,p} = Q_{n,p}^* \quad (2.21)$$

The p- and q-vectors are constructed similarly with their corresponding multiplicities:

$$p_{n,p} = \sum_{k=1}^{m_p} w^k e^{in\varphi_k}, \quad p_{-n,p} = p_{n,p}^* \quad (2.22)$$

$$q_{n,p} = \sum_{k=1}^{m_q} w^k e^{in\varphi_k}, \quad q_{-n,p} = q_{n,p}^*. \quad (2.23)$$

It is also possible to correlate particles coming from either the same or different p_T intervals. When correlating particles from two different p_T intervals, one particle is denoted the *associate* particle and the other the *trigger* particle. Correlations of this type need a p-vector constructed in the trigger particle p_T^t interval:

$$p_{n,p}^t = \sum_{k=1}^{m_t} w^k e^{in\varphi_k}, \quad p_{-n,p}^t = p_{n,p}^{t*}. \quad (2.24)$$

Where m_t is the number of particles labeled as POI in the p_T^t interval.

Well known examples of particle weights are so-called φ -weights, w_φ , which deal with the systematic bias due to non-uniform acceptance in azimuth (see section 4.4), and p_T -weights, w_{p_T} , which deal with the non-uniform reconstruction efficiency in different transverse momentums of produced particles. In general, the particle weight w is allowed to be the most general function of the azimuthal angle, transverse momentum, pseudorapidity, particle type, etc.:

$$w = w(\varphi, p_T, \eta, \text{PID}, \dots). \quad (2.25)$$

With the weights the average m -particle correlation in harmonics n_1, n_2, \dots, n_m is given by the following generic definition:

$$\begin{aligned} \langle m \rangle_{n_1, n_2, \dots, n_m} &\equiv \left\langle e^{i(n_1\varphi_{k_1} + n_2\varphi_{k_2} + \dots + n_m\varphi_{k_m})} \right\rangle \\ &= \frac{\sum_{\substack{k_1, k_2, \dots, k_m=1 \\ k_1 \neq k_2 \neq \dots \neq k_m}}^M w_{k_1} w_{k_2} \dots w_{k_m} e^{i(n_1\varphi_{k_1} + n_2\varphi_{k_2} + \dots + n_m\varphi_{k_m})}}{\sum_{\substack{k_1, k_2, \dots, k_m=1 \\ k_1 \neq k_2 \neq \dots \neq k_m}}^M w_{k_1} w_{k_2} \dots w_{k_m}}. \end{aligned} \quad (2.26)$$

The Generic Framework utilizes that the expressions in the numerator and the denominator of Eq. (2.26) are trivially related. Namely, given the result for the numerator which depends on harmonics n_1, n_2, \dots, n_m , the result for the denominator can be obtained by using the result for numerator and setting all harmonics n_1, n_2, \dots, n_m to 0.

Therefore the focus is mostly on the results for the numerator in what follows, and the following shortcuts are introduced:

$$N\langle m \rangle_{n_1, n_2, \dots, n_m} \equiv \sum_{\substack{k_1, k_2, \dots, k_m=1 \\ k_1 \neq k_2 \neq \dots \neq k_m}}^M w_{k_1} w_{k_2} \cdots w_{k_m} e^{i(n_1 \varphi_{k_1} + n_2 \varphi_{k_2} + \dots + n_m \varphi_{k_m})}, \quad (2.27)$$

$$\begin{aligned} D\langle m \rangle_{n_1, n_2, \dots, n_m} &\equiv \sum_{\substack{k_1, k_2, \dots, k_m=1 \\ k_1 \neq k_2 \neq \dots \neq k_m}}^M w_{k_1} w_{k_2} \cdots w_{k_m} \\ &= N\langle m \rangle_{0, 0, \dots, 0}. \end{aligned} \quad (2.28)$$

The results for the case of reference two- and four-particle correlators expressed analytically in terms of Q -vectors defined in Eq. (2.10) are presented here. For two-particle reference flow it follows:

$$N\langle 2 \rangle_{n_1, n_2} = Q_{n_1, 1} Q_{n_2, 1} - Q_{n_1+n_2, 2}, \quad (2.29)$$

$$\begin{aligned} D\langle 2 \rangle_{n_1, n_2} &= N\langle 2 \rangle_{0, 0} \\ &= Q_{0, 1}^2 - Q_{0, 2}. \end{aligned} \quad (2.30)$$

For 4-particle correlators the following is obtained:

$$\begin{aligned} N\langle 4 \rangle_{n_1, n_2, n_3, n_4} &= Q_{n_1, 1} Q_{n_2, 1} Q_{n_3, 1} Q_{n_4, 1} - Q_{n_1+n_2, 2} Q_{n_3, 1} Q_{n_4, 1} - Q_{n_2, 1} Q_{n_1+n_3, 2} Q_{n_4, 1} \\ &\quad - Q_{n_1, 1} Q_{n_2+n_3, 2} Q_{n_4, 1} + 2Q_{n_1+n_2+n_3, 3} Q_{n_4, 1} - Q_{n_2, 1} Q_{n_3, 1} Q_{n_1+n_4, 2} \\ &\quad + Q_{n_2+n_3, 2} Q_{n_1+n_4, 2} - Q_{n_1, 1} Q_{n_3, 1} Q_{n_2+n_4, 2} + Q_{n_1+n_3, 2} Q_{n_2+n_4, 2} \\ &\quad + 2Q_{n_3, 1} Q_{n_1+n_2+n_4, 3} - Q_{n_1, 1} Q_{n_2, 1} Q_{n_3+n_4, 2} + Q_{n_1+n_2, 2} Q_{n_3+n_4, 2} \\ &\quad + 2Q_{n_2, 1} Q_{n_1+n_3+n_4, 3} + 2Q_{n_1, 1} Q_{n_2+n_3+n_4, 3} - 6Q_{n_1+n_2+n_3+n_4, 4}, \end{aligned} \quad (2.31)$$

$$\begin{aligned} D\langle 4 \rangle_{n_1, n_2, n_3, n_4} &= N\langle 4 \rangle_{0, 0, 0, 0} \\ &= Q_{0, 1}^4 - 6Q_{0, 1}^2 Q_{0, 2} + 3Q_{0, 2}^2 + 8Q_{0, 1} Q_{0, 3} - 6Q_{0, 4}. \end{aligned} \quad (2.32)$$

The two-particle correlation of particles coming from the same associate p_T^a intervals is given by:

$$N\langle 2 \rangle_{n_1, n_2} = p_{n_1, 1}^a p_{n_2, 1}^a - p_{n_1+n_2, 2}^a, \quad (2.33)$$

$$\begin{aligned} D\langle 2 \rangle_{n_1, n_2} &= N\langle 2 \rangle_{0, 0} \\ &= p_{0, 1}^a{}^2 - p_{0, 2}^a, \end{aligned} \quad (2.34)$$

where the p -vector has been trivially relabelled as the p^a -vector to denote that the particles are associate particles selected from p_T^a . This is essentially the same as the reference flow case, but selected in a narrow p_T interval. Similarly, the four-particle correlation $\langle 4 \rangle_{p_T^a}$ follows from Eq. (2.32) with the p^a -vector replacing the Q -vector.

The two-particle correlation of particles coming from different p_T intervals is given by:

$$N\langle 2 \rangle_{n_1, n_2} = p_{n_1, 1}^a p_{n_2, 1}^t \quad (2.35)$$

$$\begin{aligned} D\langle 2 \rangle_{n_1, n_2} &= N\langle 2 \rangle_{0, 0} \\ &= p_{0, 1}^a p_{0, 1}^t. \end{aligned} \quad (2.36)$$

This assumes that $p_T^a \neq p_T^t$, otherwise Eq. (2.33) should be used.

One of the great advantages of the Generic Framework is that it uses generic equations to calculate correlations of any harmonics. This is in contrast to the Q-cumulant method, which requires a different equation for each combination of harmonics. As an example, the four-particle correlations of $(6, -2, -2, -2)$, $(2, -2, 2, -2)$ and $(3, 2, -3, -2)$ will require three different equations in the Q-cumulant method, but only one in the Generic Framework, namely Eq. (2.31).

2.2 Subevent method

The process of measuring anisotropic flow coefficients using azimuthal correlations assumes that all the particles are correlated with some common symmetry plane. In practice, however, the results are often contaminated with *non-flow* effects. These come from processes, typically involving few particles, that are not connected to the global symmetry planes. Common non-flow effects arise from short-range ($\Delta\eta \approx 0$) correlations between particles in jets and resonance decays. Particles that are part of a jet are correlated with respect to the jet symmetry plane, which is not necessarily similar to the global collision symmetry planes. Particles originating from a resonance decay will be strongly correlated with each other, but not the symmetry plane. These effects are picked up, when measuring azimuthal correlations and introduce contaminations in the measurements, since they will produce a false flow signal, that is not due to collective behaviour. The subevent method [44] was developed to suppress non-flow effects in m -particle correlations. This section presents concepts of the subevent method and subsequently, its implementation in the Generic Framework.

The standard procedure, when calculating azimuthal correlations, is to correlate the particles within a certain detector acceptance. Figure 2.1 shows a sketch of the side view of the detector and an example of a two-particle correlation. Since the whole detector acceptance is used, the correlations will include non-flow effects from short-range correlation as mentioned above.

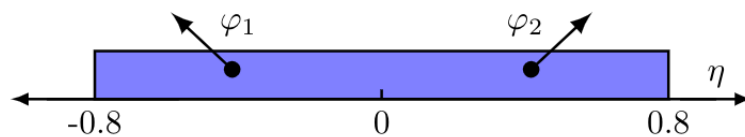


Figure 2.1: Sketch of side view of detector showing a two-particle correlation with no subevent.

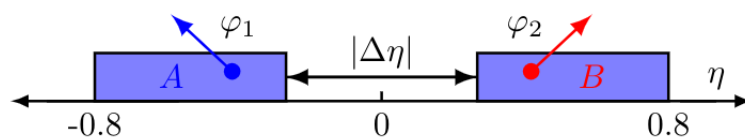


Figure 2.2: Sketch of side view of detector showing a two-particle correlation with two subevents and a $|\Delta\eta|$ gap separating them.

The subevent method suppresses the effects by dividing the detector acceptance into two subevents as shown in figure 2.2. The two-particle correlation is then given by:

$$\langle\langle 2 \rangle\rangle_{n,2\text{sub}} = \langle\langle e^{in(\varphi_1 - \varphi_2)} \rangle\rangle. \quad (2.37)$$

Here it is required that one particle is selected from subevent A represented by the colour blue, and the other from subevent B represented by the colour red. The subevent method exploits the fact that it is less probable to select a pair of particles, where both originate from a non-flow process, because the particles are forced to be separated in space by the pseudorapidity gap.

The subevent method does not impose a $|\Delta\eta|$ gap between each pair of particles, but instead puts a gap between the region from which the Q_n -vectors are constructed. However, as soon as an $|\Delta\eta|$ gap is applied between the two subevents, it is guaranteed that the η separation between any two particles will be larger than the $|\Delta\eta|$ gap.

In the case where $|\Delta\eta| > 0.0$, it is still possible for short-range correlations to contribute to the measurements at the shared edge of the subevents. A larger separation in pseudorapidity should therefore be used between the subevents. However, as $|\Delta\eta|$ increases, the number of particles in the subevents decreases, since the particles in the region excluded by the pseudorapidity gap are not used in the measurement. The fewer pairs of particles in the correlations with increasing $|\Delta\eta|$ gap will cause larger statistical uncertainties. Thus, a compromise between the suppression of non-flow effects and sufficient statistics must be maintained.

Four-particle cumulants are less sensitive to non-flow processes involving less than four particles [40, 45], such as resonance decays into two particles. This is due to the lower order correlations being subtracted in the cumulants. Non-flow processes of the same order of particles can still contaminate the measurements, however, so the subevent method still provides a good suppression of non-flow contributions. Figure 2.3 shows how the subevent method can be used to enforce a pseudorapidity gap between the four correlated particles. The four-particle correlation is thus given by

$$\langle 4 \rangle_{n,2\text{sub}} = \langle e^{in(\varphi_1 + \varphi_2 - \varphi_3 - \varphi_4)} \rangle. \quad (2.38)$$

Different signs are chosen for (φ_1, φ_2) and (φ_3, φ_4) , so that there is no correlation between the particles selected from the same subevent.

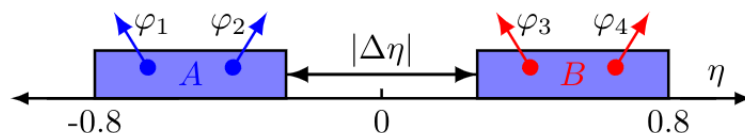


Figure 2.3: Sketch of the side view of the detector showing a four-particle correlation with two subevents and a $|\Delta\eta|$ gap separating them.

2.2.1 Implementation of the subevent method in the Generic Framework

The subevent method is already implemented in the Generic Framework [43] for some of the correlations used in this thesis. The author of this thesis has implemented the remaining correlations.

For the simple case of two-particle reference flow, the two-particle correlation with subevent method is given by:

$$N\langle 2 \rangle_{n1,n2} = Q_{n1,1}^A Q_{n2,1}^B. \quad (2.39)$$

Here the two Q-vectors are constructed in the different subevents:

$$Q_{n,p}^A = \sum_{k=1}^{M^A} w_k^p e^{in\varphi_k} \quad (2.40)$$

$$Q_{n,p}^B = \sum_{k=1}^{M^B} w_k^p e^{in\varphi_k}. \quad (2.41)$$

In similar fashion, the vectors of POIs for different p_T can be constructed in subevents A and B:

$$p_{n,p}^A = \sum_{k=1}^{m_p^A} w_k^p e^{in\varphi_k} \quad p_{n,p}^B = \sum_{k=1}^{m_p^B} w_k^p e^{in\varphi_k} \quad (2.42)$$

$$p_{n,p}^{tA} = \sum_{k=1}^{m_t^A} w_k^p e^{in\varphi_k} \quad p_{n,p}^{tB} = \sum_{k=1}^{m_t^B} w_k^p e^{in\varphi_k}. \quad (2.43)$$

Here m_p^A , m_p^B , m_t^A and m_t^B are the number of particles labeled POI in the respective p_T interval and subevent.

Unlike in Eq. (2.30), no auto-correlation needs to be subtracted in Eq. (2.39), since the particles used in the two Q-vectors are separated in space by the $|\Delta\eta|$ gap.

For the four-particle correlation with two particles selected from each subevent, as shown in figure 2.3 the following is obtained using the subevent method in the Generic Framework:

$$N\langle 4 \rangle_{n1,n2,n3,n4} = Q_{n1,1}^A Q_{n2,1}^A Q_{n3,1}^B Q_{n4,1}^B - Q_{n1+n2,2}^A Q_{n3,1}^B Q_{n4,1}^B \quad (2.44)$$

$$- Q_{n1,1}^A Q_{n2,1}^A Q_{n3+n4,2}^B + Q_{n1+n2,2}^A Q_{n3+n4,2}^B. \quad (2.45)$$

The subevent method removes 11 out of the 15 terms in the calculation with no subevent in Eq. (2.32). This is due to the fact that a lot of auto-correlations no longer need to be subtracted, since the particles only share subevent with one other particle (e.g. no auto-correlation between φ_1 and φ_3).

A more straightforward method of obtaining the higher-order correlations in the Generic Framework exists [44]. In this method, higher-order correlations are written as the product of lower-order correlations. This method is critical for obtaining higher order correlations since the number of terms quickly increases (8-particle correlations have 4140 terms [43]), and finding and removing the correct auto-correlation terms become untenable. It is still useful in the case of the four-particle correlations used in this thesis, where it can be written as the product $N\langle 2 \rangle_{n1,n2}^A$ and $N\langle 2 \rangle_{n3,n4}^B$, where the two two-particle correlations are calculated independently in subevent A and B. That this gives the correct four-particle correlation is easily seen:

$$N\langle 4 \rangle_{n1,n2,n3,n4} = N\langle 2 \rangle_{n1,n2} N\langle 2 \rangle_{n3,n4} \quad (2.46)$$

$$= (Q_{n1,1}^A Q_{n1,1}^A - Q_{n1+n2,2}^A) (Q_{n3,1}^B Q_{n4,1}^B - Q_{n3+n4,2}^B) \quad (2.47)$$

$$= Q_{n1,1}^A Q_{n2,1}^A Q_{n3,1}^B Q_{n4,1}^B - Q_{n1+n2,2}^A Q_{n3,1}^B Q_{n4,1}^B \quad (2.48)$$

$$- Q_{n1,1}^A Q_{n2,1}^A Q_{n3+n4,2}^B + Q_{n1+n2,2}^A Q_{n3+n4,2}^B. \quad (2.49)$$

The method correctly returns the explicit four-particle correlation in Eq. (2.45).

The next section will show how the observables used in the thesis are obtained from the correlations using the method described in this section.

2.3 From correlations to flow observables

The previous section showed some simple examples of how the subevent method can be used to calculate m -particle correlations. This section shows how the specific observables discussed in section 5 are calculated with the subevent method using the Generic Framework [43]. These observables are the ratio $v_n\{2\}/v_n[2]$, the factorization ratio r_n and the single-differential normalized symmetric cumulant $NSC(n, m_{p_T})$. Since the observables will be discussed in detail in section 5, their forms are listed here for convenience:

$$\frac{v_n\{2\}}{v_n[2]} = \frac{\langle v_n(p_T) v_n \cos n[\Psi_n(p_T) - \Psi_n] \rangle}{\sqrt{\langle v_n(p_T)^2 \rangle} \sqrt{\langle v_n^2 \rangle}} \quad (2.50)$$

$$r_n = \frac{\langle v_n(p_T^a) v_n(p_T^t) \cos[n(\Psi_n(p_T^a) - \Psi_n(p_T^t))] \rangle}{\sqrt{\langle v_n(p_T^a)^2 \rangle} \sqrt{\langle v_n(p_T^t)^2 \rangle}} \quad (2.51)$$

$$NSC(n, m_{p_T}) = \frac{\langle v_n \rangle^2 \langle v_m(p_T)^2 \rangle - \langle v_n \rangle \langle v_m(p_T)^2 \rangle}{\langle v_n^2 \rangle \langle v_m(p_T)^2 \rangle}. \quad (2.52)$$

The implementation of the newly proposed angle decorrelation observable $C(\Psi_n)$ into the Generic Framework is shown in section 5.1.3, since it constitutes part of the work of this thesis.

$v_n\{2\}/v_n[2]$

The p_T -differential $v_n\{2\}$ is obtained from the reference cumulant and differential cumulant. Following the general formalism of the cumulants introduced by Borghini *et al.* [45, 46] and extended to the Generic Framework in [43], the second-order cumulant, $c_n\{2\}$, is simply an average of the two-particle correlations defined in Eq. (2.26). The reference flow v_n calculated with the subevent method in the Generic Framework is given by:

$$N\langle 2 \rangle_{n_1, n_2} = Q_{n_1, 1}^A Q_{n_2, 1}^B \quad (2.53)$$

$$c_n\{2\} = \langle N\langle 2 \rangle_{n_1, n_2} / D\langle 2 \rangle_{n_1, n_2} \rangle \quad (2.54)$$

$$v_n^{\text{ref}}\{2\} = \sqrt{c_n\{2\}}. \quad (2.55)$$

Here the $\langle \rangle$ denotes the event average since the averaging over particles is done by construction in the Generic Framework.

The p_T -differential $v_n\{2\}$ uses the measurement of the reference flow and is obtained in similar fashion with one particle selected as POI and the other as RP:

$$N\langle 2' \rangle_{n_1, n_2} = p_{n_1, 1}^A Q_{n_2, 1}^B \quad (2.56)$$

$$d_n\{2\} = \langle N\langle 2' \rangle_{n_1, n_2} / D\langle 2' \rangle_{n_1, n_2} \rangle \quad (2.57)$$

$$v_n\{2\} = \frac{d_n\{2\}}{\sqrt{c_n\{2\}}} \quad (2.58)$$

For the case where both particles are selected as POI from a narrow p_T interval, the $v_n[2]$ observable is obtained:

$$N\langle 2 \rangle_{n_1, n_2}^{p_T^a} = p_{n_1, 1}^A p_{n_2, 1}^B \quad (2.59)$$

$$c_n\{2\}(p_T^a) = \langle N\langle 2 \rangle_{n_1, n_2}^{p_T^a} / D\langle 2 \rangle_{n_1, n_2}^{p_T^a} \rangle \quad (2.60)$$

$$v_n[2] = \sqrt{c_n\{2\}(p_T^a)} \quad (2.61)$$

The ratio $v_n\{2\}/v_n[2]$ can then trivially be calculated.

Factorization ratio r_n

The factorization ratio correlates one particle from associate particle p_T^a interval with the other from trigger particle p_T^t interval as illustrated in figure 2.4.

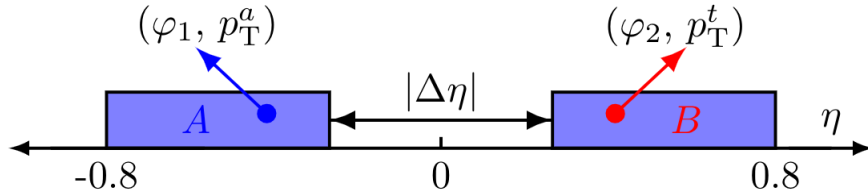


Figure 2.4: Sketches of side view of the detector showing a two-particle correlation with two subevents and $|\Delta\eta|$ gap separating them. The particles are selected from different subevents and p_T intervals.

In the Generic Framework, this is implemented as:

$$N\langle 2 \rangle_{n_1, n_2}^{p_T^a, p_T^t} = p_{n_1, 1}^A p_{n_2, 1}^B \quad (2.62)$$

$$c_n\{2\}(p_T^a, p_T^t) = \langle N\langle 2 \rangle_{n_1, n_2}^{p_T^a, p_T^t} / D\langle 2 \rangle_{n_1, n_2}^{p_T^a, p_T^t} \rangle \quad (2.63)$$

$$r_n = \frac{c_n\{2\}(p_T^a, p_T^t)}{\sqrt{c_n\{2\}(p_T^a) c_n\{2\}(p_T^t)}} \quad (2.64)$$

By construction $r_n = 1$, when $p_T^a = p_T^t$.

Normalized symmetric cumulant

The single-differential normalized symmetric cumulant is given by:

$$NSC(n, m_{p_T}) = \frac{\langle v_n \rangle^2 \langle v_m(p_T^2) \rangle - \langle v_n \rangle \langle v_m(p_T^2) \rangle}{\langle v_n^2 \rangle \langle v_m(p_T^2) \rangle}, \quad (2.65)$$

and differs from the previous observables in that the calculation does not use the subevent method for the two- and four-particle correlations in the numerator. The

four-particle correlation is obtained in the Generic Framework as:

$$\begin{aligned}
\langle v_n(p_T)^2 v_m^{\text{ref}^2} \rangle_{\text{No-sub}} &= \text{N}\langle 4 \rangle_{n_1^a, n_2^{\text{ref}}, n_3^a, n_4^{\text{ref}}} / \text{D}\langle 4 \rangle_{n_1^a, n_2^{\text{ref}}, n_3^a, n_4^{\text{ref}}} & (2.66) \\
\text{N}\langle 4 \rangle_{n_1^a, n_2^{\text{ref}}, n_3^a, n_4^{\text{ref}}} &= p_{n_1,1} Q_{n_2,1} p_{n_3,1} Q_{n_4,1} - q_{n_1+n_2,2} p_{n_3,1} Q_{n_4,1} - Q_{n_2,1} q_{n_1+n_3,2} Q_{n_4,1} \\
&- p_{n_1,1} q_{n_2+n_3,2} Q_{n_4,1} + 2q_{n_1+n_2+n_3,3} Q_{n_4,1} - Q_{n_2,1} p_{n_3,1} q_{n_1+n_4,2} \\
&+ q_{n_2+n_3,2} q_{n_1+n_4,2} - p_{n_1,1} p_{n_3,1} Q_{n_2+n_4,2} + q_{n_1+n_3,2} Q_{n_2+n_4,2} \\
&+ 2p_{n_3,1} q_{n_1+n_2+n_4,3} - p_{n_1,1} Q_{n_2,1} q_{n_3+n_4,2} + q_{n_1+n_2,2} q_{n_3+n_4,2} \\
&+ 2Q_{n_2,1} q_{n_1+n_3+n_4,3} + 2p_{n_1,1} q_{n_2+n_3+n_4,3} - 6q_{n_1+n_2+n_3+n_4,4}. & (2.67)
\end{aligned}$$

The two-particle correlations in the numerator are given by Eq. (2.30) with the p-vector replacing Q_n for $\langle v_m(p_T)^2 \rangle_{\text{No-sub}}$. The two-particle correlations in the denominator are given by Eqs. (2.55) and (2.61).

3 Experimental setup

In this section, the experiment, which takes the data used in this thesis, is presented. The Large Hadron Collider (LHC) is presented in section 3.1. The ALICE detector and the subdetectors inside it are presented in section 3.2.

3.1 The Large Hadron Collider

The data used for the analysis presented in this thesis is collected at the Large Hadron Collider [47]. The LHC is a two-ring-superconducting hadron accelerator and collider. It is located 100 m (on average) underground in the roughly 27km long tunnel that previously housed the Large Electron-positron Collider (LEP) machine. The tunnel and the accelerator are divided into eight straight sections and eight arcs.

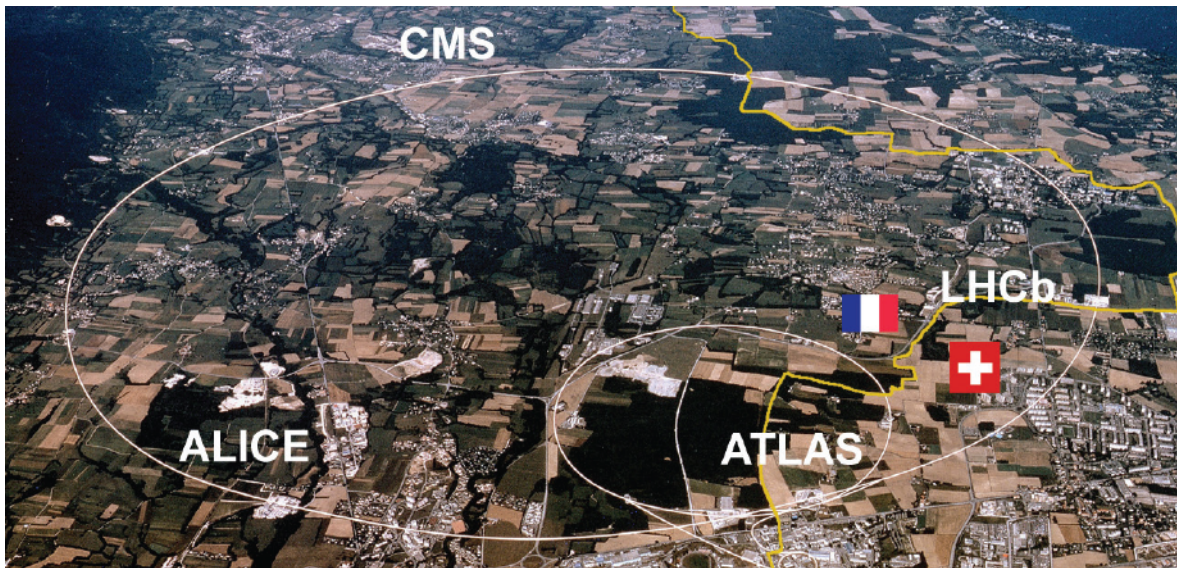


Figure 3.1: Illustration of the location of the LHC tunnel at the border of France and Switzerland [48].

The LHC can accommodate collisions of different particles at different beam energies. The collision systems that are of interest to this thesis are the collisions of lead ions, which have been recorded at $\sqrt{s_{NN}} = 2.76$ TeV in Run1 and $\sqrt{s_{NN}} = 5.02$ TeV in Run2. In addition Xenon-Xenon collisions at $\sqrt{s_{NN}} = 5.44$ TeV are studied.

Acceleration of particles occurs in one of the straight sections via radiofrequency (RF) systems. Since the LHC collides particles of the same sign charge, it has two rings with counter-rotating beams and therefore, also has two independent RF systems, one for each beam. The beams cross at four locations, corresponding to four experiments: ATLAS, CMS, ALICE, and LHCb. These four interaction points and the layout of the LHC are illustrated in figure 3.1.

The RF system [49] responsible for accelerating the particles consist of metallic chambers that are filled by an electromagnetic field. These chambers are known as RF cavities. The LHC has 16 RF cavities located in four cryomodules (two pr. beam), which allow the RF cavities to operate in a superconducting state. The RF field in a cavity oscillates at 400 MHz. This ensures that particles with the right energy will not

accelerate when the LHC is at full energy. Particles with different energies will be accelerated to match the desired beam energy. By this process, the particles are sorted into particle bunches.

The LHC uses superconducting magnets to guide the particles around the beam pipe and focus the beam. Dipole magnets make up the majority of the LHC tunnel length and are responsible for bending the particles along the beam pipe. The magnets are of the "twin-bore" design, which means magnets for both beam pipes are housed in the same cold mass and cryostat. A total of 1232 main dipoles is accommodated in the LHC ring. Quadrupole and other multipole magnets are used to keep the beam pipe focused and corrected and are also responsible for injecting particles at various points. The whole system is cooled down to 1.9 K by liquid helium to reach the required superconducting state.

3.2 A Large Ion Collider Experiment (ALICE)

ALICE is a general-purpose heavy-ion experiment at the LHC. Its primary focus is to study the strongly interacting matter in the QCD sector of the Standard Model, the so-called quark-gluon plasma (QGP), which is created under the extreme energy densities and temperatures present in nucleus-nucleus collisions.

The ALICE detector is composed of a central barrel part, which is encased in a large solenoid magnet and houses the Inner Tracking System (ITS), the Time-Projection Chamber (TPC), the particle identification arrays Time-of-Flight (TOF), Ring Imaging Cherenkov (HMPID), the Transition Radiation (TRD) detectors and two electromagnetic calorimeters (PHOS and EMCal). The forward muon arm has an arrangement of absorbers, a large dipole magnet as well as tracking and triggering chambers. A series of smaller detectors (ZDC, PMD, FMD, T0, V0) are located at small angles and are used for global event characterization and triggering purposes. A schematic layout of the detector is shown in figure [3.2](#).

This section will detail the parts of the detector that are of most importance to the analysis, i.e., the ITS, TPC, and V0, as well as the track reconstruction and triggering systems. This section's information is mostly inspired by the ALICE journal of instrumentation [\[50\]](#) and is otherwise cited.

3.2.1 Inner Tracking System (ITS)

The Inner Tracking System (ITS) is the innermost detector in the ALICE experiment. Its primary function is to localize the primary vertex with resolution better than $100 \mu\text{m}$, to reconstruct secondary vertices, and to track and identify low momentum particles ($p_{\text{T}} < 200 \text{ MeV}/c$). It also improves momentum and angle resolution for particles reconstructed by the Time-Projection Chamber (TPC). It can also assist in the reconstruction of tracks of particles that have traversed dead zones of the TPC.

The ITS is located immediately around the beam pipe and consists of six cylindrical layers of silicon detectors, as seen in figure [3.3](#). It covers the pseudo-rapidity range $|\eta| < 0.9$; however the first layer has a broader coverage ($|\eta| < 1.98$) in order to provide continuous coverage of charged-particle multiplicity together with the Forward Multiplicity Detector (FMD). Since the ITS has to operate in very high particle density, Silicon Pixel Detectors (SPD) has been chosen for the two innermost layers, followed by Silicon Drift Detectors (SDD) for the next two, and then Silicon micro-Strip

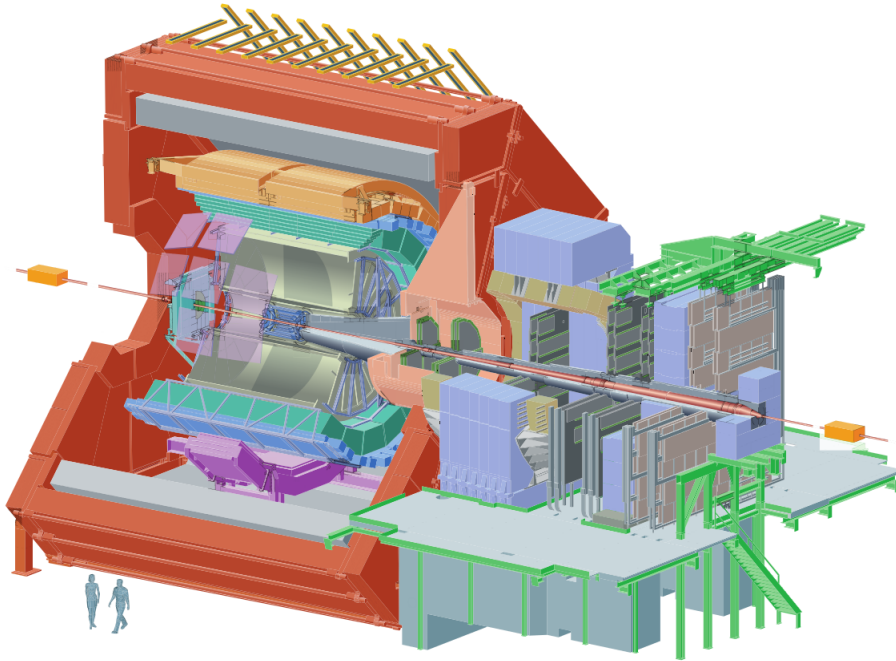


Figure 3.2: Schematic layout of the ALICE experiment.

Detectors (SSD) for the final two layers. The outer four layers use analogue readout and can thus be used for Particle IDentification (PID) via dE/dx measurements in the non-relativistic region. The dynamic range of the analogue readouts allows for dE/dx measurements down to $\sim 100 \text{ MeV}/c$, the lowest momentum at which track reconstruction is still possible. This allows for the ITS to function as a stand-alone low- p_T particle spectrometer. The amount of material in the detector has been kept to a minimum to reduce scattering effects, which dominate momentum and impact parameter resolution. The spatial resolution of the ITS is of the order of a few tens of μm with the best precision in the detectors closest to the primary vertex. This spatial resolution is essential for the momentum resolution at high momentum.

The SPD makes up the two innermost layers of the ITS and is based on hybrid silicon pixels, consisting of a two-dimensional matrix of reverse-biased silicon detector diodes bump-bonded to readout chips. The SDD makes up the following two layers and is made from Neutron Transmutation Doped (NPD) silicon with a sensitive area divided into two drift regions by a central cathode strip. The SSD makes up the two outer layers and helps match tracks from the TPC to the ITS. The SSD provides both a two-dimensional measurement of the track position and dE/dx information, which is used for particle identification.

3.2.2 Time Projection Chamber (TPC)

The Time Projection Chamber (TPC) is the primary detector of the ALICE detector central barrel. It is optimized for high-resolution charged-particle momentum measurements in a large range from several $100 \text{ MeV}/c$ up to $100 \text{ GeV}/c$. The TPC phase space coverage in pseudo-rapidity is $|\eta| < 0.9$ for tracks with full radial track lengths and can go up to $|\eta| < 1.5$ for tracks with reduced track length. It covers the full azimuthal angle (φ) with the exception of some dead zones (See section [4.4](#)).

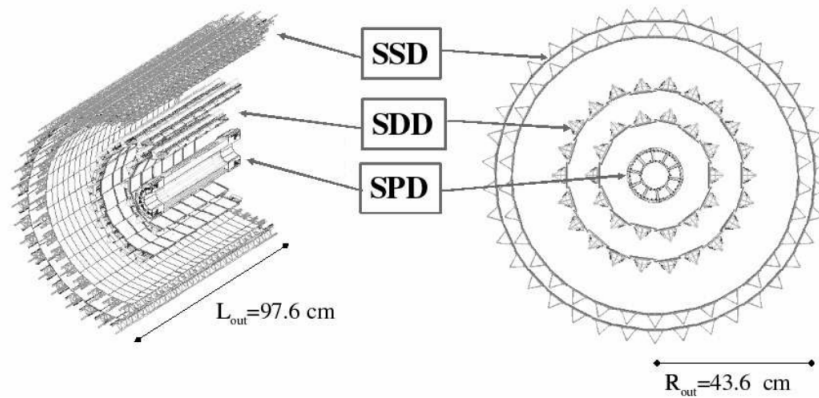


Figure 3.3: Layout of the ITS

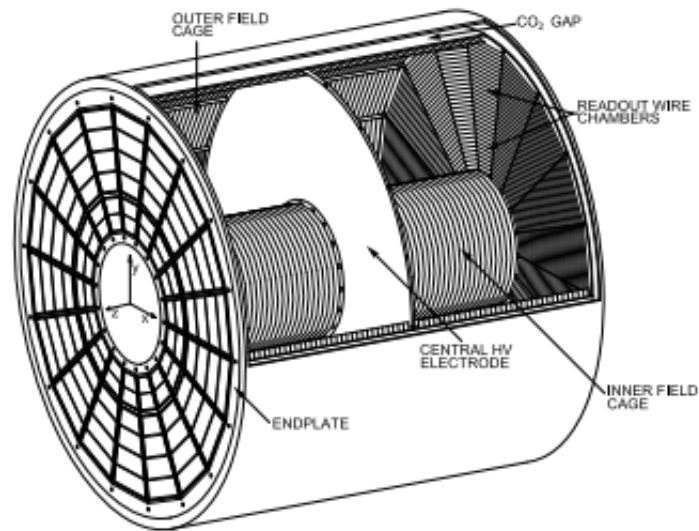


Figure 3.4: 3D view of the TPC field cage [51].

The TPC is a drift gas detector and uses a Ne/CO₂/N₂ mixture as drift gas. This mixture optimizes drift speed and ensures low diffusion, low radiation length, small space-charge effect, and ageing and stability properties. However, the drift velocity of the mixture has a strong temperature dependence, and the TPC must therefore have thermal stability with $\Delta T \leq 0.1$ K in the drift volume. The gas is circulated and purified by a gas system so that the drift velocity and gas gain of the readout chambers are kept stable. The thermal stability is ensured by a system of heat screens and cooling circuits. These include heat screens at the outer radius between TPC and TRD and at the inner radius shielding from the ITS. The cooling circuits operate at below ambient pressure in order to avoid leaks. When particles traverse the TPC, the gas is ionized. An electromagnetic field in the beam direction attracts the electron towards the endplates of the TPC.

Readout chambers are located at the two endplates of the TPC. The chambers are multi-wire proportional chambers and consist of a grid of anode wires above a pad plane, a cathode wire plane, and a gating grid. The design and alignment of inner and outer chambers optimize the active area and momentum precision for detected

high-momentum tracks but has the disadvantage of creating the aforementioned dead zones in the azimuthal coverage. The readout chamber is closed by the gating grid when not triggered. This ensures that electrons from the drift volume and ions from the amplification region do not pass through the readout chamber in non-triggered interactions. The gate is only opened by the L1 trigger $6.5 \mu\text{s}$ after collisions and stays open for one drift-time interval of about $90 \mu\text{s}$.

Distortions due to ExB effects and mechanical misalignment can affect the measurements of the TPC. These effects can be corrected by using tracks generated by the TPC laser system [52] after readout and track reconstruction. These straight tracks are generated at known positions in the TPC drift volume. This makes it possible to measure spatial and temporal variations of the drift velocity within a relative error of 10^{-4} .

The charges detected by the pads in the readout chambers at the TPC end caps are read out by the front-end electronics. This system of amplifiers, shapers, and filters is responsible for converting the signal from the TPC into usable data.

3.2.3 VZERO (V0) system

The VZERO (V0) system [53] is designed to provide triggers for the experiment and to separate beam-beam interactions from the background, such as beam-gas interactions. It is also used to measure charged-particle multiplicity and azimuthal distributions. The charged-particle multiplicity is essential to determine the centrality of nucleus-nucleus collisions, and the azimuthal distribution is used to determine the collision reaction plane in Pb–Pb collisions.

The V0 system consists of two arrays, V0-A and V0-C, which cover the pseudorapidity ranges of $2.8 < \eta < 5.1$ and $-3.7 < \eta < -1.7$ respectively. Each of the arrays is segmented into four rings, further divided into eight sections in the azimuthal direction. Figure 3.5 shows the segmentation of the arrays. The V0-A is located on the side opposite to the muon spectrometer at a distance of 329 cm from the nominal vertex, whereas the V0-C is positioned at the front face of the hadronic absorber. Plastic scintillators are used for each section of the arrays. Optic fibers transfer the light created in the scintillators to photomultiplier tubes (PMT). The PMT output is then sent to the Front-End Electronics (FEE) and converted to a digital signal.

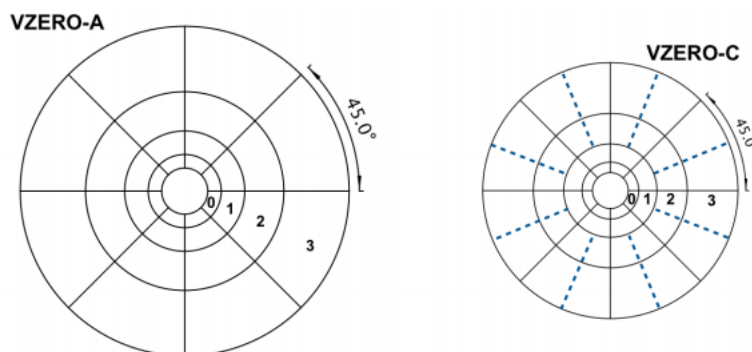


Figure 3.5: Sketches of VZERO-A and VZERO-C arrays.

One of the main roles of the V0 system is to provide ALICE with Minimum Bias (MB) trigger in both pp and Pb–Pb collisions and centrality-based triggers in Pb–Pb collisions. In Pb–Pb collisions, the interaction trigger requires: 1) two pixel-chips hit in the outer

layer of the SPD, 2) signal in V0-A, and 3) signal in V0-C. This ensures high efficiency for hadronic interactions.

Another function of the V0 system, which is crucial for the study of flow, is the determination of centrality of Pb–Pb collisions. The charged particle multiplicity, $dN_{\text{ch}}/d\eta$, is inferred from the amplitudes measured by the V0 system based on energy deposited in the scintillators. By fitting the distribution of V0 amplitudes using a Glauber model [54], the centralities can be obtained down to very low amplitudes (corresponding to peripheral collisions). A typical distribution of V0 amplitudes is shown in figure 3.6 for Pb–Pb collisions at $\sqrt{s_{\text{NN}}} = 2.76$ TeV. The shaded areas correspond to the centrality classes that are used in physics analyses.

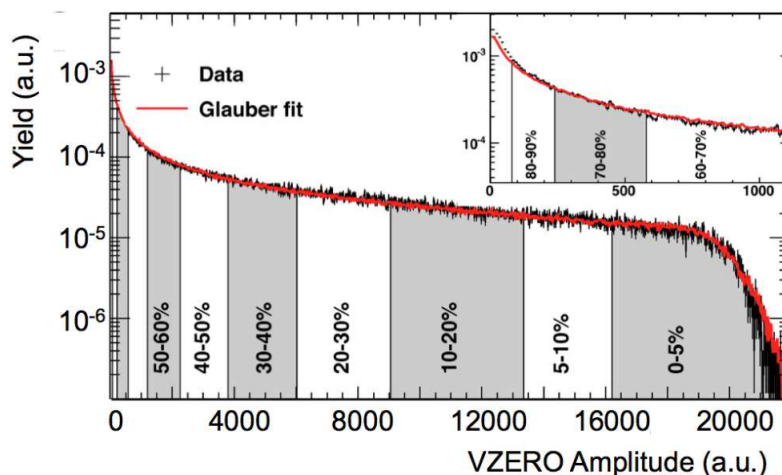


Figure 3.6: Distribution of the sum of amplitudes in the two VZERO arrays in Pb–Pb collisions at $\sqrt{s_{\text{NN}}} = 2.76$ TeV. The red line shows the fit with the Glauber model. The shaded areas define the different centrality classes of hadronic collisions. The inset shows the low amplitude part of the distribution [53].

3.2.4 Track Reconstruction

Reconstruction of the tracks in the central barrel is done in the following steps [55]:

First, the detector data is converted into clusters, which are characterized by position, signal amplitudes and times, etc., after which the preliminary interaction vertex is determined in the SPD as the space point, to which a maximum number of tracklets converge. The tracklets are lines defined by pairs of clusters, one from each layer of the SPD.

After the preliminary primary vertex has been found, the track finding and fitting are then done in the ITS and the TPC in three steps following and inward-outward-inward scheme. The first step involves finding tracks in the TPC. The TPC has 159 readout pads in the radial direction of the endplates. This means a maximum of 159 clusters, corresponding to 159 space points, can be produced in the TPC. The tracks are reconstructed from the outer radius going in. The next step is propagating the TPC tracks to the outermost layers of the ITS. In the ITS, a tree of track hypotheses is produced for each TPC track, and the highest quality candidate is selected for the reconstructed event. The tracks are extrapolated to the point of closest approach to the preliminary interaction vertex and are then propagated outwards and fitted with

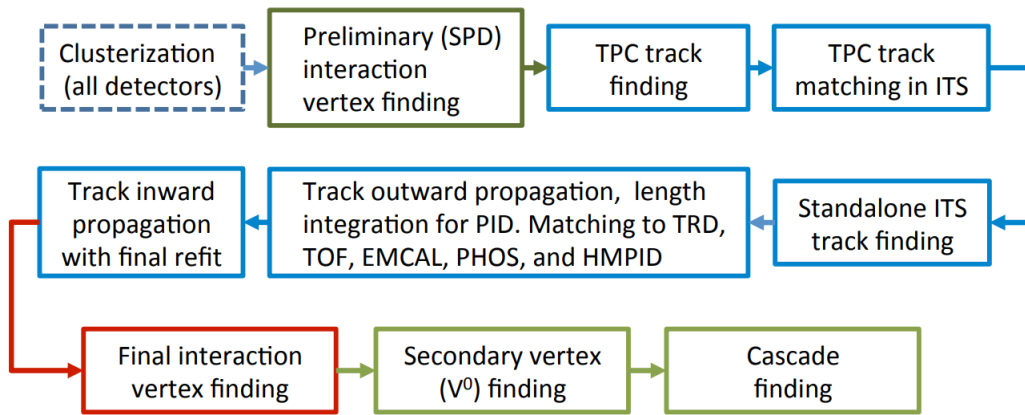


Figure 3.7: Event reconstruction flow [55].

the Kalman filter [56]. These tracks are then matched to other central barrel detectors, such as TRD, TOF, EMCAL, and PHOS, with an additional fit. In the final step of the track reconstruction, the tracks are propagated inwards from the TPC's outer radius of and refitted. Secondary tracks from decays and secondary interactions are suppressed using cuts on the longitudinal and transverse Distance of Closest Approach (DCA) to the primary vertex.

Determination of the final interaction vertex is then done using the reconstructed tracks. This offers higher precision than using the SPD tracklets alone. An iterative version of vertex-finding is used under data-taking conditions, where a high pileup rate is expected. Once the tracks are reconstructed, and the primary interaction vertex has been found, a search for photon conversions and secondary vertices concludes the track reconstruction.

3.2.5 Triggering

The rate of collisions in the ALICE detector is so high, that not all collisions can be recorded. The ALICE Central Trigger Processor (CTP) [57, 58] is designed to select events with a variety of different features, and to optimize the triggered events for the different running modes: Heavy-ion collisions, ion-proton collisions or proton-proton collisions. The CTP makes decision on whether to accept the event or not, and if the event is accepted sends a signal back to the detectors to start the readout. The CTP is divided into three levels: L0, L1 and L2.

The first trigger response has to be fast to match the detector requirements, which are first of all designed to cope with the large multiplicities in Pb–Pb collisions at an interaction rate of 8 kHz. This is done by splitting the first 'fast' response into two levels: The level 0 (L0) signal, which reaches the detector in $1.2 \mu\text{s}$, which is too fast to capture all trigger inputs, and the level 1 (L1) signal, which arrives at $6.5 \mu\text{s}$, in order to pick up the remaining fast inputs. The high multiplicities in Pb–Pb collisions make events with more than one central collision unreconstructable. Therefore, past-future protection is implemented in the CTP to ensure that events selected for readout are not spoiled by pileup events (events happening close in time to the triggered events, which results in tracks from the two events being mixed). The level 2 (L2) signal waits for the end of the past-future protection interval of $88 \mu\text{s}$ to verify that the event can be taken. The trigger inputs can be combined with different logical conditions and for different

trigger detectors. The different combinations correspond to different trigger classes. These classes can select events of specific properties such as the common minimum-bias event or more rare events such as high-multiplicity pp collisions. It is possible to have several trigger classes running concurrently for more efficient data taking.

After passing all the triggers in the CTP, the event will pass to the Data Acquisition (DAQ) system, where it is prepared for permanent storage so that it can be used for final analysis by the ALICE users.

4 Analysis Details

This section covers the details of the specific analysis used to obtain the results presented in this thesis. First, the data processing is described in section 4.1, followed by the event and track selection in section 4.2 and 4.3. The non-uniform acceptance corrections are described in section 4.4 and a discussion of the systematic and statistical uncertainties are described in section 4.5.

4.1 Data processing

The raw data sent from the electronics in the detector is not suitable for analysis by the end-user. Before it can be used, it needs to be processed, e.g., in the form of track reconstruction, as introduced in section 3.2.4. The final data can be stored in two formats: The Event Summary Data (ESD) or the Analysis Object Data (AOD). The ESD contains more information than the AOD, but due to the high memory requirements of the data, it is preferable to use the AOD format for data analysis. The data is saved and read in the ROOT program [59], a C++ framework for data processing developed at CERN for high-energy particle physics. Even with the AOD format, the data still takes up too much memory to be processed locally. Therefore, analysis is processed on the Grid, where tasks are performed on fractions of the data at different supercomputers around the world. The output of the analysis can then be merged into the final output, which is usually limited in size and can be processed further locally. Rather than manually submitting tasks to the Grid, it is possible to run the analysis through the LEGO train framework [60], which is a centralized system created to increase the CPU efficiency of ALICE user analysis jobs.

The ALICE collaboration uses two custom ROOT extensions: AliRoot [61] and AliPhysics [62]. AliRoot contains classes needed by all users for data processing and reconstruction specific to the ALICE detector, and AliPhysics contains the individual user analyses. The user analyses are stored as a C++ class.

This thesis uses the class AliAnalysisDecorrTask, which is a custom made class created by the author of this thesis for the purpose of studying p_T -dependent flow vector fluctuations. The desired correlations are specified through an auxiliary custom class, which also contain information about the type of flow to be studied (Reference flow, differential flow, double-differential flow). The workflow of the analysis is shown in figure 4.1, and the class is available at

- <https://github.com/alisw/AliPhysics/blob/master/PWGCF/FLOW/GF/AliAnalysisDecorrTask.cxx>
- <https://github.com/alisw/AliPhysics/blob/master/PWGCF/FLOW/GF/AliAnalysisDecorrTask.h>

and the auxiliary class at

- <https://github.com/alisw/AliPhysics/blob/master/PWGCF/FLOW/GF/AliDecorrFlowCorrTask.cxx>
- <https://github.com/alisw/AliPhysics/blob/master/PWGCF/FLOW/GF/AliDecorrFlowCorrTask.h>

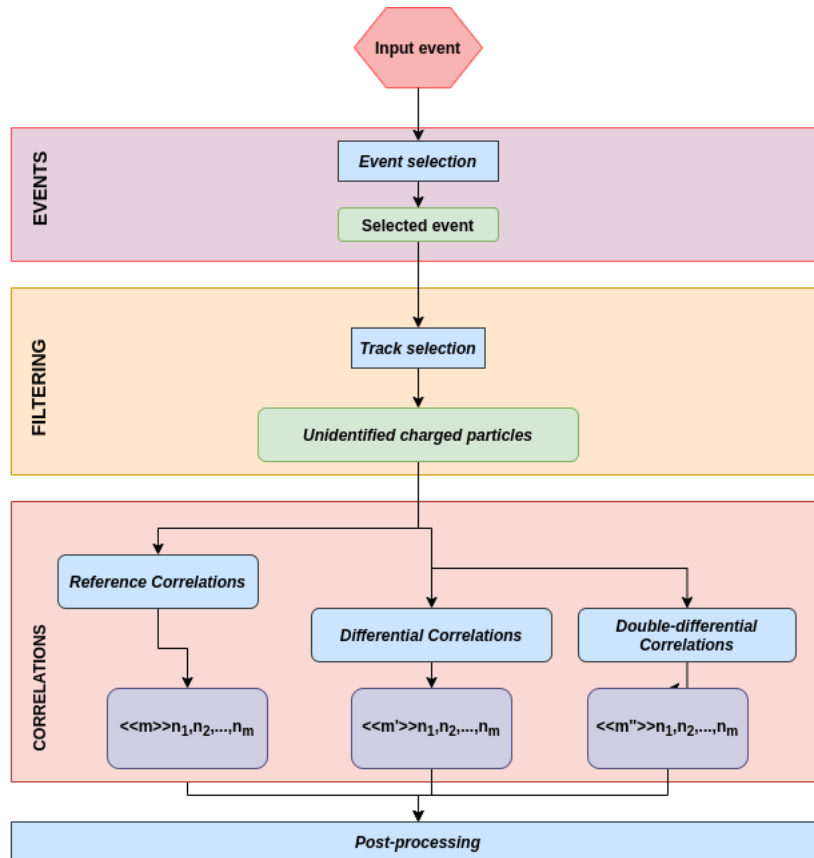


Figure 4.1: Diagram of the analysis workflow.

The data taken at the LHC is divided into *periods*. Each period corresponds to the detector running under some specific settings, e.g. the type of collision system, or collisions energies. The periods are further divided into *runs*, which correspond to continuous data taking without breaks or changes in the detector. The runs are uniquely identified by a six digit ID. During a run, the experiment collects information about each collision of particles, called an *event*, and a run will contain many such events. This thesis uses data from Pb–Pb collisions at $\sqrt{s_{NN}} = 5.02$ TeV and Xe–Xe collisions at $\sqrt{s_{NN}} = 5.44$ TeV from the LHC Run2 data taking period. The periods used are shown in table 1. The run lists for each period can be seen in appendix A.

Collision system	Collision energy	Periods
Pb–Pb	$\sqrt{s_{NN}} = 5.02$ TeV	LHC15o, LHC18q, LHC18r
Xe–Xe	$\sqrt{s_{NN}} = 5.44$ TeV	LHC17n

Table 1: Collision systems, energy and corresponding periods used in this thesis.

4.2 Event Selection

The events are selected according to a set of standard cuts implemented in the ALICE software to select events appropriate for the general analysis. The first step is selecting events fired by the selected trigger. This analysis uses one trigger for the LHC15o period and a different set of triggers for the LHC18q and LHC18r periods. The minimum

bias trigger (kInt7) was used for the LHC15o period. This trigger requires one hit in the SPD and one hit in each of the V0 arrays (V0A and V0C). For the LHC18q and LHC18r periods, the kINT7 trigger is also used, but with different triggers in central and semi-central collisions. The central trigger (kCentral) is used in 0-10% centrality classes and the semi-central trigger (kSemiCentral) is used in 30-50% centrality classes. Otherwise, the kINT7 trigger is used. For the Xe–Xe collisions, the minimum bias trigger is also used. The centrality of the event is determined through the AliMultSelection framework. This framework estimates the centrality based on the selected centrality estimator. For this analysis, the V0M estimator, which is the combination of the V0A and V0C multiplicity measurements, is used to determine the centrality class of the collisions. Centrality classes estimated from SPD multiplicity are used in the systematic studies via the CL0 and CL1 centrality estimators. Figure 4.2 show the correlation between the V0M and CL0 centrality estimators, and that they are compatible after event cuts.

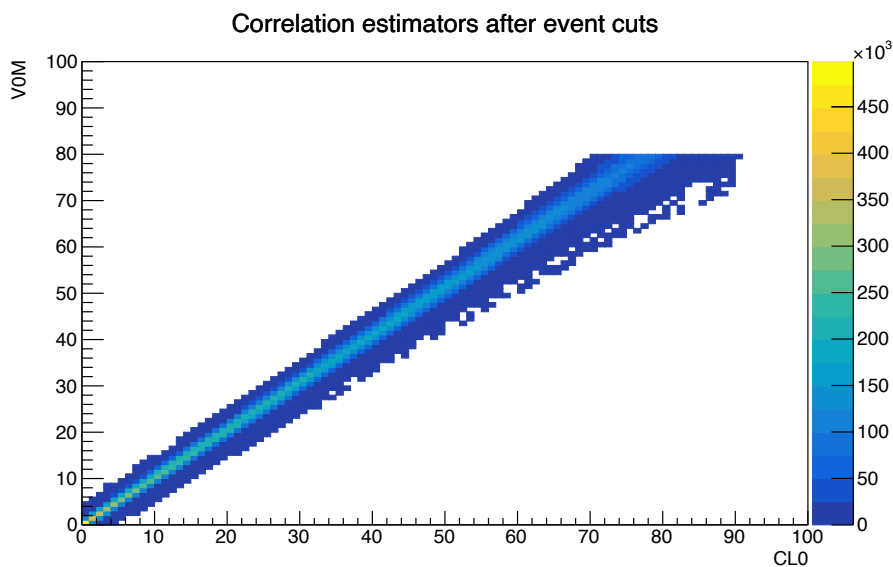


Figure 4.2: Correlation of centrality classes from centrality estimators V0M and CL0.

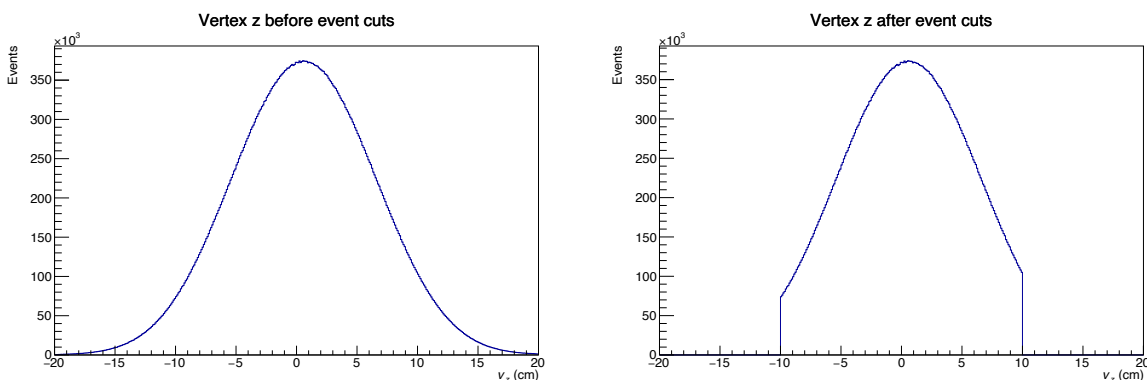


Figure 4.3: Selection of the primary $|V_z|$ vertex in 2015 Pb–Pb collisions at $\sqrt{s_{NN}} = 5.02$ TeV before event cuts (left) and after event cuts (right).

Primary vertex selection

Events are selected with a primary vertex found within 10 cm from the center of the detector along the beamline. This is to ensure a somewhat uniform acceptance in the central pseudo-rapidity region $|\eta| < 0.8$. The position of the primary vertex of each event is determined with the SPD, which is closest to the interaction point. It is also possible to determine the vertex with the fully reconstructed tracks from the TPC and ITS information. These two methods should yield a similar result if the tracks are properly reconstructed, so a cut on the correlation between the two methods is applied. The distribution of the primary vertex can be seen in figure 4.3 before and after event selection.

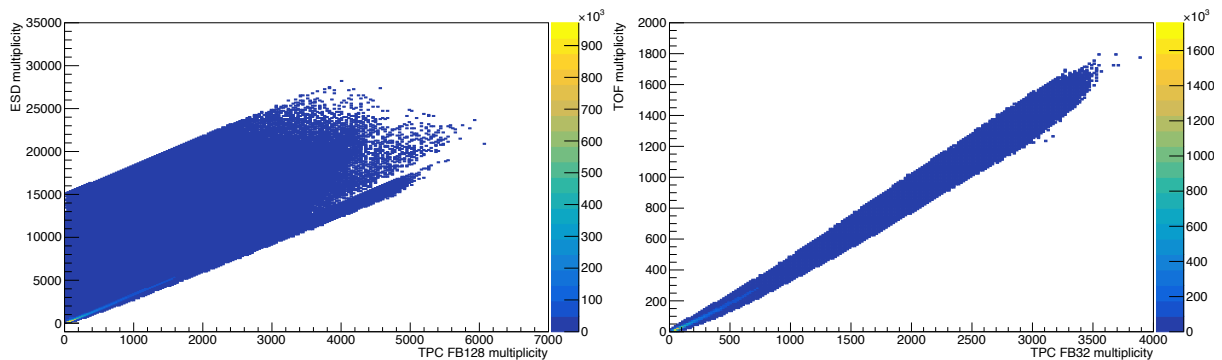


Figure 4.4: Correlations between the number of ESD tracks and track using only TPC information used for the rejection of pileup events (left) and the correlation between TPC+ITS tracks and the same TPC+ITS+TOF tracks used for rejection of out-of-bunch crossing pileup events.

Pileup rejection

The high interaction rate during the data taking makes it very challenging for the trigger to isolate the triggered events from pileup events completely. These are events that happen during the reconstruction of the triggered event, which results in the event mixing particles from different collisions. Pileup events are divided into same-bunch and out-of-bunch pileup. Same-bunch pileup refers to events from the same bunch crossing being mixed, and out-of-bunch pileup is when the triggered event gets mixed with events from a different bunch crossing, which happens shortly before or after the triggered event.

The rejection of pileup events cannot be done completely by the trigger, because of the high interaction rate. Therefore additional cuts are needed in order to select the proper triggered events. The additional tracks coming from the pileup events will lead to a larger number of TPC clusters being fired compared to a non-pileup event. A cut on the correlation between the number of ESD tracks and tracks using only TPC information removes these pileup events. The cut is on the difference in multiplicity from the ESD tracks versus the TPC tracks and is different for the different periods. The specific formulas used are given in table 2. Another cut on the correlation between tracks using ITS+TPC information and the same tracks with matching of the tracks with the TOF detector is used to reject out-of-bunch pileup events.

The event cuts are also shown in table 2.

Data	Type	Value
LHC15o	Trigger	kInt7
	Vertex z	$< 10 $ cm
	Pileup cut $N_{\text{ESD}} - 3.38N_{\text{TPC}}$	> 500
LHC18r and LHC18q	Trigger	kCentral, kSemiCentral and kInt7
	Vertex z	$< 10 $ cm
LHC17n	Trigger	kInt7
	Vertex z	$< 10 $ cm
	Pileup cut $N_{\text{ESD}} - 6.6164N_{\text{TPC}} + 0.000126397N_{\text{TPC}}^2$	> 1000

Table 2: Event selection for candidate events. An explanation of the cuts are given in section [4.2](#).

4.3 Track Selection

After selecting the suitable events, the tracks are selected according to the desired analysis. The ALICE software allows for a track selection using predefined cuts contained in so-called *filter bits*. In this thesis, filter bit 96, which is also called global tracks, is used. These are tracks of high-quality that uses information from both the TPC and ITS. The cuts are as follows:

- A minimum of 70 TPC clusters out of a maximum of 159 (See setion [3.2.4](#)).
- Maximum $\chi^2 < 4$ of the track fit per TPC cluster.
- A minimum of one hit in the SPD detector.
- If no hit in the SPD, then at least one hit in the SDD detector.
- Maximum $\chi^2 < 36$ of the track fit per ITS cluster.
- A cut on the longitudinal distance of closest approach $|DCA_z| < 2$.
- A cut on the transverse distance of closest approach $|DCA_{xy}| < 0.0105 + 0.0350/p_T^{1.1}$.
- A converged track fit in the final stages of track reconstruction.

Additional kinematic cuts on the transverse momentum $0.2 < p_T < 5.0$ GeV/ c and on the pseudorapidity $|\eta| < 0.8$ are also performed. The p_T cuts ensure that 1) tracks with poor tracking are rejected and 2) hard processes are excluded, which could significantly bias the flow measurements. The pseudorapidity cut is chosen in order to use the whole volume of the TPC without loss of efficiency at the edges. Distributions of these kinematic variables are seen in figure [4.5](#) and the track selection is also shown in table [3](#).

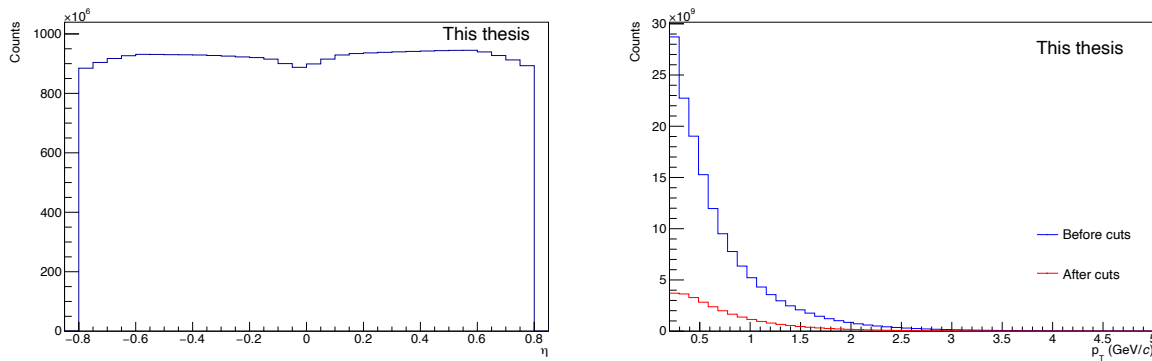


Figure 4.5: Distributions of η and p_T for Pb–Pb collisions at $\sqrt{s_{\text{NN}}} = 5.02$ TeV from LHC15o period.

Physics	Type	Range
	p_t [GeV/c]	[0.2, 5.0]
	η	[-0.8, 0.8]
Detector	Type	Requirement
	Track type	FilterBit 96
	TPC clusters	> 70
	NUA weights	(ϕ, η, V_z)

Table 3: Track selection for candidate tracks. An explanation of the cuts are given in section [4.3](#).

4.4 Non-uniform Acceptance Correction

As described in section [3.2.2](#) the TPC has some zones with lower efficiency in the azimuthal coverage, which creates a non-uniform acceptance in the detector. This introduces a bias in the results, which could result in false correlation of particles. The event-by-event fluctuation of the symmetry plane Ψ_n means that the event averaged φ distribution should be uniform in a fully efficient detector. The Generic Framework [\[43\]](#) allows for corrections of these non-uniformities by weighting the Q-vectors with a weight w per particle as described in section [2.1.3](#) in Eq. [\(2.21\)](#). The weights used in this analysis correct for non-uniformities in the φ, η and primary z-vertex V_z distributions. The three dimensional distribution of φ, η and V_z without NUA correction is shown in figure [4.6](#) for selected tracks, and the two-dimensional distribution of φ and η is shown in figure [4.7](#).

The weights are obtained by running over the data and obtaining these distributions, after which the analysis can be performed with the weights. This means that two runs over the data is required. The data-driven approach ensures that the detector conditions are reflected in the weights, which is not always the case for the correction based on a Monte Carlo simulations. The weights are calculated for each run due to potential differences in the distributions from the different runs and are given by:

$$w_{\phi, \eta, V_z} = \frac{N^{\max}(\eta)}{N(\phi, \eta, V_z)}, \quad (4.1)$$

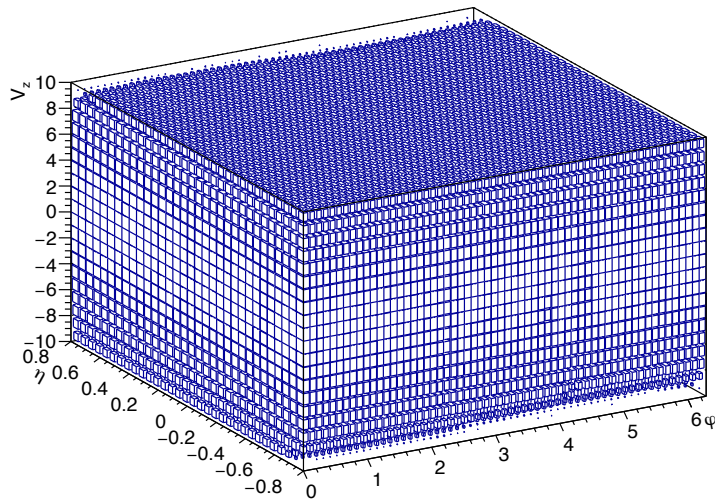


Figure 4.6: The three-dimensional distribution of φ , η and V_z without NUA corrections for Pb–Pb at $\sqrt{s_{\text{NN}}}=5.02$ TeV for run 246276 for tracks passing the selection cuts.

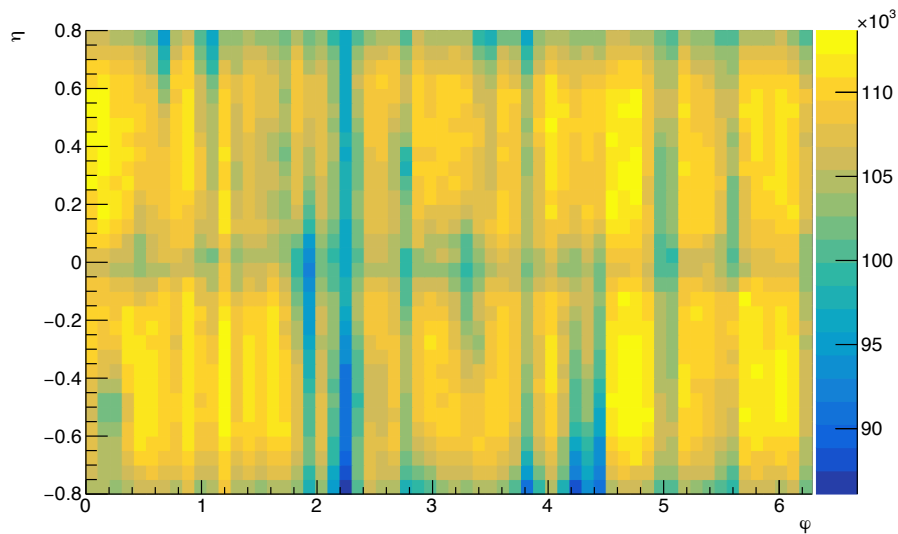


Figure 4.7: The two-dimensional distribution of φ and η without NUA correction for Pb–Pb run 246276 with $\sqrt{s_{\text{NN}}}=5.02$ TeV for tracks passing the selection cuts.

where N is the multiplicity of a three-dimensional histogram filled with the three observables. These are then applied to each particle i for each event, when constructing the flow vector. A three-dimensional set of weights is chosen over the more traditional two-dimensional (φ, η) -weights, due to the slight skewness of the V_z -distribution in figure 4.3, which could bias the measurements. Figure 4.8 shows the φ -distribution of run 246276 before and after the NUA correction. After the weights are applied, the desired uniformity in φ distribution is achieved. Traditionally, a correction of the Non-Uniform Efficiency of the transverse momentum measurements could also be applied to the Q-vectors. These weights are obtained from Monte Carlo simulations, such as in [44]. In this thesis, NUE weights are not applied, since the focus is on observables that

are ratios of differential quantities. As such, the NUE corrections will be cancelled out automatically.

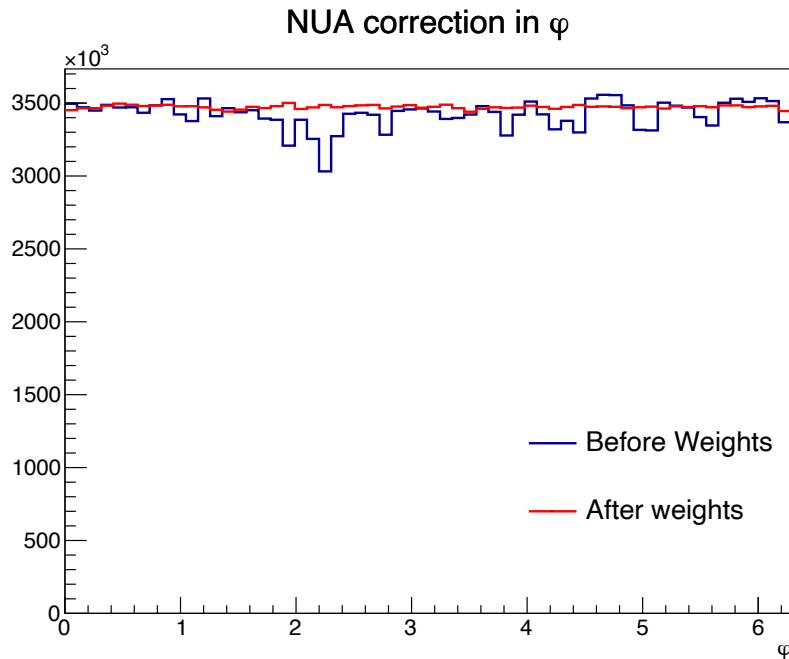


Figure 4.8: φ -distribution for run 246276 in LHC15o before and after NUA corrections are applied.

4.5 Systematic uncertainties

Systematic uncertainty reflects the choice the analyser has in choosing different analysis parameters such as different event or track cuts. The cuts used for the systematic study are tighter than the default cuts (except for pileup), as this will show how the results change when events or tracks of higher quality are used. One cut is changed at a time in order to quantify the contribution from that specific cut. The whole analysis is repeated for each of these new cuts and is compared with the default cuts.

The systematic uncertainty for the event selections is investigated by varying the centrality determination, changing the cut on the position of the primary vertex along the beam direction $|V_z|$, testing different magnetic field polarities as well as different pileup cuts. The first one is performed by conducting the full analysis with the SPD's signal amplitudes as alternative centrality estimators, rather than multiplicity measurements in the V0 detector. The systematic uncertainty from different primary vertex cut is studied by changing the cuts from $|V_z| < 10$ cm to $|V_z| < 7$ cm, 8 cm and 9 cm. The magnetic field polarities are tested by running the full analysis using only tracks from either positive or negative magnetic field polarity. The systematic effect of pileup is estimated by changing the pileup cut in centrality classes 0-10%. For the LHC15o period, the pileup cut is loosened from 500 to 700.

The particle/track selections are also varied. Since global tracks are used in this analysis, hybrid tracks, which have full acceptance in azimuthal angle φ distribution, are also considered by varying the filter bit from 96 (global tracks) to 768 (hy-

brid tracks). Furthermore, the effects of the binning for the non-uniform acceptance (NUA) weights are estimated from 60 to 120 bins in the φ -distributions. For the number of TPC space points the systematic study varies from the default cut of > 70 to > 80 and > 90 . Since non-flow contributions can contaminate the results of the two-particle correlations, the effect of changing the $|\Delta\eta|$ -gap and using only particles of like-sign charge is also considered. These last two sources are only considered for two-particle correlations. Pseudorapidity gaps of $|\Delta\eta| < 0.6, 1.0, 1.2$ are tested for their contribution to non-flow effects. The cuts are summarized in table 4.

Variable	Default cut	Variation cut
$ V_z $	< 10 cm	< 7 cm < 8 cm < 9 cm
Magnetic field polarity	both	Positive Negative
ESD vs. TPC tracks (pileup)	500	700
Centrality estimator	V0M	CL0 CL1
# of TPC clusters	> 70	> 80 > 90
Track type	global	hybrid
$ \Delta\eta $	> 0.8	> 0.6 > 1.0 > 1.2
Particle charge	Combined	Positive Negative
NUA binning	60	120

Table 4: The cuts varied for the systematic study of p_T -dependent flow vector fluctuations in Pb–Pb collisions at $\sqrt{s_{NN}} = 5.02$ TeV in this analysis.

The different sources are estimated for centralities and trigger particle p_T^t (where relevant) separately, with a Barlow test [63] against the results using the default cuts. The Barlow test checks whether the variation cuts are statistically significant and is given by:

$$\frac{|x_{\text{def}} - x_{\text{sys}}|}{\sqrt{|\sigma_{\text{def}}^2 - \sigma_{\text{sys}}^2|}} > 1 \quad (4.2)$$

The value of the Barlow test is averaged over p_T bins and checked if greater than unity. The ratio of the variation and default cut is fitted with either a pol0 or pol1 fit for each source of systematic. If the averaged Barlow is higher than unity a systematic uncertainty is assigned as the difference between the appropriate fit and unity. Figure 4.9 shows the values of the Barlow test for the observable $v_2\{2\}/v_2[2]$ in Pb–Pb collisions at $\sqrt{s_{NN}} = 5.02$ TeV. The ratio of $v_2\{2\}/v_2[2]$ with varying cuts and $v_2\{2\}/v_2[2]$ with default cuts is shown in figure 4.10. Tables of the estimated systematic uncertainties for $v_2\{2\}/v_2[2]$ can be found in Appendix B, along with figures for the systematic study of the other observables presented in this thesis. Additional manual checks of the sys-

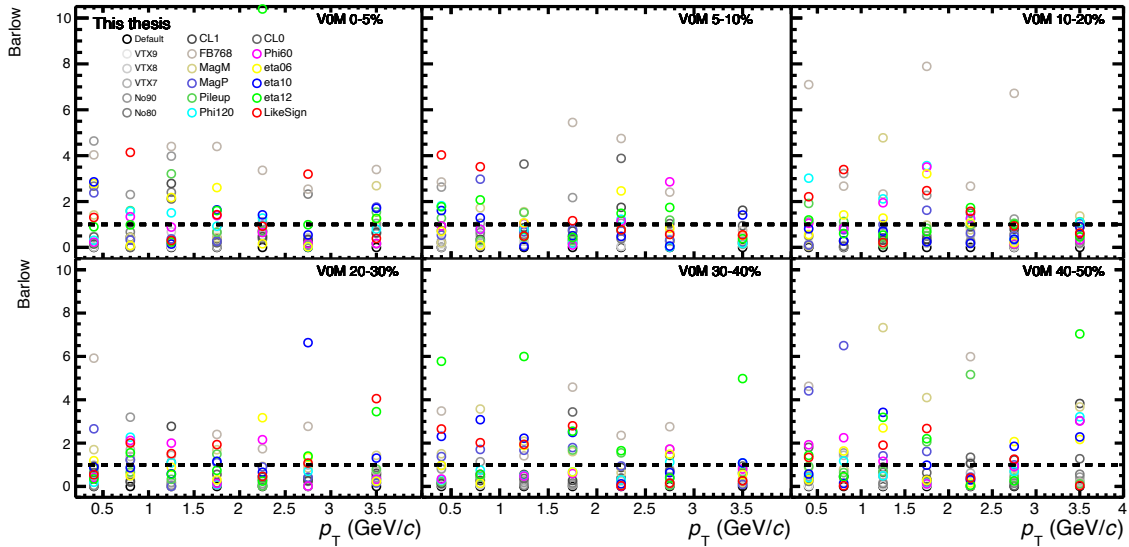


Figure 4.9: The values of the Barlow test compared against unity (dotted line) for each variation cut on $v_2\{2\}/v_2[2]$ in Pb–Pb collisions at $\sqrt{s_{NN}} = 5.02$ TeV.

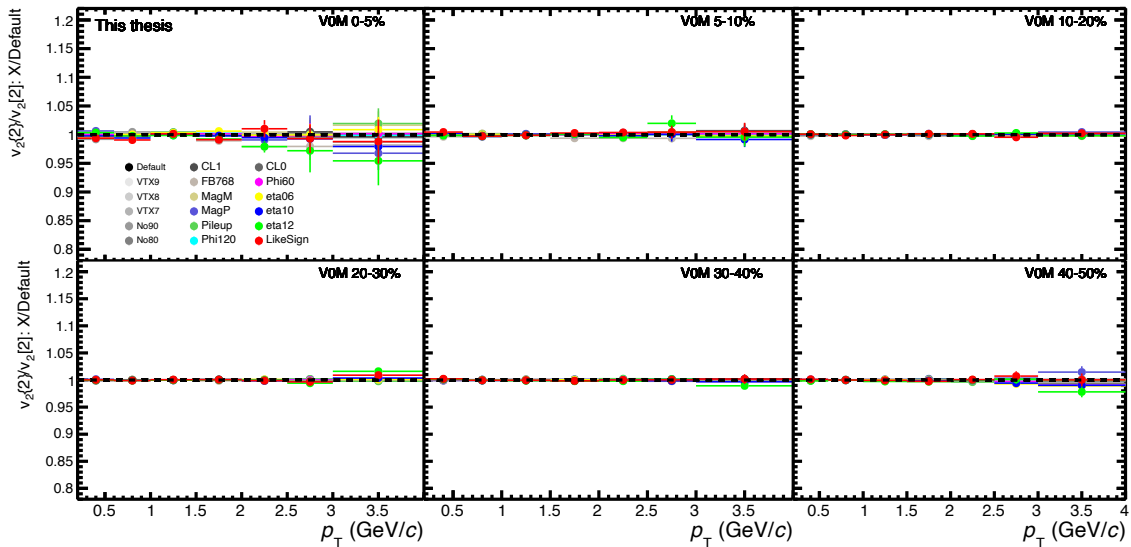


Figure 4.10: The ratio of $v_2\{2\}/v_2[2]$ with different variations of the cuts to $v_2\{2\}/v_2[2]$ with default cuts in Pb–Pb collisions at $\sqrt{s_{NN}} = 5.02$ TeV.

tematics are done in cases, where individual bins show unusual deviations from the rest.

The total systematic uncertainty is calculated as the quadratic sum of these individual sources. For sources with more than one variation cut, only the cut with the largest uncertainty is considered.

Statistical uncertainty

Since the various particle correlations are not independent observables, it is not possible to use standard error propagation when calculating the statistical uncertainty of the observables. Instead, the bootstrap method [64] is utilized, which uses random sampling with replacement. The output of the analysis is in the form of histograms

for each correlation $\langle\langle m \rangle\rangle_{n_1, \dots, n_m}$. For each correlation histogram, histograms from ten subsamples are created. The particle correlation is filled randomly into one of the ten histograms by an index between 1 and 10 drawn from a normal distribution. This is done on an event-by-event basis. For the measurements of the correlations themselves, the subsamples are merged, weighted with the statistical uncertainty of the histograms. Thus, the estimator for the correlation becomes:

$$\hat{\theta} = \frac{\sum_{i=1}^{10} w_i X_i}{\sum_{i=1}^{10} w_i}, \quad (4.3)$$

where X_i is the subsample, and w_i is the statistical weight of the subsample.

The final statistical uncertainty is calculated by creating a larger bootstrap sample distribution drawn from the ten subsamples with replacement. For this thesis a bootstrap sample size of $N = 1000$ is used. The uncertainty is then estimated from the variance of the bootstrap sample:

$$\sigma = \sqrt{\frac{1}{N-1} \sum_{i=1}^N (X_i - \hat{\theta})^2} \quad (4.4)$$

and the final statistical uncertainty becomes $\sigma_{\hat{\theta}} = \sigma / \sqrt{N}$.

5 Results & Discussion

The high energy density and temperature phase of Quantum Chromodynamics (QCD), the so-called Quark-Gluon Plasma (QGP), has been the subject of study for almost half a century. The advent of high-energy particle accelerators, such as the Large Hadron Collider (LHC) or the Relativistic Heavy-Ion Collider (RHIC), made recreating these conditions in the laboratory possible and allowed us to probe the properties of the QGP matter experimentally. The expansion of the matter happens under large pressure gradients. These pressure gradients transfer the initial geometric anisotropy of the colliding nuclei into azimuthal anisotropy of the produced particles. This azimuthal anisotropy is a key probe of the QGP and is characterized by the flow coefficient v_n of the Fourier expansion of the azimuthal distribution of final state particles. Measurements at the Large Hadron Collider (LHC) has shown large flow coefficients v_n [32, 65, 66, 33]. These measurements constrain the initial conditions (e.g., energy and entropy density) and the transport coefficients (e.g., shear viscosity over entropy density) of the system. The comparison of the measurements with hydrodynamic models suggests that the system has a near-zero value of η/s , which corresponds to a ‘perfect fluid’. Both the angle Ψ_n and the magnitude v_n of the flow vector V_n fluctuate from event to event [67, 68, 69]. Proposed observables to measure the flow vector fluctuations are the ratio $v_n\{2\}/v_n\{2\}$ [70] and the factorization ratio r_n [71]. Measurements of these observables have shown significant fluctuations of the flow vector in central collisions [72, 73]. One open question in the field is whether the flow vector fluctuations are due to fluctuations of the flow angle, flow magnitude, or both. If the answer is both, is it possible to quantify how much the flow angle Ψ_n and flow magnitude v_n each contributes to the fluctuations of the flow vector? Answering this question will help us constrain the initial conditions of the heavy-ion collisions and understand the dynamic properties of the expanding QGP.

In this section, the previous work done within the field of p_T -dependent flow vector fluctuations are discussed, before showing the results from the analysis for this thesis. The results presented in this section are based on the 2015 data in the LHC15o period. The results from 2018 data from the LHC18q and LHC18r periods are also mentioned and are further explored in appendix C. Results with the **ALI-PREL-XXXXXX** watermark in the lower left have been approved by the ALICE Collaboration as ALICE preliminary results. All new results for Pb–Pb collisions at much higher collision energy compared to previous measurements and with much better statistics are presented in section 5.1.1 and 5.1.2. Measurements of p_T -dependent flow vector fluctuations in Xe–Xe collisions at $\sqrt{s_{NN}} = 5.44$ TeV are also presented and discussed. Furthermore, new observables are proposed, based on the multi-particle correlations to separate the p_T -dependent flow angle and flow magnitude fluctuations from the overall flow vector fluctuations. The flow angle fluctuations will be due to particles with different transverse momentum being correlated with different symmetry planes, even for the same harmonic. The newly proposed observable probes the p_T -dependent fluctuations of the flow angle, which, in turn, indicates how the flow magnitude fluctuates with p_T , which must be responsible for the remaining fluctuations of the flow vector. This is explored in section 5.1.3. Finally, the correlation of different flow harmonics is probed with the p_T -differential normalized symmetric cumulant $NSC(n, m_{p_T})$. This thesis offers a new way to approach the p_T -differential symmetric cumulant, which has traditionally been measured with p_T -integrated information. This new approach con-

sist of taking one of the harmonics as a p_T -differential harmonic $v_n(p_T)$ and correlating it with a p_T -integrated harmonic v_m . This is shown in section [5.2](#).

5.1 Flow vector fluctuations

5.1.1 $v_n\{2\}/v_n[2]$

The p_T -dependence of the flow coefficient is traditionally studied with the differential flow coefficient $v_n\{2\}(p_T)$:

$$v_n\{2\}(p_T^a) = \frac{\langle\langle\cos[n(\varphi_1^a - \varphi_2^a)]\rangle\rangle}{\sqrt{\langle\langle\cos[n(\varphi_1 - \varphi_2)]\rangle\rangle}} = \frac{\langle v_n(p_T^a) v_n \cos[n(\Psi_n(p_T^a) - \Psi_n)] \rangle}{\sqrt{\langle v_n^2 \rangle}}. \quad (5.1)$$

The single set of brackets denotes an average over events, while the double set of brackets denotes an average over both particles and events. φ^a and φ^{ref} refer to the azimuthal angles of the *particles of interest* (particles selected from p_T^a region of interest) and the *reference flow particles* (usually particles from a wide kinematic range). $\Psi_n(p_T^a)$ represents the p_T -differential symmetry plane angle at p_T^a , which might fluctuate around the reference symmetry plane angle Ψ_n . The effect of the difference between $\Psi_n(p_T^a)$ and Ψ_n , due to p_T -dependent flow angle fluctuations, are quantified in the cosine term $\langle\cos[n(\Psi_n(p_T^a) - \Psi_n)]\rangle$. The effects of the p_T -dependent flow coefficient fluctuations are observed in the non-factorization of $\langle v_n(p_T^a) v_n^{\text{ref}} \rangle$ into the product of $\sqrt{\langle v_n(p_T^a)^2 \rangle}$ and $\sqrt{\langle v_n^{\text{ref}2} \rangle}$. Aside from effects of the p_T -dependent fluctuations of the flow angle and the flow coefficient, $v_n\{2\}$ also has contributions from non-flow sources.

Another two-particle correlation was proposed in [\[70\]](#):

$$\begin{aligned} v_n[2](p_T^a) &= \sqrt{\langle\langle\cos[n(\varphi_1^a - \varphi_2^a)]\rangle\rangle} \\ &= \sqrt{\langle\langle\cos[n(\varphi_1^a - \Psi_n(p_T^a)) - n(\varphi_2^a - \Psi_n(p_T^a))]\rangle\rangle} \\ &= \sqrt{\langle v_n(p_T^a)^2 \rangle}. \end{aligned} \quad (5.2)$$

This new observable, $v_n[2]$, is not affected by fluctuations in flow angle or flow coefficient, but may still be affected by non-flow effects. The difference between $v_n\{2\}$ and $v_n[2]$ is that the former takes the reference flow from a wide kinematic range and the POIs from a small p_T interval, and the latter is essentially the reference flow calculated in a narrow p_T interval. Since $v_n[2]$ is not affected by the flow angle and flow magnitude fluctuations, the p_T -dependent flow vector fluctuations can be probed by taking the ratio of $v_n\{2\}$ and $v_n[2]$:

$$\frac{v_n\{2\}}{v_n[2]} = \frac{\langle v_n(p_T^a) v_n \cos n[\Psi_n(p_T^a) - \Psi_n] \rangle}{\sqrt{\langle v_n(p_T^a)^2 \rangle} \sqrt{\langle v_n^2 \rangle}} \quad (5.3)$$

The existing results are nicely summarized in [\[72\]](#) as seen in figure [5.1](#), where measurements of $v_2\{2\}/v_2[2]$ in Pb–Pb collisions at $\sqrt{s_{\text{NN}}} = 2.76$ TeV show that the ratio is consistent with unity up to $p_T \approx 2$ GeV/ c , and then starts to deviate with increasing p_T in the central collisions. In the non-central collisions the deviations are within 10%. The measurements are compared to two different hydrodynamic frameworks from other works. The VISH2+1 hydrodynamic calculations with MC-Glauber and MC-KLN initial conditions were first presented in [\[70\]](#). The iEBE-VISHNU hydrodynamic

calculations with TRENTo and AMPT initial condition were shown in [28]. The hydrodynamic calculations with MC-KLN, TRENTo and AMPT are shown to reproduce the data well in all centrality classes, while the model with MC-Glauber initial conditions only reproduce the data in semi-central and peripheral collisions. It is observed that the MC-KLN and AMPT initial conditions with $\eta/s = 0.20$ reproduce the measured $v_2\{2\}/v_2[2]$. These measurements seem to indicate the presence of p_T -dependent V_2 fluctuations in Pb–Pb collisions, and implies that $v_2\{2\}$ should indeed be interpreted as the correlation of the azimuthal angle of final state particles with respect to the p_T -integrated flow vector over a certain kinematic range. The measurements are limited by the statistics of Run1 data. The large statistical uncertainties in figure 5.1 means that no strong conclusion can be drawn on the initial conditions or transport coefficients of the system. Higher precision measurements of the ratio $v_n\{2\}/v_n[2]$ with ALICE Run2 data will therefore help constrain the initial conditions of the system in heavy-ion collisions by allowing a better comparison to theoretical models. A more precise quantitative understanding of the fluctuations of V_n can also be obtained.

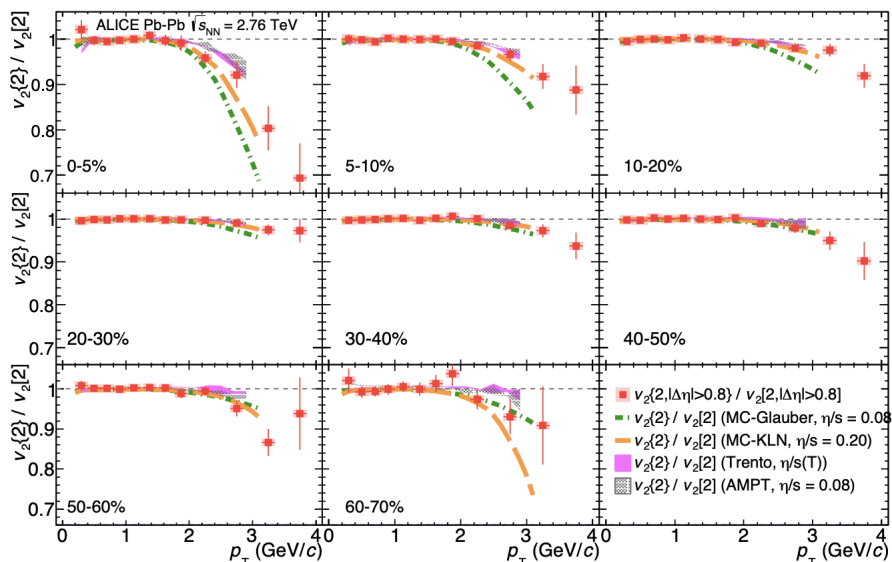


Figure 5.1: The ratio $v_2\{2, |\Delta\eta| > 0.8\}/v_2[2, |\Delta\eta| > 0.8]$ in Pb–Pb collisions at $\sqrt{s_{NN}} = 2.76$ TeV. Hydrodynamic calculations with MC-Glauber [74], MC-KLN [74], TRENTo [28] and AMPT [28] initial conditions are shown with the coloured curves. Figure taken from [72].

In this thesis, new precision measurements of $v_n\{2\}$, $v_n[2]$ and the ratio $v_n\{2\}/v_n[2]$ are presented up to $n = 4$ in Pb–Pb collisions at $\sqrt{s_{NN}} = 5.02$ TeV. Figures 5.2 and 5.3 show $v_2\{2\}$ and $v_2[2]$ as a function of p_T , with a pseudorapidity gap of 0.8 for centrality classes 0-5% to 40-50%. A strong centrality dependence is observed for both $v_2\{2\}$ and $v_2[2]$ with the highest values of v_2 measured in peripheral collisions. Increasing values of $v_2\{2\}$ is observed up to $p_T \approx 3$ GeV/c after which $v_2\{2\}$ start to decrease. This is consistent with what published measurements have shown [32]. The results are shown with hydrodynamic predictions from the iEBE-VISHNU hydrodynamic framework with: 1) TRENTo initial conditions, and transport coefficient which are allowed to evolve as function of the temperature of the system: $\eta/s(T)$ and $\zeta/s(T)$; and 2) AMPT initial conditions and $\eta/s = 0.08$ for QGP. In central and peripheral collisions, both $v_2\{2\}$ and $v_2[2]$ are described well by AMPT initial conditions, but are overesti-

mated by the hydrodynamic model with TRENTo initial conditions, especially as the collisions become more peripheral. Such a conclusion was also reached in other p_T -differential studies [75, 76].

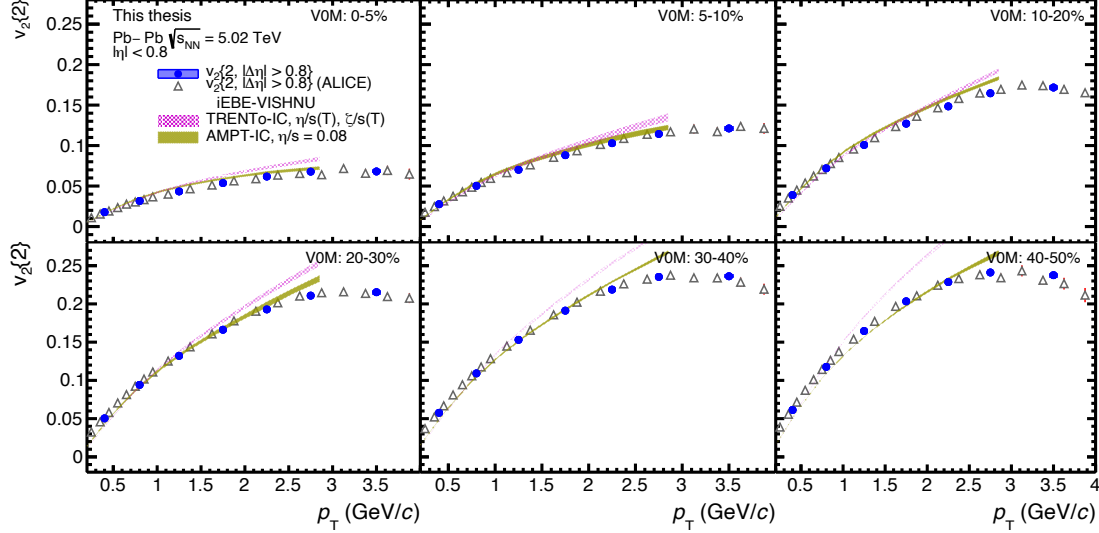


Figure 5.2: $v_2\{2\}$ in Pb–Pb collisions at $\sqrt{s_{NN}}=5.02$ TeV. Comparison with published Run1 measurements in Pb–Pb collisions at $\sqrt{s_{NN}}=2.76$ TeV shown with open triangles [32]. Comparison with iEBE-VISHNU hydrodynamic model with TRENTo initial conditions and temperature dependent $\eta/s(T)$ and $\zeta/s(T)$ [28], and with AMPT initial conditions and $\eta/s=0.08$ [28] are shown in coloured bands.

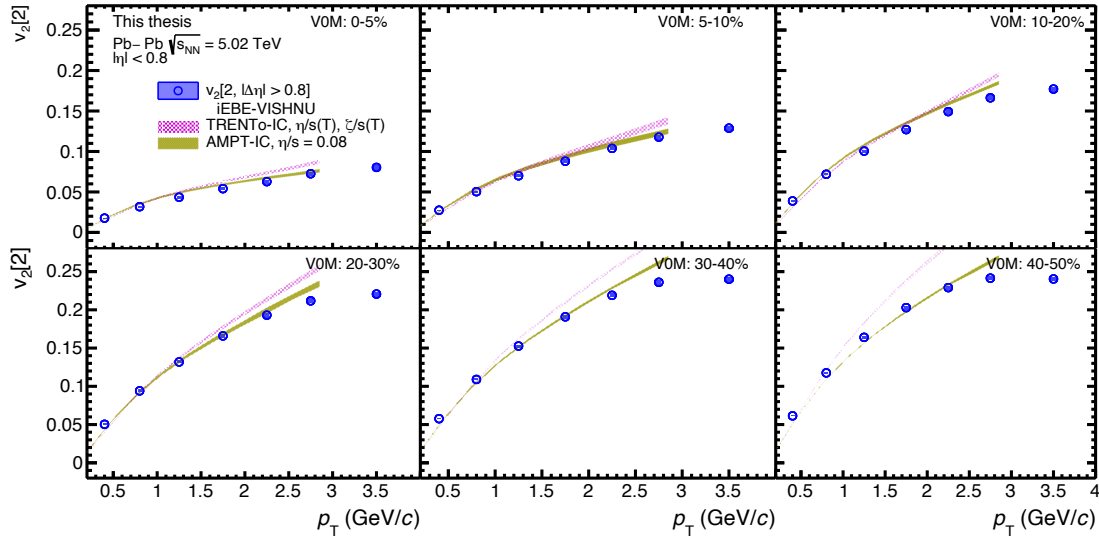


Figure 5.3: $v_2[2]$ in Pb–Pb collisions at $\sqrt{s_{NN}}=5.02$ TeV. Comparison with iEBE-VISHNU hydrodynamic model with TRENTo initial conditions and temperature dependent $\eta/s(T)$ and $\zeta/s(T)$ [28], and with AMPT initial conditions and $\eta/s=0.08$ [28] are shown in coloured bands.

Figure 5.4 show the ratio $v_n\{2\}/v_n[2]$ with $|\Delta\eta| > 0.8$ as a function of p_T for centrality classes 0-5% to 40-50%. This ratio serves as a quantitative probe of p_T -dependent flow vector fluctuations. For 0-5% most central collisions, the ratio is consistent with

unity up to $p_T \approx 2$ GeV/ c and starts to deviate from unity as p_T increases up to 15% in the presented p_T range. For centrality classes larger than 20%, the deviations from unity are very weak and within 2%. This trend was also observed with measurements done for ALICE Run1 data at $\sqrt{s_{NN}} = 2.76$ GeV/ c in [72]. As mentioned in 4.5, possible non-flow contributions to the ratio are tested with the like-sign method as well as by applying different η -gaps. The difference in $v_2\{2\}/v_2[2]$ from the above checks is less than 1% in the central collisions. This indicates that the deviations from unity are not due to non-flow effects from short-range correlations such as resonance decay, but explained by flow vector fluctuations. Also, the iEBE-VISHNU hydrodynamic predictions with TRENTo and AMPT initial conditions are presented for comparison. The hydrodynamic calculations with both TRENTo and AMPT initial conditions qualitatively describe the data within large uncertainties. The large uncertainties of the hydrodynamic calculations are due to limited statistics in the production of Monte Carlo events for the hydrodynamic calculation. Furthermore, the viscous hydrodynamic models only work up to $p_T \approx 3$ GeV/ c (where hard processes are expected to take over), So the models cannot predict the deviations from unity observed in the data above this limit. The larger statistics available in the 2018 data set enable an even more precise measurement of $v_n\{2\}/v_n[2]$. Figure 5.5 shows the comparison of $v_2\{2\}/v_2[2]$ for 2015 data and 2018 data in centrality classes 0-5% to 40-50%. The results are consistent with each other within 0.5%. Since the data sets are independent of each other, the results can be merged to obtain even better statistics. Appendix C offers more details on the 2018 measurements. The results of $v_2\{2\}/v_2[2]$ measured in Xe–Xe collisions is shown in figure 5.6. The data from Xe–Xe collisions is limited in statistics, since only ~ 1 M Xe–Xe events are recorded compared to the ~ 65 M Pb–Pb events. This is reflected in the high uncertainty of $v_2\{2\}/v_2[2]$ in the Xe–Xe collisions. The Xe–Xe measurement shows qualitatively the same trend as the Pb–Pb collisions, but more data is needed in order to conclude whether p_T -dependent flow vector fluctuations are present in Xe–Xe collisions. A study by the ATLAS collaboration [77] showed η -dependent decorrelation of v_n in Xe–Xe collisions, so decorrelations of v_n are known to exist in Xe–Xe collisions. The higher order $v_n\{2\}/v_n[2]$ measurements are even more affected by the limited statistics and will not be shown in this thesis.

Higher order anisotropic flow measurements were measured for the first time in [33] and were found to be more sensitive to the initial conditions and properties of QGP. Figures 5.7 and 5.8 show $v_3\{2\}$ and $v_3[2]$ as function of p_T in different centrality classes. Unlike v_2 , which has a strong centrality dependence, v_3 only shows a very weak dependence. This is due to v_3 being driven by fluctuations in the initial state, and does not depend as much on the initial geometry. This is in contrast to v_2 , which is heavily affected by the initial spatial anisotropy. The magnitude of v_3 peaks at around $p_T \approx 3$ GeV/ c , which was also observed for v_2 . The comparison with hydrodynamic models show that the hydrodynamic calculations with both AMPT initial conditions and TRENTo initial conditions describe the data well in 0-10% most central collisions, but in centralities greater than 10% the model with AMPT initial conditions best describe the data, while TRENTo initial conditions overestimates the data.

The ratio $v_3\{2\}/v_3[2]$ with $|\Delta\eta| > 0.8$ is shown in figure 5.9. It is found to agree with unity in the presented centrality and p_T range, unlike $v_2\{2\}/v_2[2]$, which is shown in figure 5.4. The agreement of $v_3\{2\}/v_3[2]$ with unity suggests that the triangular

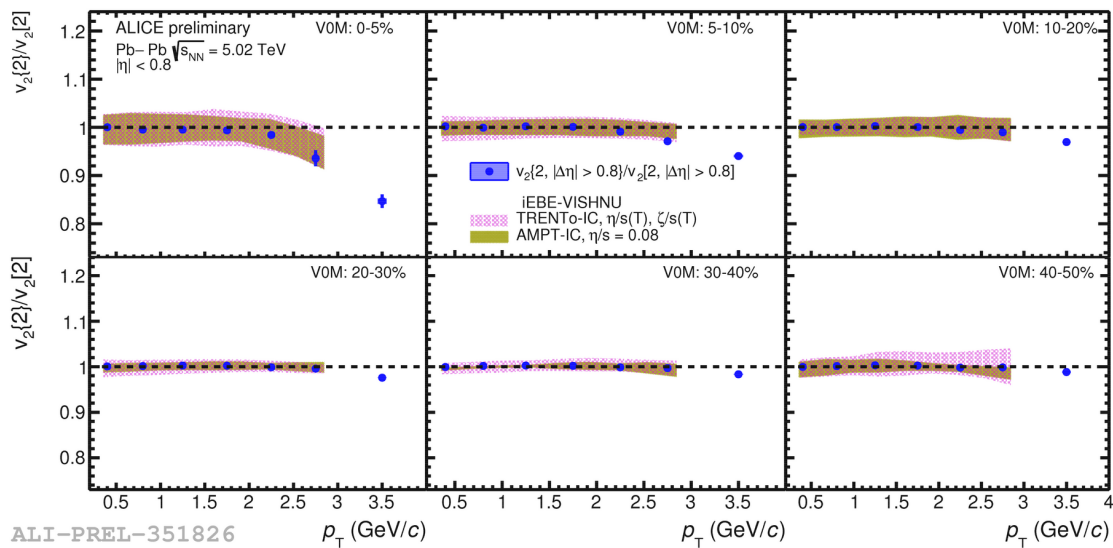


Figure 5.4: The ratio $v_2\{2\}/v_2[2]$ in Pb–Pb collisions at $\sqrt{s_{\text{NN}}}= 5.02$ TeV. Comparison with iEBE-VISHNU hydrodynamic model with TRENTo initial conditions and temperature dependent $\eta/s(T)$ and $\zeta/s(T)$ [28], and with AMPT initial conditions and $\eta/s = 0.08$ [28] are shown in coloured bands.

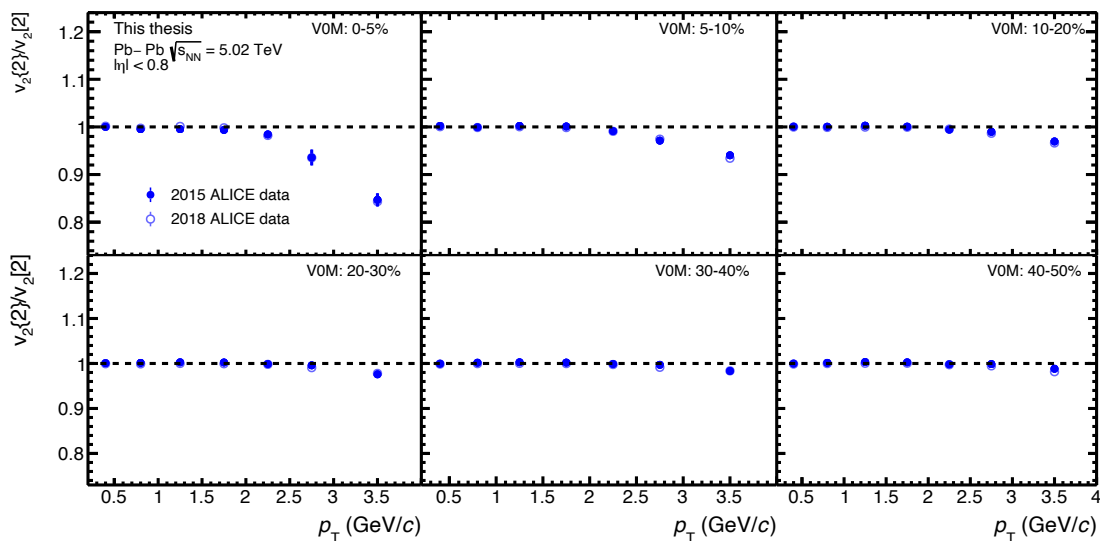


Figure 5.5: Comparison of the ratio $v_2\{2\}/v_2[2]$ in Pb–Pb collisions at $\sqrt{s_{\text{NN}}}= 5.02$ TeV for the different data sets. The 2015 data (solid circles) are compared to the 2018 data (open circles).

flow vector V_3 does not fluctuate strongly with p_T in the presented p_T and centrality range. Previous published measurements for Run1 [72] has very large uncertainties for $v_3\{2\}/v_3[3]$, and thus could not conclude whether there are p_T -dependent flow vector fluctuations of V_3 . With these new Run2 results we can draw a firm conclusion that there is no p_T -dependent V_3 fluctuations. The hydrodynamic calculations with the iEBE-VISHNU hydrodynamic models describe the ratio rather well, since it is independent of the magnitude of v_3 . Both TRENTo and AMPT initial conditions show agreement with unity and the data. A small deviation from unity is seen in the hydro-

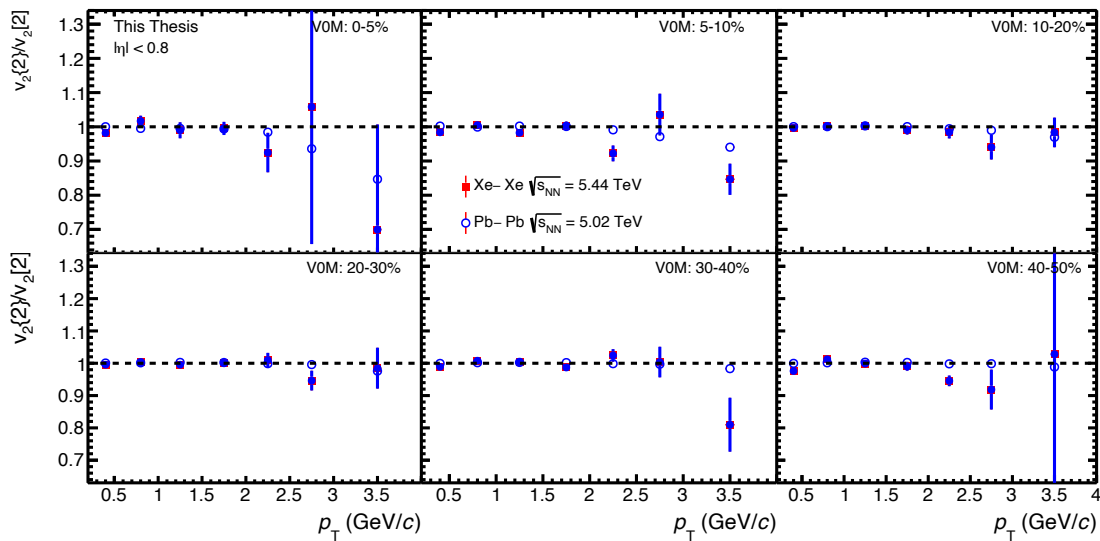


Figure 5.6: The ratio $v_2\{2\}/v_2[2]$ in Xe–Xe collisions at $\sqrt{s_{\text{NN}}} = 5.44$ TeV. Comparison with the Pb–Pb measurements is shown in open circles.

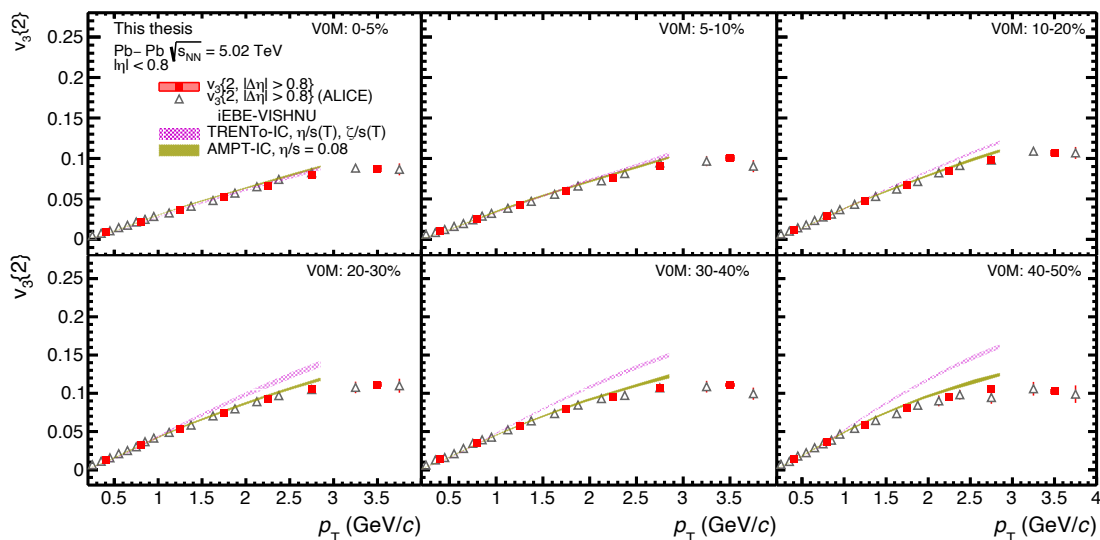


Figure 5.7: $v_3\{2\}$ for Pb–Pb collisions at $\sqrt{s_{\text{NN}}} = 5.02$ TeV. Comparison with published Run1 measurements in Pb–Pb collisions at $\sqrt{s_{\text{NN}}} = 2.76$ TeV shown with open triangles [32]. Comparison with iEBE-VISHNU hydrodynamic model with TRENTo initial conditions and temperature dependent $\eta/s(T)$ and $\zeta/s(T)$ [28], and with AMPT initial conditions and $\eta/s = 0.08$ [28] are shown in coloured bands.

dynamic predictions at low p_T , which is within $\sim 1\sigma$ of the data. This effect was observed to be significant in the Run1 hydrodynamic calculations [72], which has larger statistics than the hydrodynamic calculations presented here. However, we still do not have the precision to probe this effect.

Results of $v_4\{2\}$ and $v_4[2]$ are shown in figures 5.10 and 5.11 with $|\Delta\eta| > 0.8$ for $0.2 < p_T < 4.0$ GeV/c in centrality classes 0-5% to 40-50%. v_4 shows only a weak centrality dependence as was the case for v_3 . Unlike v_3 , which is purely driven by fluctuations of the initial anisotropy, v_4 has linear and non-linear flow modes [78]. This means v_4 has contributions from both the initial spatial anisotropy of the same harmonic described

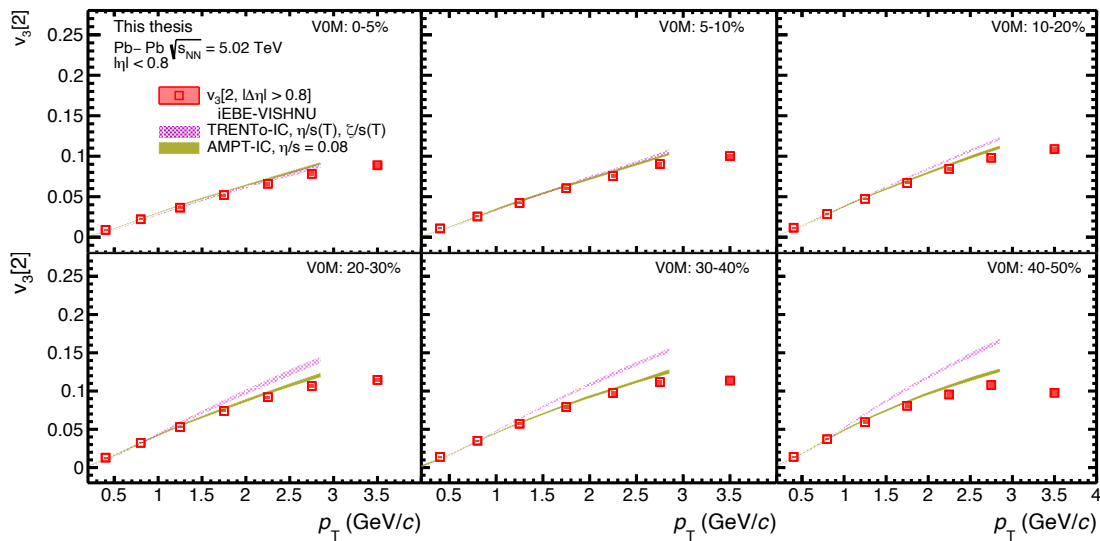


Figure 5.8: $v_3\{2\}$ for Pb–Pb collisions at $\sqrt{s_{NN}} = 5.02$ TeV. Comparison with iEBE-VISHNU hydrodynamic model with TRENTo initial conditions and temperature dependent $\eta/s(T)$ and $\zeta/s(T)$ [28], and with AMPT initial conditions and $\eta/s = 0.08$ [28] are shown in coloured bands.

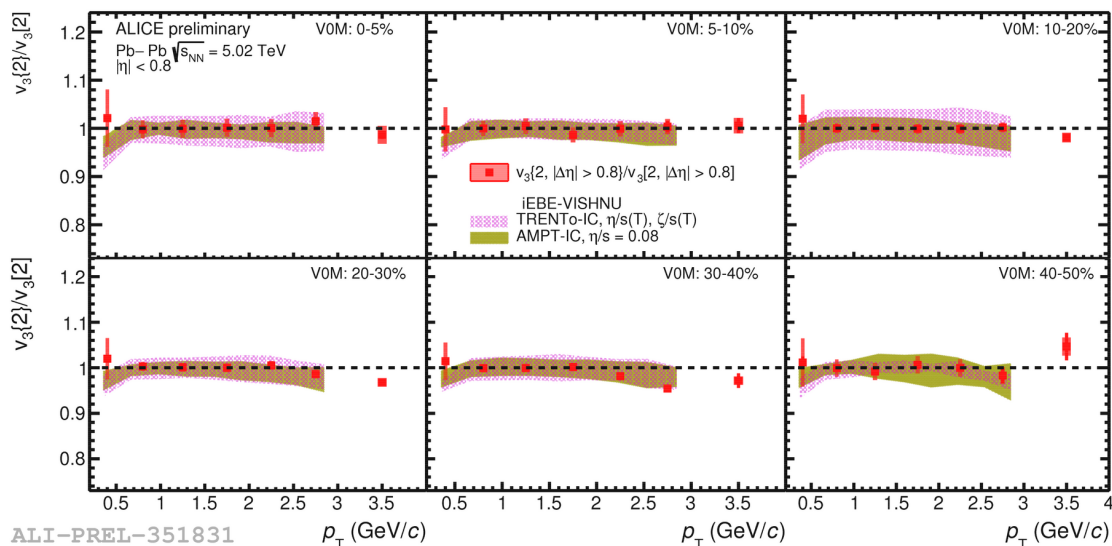


Figure 5.9: The ratio $v_3\{2\}/v_3[2]$ for Pb–Pb collisions at $\sqrt{s_{NN}} = 5.02$ TeV. Comparison with iEBE-VISHNU hydrodynamic model with TRENTo initial conditions and temperature dependent $\eta/s(T)$ and $\zeta/s(T)$ [28], and with AMPT initial conditions and $\eta/s = 0.08$ [28] are shown in coloured bands.

by the eccentricity ϵ_4 and also from lower order ϵ_2^2 . The iEBE-VISHNU hydrodynamic framework shows good agreement with the data in the 0-10% most central collisions for both AMPT and TRENTo initial conditions. The hydrodynamic calculations with AMPT initial conditions continue to describe the data in centrality classes greater than 20%, whereas the one with TRENTo initial conditions overestimates the data above this centrality as was seen for both v_2 and v_3 .

The ratio $v_4\{2\}/v_4[2]$ with $|\Delta\eta| > 0.8$ shown in figure 5.12 is consistent with unity within

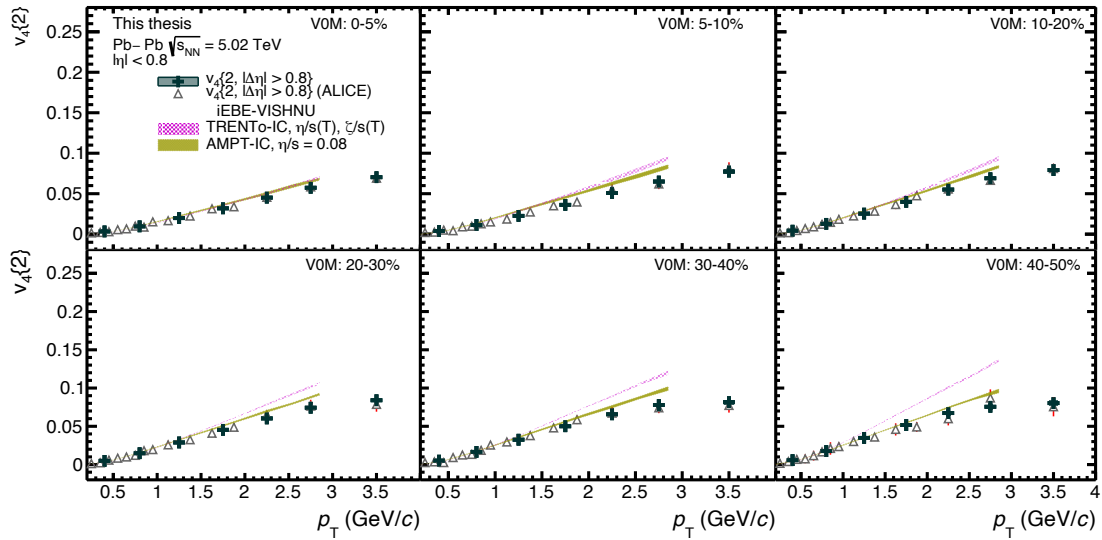


Figure 5.10: $v_4\{2\}$ for Pb–Pb collisions at $\sqrt{s_{\text{NN}}} = 5.02$ TeV. Comparison with published Run1 measurements in Pb–Pb collisions at $\sqrt{s_{\text{NN}}} = 2.76$ TeV shown with open triangles [32]. Comparison with iEBE-VISHNU hydrodynamic model with TRENTo initial conditions and temperature dependent $\eta/s(T)$ and $\zeta/s(T)$ [28], and with AMPT initial conditions and $\eta/s = 0.08$ [28] are shown in coloured bands.

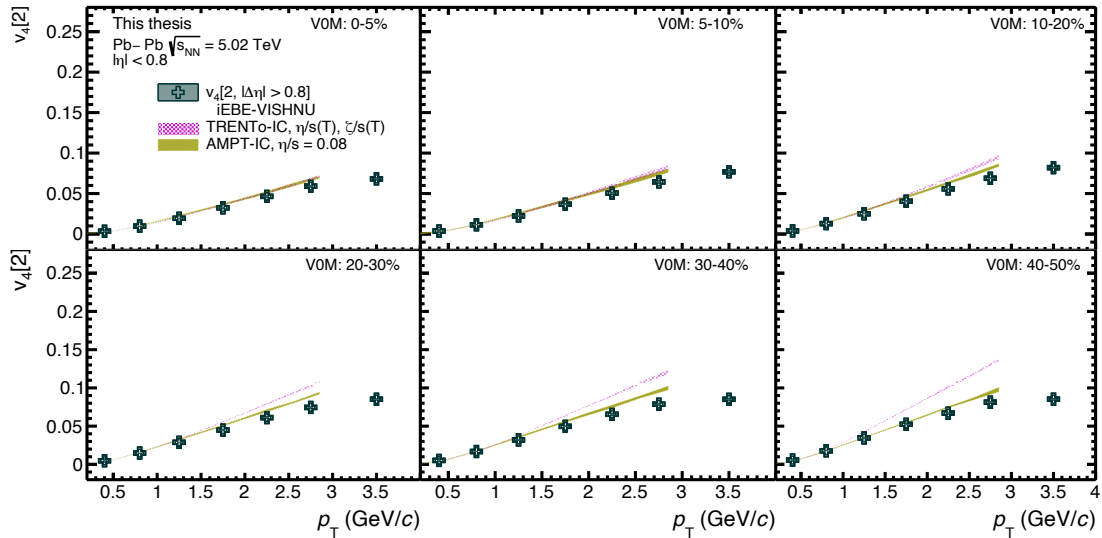


Figure 5.11: $v_4[2]$ for Pb–Pb collisions at $\sqrt{s_{\text{NN}}} = 5.02$ TeV. Comparison with iEBE-VISHNU hydrodynamic model with TRENTo initial conditions and temperature dependent $\eta/s(T)$ and $\zeta/s(T)$ [28], and with AMPT initial conditions and $\eta/s = 0.08$ [28] are shown in coloured bands.

large uncertainties. The large systematic uncertainty in the lowest p_T bin is purely due to variation of the track type from global to hybrid. This can be improved further by a more detailed study on the different track types. Run1 measurements of $v_4\{2\}/v_4[2]$ [72] had huge statistical uncertainties, which did not allow a conclusion to be drawn on whether p_T -dependent V_4 fluctuations were present in the Pb–Pb collisions. The results presented in this thesis allows us to firmly conclude that V_4 does not fluctuate as function of transverse momentum. The hydrodynamic calculations are consistent with

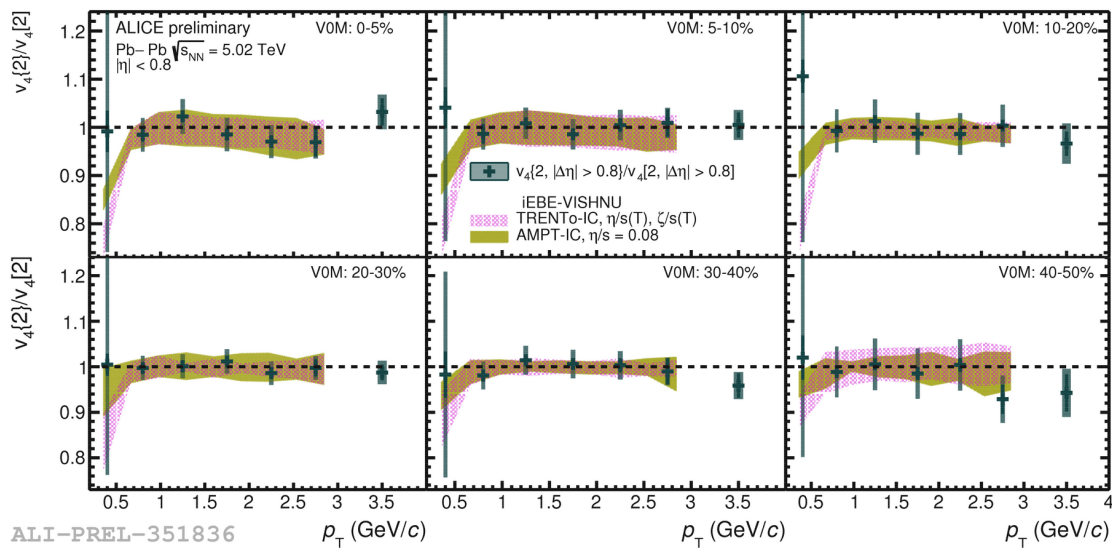


Figure 5.12: The ratio $v_4\{2\}/v_4[2]$ for Pb–Pb collisions at $\sqrt{s_{\text{NN}}} = 5.02$ TeV. Comparison with iEBE-VISHNU hydrodynamic model with TRENTo initial conditions and temperature dependent $\eta/s(T)$ and $\zeta/s(T)$ [28], and with AMPT initial conditions and $\eta/s = 0.08$ [28] are shown in coloured bands.

unity for $p_T > 0.6$ GeV/c, but show a deviation from unity at low p_T . This deviation from unity was also seen in hydrodynamic calculations of $v_3\{2\}/v_3[2]$, and it is even more pronounced for $v_4\{2\}/v_4[2]$.

5.1.2 Factorization ratio r_n

Another way to study flow vector fluctuations is to study the factorization of two-particle correlations from different transverse momentum regions. This factorization of two-particle correlations into a product of a function of properties of only one of the particles times a function of the properties of the other was observed in [74, 65, 66, 79]. The factorization was tested for pairs of particles in various bins of p_T in [74] as:

$$V_{n\Delta}(p_T^a, p_T^t) \equiv \langle \langle \cos n(\varphi^a - \varphi^t) \rangle \rangle \stackrel{?}{=} v_n(p_T^a) \times v_n(p_T^t). \quad (5.4)$$

This measured values of $V_{n\Delta}(p_T^a, p_T^t)$ was fitted with a so-called global fit, which generates the product $v_n(p_T^a) \times v_n(p_T^t)$ that minimizes the χ^2 for all $V_{n\Delta}$ points. This is shown in figure 5.13. It was observed that the factorization holds for $n \geq 2$ at low values of p_T^a ($\lesssim 2$ GeV/c). The symmetric function of the two variables on the left hand side does not, in general, factorize into a product of v_n of each variable separately. The fact that the factorization holds (approximately) means it carries information about the structure of the correlation.

In pure hydrodynamics, particles are emitted independently, and thus carry no intrinsic correlation among each other. Therefore, it had been stated that the factorization should hold perfectly in an ideal hydrodynamic picture [65, 80, 81]. It was shown, however, that the factorization in Eq. (5.4) is not necessarily present even in ideal hydrodynamic circumstances [71]. This was tested with the factorization ratio [71]:

$$r_n = \frac{V_{n\Delta}(p_T^a, p_T^t)}{\sqrt{V_{n\Delta}(p_T^a, p_T^a)V_{n\Delta}(p_T^t, p_T^t)}}, \quad (5.5)$$

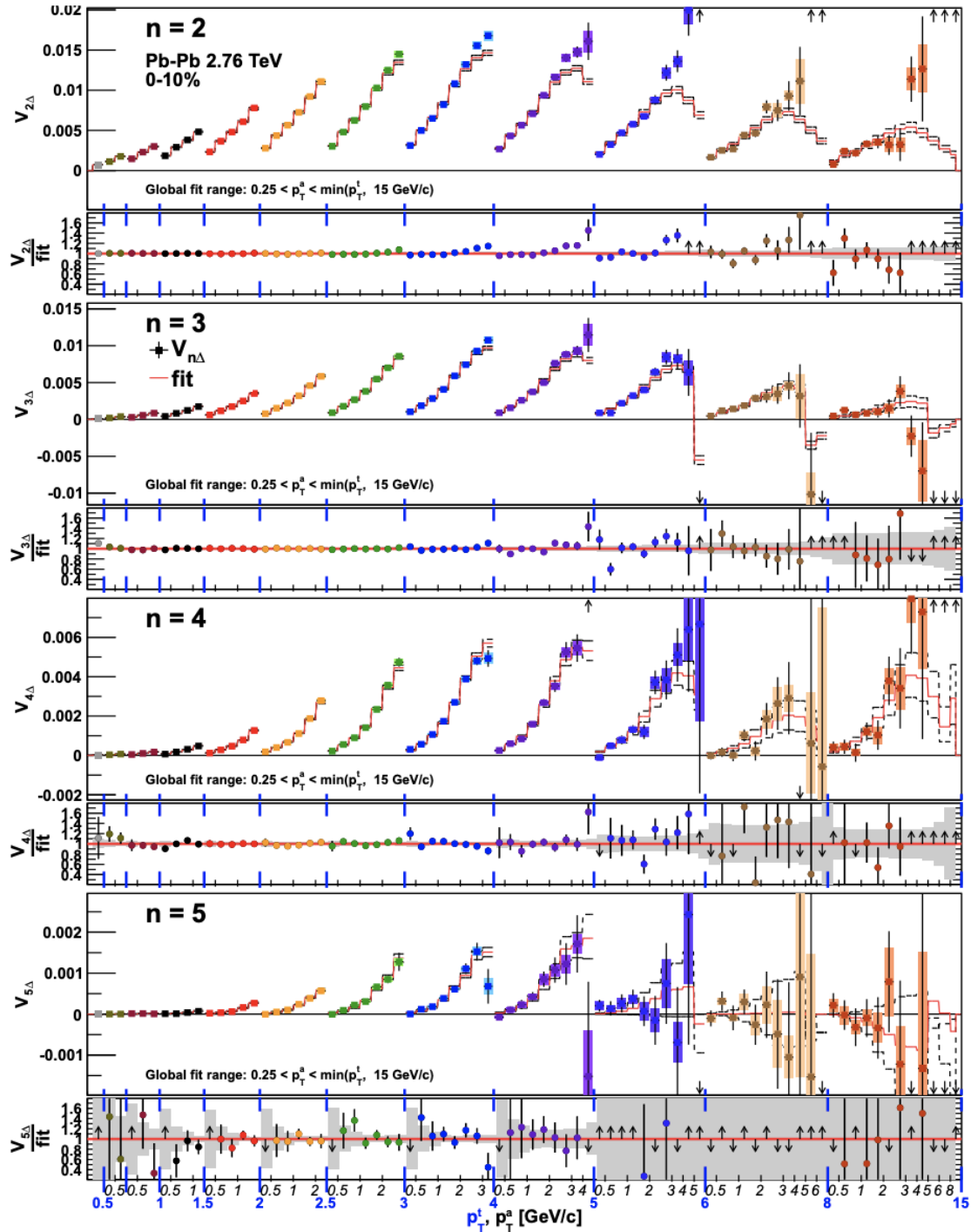


Figure 5.13: Examples of the global fit in 0–10% centrality events for $n = 2, 3, 4$ and 5 . The measured $V_{n\Delta}$ coefficients are plotted on an interleaved p_T^t, p_T^a axis in the upper panels, and the red curves denote the global fit function (Eq. (5.4)). The ratio of the data to the fit is shown in the lower section of each panel. Figure taken from [74].

where $V_{n\Delta}(p_T^a, p_T^t)$ is the n^{th} -order harmonic of the two-particle correlations of triggered and associated particles from p_T^a and p_T^t , and is calculated as:

$$V_{n\Delta}(p_T^a, p_T^t) = \langle \langle \cos[n(\varphi_1^a - \varphi_2^t)] \rangle \rangle = \langle v_n(p_T^a) v_n(p_T^t) \cos[n(\Psi_n(p_T^a) - \Psi_n(p_T^t))] \rangle. \quad (5.6)$$

When both particles are selected from p_T^a or p_T^t the following is obtained:

$$V_{n\Delta}(p_T^a, p_T^a) = \langle \langle \cos[n(\varphi_1^a - \varphi_2^a)] \rangle \rangle = \langle v_n(p_T^a)^2 \rangle. \quad (5.7)$$

$$V_{n\Delta}(p_T^t, p_T^t) = \langle \langle \cos[n(\varphi_1^t - \varphi_2^t)] \rangle \rangle = \langle v_n(p_T^t)^2 \rangle. \quad (5.8)$$

With this r_n becomes:

$$r_n = \frac{\langle v_n(p_T^a) v_n(p_T^t) \cos[n(\Psi_n(p_T^a) - \Psi_n(p_T^t))] \rangle}{\sqrt{\langle v_n(p_T^a)^2 \rangle \langle v_n(p_T^t)^2 \rangle}} \quad (5.9)$$

Most known sources of non-flow do not factorize at low p_T [82], so $r_n = 1$ will not always hold true. In a system dominated by flow, with no or negligible non-flow effects, $r_n \leq 1$, due to the Cauchy-Schwarz inequality [71]. When $r_n = 1$, the factorization holds; while $r_n < 1$ indicates the presence of p_T -dependent flow vector fluctuations.

If the triggered particles are selected from a wide kinematic range, then r_n becomes identical to $v_n\{2\}/v_n[2]$. In general, however, r_n provides information about the correlation structure of the two-particle correlation for triggered and associate particles, and probes the fluctuations of the flow vector at p_T^a and p_T^t . For $v_n\{2\}/v_n[2]$, it includes the p_T -integrated information and probes the p_T -differential flow vector with respect to the p_T -integrated flow vector. Furthermore, the factorization ratio is constructed such that $r_n = 1$, when $p_T^a = p_T^t$.

Measurements of r_n , which builds upon the factorization study, were presented in both [72] and [73] for Pb–Pb collisions at $\sqrt{s_{\text{NN}}} = 2.76$ TeV. The former work is from the ALICE collaboration and the latter from the CMS collaboration. These measurements of r_2 are shown in figure 5.14. The approach used in the ALICE measurements takes the triggered and associate particles from different subevents. This removes auto-correlations that might arise from selecting $p_T^a = p_T^t$ and eliminates the need for a $p_T^t \geq p_T^a$ cut, which is used in both figure 5.13 and for the CMS measurements shown in 5.14. The subevent method is also used in this thesis. Regardless of the method, the two sets of measurements in figure 5.14 show that r_2 deviates from unity as the difference $|p_T^a - p_T^t|$ increases in central collisions, and indicate that p_T -dependent flow vector fluctuations are present in V_2 . The ALICE measurement in [72] was limited by the statistics available at the time, since the analysis was performed on Pb–Pb collisions at $\sqrt{s_{\text{NN}}} = 2.76$ TeV collected during the Run1 data taking period. This is observed in the large statistical uncertainty at higher values of p_T^a .

In this thesis, precision measurements of r_n in Pb–Pb collisions at $\sqrt{s_{\text{NN}}} = 5.02$ TeV are shown up to $n = 3$. Figure 5.15 show the factorization ratio r_2 with a pseudorapidity gap larger than 0.8 as a function of p_T^a in centrality classes 0-5%, 10-20% and 40-50% in various bins of p_T^t . For all p_T^t bins, it is observed that the deviations from unity are largest in the central collisions, and that the effect becomes more pronounced as the difference $|p_T^a - p_T^t|$ increases. That the effects are strongest in the central collisions are expected, as this is where the fluctuations of the initial state geometry dominate. The largest deviation from unity is observed in the central collisions for the lowest p_T^t bin up to 14% as p_T^a increases, with only a small deviation of around 3% from unity in

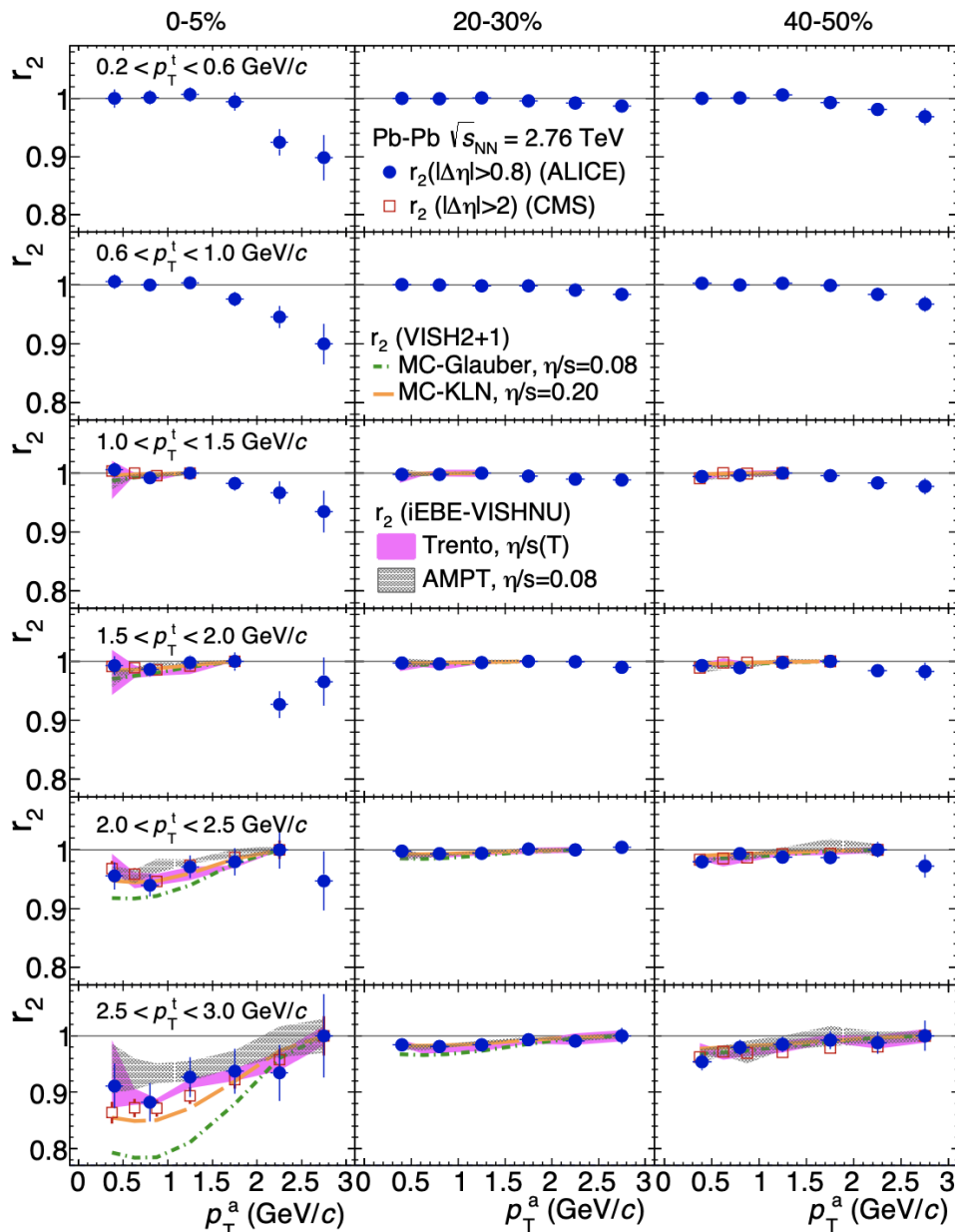


Figure 5.14: The ALICE measurements of the factorization ratio r_2 as function of p_T^a in bins of p_T^t for centrality classes 0-5%, 20-30% and 40-50% in Pb–Pb collisions at $\sqrt{s_{NN}}=2.76$ TeV with comparison to hydrodynamic models with TRENTo initial conditions [28] and AMPT initial conditions [28] are shown in coloured curves. Figure taken from [72].

the peripheral collisions. This indicates that factorization is broken in the central collisions, which, in turn, implies the presence of p_T -dependent flow vector fluctuations as described in [71]. At higher p_T^t , the deviations from unity become less pronounced, since the difference $|p_T^a - p_T^t|$ reaches the largest value in the lowest p_T^t bin. A comparison with r_2 results for Run1 Pb–Pb collisions at $\sqrt{s_{NN}}=2.76$ GeV/c from [72] is shown with orange crosses. The deviations from unity measured in Run1, while significant, had large uncertainties that are improved by the Run2 measurements presented here. The precision of r_2 is drastically improved, with the deviations from unity being significant

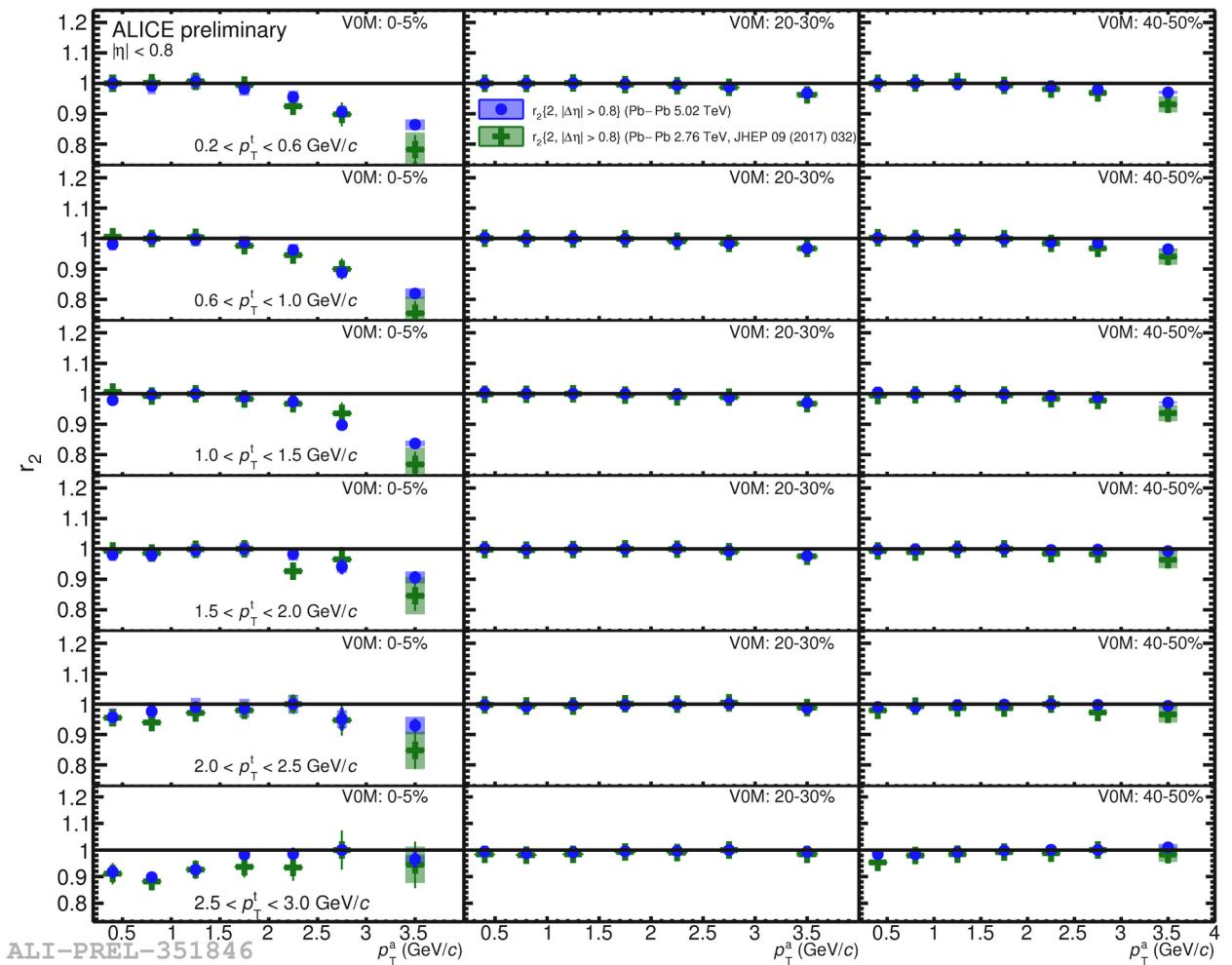


Figure 5.15: The factorization ratio r_2 for Pb–Pb collisions at $\sqrt{s_{\text{NN}}} = 5.02$ TeV in different bins of p_{T}^t and centrality. Run1 ALICE measurements in Pb–Pb collisions at $\sqrt{s_{\text{NN}}} = 2.76$ GeV/c are presented as orange crosses [72].

to more than 5σ .

The centrality dependence of r_2 is more clearly seen in figure 5.16, where r_2 is presented in centrality classes 0-5% to 40-50% in the lowest p_{T}^t bin: $0.2 < p_{\text{T}}^t < 0.6$ GeV/c. The comparison with hydrodynamic calculation from iEBE-VISHNU with AMPT and TRENTo initial conditions are presented for centrality classes 0-5% up to 40-50%. Both hydrodynamic calculations qualitatively describe the trend of r_2 , however they also underestimate the deviations from unity at higher p_{T} in central collisions. The hydrodynamic model with AMPT initial conditions quantitatively describe r_2 better in central collisions than the one with TRENTo initial conditions. Good agreement with the data is observed in peripheral collisions for both hydrodynamic calculations. Measurements of r_2 in Xe–Xe collisions are presented in figure 5.17. Due to the limited Xe–Xe data, no firm conclusion can be made about the presence of p_{T} -dependent flow vector fluctuations in Xe–Xe collisions.

Figure 5.18 shows r_3 with $|\Delta\eta| > 0.8$ as a function of p_{T}^a for different bins of p_{T}^t , and in centrality classes 0-5%, 10-20% and 40-50%. r_3 is consistent with unity in the presented centrality and p_{T} range for all bins of p_{T}^t . Systematic uncertainty of up to $\sim 10\%$ is assigned in the lowest bin of p_{T}^t , which is mostly due to variation of the track type

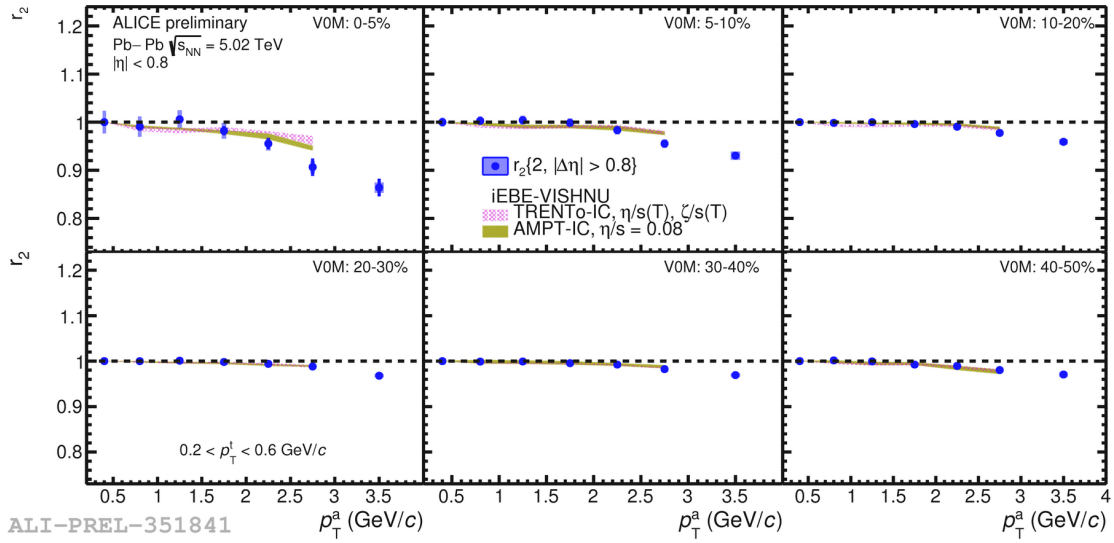


Figure 5.16: The factorization ratio r_2 for Pb–Pb collisions at $\sqrt{s_{\text{NN}}} = 5.02$ TeV. Comparison with iEBE-VISHNU hydrodynamic model with TRENTo initial conditions and temperature dependent $\eta/s(T)$ and $\zeta/s(T)$ [28], and with AMPT initial conditions and $\eta/s = 0.08$ [28] are shown in coloured bands.

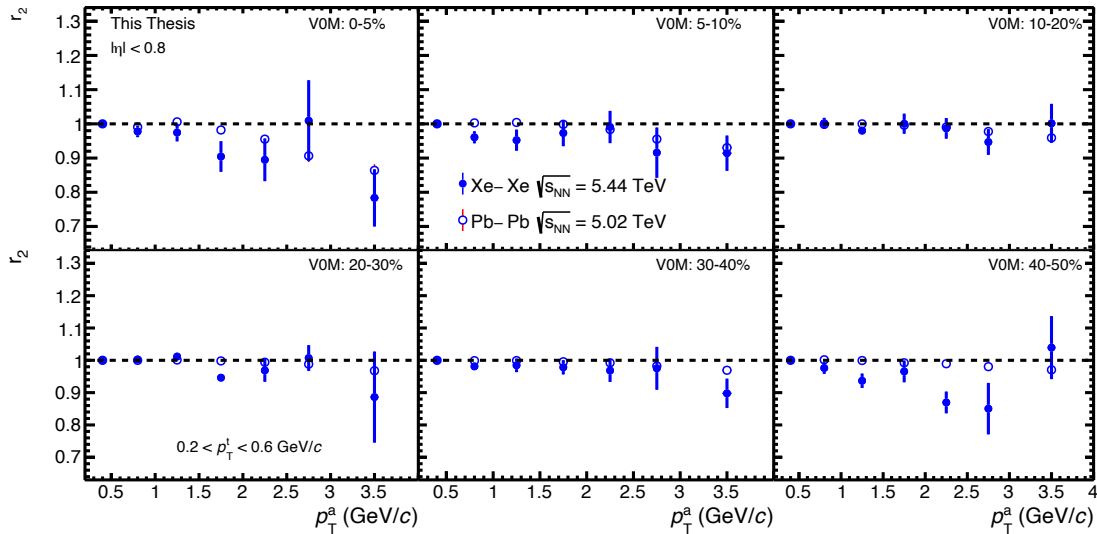


Figure 5.17: The factorization ratio r_2 for Xe–Xe collisions at $\sqrt{s_{\text{NN}}} = 5.44$ TeV. Comparison with r_2 in Pb–Pb collisions at $\sqrt{s_{\text{NN}}} = 5.02$ TeV is shown in open circles.

cut. The agreement with unity over the presented centrality range suggests that the factorization of the two-particle correlation $V_{3\Delta}$ is independent of centrality. This is consistent with the picture that triangular flow is driven by fluctuations of the initial state. The factorization is also observed to hold over the entirety of the presented range of p_{T}^a , p_{T}^t , as opposed to r_2 . The results are compared with the Run1 ALICE measurements of r_3 in Pb–Pb collisions at $\sqrt{s_{\text{NN}}} = 2.76$ TeV [72], which are shown in figure 5.18 as orange points. The Run1 measurements show deviations from unity at high p_{T} in several bins of p_{T}^t , and it was noted that a possible breakdown of the factorization would be within 10%, when both p_{T}^a and p_{T}^t are below 3 GeV/c. The precision measurements presented in this thesis constrain this even further down to 5% if such a

breakdown of factorization exists.

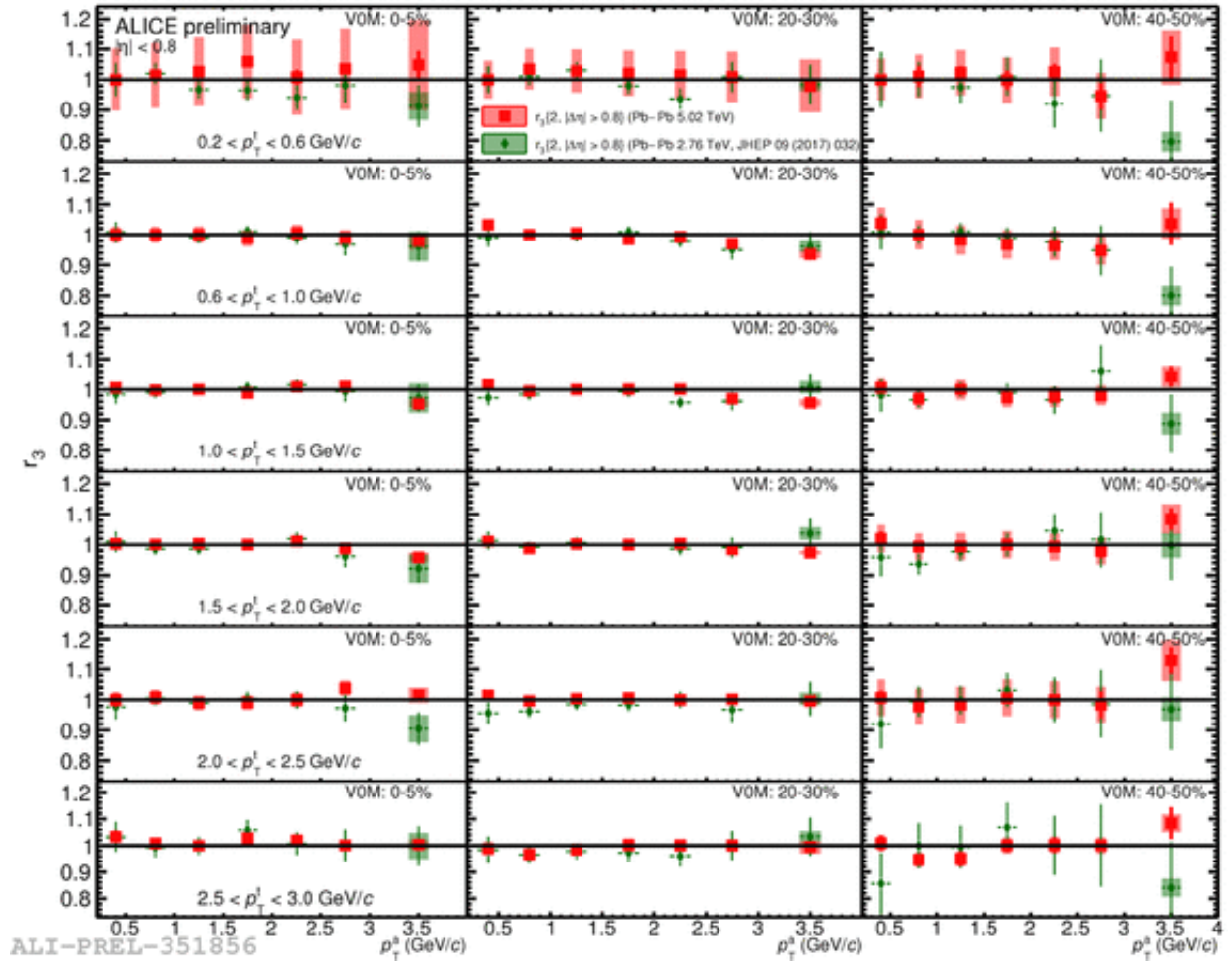


Figure 5.18: The factorization ratio r_3 for Pb–Pb collisions at $\sqrt{s_{NN}}=5.02$ TeV for different trigger particle p_T^t intervals. Run1 ALICE measurements in Pb–Pb collisions at $\sqrt{s_{NN}}=2.76$ GeV/c are presented as orange points [72].

5.1.3 Angle decorrelation $C(\Psi_n)$

Both the ratio $v_n\{2\}/v_n[2]$ and the factorization ratio r_n carry information about fluctuations of both the flow angle $\Psi_n(p_T)$ and the flow coefficient $v_n(p_T)$. The presented measurements of $v_n\{2\}/v_n[2]$ and r_n have shown deviations from unity, which suggests the presence of p_T -dependent flow vector fluctuations. However, same as the Run1 measurements [72], it is unclear whether this is due to fluctuations of the flow angle or the flow magnitude. Thus, it is desirable to separate these two effects in order to quantify the contributions from each source.

A new observable $C(\Psi_n)$ is proposed in this thesis, which isolates the p_T -dependent fluctuations of the flow angle $\Psi_n(p_T)$.

$$C(\Psi_n^a, \Psi_n) = \frac{\langle \langle \cos[n(\varphi_1^a + \varphi_2^a - \varphi_3 - \varphi_4)] \rangle \rangle}{\langle \langle \cos[n(\varphi_1^a + \varphi_2 - \varphi_3^a - \varphi_4)] \rangle \rangle} = \frac{\langle v_n(p_T^a)^2 v_n^2 \cos 2n[\Psi_n(p_T^a) - \Psi_n] \rangle}{\langle v_n(p_T^a)^2 v_n^2 \rangle \langle \cos 2n[\Psi_n(p_T^a) - \Psi_n] \rangle}, \quad (5.10)$$

where the third equality holds if the non-flow of the numerator and denominator is approximately the same. $C(\Psi_n^a, \Psi_n)$ probes the correlation of the p_T -dependent flow angle with the reference flow angle, since the flow angle $\Psi_n(p_T)$ might fluctuate around the average flow angle Ψ_n . If the flow angle fluctuates as function of p_T , we have $C(\Psi_n^a, \Psi_n) < 1$. In the case of no p_T -dependent fluctuations of the flow angle, we have $C(\Psi_n^a, \Psi_n) = 1$.

Since this is a completely new and non-trivial correlation, it has not been implemented in the Generic Framework [43]. The implementation of $C(\Psi_n^a, \Psi_n)$ into the Generic Framework is presented here, and the reader is referred to section 2 for the definitions of the Q-vector, p^a -vector and q-vector used in the Generic Framework. $C(\Psi_n^a, \Psi_n)$ is calculated with the subevent method, which was described in section 2.2. An illustration of the four-particle correlation in the numerator of Eq. (5.10) is shown in figure 5.19, where the particles from the p_T region of interest are selected from the same subevent, and the reference particles are selected from the other. The four-particle correlation in the denominator is illustrated in figure 5.20. Here, one particle from the p_T region of interest is selected from each subevent together with a reference particle. Since $C(\Psi_n^a, \Psi_n)$ is obtained with four-particle correlations using the subevent method, it can be constructed as a product of two-particle correlations as mentioned in section 2.2.1. The numerator in Eq. (5.10) is given as:

$$\langle \cos[n(\varphi_1^a + \varphi_2^a - \varphi_3 - \varphi_4)] \rangle = N\langle 4 \rangle_{n_1^a, n_2^a, n_3, n_4} / D\langle 4 \rangle_{n_1^a, n_2^a, n_3, n_4} \quad (5.11)$$

$$\begin{aligned} N\langle 4 \rangle_{n_1^a, n_2^a, n_3, n_4} &= N\langle 2 \rangle_{n_1^a, n_2^a}^A N\langle 2 \rangle_{n_3, n_4}^B \\ &= (p_{n_1,1}^{aA} p_{n_2,1}^{aA} - p_{n_1+n_2,2}^{aA}) (Q_{n_3,1}^B Q_{n_4,1}^B - Q_{n_3+n_4,2}^B), \end{aligned} \quad (5.12)$$

and the denominator as:

$$\langle \cos[n(\varphi_1^a + \varphi_2 - \varphi_3^a - \varphi_4)] \rangle = N\langle 4 \rangle_{n_1^a, n_2, n_3^a, n_4} / D\langle 4 \rangle_{n_1^a, n_2, n_3^a, n_4} \quad (5.13)$$

$$\begin{aligned} N\langle 4 \rangle_{n_1^a, n_2, n_3^a, n_4} &= N\langle 2 \rangle_{n_1^a, n_2}^A N\langle 2 \rangle_{n_3^a, n_4}^B \\ &= (p_{n_1,1}^{aA} Q_{n_2,1}^A - q_{n_1+n_2,2}^A) (p_{n_3,1}^{aB} Q_{n_4,1}^B - q_{n_3+n_4,2}^B). \end{aligned} \quad (5.14)$$

These equations can be used to calculate the particle-averaged four-particle correlations, which are then averaged over events in order to obtain $C(\Psi_n^a, \Psi_n)$.

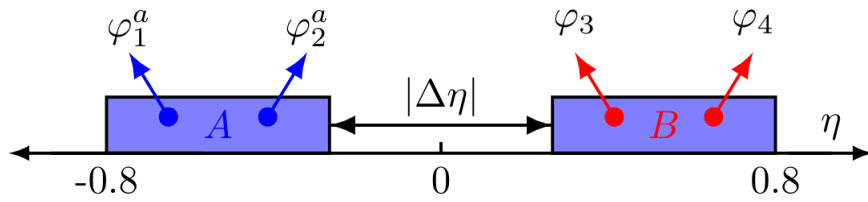


Figure 5.19: Sketches of side view of the detector showing a four-particle correlation with two subevents and $|\Delta\eta|$ gap separating them. The particles of interest are selected from the *same* subevent.

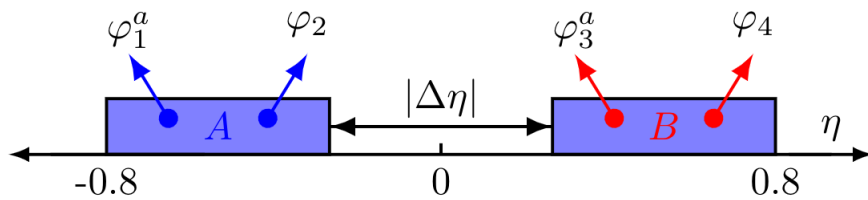


Figure 5.20: Sketches of side view of the detector showing a four-particle correlation with two subevents and $|\Delta\eta|$ gap separating them. The particles of interest are selected from *different* subevents.

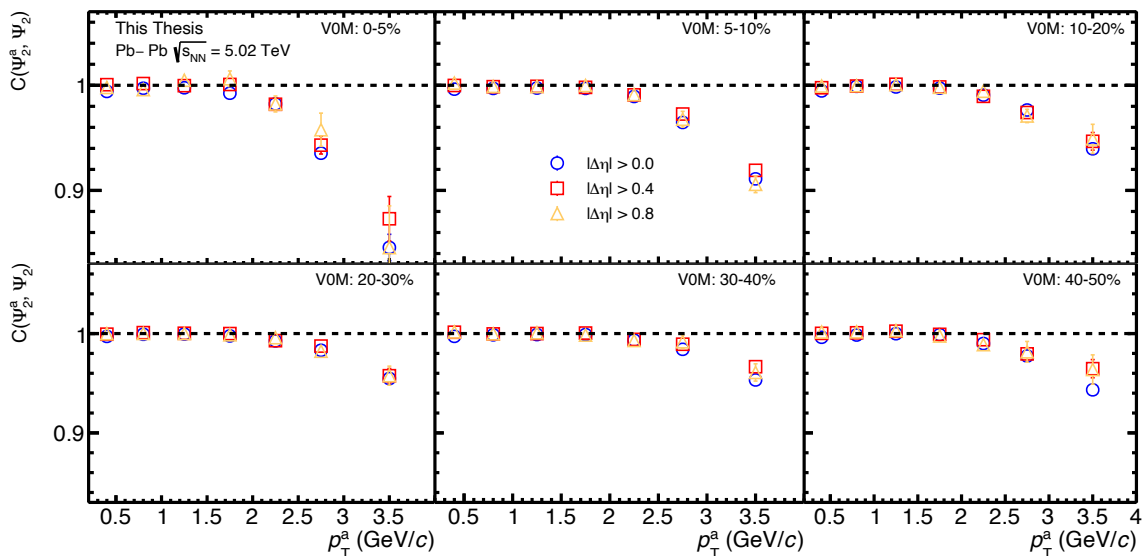


Figure 5.21: The single p_T -differential flow angle decorrelation $C(\Psi_2^a, \Psi_2)$ in Pb–Pb collisions at $\sqrt{s_{NN}} = 5.02$ TeV for different gaps in pseudorapidity.

The decorrelation of the elliptic flow angle $C(\Psi_2^a, \Psi_2)$ is presented with different gaps in pseudorapidity as a function of p_T in centrality classes 0-5% to 40-50% in figure 5.21. It is observed that $C(\Psi_2^a, \Psi_2)$ is independent of the size of the pseudorapidity gap, which suggests that non-flow effects does not contribute greatly to $C(\Psi_2^a, \Psi_2)$. Deviation of $C(\Psi_2^a, \Psi_2)$ from unity is observed for $p_T \gtrsim 2$ GeV/c in 0-5% most central collisions and at slightly higher values of p_T in collisions with greater than 5% centrality. Since the deviations cannot be attributed to non-flow effects, as shown by the study with various pseudorapidity gaps, the measurements of $C(\Psi_2^a, \Psi_2)$ indicate that the flow angle

Ψ_2 in fact fluctuates as function of the transverse momentum of the final state particles $\Psi_2(p_T)$.

The observable $C(\Psi_n^a, \Psi_n) \approx \langle \cos 2n[\Psi_n(p_T^a) - \Psi_n] \rangle$ is comparable with the ratio $v_n\{2\}/v_n[2]$, which also probes the decorrelation of the p_T -dependent flow angle against the reference flow angle albeit with contributions from fluctuations of the flow magnitude. $C(\Psi_n^a, \Psi_n)$ in fact corresponds to the cosine term in Eq. (5.3), but with twice the angle. The trigonometric double-angle formula is given as:

$$\cos 2x = 2 \cos^2 x - 1 \Leftrightarrow \cos x = \sqrt{\frac{\cos 2x + 1}{2}}, \quad (5.15)$$

where in this case $x = n[\Psi_n(p_T^a) - \Psi_n]$. Since $C(\Psi_n^a, \Psi_n)$ is an average over events, the relation becomes:

$$\langle \cos 2x \rangle = \langle 2 \cos^2 x - 1 \rangle = 2 \langle \cos^2 x \rangle - 1 \Leftrightarrow \langle \cos^2 x \rangle = \frac{\langle \cos 2x \rangle + 1}{2} = \frac{C(\Psi_n^a, \Psi_n) + 1}{2}, \quad (5.16)$$

where $\langle \cos^2 x \rangle \geq \langle \cos x \rangle^2$. Using the trigonometric relation in Eq. (5.16) enables the comparison with $v_2\{2\}/v_2[2]$ as shown in figure 5.22. The upper limit of the cosine term $\langle \cos 2[\Psi_2(p_T) - \Psi_2] \rangle$ is shown for different pseudorapidity gaps as function of p_T from 0-5% most central collisions to 40-50% peripheral collisions. The ratio $v_2\{2\}/v_2[2]$ is also shown, so that the size of the flow angle fluctuations compared to the overall flow vector fluctuations can be visualized. It is observed that the p_T -dependent fluctuations of the flow angle against the reference flow angle contribute a non-negligible part of the flow vector fluctuations probed by $v_2\{2\}/v_2[2]$.

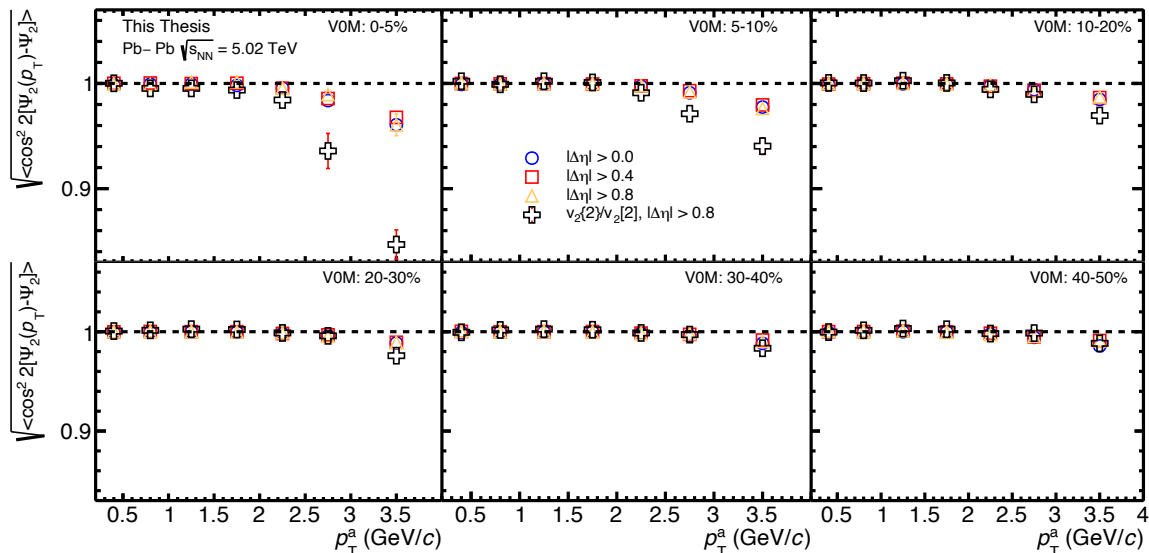


Figure 5.22: The the upper limit on the cosine term $\langle \cos 2[\Psi_2(p_T^a) - \Psi_2] \rangle$ in Pb–Pb collisions at $\sqrt{s_{NN}} = 5.02$ TeV for different pseudorapidity gaps. $v_2\{2\}/v_2[2]$ is shown for comparison with black crosses.

It is also possible to probe the lower limit on the fluctuations of the flow magnitude, since these must correspond to the remaining fluctuations of the flow vector. The ratio

with $v_n\{2\}/v_n[2]$ quantify the lower limit of the flow magnitude fluctuations, since:

$$\frac{v_n\{2\}/v_n[2]}{\sqrt{\langle \cos^2 x \rangle}} \leq \frac{v_n\{2\}/v_n[2]}{\langle \cos x \rangle} \quad (5.17)$$

So in order to quantify the flow magnitude decorrelation we define:

$$\begin{aligned} R(v_n^a, v_n) &\equiv \frac{v_n\{2\}/v_n[2]}{\sqrt{\langle \cos^2 n[\Psi_n(p_T^a) - \Psi_n] \rangle}} \\ &\lesssim \frac{v_n\{2\}/v_n[2]}{\langle \cos n[\Psi_n(p_T^a) - \Psi_n] \rangle} \\ &= \frac{\langle v_n(p_T^a) v_n \cos n[\Psi_n(p_T^a) - \Psi_n] \rangle}{\sqrt{\langle v_n(p_T^a)^2 \rangle} \sqrt{\langle v_n^2 \rangle} \langle \cos n[\Psi_n(p_T^a) - \Psi_n] \rangle} \\ &\approx \frac{\langle v_n(p_T^a) v_n \rangle}{\sqrt{\langle v_n(p_T^a)^2 \rangle} \sqrt{\langle v_n^2 \rangle}} \end{aligned} \quad (5.18)$$

The fluctuations of the flow magnitude are shown with the ratio $R(v_2)$ in figure 5.23 for the same centrality and p_T range. The results reflect a lower limit on the flow magnitude fluctuation, and indicate that the p_T -dependent fluctuations of the flow magnitude almost explains most of the flow vector fluctuations in the central collisions.

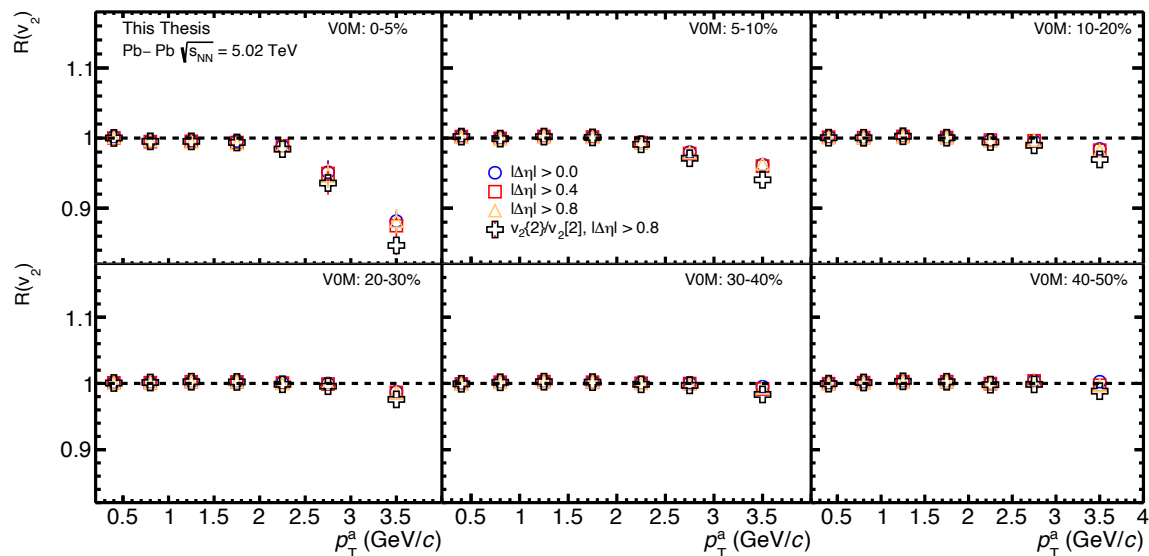


Figure 5.23: The ratio $R(v_2^a, v_2)$ for different pseudorapidity gaps in Pb–Pb collisions at $\sqrt{s_{\text{NN}}} = 5.02$ TeV. Comparison with $v_2\{2\}/v_2[2]$ is shown with black crosses.

Table 5 shows the deviations of $v_2\{2\}/v_2[2]$, $\sqrt{\langle \cos^2 2[\Psi_2(p_T^a) - \Psi_2] \rangle}$ and $R(v_2^a, v_2)$ from unity in each centrality for $3.0 < p_T^a < 4.0$ GeV/c, which is the highest p_T bin presented. The relative contribution of the flow angle and flow magnitude fluctuations to the deviation of $v_2\{2\}/v_2[2]$ from unity are shown in figure 5.24. Here, It is observed that the flow angle fluctuations contribute less than 25% of the overall flow vector fluctuations in the 0-5% most central collisions. As the collisions become more peripheral the relative contribution of the flow angle fluctuations increases, although the overall flow vector fluctuations are relatively small in the peripheral collisions. The flow magnitude fluctuations dominate in the central collisions, and then the relative contribution

decreases as the collisions become more peripheral. This is the first time such limits on flow angle and flow magnitude fluctuations have been measured. These studies provide us with much greater understanding of the p_T -dependent fluctuations of the flow vector, which can contribute to the constraints on the transport coefficients η/s , ζ/s of the QGP and the initial conditions of the heavy-ion collisions.

Centrality	Deviations from unity for $3.0 < p_T^a < 4.0$ GeV/c					
	$v_2\{2\}/v_2[2]$	N_σ	$\sqrt{\langle \cos^2 2[\Psi_2(p_T^a) - \Psi_2] \rangle}$	N_σ	$R(v_2^a, v_2)$	N_σ
0-5%	$15\% \pm 1.4\%$	> 5	$\leq 3.9\% \pm 0.33$	> 5	$\geq 11\% \pm 1.4$	> 5
5-10%	$6\% \pm 0.79\%$	> 5	$\leq 2.3\% \pm 0.044$	> 5	$\geq 3.7\% \pm 0.79$	> 5
10-20%	$3.1\% \pm 0.28\%$	> 5	$\leq 1.5\% \pm 0.099$	> 5	$\geq 1.5\% \pm 0.29$	> 5
20-30%	$2.4\% \pm 0.33\%$	> 5	$\leq 1.1\% \pm 0.097$	> 5	$\geq 1.3\% \pm 0.34$	~ 4
30-40%	$1.7\% \pm 0.45\%$	~ 4	$\leq 1.2\% \pm 0.082$	> 5	$\geq 0.49\% \pm 0.46$	~ 1
40-50%	$1.2\% \pm 0.67\%$	~ 2	$\leq 1.4\% \pm 0.15$	> 5	$\geq 0.26\% \pm 0.69$	~ 0

Table 5: Deviations of $v_2\{2\}/v_2[2]$, $\sqrt{\langle \cos^2 2[\Psi_2(p_T^a) - \Psi_2] \rangle}$ and $R(v_2^a, v_2)$ from unity for $3.0 < p_T^a < 4.0$ GeV/c along with the number of standard deviations from unity N_σ . Systematic uncertainties have not been considered, but should be smaller than the statistical uncertainty.

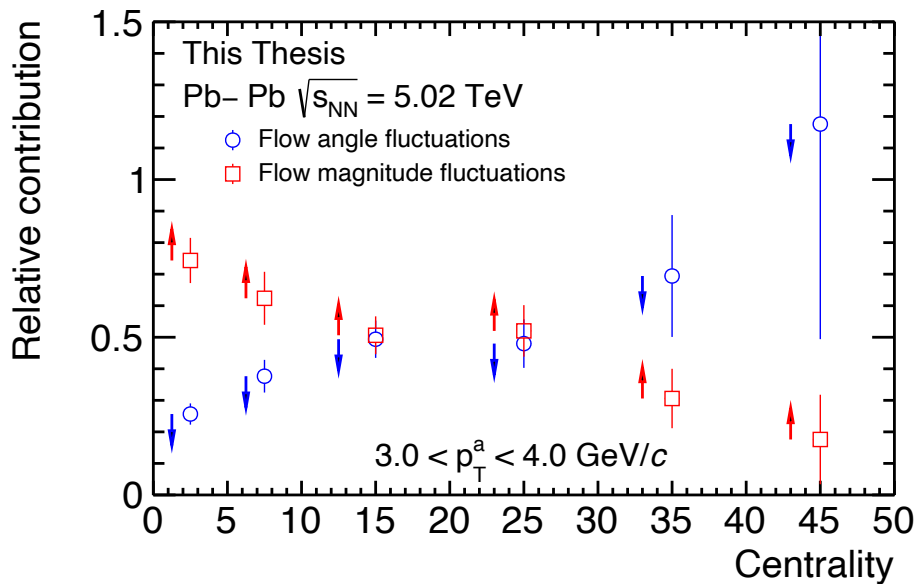


Figure 5.24: The relative contribution of flow angle and flow magnitude fluctuations to the deviation of $v_2\{2\}/v_2[2]$ from unity in Pb-Pb collisions at $\sqrt{s_{NN}} = 5.02$ TeV for $3.0 < p_T^a < 4.0$ GeV/c. The upper and lower limits are denoted by coloured arrows.

It is possible to modify C_n so that it probes the decorrelation of the flow angle at dif-

ferent transverse momenta:

$$C_n(\Psi_n^a, \Psi_n^t) = \frac{\langle \langle \cos[n(\varphi_1^a + \varphi_2^a - \varphi_3^t - \varphi_4^t)] \rangle \rangle}{\langle \langle \cos[n(\varphi_1^a + \varphi_2^a - \varphi_3^a - \varphi_4^a)] \rangle \rangle} = \frac{\langle v_n(p_T^a)^2 v_n(p_T^t)^2 \cos 2n[\Psi_n(p_T^a) - \Psi_n(p_T^t)] \rangle}{\langle v_n(p_T^a)^2 v_n(p_T^t)^2 \rangle} \approx \langle \cos 2n[\Psi_n(p_T^a) - \Psi_n(p_T^t)] \rangle, \quad (5.19)$$

where again the third equality holds under the assumption that non-flow is the same in the numerator and denominator. This observable probes the fluctuations of the flow angles at p_T^a and p_T^t . The double-differential $C_n(\Psi_n^a, \Psi_n^t)$ is implemented into the Generic Framework with the subevent method in a similar manner as $C(\Psi_n^a, \Psi_n)$. Again, the reader is referred to section 2 for definitions of the p^a -vector and p^t -vector. Special care needs to be taken when $p_T^a = p_T^t$, in order to avoid auto-correlations. In the case, where $p_T^a \neq p_T^t$, the numerator of Eq. (5.19) is given as:

$$\langle \cos[n(\varphi_1^a + \varphi_2^a - \varphi_3^t - \varphi_4^t)] \rangle = N\langle 4 \rangle_{n_1^a, n_2^a, n_3^t, n_4^t} / D\langle 4 \rangle_{n_1^a, n_2^a, n_3^t, n_4^t} \quad (5.20)$$

$$\begin{aligned} N\langle 4 \rangle_{n_1^a, n_2^a, n_3^t, n_4^t} &= N\langle 2 \rangle_{n_1^a, n_2^a}^A N\langle 2 \rangle_{n_3^t, n_4^t}^B \\ &= p_{n_1,1}^{aA} p_{n_2,1}^{aA} p_{n_3,1}^{tB} p_{n_4,1}^{tB}, \end{aligned} \quad (5.21)$$

and the denominator as:

$$\langle \cos[n(\varphi_1^a + \varphi_2^t - \varphi_3^a - \varphi_4^t)] \rangle = N\langle 4 \rangle_{n_1^a, n_2^t, n_3^a, n_4^t} / D\langle 4 \rangle_{n_1^a, n_2^t, n_3^a, n_4^t} \quad (5.22)$$

$$\begin{aligned} N\langle 4 \rangle_{n_1^a, n_2^t, n_3^a, n_4^t} &= N\langle 2 \rangle_{n_1^a, n_2^t}^A N\langle 2 \rangle_{n_3^a, n_4^t}^B \\ &= p_{n_1,1}^{aA} p_{n_2,1}^{tA} p_{n_3,1}^{aB} p_{n_4,1}^{tB}. \end{aligned} \quad (5.23)$$

When $p_T^a = p_T^t$, subtraction of auto-correlations is necessary in order to get the proper correlations. In this case, the p^a -vector and the p^t -vector are identical to the p -vector, and the equations become

$$\langle \cos[n(\varphi_1^a + \varphi_2^a - \varphi_3^t - \varphi_4^t)] \rangle = N\langle 4 \rangle_{n_1^a, n_2^a, n_3^t, n_4^t} / D\langle 4 \rangle_{n_1^a, n_2^a, n_3^t, n_4^t} \quad (5.24)$$

$$\begin{aligned} N\langle 4 \rangle_{n_1^a, n_2^a, n_3^t, n_4^t} &= N\langle 2 \rangle_{n_1^a, n_2^a}^A N\langle 2 \rangle_{n_3^t, n_4^t}^B \\ &= (p_{n_1,1}^A p_{n_2,1}^A - p_{n_1+n_2,2}^A) (p_{n_3,1}^B p_{n_4,1}^B - p_{n_3+n_4,2}^B), \end{aligned} \quad (5.25)$$

for the numerator, and

$$\langle \cos[n(\varphi_1^a + \varphi_2^t - \varphi_3^a - \varphi_4^t)] \rangle = N\langle 4 \rangle_{n_1^a, n_2^t, n_3^a, n_4^t} / D\langle 4 \rangle_{n_1^a, n_2^t, n_3^a, n_4^t} \quad (5.26)$$

$$\begin{aligned} N\langle 4 \rangle_{n_1^a, n_2^t, n_3^a, n_4^t} &= N\langle 2 \rangle_{n_1^a, n_2^t}^A N\langle 2 \rangle_{n_3^a, n_4^t}^B \\ &= (p_{n_1,1}^A p_{n_2,1}^A - p_{n_1+n_2,2}^A) (p_{n_3,1}^B p_{n_4,1}^B - p_{n_3+n_4,2}^B), \end{aligned} \quad (5.27)$$

for the denominator. From this it is observed that $C(\Psi_n^a, \Psi_n^t) = 1$ by construction, when $p_T^a = p_T^t$. The four-particle correlations in the numerator and denominator of Eq. (5.19) are illustrated in figures 5.25 and figure 5.26.

The results of $C(\Psi_2^a, \Psi_2^t)$ as function of p_T^a are shown in figure 5.27 with pseudorapidity gap greater than 0.8 in different bins of p_T^t and centrality. $C(\Psi_2^a, \Psi_2^t)$ shows deviations from unity in the 0-5% centrality class albeit with large statistical uncertainties. The more peripheral collisions in 20-30% and 40-50% centrality shows only a very small deviation of $C(\Psi_2^a, \Psi_2^t)$ from unity.

Figure 5.28 shows $C(\Psi_2^a, \Psi_2^t)$ for more centrality classes with the trigger particle selected from $0.2 < p_T^t < 0.6$ GeV/c. The low transverse momentum of trigger particle,

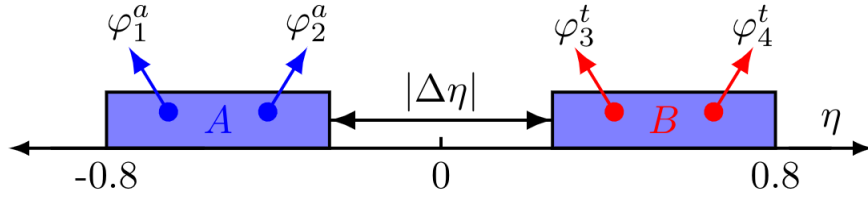


Figure 5.25: Sketches of side view of the detector showing a four-particle correlation with two subevents and $|\Delta\eta|$ gap separating them. The particles from the *same* p_T interval are selected from the *same* subevent.

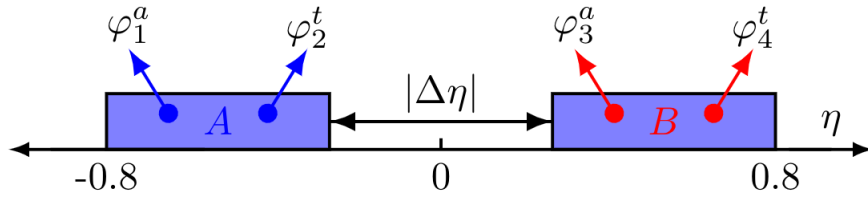


Figure 5.26: Sketches of side view of the detector showing a four-particle correlation with two subevents and $|\Delta\eta|$ gap separating them. The particles from the *same* p_T interval are selected from *different* subevents.

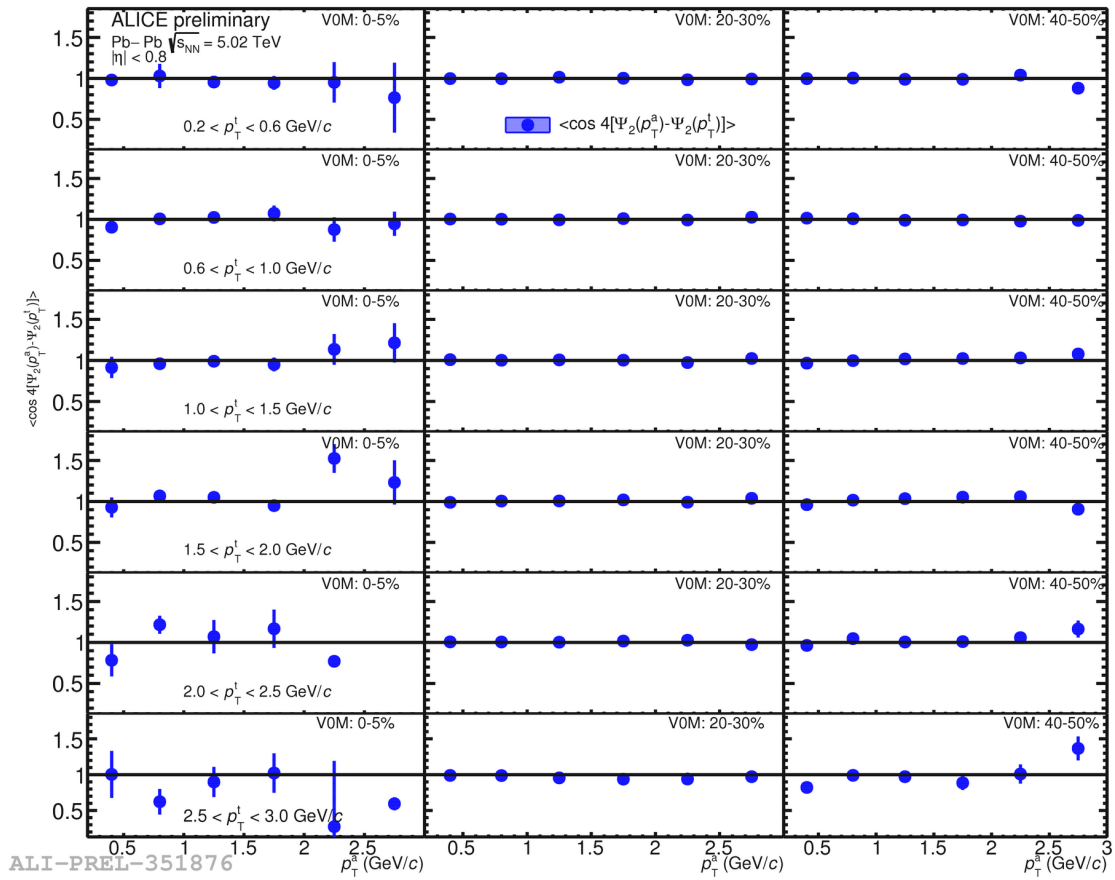


Figure 5.27: The double p_T -differential flow angle decorrelation $C(\Psi_2^a, \Psi_2^t)$ for Pb–Pb collisions at $\sqrt{s_{NN}} = 5.02$ TeV in different bins of p_T^t and centrality.

p_T^t , is selected in order to maximize the available statistics, since this is close to the mean p_T . Deviations of $C(\Psi_2^a, \Psi_2^t)$ from unity is seen in both the central collisions of 0-5% and 5-10% at $p_T^a > 2$ GeV/c, however the statistical uncertainty in the 0-5% most central collisions are too large to firmly conclude whether p_T -dependent flow angle fluctuations are present in the 0-5% most central collisions. The 5-10% central collisions show significant fluctuations of the flow vector. Results with 2018 data with central trigger is expected to significantly improve these results.

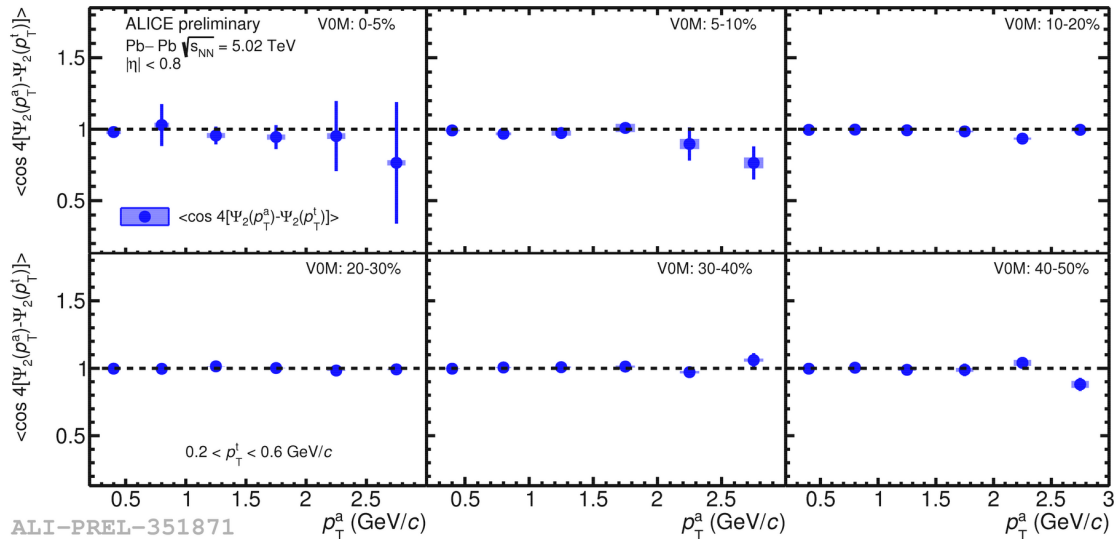


Figure 5.28: The double p_T -differential flow angle decorrelation $C(\Psi_2^a, \Psi_2^t)$ for Pb–Pb collisions at $\sqrt{s_{NN}} = 5.02$ TeV for all centrality classes up to 40-50% with trigger particle $0.2 < p_T^t < 0.6$ GeV/c.

The trigonometric double-angle formula in Eq. (5.15) makes it possible to quantify the p_T -dependent fluctuations of the flow vector, that are due to the fluctuations of the flow angle by comparison with r_n . The half-angle of $C(\Psi_n^a, \Psi_n^t)$ corresponds to the upper limit of the cosine factor in the factorization ratio, just as the half-angle of $C(\Psi_n^a, \Psi_n)$ correspond to the upper limit of the cosine factor in $v_2\{2\}/v_2[2]$. This upper limit on the cosine factor $\langle \cos[2(\Psi_2(p_T^a) - \Psi_2(p_T^t))] \rangle$ is shown in figure 5.29 for different pseudorapidity gaps as function of p_T^a in different bins of p_T^t and centrality. No strong dependence on pseudorapidity gaps is observed, although the measurements with pseudorapidity gap greater than 0.8 suffers from a lack of statistics, as was the case in figure 5.27. These studies show that non-flow effects do not contribute to $C(\Psi_n^a, \Psi_n^t)$, and that the assumption in Eq. (5.19) therefore is valid. Deviation of the flow angle component from unity is observed in the 0-5% centrality bin in most of the p_T^t bins. In figure 5.30, the flow angle decorrelation $\sqrt{\langle \cos^2 2[\Psi_2(p_T^a) - \Psi_2(p_T^t)] \rangle}$ is shown for several centrality bins with the trigger particle selected from the lowest p_T^t bin in order to maximize the statistics. Deviations from unity are observed in all centrality classes, although the effects are most pronounced in the central collisions. In peripheral collisions the deviations are within ~ 1 -2%. The measurements bear strong resemblance to those in figure 5.22, which can be explained by the trigger particles being selected from a p_T^t region close to the mean p_T . The flow magnitude fluctuations are probed with a

ratio similar to the one in Eq. (5.18):

$$R(v_n^a, v_n^t) \equiv \frac{r_n}{\sqrt{\langle \cos^2 2[\Psi_2(p_T^a) - \Psi_2(p_T^t)] \rangle}} \quad (5.28)$$

$$\leq \frac{r_n}{\langle \cos 2[\Psi_2(p_T^a) - \Psi_2(p_T^t)] \rangle} \quad (5.29)$$

$$\approx \frac{\langle v_n(p_T^a) v_n(p_T^t) \rangle}{\sqrt{\langle v_n(p_T^a)^2 \rangle} \sqrt{\langle v_n(p_T^t)^2 \rangle}} \quad (5.30)$$

This ratio is shown in figure 5.31 in centrality 0-5% to 40-50%. These results are compatible with the measurements of $R(v_2)$ in figure 5.23, and also suggest that the flow magnitude fluctuations are responsible for most of the flow vector fluctuations in central collisions. The results of $R(v_2^a, v_2^t)$ and $R(v_2^a, v_2)$ are comparable, when selecting trigger particle $0.2 < p_T^t < 0.6$, since this is close to the mean p_T . If the trigger particle p_T^t is selected from a wider kinematic range, then they are identical.

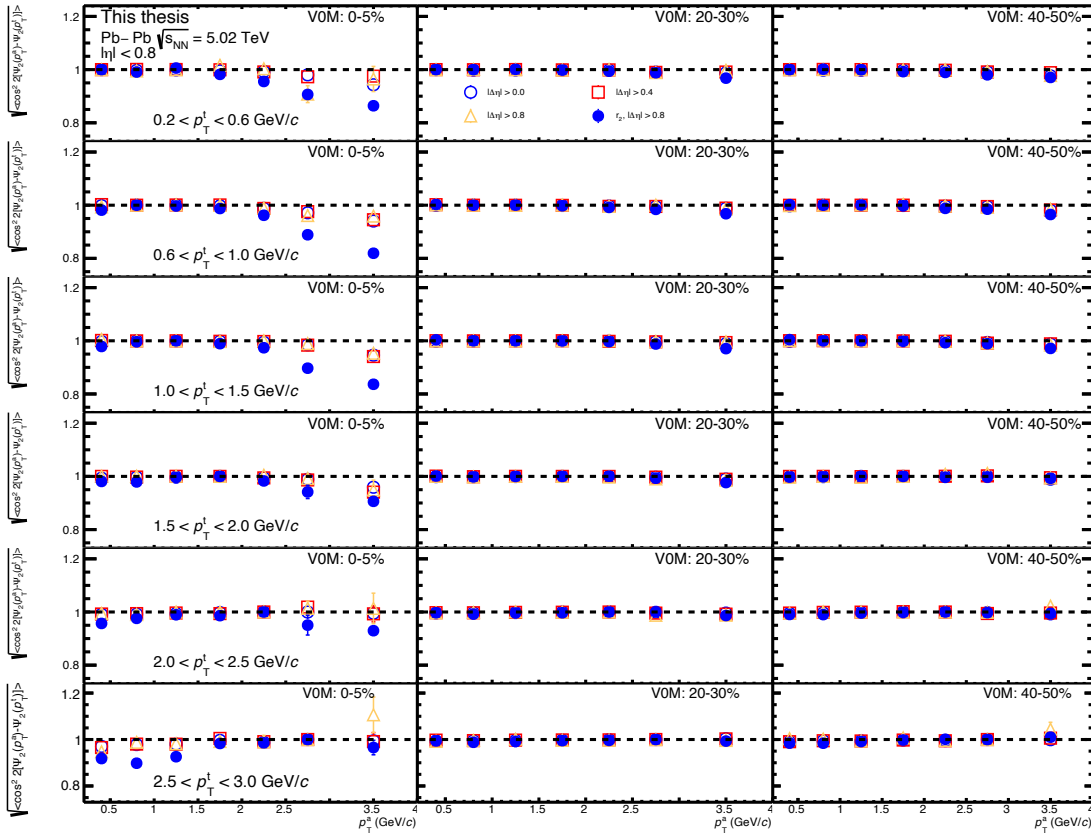


Figure 5.29: The double-differential flow angle decorrelation $\sqrt{\langle \cos^2 2[\Psi_2(p_T^a) - \Psi_2(p_T^t)] \rangle}$ and r_2 in different bins of p_T^t and centrality in Pb–Pb collisions at $\sqrt{s_{NN}} = 5.02$ TeV.

Table 6 shows the deviations of r_2 , $\sqrt{\langle \cos^2 2[\Psi_2(p_T^a) - \Psi_2(p_T^t)] \rangle}$ and $R(v_2^a, v_2^t)$ for associate particle $3.0 < p_T^a < 4.0$ GeV/c and trigger particle $0.2 < p_T^t < 0.6$ GeV/c. The relative contribution of the flow angle and flow magnitude fluctuations to the deviation of r_2 from unity are shown in figure 5.32. It is observed that fluctuations of the flow magnitude seem to contribute the most to the flow vector fluctuations in central collisions, consistent with what was found for $C(\Psi_2^a, \Psi_2)$, but the relative contribution of the flow angle

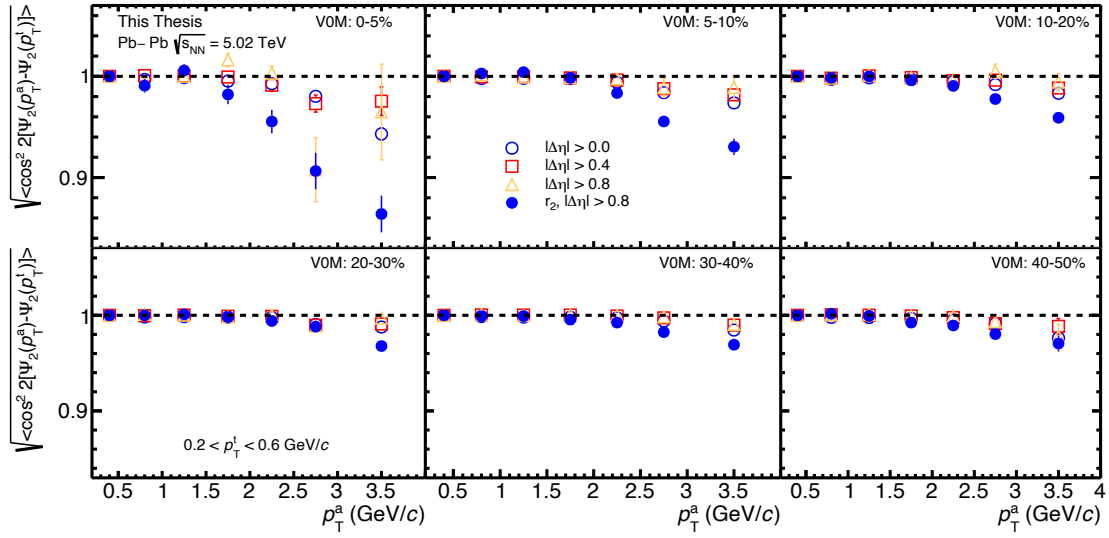


Figure 5.30: The double-differential flow angle decorrelation $\sqrt{\langle \cos^2 2[\Psi_2(p_T^a) - \Psi_2(p_T^t)] \rangle}$ and r_2 for trigger particle selected from $0.2 < p_T^t < 0.6$ GeV/c in Pb–Pb collisions at $\sqrt{s_{\text{NN}}} = 5.02$ TeV.

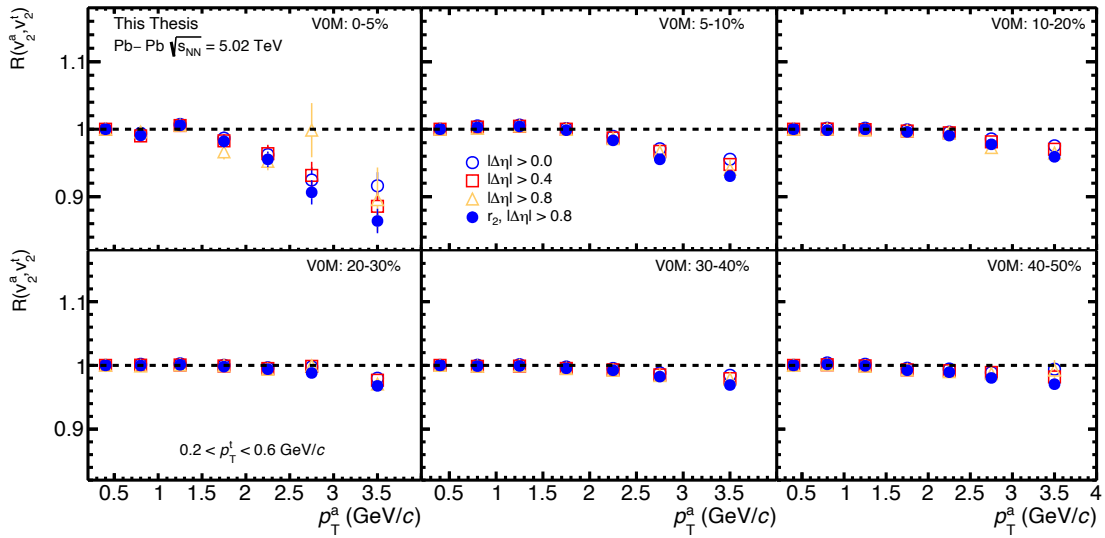


Figure 5.31: The ratio $R(v_2^a, v_2^t)$ of r_n with $\sqrt{\langle \cos^2 2[\Psi_2(p_T^a) - \Psi_2(p_T^t)] \rangle}$ for trigger particle selected from $0.2 < p_T^t < 0.6$ GeV/c in Pb–Pb collisions at $\sqrt{s_{\text{NN}}} = 5.02$ TeV. The comparison with r_2 is shown with solid circles.

fluctuations are larger in the double-differential case. This could be due to statistical fluctuations, since the double-differential case requires much more statistics than the single-differential study.

The measurements of $C(\Psi_2^a, \Psi_2)$ and $C(\Psi_2^a, \Psi_2^t)$ and the comparison of the half-angle to $v_2\{2\}/v_2\{2}$ and r_2 , respectively, has allowed a quantitative study of the separation of flow angle and flow magnitude effects in the flow vector fluctuations. The observation that flow magnitude fluctuations dominate in central collisions is consistent with the picture of v_2 depending heavily on the initial geometry. In central collisions, v_2 is small,

Centrality	Deviations from unity					
	r_2	N_σ	$\sqrt{\langle \cos^2 2[\Psi_2(p_T^a) - \Psi_2(p_T^t)] \rangle}$	N_σ	$R(v_2^a, v_2^t)$	N_σ
0-5%	$14\% \pm 1.8\%$	> 5	$< 5.7\% \pm 0.61$	> 5	$> 7.9\% \pm 1.9$	~ 4
5-10%	$7\% \pm 0.81\%$	> 5	$< 2.6\% \pm 0.17$	> 5	$> 4.3\% \pm 0.83$	> 5
10-20%	$4.1\% \pm 0.44\%$	> 5	$< 1.7\% \pm 0.31$	> 5	$> 2.4\% \pm 0.54$	~ 4
20-30%	$3.2\% \pm 0.23\%$	> 5	$< 1.2\% \pm 0.28$	~ 4	$> 2\% \pm 0.36$	> 5
30-40%	$3.1\% \pm 0.63\%$	~ 5	$< 1.5\% \pm 0.16$	> 5	$> 1.5\% \pm 0.65$	~ 2
40-50%	$2.9\% \pm 0.85\%$	~ 4	$< 2.4\% \pm 0.27$	> 5	$> 0.58\% \pm 0.89$	~ 0

Table 6: Deviations of r_2 , $\sqrt{\langle \cos^2 2[\Psi_2(p_T^a) - \Psi_2(p_T^t)] \rangle}$ and $R(v_2^a, v_2^t)$ from unity for $0.2 < p_T^t < 0.6$ GeV/c and $3.0 < p_T^a < 4.0$ GeV/c along with the number of standard deviations from unity N_σ . Systematic uncertainties have not been considered, but should be smaller than the statistical uncertainty.

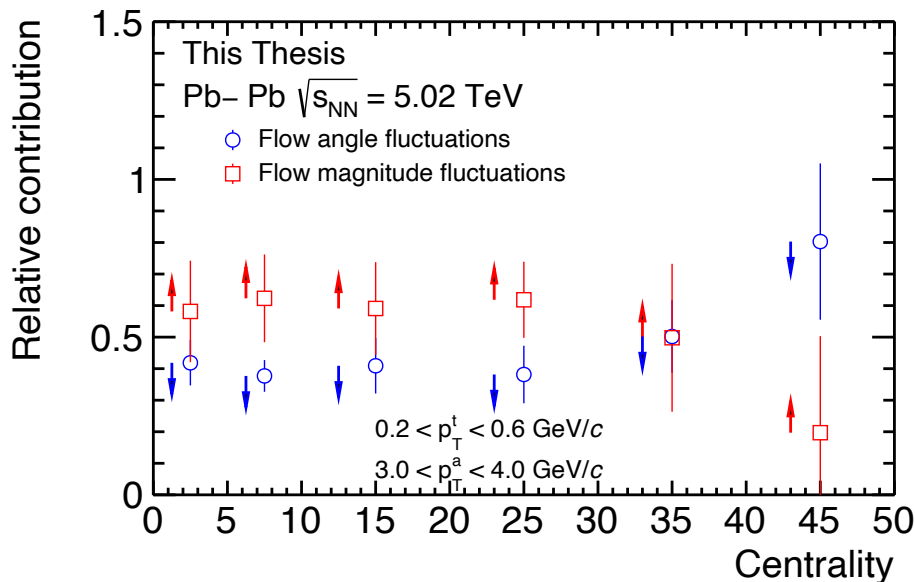


Figure 5.32: The relative contribution of flow angle and flow magnitude fluctuations to the deviation of r_2 from unity in Pb–Pb collisions at $\sqrt{s_{NN}} = 5.02$ TeV for $3.0 < p_T^a < 4.0$ GeV/c and $0.2 < p_T^t < 0.6$ GeV/c. The upper and lower limits are denoted by coloured arrows.

since the geometry is almost circular, and will be more heavily affected by fluctuations. As the collisions become more peripheral, v_2 becomes larger and will be less affected by fluctuations. The flow angle also contributes significantly to the fluctuations of the flow vector in central collisions, and starts to completely dominate the relatively small flow vector fluctuations in peripheral collisions. Since neither $C(\Psi_n^a, \Psi_n)$, nor $C(\Psi_n^a, \Psi_n^t)$ appear to depend on pseudorapidity, a small gap can be chosen to maximize the available statistics. This new evidence of both flow angle and flow magnitude fluctuations will significantly improve our understanding of the dynamic evolution of the created system in heavy-ion collisions. Comparison of these new observables with hydrodynamic models can help constrain the initial conditions of the heavy-ion collisions and

the transport properties of the QGP even further.

5.1.4 Outlook - Flow vector fluctuations in small systems

Small systems refer to collisions between protons or collisions of protons with heavy ions. Traditionally, pp and p–Pb collisions have served as a baseline for Pb–Pb collisions. However, data from pp and p–Pb collisions have shown collective behaviour [83, 84, 85, 86], and studies of collectivity in small systems are at the frontier of heavy-ion physics and the search for QGP. The measurements that triggered the discussion on flow in small systems was the observation of a near-side ($\pi \approx 0$) ridge in high multiplicity pp collisions [85] and high multiplicity p–Pb collisions [84]. This indication of collectivity in small systems led to further investigations with multi-particle correlations to determine whether there is flow in small systems. Negative signs of the four-particle cumulant $c_2\{2\}$, which is typically attributed to the hydrodynamic expansion of the QGP, were observed in p–Pb [87, 88] and even in pp collisions [89]. The measurements of collectivity in pp collisions were soon understood to be due to non-flow correlations, which are highly significant in small systems, and non-flow fluctuations, which are due to the cumulants being calculated over too large a multiplicity range. The study in [87], which was free from non-flow fluctuations, could not confirm the observation of collectivity in pp collisions. Furthermore, the origin of collectivity in small systems is also debated. In heavy-ion collisions, the collectivity is interpreted as the anisotropies of the initial geometry being transferred into momentum correlations by final state interactions. However, theoretical calculations show that initial state momentum correlations are also present in small systems and can contribute to the observables [90]. The measurements presented in this thesis of p_T -dependent flow vector

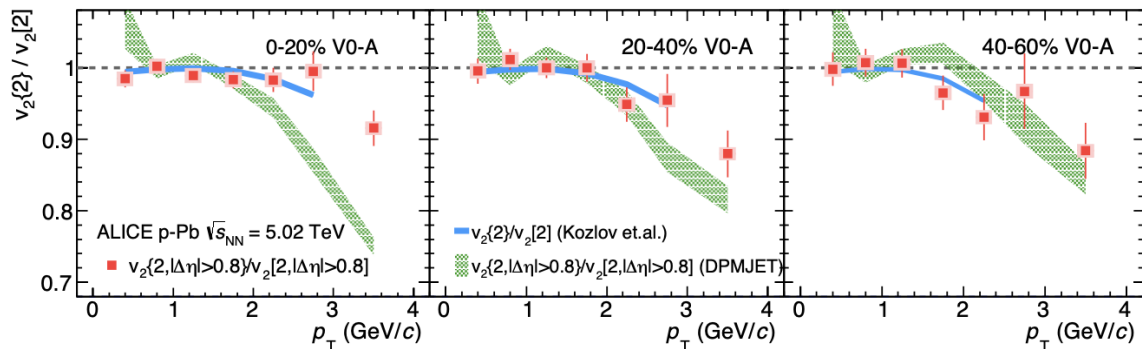


Figure 5.33: Measurements of $v_2\{2\}/v_2[2]$ with $|\Delta\eta| > 0.8$ for various multiplicity classes in p–Pb collisions at $\sqrt{s_{\text{NN}}} = 5.02$ TeV. DPMJet calculations [91] are shown as green-shaded lines. Hydrodynamic calculations (MUSIC) [92] with modified MC-Glauber initial conditions and $\eta/s = 0.08$ are shown as blue lines. Figure taken from [72].

fluctuations can also be performed in small systems. If pp or p–Pb collisions show an indication of flow vector fluctuations, it could hint at QGP formation in small systems. Measurements of $v_2\{2\}/v_2[2]$ in p–Pb collisions show deviations of unity, as shown in figure 5.33, which hints at p_T -dependent V_2 fluctuations in high multiplicity events [72]. The centrality intervals in the measurements are huge, and ideally, one would go to very high N_{ch} in p–Pb and pp collisions. Non-flow subtraction also plays a critical

role in small systems and has not been done for the Run1 measurements, which explains why both the non-flow model DPMJET [91] and the hydrodynamic model with modified MC-Glauber initial conditions and $\eta/s = 0.08$ [92] can describe the data. High multiplicity measurements with proper non-flow subtraction are necessary to give specific answers regarding p_T -dependent V_n fluctuations in p-Pb collisions. Comparison with the newest hydrodynamic models is also crucial to understand the origin of the collectivity observed in the small systems.

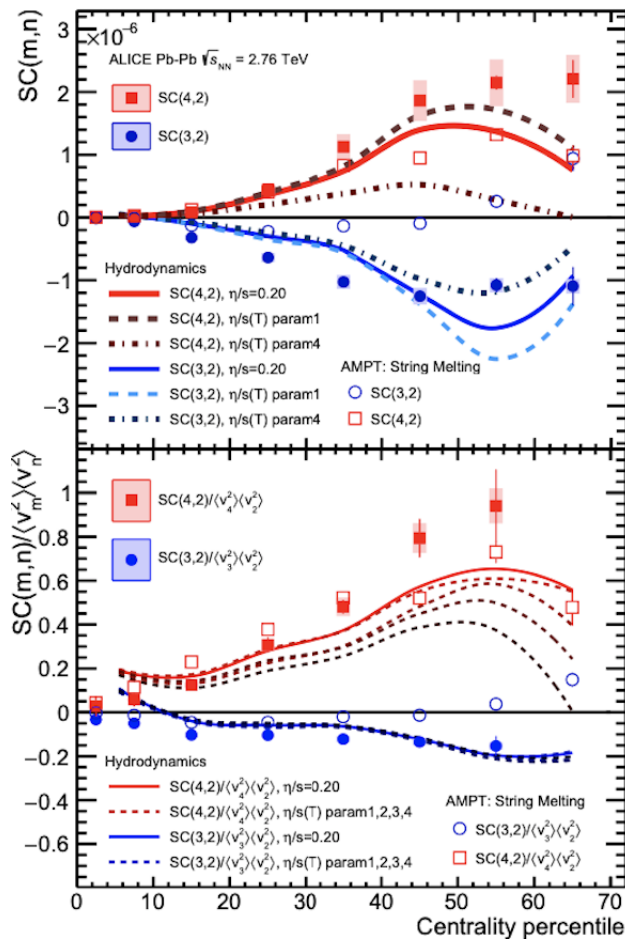


Figure 5.34: The p_T -integrated symmetric cumulants $SC(4,2)$ and $SC(3,2)$ as function of centrality in Pb–Pb collisions at $\sqrt{s_{NN}} = 2.76$ TeV and hydrodynamic calculations (top). The normalized symmetric cumulants $NSC(4,2)$ and $NSC(3,2)$ as function of centrality in Pb–Pb collisions at $\sqrt{s_{NN}} = 2.76$ TeV and hydrodynamic calculations (bottom). Figure adapted from [93].

5.2 Correlations of flow

Studies of the correlation between different order flow harmonics can help understand the origin of higher order harmonics ($n > 3$) [94]. It also provides additional constraints on the initial conditions and the transport coefficients of the QGP. The correlation between harmonics v_n and v_m can be quantified with the Symmetric Cumulants $SC(m, n)$ [43]:

$$SC(m, n) = \langle v_n^2 v_m^2 \rangle - \langle v_n^2 \rangle \langle v_m^2 \rangle \quad (5.31)$$

The symmetric cumulant can be normalized in order to remove the dependence on the individual flow coefficients:

$$NSC(n, m) = \frac{\langle v_n^2 v_m^2 \rangle - \langle v_n^2 \rangle \langle v_m^2 \rangle}{\langle v_n^2 \rangle \langle v_m^2 \rangle} \quad (5.32)$$

The normalized correlation between v_2 and v_3 is particularly sensitive to initial conditions, due to their linear response to the initial eccentricity ϵ_n . Correlations with higher

order v_n offer insight into the hydrodynamic response. The p_T -integrated symmetric cumulant is shown in figure 5.34 where it is observed that v_2 and v_3 are anti-correlated in all centralities albeit with different centrality dependence in the fluctuation-dominated central collisions compared to the geometry-dominated peripheral collisions [93]. The correlations between v_2 and v_4 are observed to have a positive sign for all centralities. These observations are consistent with measurements done by the ATLAS collaboration using the ESE technique [94, 95, 96]. Here it was found that selecting events with large v_2 in a single event compared to the event-averaged $\langle v_2 \rangle$, will also select a smaller v_3 and larger v_4 compared to the event-averaged $\langle v_3 \rangle$ and $\langle v_4 \rangle$. These measurements only explore the correlations of harmonics as function of the collision centrality. The differential study of p_T and η might bring better sensitivity to initial conditions or η/s , and ζ/s and comparison to theoretical models can better constrain initial conditions and the transport properties of the QGP.

This thesis investigates the single p_T -differential symmetric cumulant, which has only been proposed in this thesis. The single p_T -differential NSC takes one harmonic as p_T -differential and the other as reference harmonic:

$$SC(n, m_{p_T}) = \langle v_n(p_T)^2 v_m^2 \rangle - \langle v_n(p_T)^2 \rangle \langle v_m^2 \rangle. \quad (5.33)$$

This can be normalized with the two-particle correlations to obtain the single p_T -differential normalized symmetric cumulant $NSC(n, m_{p_T})$:

$$NSC(n, m_{p_T}) = \frac{\langle v_n^2 v_m(p_T)^2 \rangle - \langle v_n^2 \rangle \langle v_m(p_T)^2 \rangle}{\langle v_n^2 \rangle \langle v_m(p_T)^2 \rangle}. \quad (5.34)$$

Here $\langle v_n^2 \rangle$ is the same as the previously mentioned reference flow, and $\langle v_m(p_T)^2 \rangle$ is the same as $v_m[2]$. With this the correlation between the p_T -integrated harmonic $v_n(p_T^a)$ and the p_T -differential v_m can be probed. Since both v_n or v_m can be chosen as the p_T -differential harmonic, we have:

$$NSC(n_{p_T}, m) = \frac{\langle v_n(p_T)^2 v_m^2 \rangle - \langle v_n(p_T)^2 \rangle \langle v_m^2 \rangle}{\langle v_n(p_T)^2 \rangle \langle v_m^2 \rangle}. \quad (5.35)$$

Thus, the single-differential NSC enables the comparison:

$$NSC(n, m_{p_T}) \stackrel{?}{=} NSC(n_{p_T}, m) \quad (5.36)$$

When integrating over the full p_T -range, one should obtain $NSC(n, m)$ regardless of the chosen differential harmonic, so no difference is expected between the two sides of the equality in Eq. (5.36).

The single-differential symmetric cumulants $SC(3, 2_{p_T})$ and $SC(4, 2_{p_T})$ are shown in figure 5.35 for centrality classes 5-10% to 40-50%. The measured symmetric cumulants are observed to depend strongly on centrality and p_T . Whether this is a property of the correlations between v_n and v_m , or if it is due to v_n and v_m themselves, can be answered with the normalized symmetric cumulant. Figure 5.36 shows the results of $NSC(3, 2_{p_T})$ and $NSC(4, 2_{p_T})$ as a function of p_T in centrality classes 5-10% to 40-50%. The anti-correlation between v_3 and v_2 is clear from the negative values of $NSC(3, 2_{p_T})$, and likewise the positive correlation between v_4 and v_2 can be inferred from the positive values of $NSC(4, 2_{p_T})$. The NSC is mostly constant with p_T , but some increasing trend is observed at low p_T . Most of the p_T -dependence observed in figure 5.35 is cancelled out

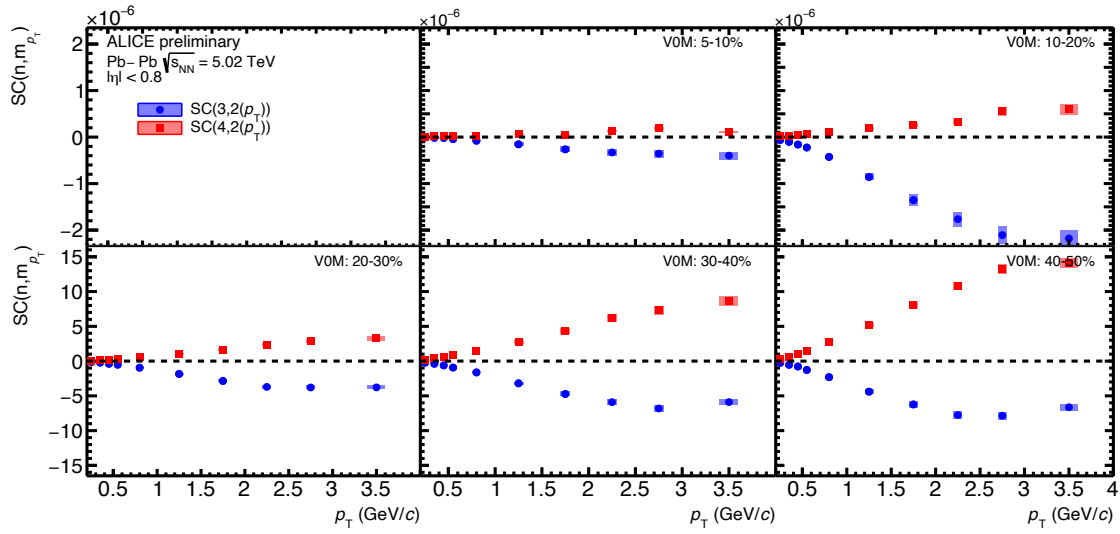


Figure 5.35: The single p_T -differential symmetric cumulants $SC(4, 2p_T)$ and $SC(3, 2p_T)$ in Pb–Pb collision at $\sqrt{s_{NN}} = 5.02$ TeV.

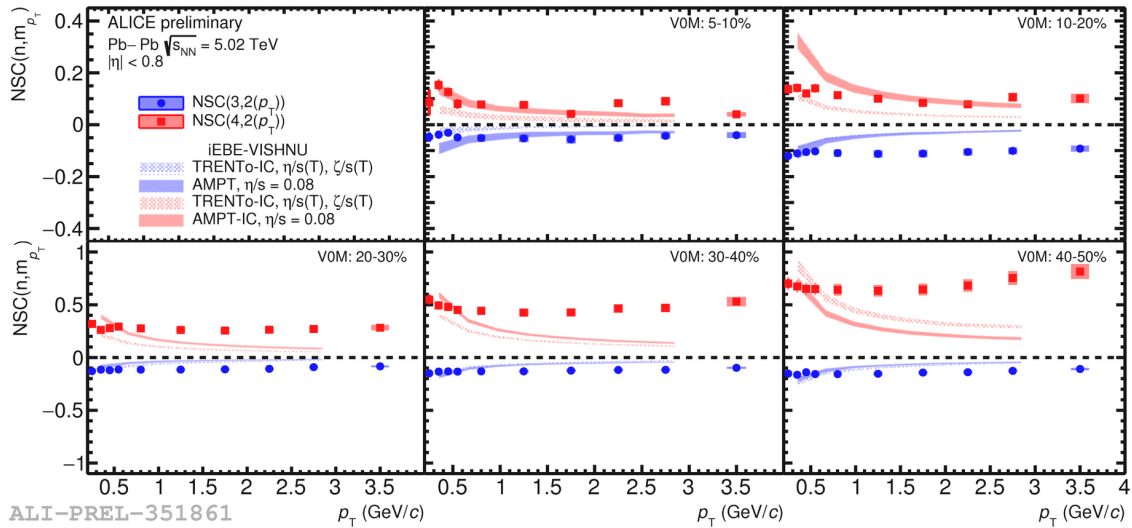


Figure 5.36: The single p_T -differential normalized symmetric cumulant $NSC(3, 2p_T)$ and $NSC(4, 2p_T)$ for Pb–Pb collisions at $\sqrt{s_{NN}} = 5.02$ TeV. Comparison with iEBE-VISHNU hydrodynamic model with TRENTo and AMPT initial conditions are shown in coloured bands.

by the normalization. The centrality dependence observed in [93] is also observed in these results with $NSC(4, 2p_T)$ increasing as the collisions becomes more peripheral and $NSC(3, 2p_T)$ showing a relatively weaker centrality dependence. The hydrodynamic predictions overestimate the measurements at low p_T and underestimate at higher p_T , but the observed increase in the magnitude of the normalized symmetric cumulants at low p_T in the data is qualitatively reproduced in the hydrodynamic predictions.

The comparison between $NSC(3, 2p_T)$ and $NSC(2, 3p_T)$ is shown in figure [5.37]. At intermediate p_T the results are compatible, but $NSC(2, 3p_T)$ show a stronger anti-correlation at low and high p_T . Whether these results are an indication of some underlying physics,

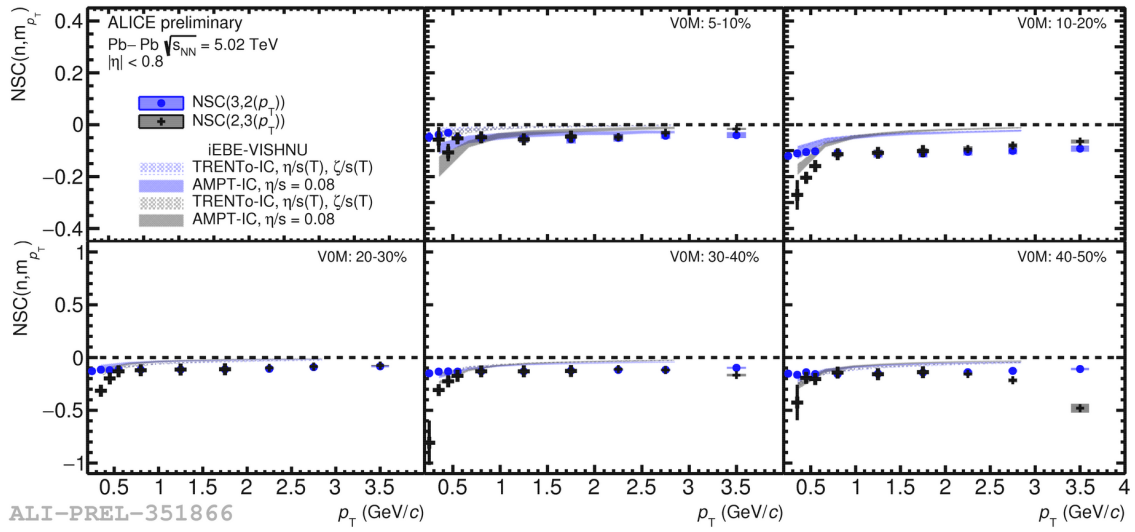


Figure 5.37: The single p_T -differential normalized symmetric cumulant $\text{NSC}(3, 2_{p_T})$ and $\text{NSC}(2, 3_{p_T})$ for Pb–Pb collisions at $\sqrt{s_{\text{NN}}} = 5.02$ TeV. Comparison with iEBE-VISHNU hydrodynamic model with TRENTo and AMPT initial conditions are shown in coloured bands.

or are a result of statistical instability of $\text{NSC}(2, 3_{p_T})$ is unclear. The v_3 signal is very small at low p_T , as is shown in figure 5.8, and as such is more strongly affected by statistical fluctuations compared to v_2 . Since both $\text{NSC}(3, 2_{p_T})$ and $\text{NSC}(2, 3_{p_T})$ should give $\text{NSC}(3, 2)$, when integrating over the full p_T -range, no difference is expected between the two observables. The hydrodynamic calculations also indicate a difference, however, so a more detailed study on this observation is required to understand what drives the difference.

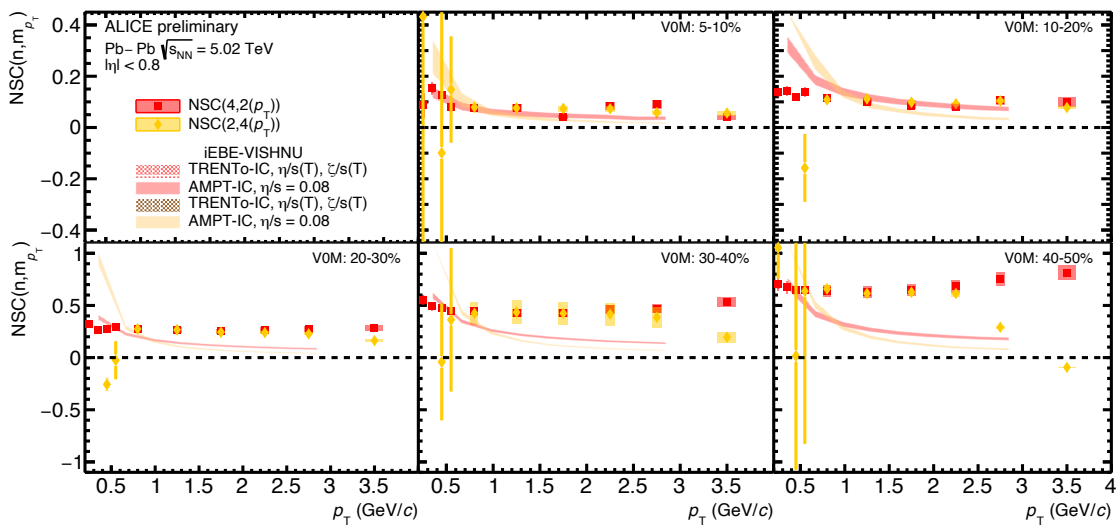


Figure 5.38: The single p_T -differential normalized symmetric cumulant $\text{NSC}(4, 2_{p_T})$ and $\text{NSC}(2, 4_{p_T})$ for Pb–Pb collisions at $\sqrt{s_{\text{NN}}} = 5.02$ TeV. Comparison with iEBE-VISHNU hydrodynamic model with TRENTo and AMPT initial conditions are shown in coloured bands.

In figure [5.38](#), the comparison between $\text{NSC}(4, 2_{p_T})$ and $\text{NSC}(2, 4_{p_T})$ is shown. The $\text{NSC}(2, 4_{p_T})$ suffers from large statistical uncertainties, due to the narrow binning at low p_T but the measurements indicate that $\text{NSC}(2, 4_{p_T})$ becomes negative at low p_T . In the intermediate p_T region $\text{NSC}(4, 2_{p_T})$ and $\text{NSC}(2, 4_{p_T})$ are compatible, but $\text{NSC}(2, 4_{p_T})$ starts to decrease at $p_T > 2.5$ GeV/ c in more peripheral collisions and even changes sign. The statistical stability of $\text{NSC}(2, 4_{p_T})$ is even more questionable than $\text{NSC}(2, 3_{p_T})$, so the results should be interpreted with some caution.

The study of the single-differential $\text{NSC}(n, m_{p_T})$ presented in this thesis shows that the correlation between the harmonics v_n and $v_m(p_T)$ are mostly constant with p_T , although some deviations are observed at low p_T . A difference between $\text{NSC}(3, 2_{p_T})$ and $\text{NSC}(2, 3_{p_T})$ is observed in the data, which is also predicted by the hydrodynamic calculations. Intuitively, such a difference is not expected, since both observables should reproduce $\text{NSC}(n, m)$, when integrated over the full p_T -range. This could hint at some interesting underlying physics with more research necessary in order to explore this phenomenon. The $\text{NSC}(n, m_{p_T})$ ($m > 2$) require a lot of statistics, and might not be statistically stable with the statistics available in the 2015 data. The 2018 data should significantly improve the results.

6 Conclusion

This thesis has presented measurements of p_T -dependent flow vector fluctuations in Pb–Pb collisions at $\sqrt{s_{NN}} = 5.02$ TeV with the ratio $v_n\{2\}/v_n[2]$ up to $n = 4$, and the factorization ratio r_n up to $n = 3$. Deviations of both $v_2\{2\}/v_2[2]$ and r_2 from unity suggests the presence of p_T -dependent V_2 fluctuations in central collisions. The p_T -dependent fluctuations of V_2 reaches $\sim 15\%$ in central collisions for $v_2\{2\}/v_2[2]$ at high p_T and for r_2 when $|p_T^a - p_T^t|$ is large. Higher order measurements of $v_n\{2\}/v_n[2]$ and r_n ($n = 3, 4$) does not indicate p_T -dependent fluctuations of V_3 and V_4 , and if such fluctuations exists, they are within a few percent. The results are consistent with previous measurements in Pb–Pb collisions at $\sqrt{s_{NN}} = 2.76$ TeV [72, 73], but offer significantly better precision. Comparison with the iEBE-VISHNU hydrodynamic model shows that the results are best described with AMPT initial conditions and $\eta/s = 0.08$ [28] compared to TRENTo initial conditions and temperature dependent $\eta/s(T)$ and $\zeta/s(T)$ [28]. However, future hydrodynamic calculations are also needed.

For the first time, the contributions of flow angle fluctuations and flow magnitude fluctuations are separated from the overall flow vector fluctuations with the proposed observable $C(\Psi_n^a, \Psi_n)$. This observable is only sensitive to fluctuations of the flow angle Ψ_n and is not sensitive to fluctuations of the flow magnitude v_n . Deviations of $C(\Psi_2^a, \Psi_2)$ from unity are observed in central collisions at $p_T^a > 2$ GeV/ c . Comparison of the half-angle of $C(\Psi_2^a, \Psi_2)$ with $v_2\{2\}/v_2[2]$ provide an upper limit on the flow angle fluctuations of $v_2\{2\}/v_2[2]$. It is found that the flow angle fluctuations contribute up to $\sim 25\%$ of the deviation of $v_2\{2\}/v_2[2]$ from unity in central collisions. There is a discovery of p_T -dependent flow angle fluctuations $\Psi_2(p_T)$ with a confidence greater than 5σ . The remaining fluctuations come from fluctuations of the flow magnitude v_2 . These results show that the p_T -dependent V_2 fluctuations in central collisions are mostly due to fluctuations of the flow magnitude v_2 , which affects the p_T -dependent V_2 fluctuations around three times more than the fluctuations of Ψ_2 . The double-differential decorrelation of the flow angle $C(\Psi_n^a, \Psi_n^t)$ is also presented. Here, deviations from unity are also observed, and it follows the same trend as r_2 , i.e., the deviations from unity increase as the difference $|p_T^a - p_T^t|$ increases. The half-angle of $C(\Psi_2^a, \Psi_2^t)$ puts an upper limit on the flow angle fluctuations probed by r_2 . Selecting the trigger particle from $0.2 < p_T^t < 0.6$ GeV/ c shows deviations from unity consistent with the flow angle fluctuations from $v_2\{2\}/v_2[2]$. These new measurements show that the p_T -dependent flow vector fluctuations observed in central collisions are mainly driven by fluctuations of the flow magnitude and have a non-negligible contribution from fluctuations of the flow angle. These measurements provide a new flow picture with both flow angle and flow magnitude fluctuations. This provides a new way to examine the theoretical models and improve our understanding of initial conditions and QGP properties.

Correlations between p_T -integrated harmonics v_n and p_T -differential harmonics $v_m(p_T)$ of different order are measured with the single-differential normalized symmetric cumulant $\text{NSC}(n, m_{p_T})$. An anti-correlation of $v_2(p_T)$ with v_3 is observed in $\text{NSC}(3, 2_{p_T})$ for all centrality classes. $\text{NSC}(4, 2_{p_T})$ shows a positive correlation between $v_2(p_T)$ and v_4 in all centrality classes. Both $\text{NSC}(3, 2_{p_T})$ and $\text{NSC}(4, 2_{p_T})$ are roughly constant with p_T . This indicates that the strength of the correlation between the harmonics does not depend overly on transverse momentum. Both the hydrodynamic calculation with AMPT initial conditions and $\eta/s = 0.08$ [28], and the one with TRENTo initial conditions and $\eta/s(T)$, $\zeta/s(T)$ [28], fail to accurately predict $\text{NSC}(3, 2_{p_T})$ and $\text{NSC}(4, 2_{p_T})$.

The comparison of $\text{NSC}(3, 2_{p_T})$ with $\text{NSC}(2, 3_{p_T})$ show that they are consistent at intermediate p_T , but differ at low and high p_T . This could be due to statistical instability of $\text{NSC}(2, 3_{p_T})$ or could hint at some interesting underlying physics. The same trend is observed in the comparison of $\text{NSC}(4, 2_{p_T})$ and $\text{NSC}(2, 4_{p_T})$. Further study is needed on $\text{NSC}(3, 2_{p_T})$ and $\text{NSC}(2, 3_{p_T})$ in both experiments and theory, to determine the origin of the observed difference.

References

- [1] Peter W. Higgs. “Broken Symmetries and the Masses of Gauge Bosons”. In: *Phys. Rev. Lett.* 13 (16 Oct. 1964), pp. 508–509. DOI: [10.1103/PhysRevLett.13.508](https://doi.org/10.1103/PhysRevLett.13.508).
- [2] F. Englert and R. Brout. “Broken Symmetry and the Mass of Gauge Vector Mesons”. In: *Phys. Rev. Lett.* 13 (9 Aug. 1964), pp. 321–323. DOI: [10.1103/PhysRevLett.13.321](https://doi.org/10.1103/PhysRevLett.13.321).
- [3] G. S. Guralnik, C. R. Hagen, and T. W. B. Kibble. “Global Conservation Laws and Massless Particles”. In: *Phys. Rev. Lett.* 13 (20 Nov. 1964), pp. 585–587. DOI: [10.1103/PhysRevLett.13.585](https://doi.org/10.1103/PhysRevLett.13.585).
- [4] *Standard Model of Elementary Particles*. URL: https://en.wikipedia.org/wiki/Standard_Model#/media/File:Standard_Model_of_Elementary_Particles.svg (visited on 08/20/2020).
- [5] O. W. Greenberg. “Spin and Unitary-Spin Independence in a Paraquark Model of Baryons and Mesons”. In: *Phys. Rev. Lett.* 13 (20 Nov. 1964), pp. 598–602. DOI: [10.1103/PhysRevLett.13.598](https://doi.org/10.1103/PhysRevLett.13.598).
- [6] M. Y. Han and Y. Nambu. “Three-Triplet Model with Double SU(3) Symmetry”. In: *Phys. Rev.* 139 (4B Aug. 1965), B1006–B1010. DOI: [10.1103/PhysRev.139.B1006](https://doi.org/10.1103/PhysRev.139.B1006).
- [7] H. Fritzsch, Murray Gell-Mann, and H. Leutwyler. “Advantages of the Color Octet Gluon Picture”. In: *Phys. Lett. B* 47 (1973), pp. 365–368. DOI: [10.1016/0370-2693\(73\)90625-4](https://doi.org/10.1016/0370-2693(73)90625-4).
- [8] David J. Gross and Frank Wilczek. “Ultraviolet Behavior of Non-Abelian Gauge Theories”. In: *Phys. Rev. Lett.* 30 (26 June 1973), pp. 1343–1346. DOI: [10.1103/PhysRevLett.30.1343](https://doi.org/10.1103/PhysRevLett.30.1343).
- [9] H. David Politzer. “Reliable Perturbative Results for Strong Interactions?” In: *Phys. Rev. Lett.* 30 (26 June 1973), pp. 1346–1349. DOI: [10.1103/PhysRevLett.30.1346](https://doi.org/10.1103/PhysRevLett.30.1346).
- [10] Tapan K. Nayak. “Heavy Ions: Results from the Large Hadron Collider”. In: *Pramana* 79 (2012). Ed. by Rohin Godbole and Naba K. Mondal, pp. 719–735. DOI: [10.1007/s12043-012-0373-7](https://doi.org/10.1007/s12043-012-0373-7).
- [11] Shusu Shi. “Event anisotropy v_2 at STAR”. PhD thesis. Hua-Zhong Normal U., 2010.
- [12] Edmond Iancu. “QCD in heavy ion collisions”. In: *2011 European School of High-Energy Physics*. 2014, pp. 197–266. DOI: [10.5170/CERN-2014-003.197](https://doi.org/10.5170/CERN-2014-003.197).

- [13] J. C. Collins and M. J. Perry. "Superdense Matter: Neutrons or Asymptotically Free Quarks?" In: *Phys. Rev. Lett.* 34 (21 May 1975), pp. 1353–1356. DOI: [10.1103/PhysRevLett.34.1353](https://doi.org/10.1103/PhysRevLett.34.1353).
- [14] N. Cabibbo and G. Parisi. "Exponential Hadronic Spectrum and Quark Liberation". In: *Phys. Lett. B* 59 (1975), pp. 67–69. DOI: [10.1016/0370-2693\(75\)90158-6](https://doi.org/10.1016/0370-2693(75)90158-6).
- [15] Edward V. Shuryak. "Quark-Gluon Plasma and Hadronic Production of Leptons, Photons and Psions". In: *Sov. J. Nucl. Phys.* 28 (1978), p. 408. DOI: [10.1016/0370-2693\(78\)90370-2](https://doi.org/10.1016/0370-2693(78)90370-2).
- [16] HotQCD, A. Bazavov et al. "Equation of state in (2+1)-flavor QCD". In: *Phys. Rev. D* 90 (2014), p. 094503. DOI: [10.1103/PhysRevD.90.094503](https://doi.org/10.1103/PhysRevD.90.094503).
- [17] STAR, Grazyna Odyniec. "Beam Energy Scan Program at RHIC (BES I and BES II) – Probing QCD Phase Diagram with Heavy-Ion Collisions". In: *PoS CORFU2018* (2019). Ed. by Konstantinos Anagnostopoulos et al., p. 151. DOI: [10.22323/1.347.0151](https://doi.org/10.22323/1.347.0151).
- [18] "The Frontiers of Nuclear Science, A Long Range Plan". In: (Sept. 2008).
- [19] Jean-Yves Ollitrault. "Relativistic hydrodynamics for heavy-ion collisions". In: *Eur. J. Phys.* 29 (2008), pp. 275–302. DOI: [10.1088/0143-0807/29/2/010](https://doi.org/10.1088/0143-0807/29/2/010).
- [20] Peter F. Kolb and Ulrich W. Heinz. "Hydrodynamic description of ultrarelativistic heavy ion collisions". In: (May 2003). Ed. by Rudolph C. Hwa and Xin-Nian Wang, pp. 634–714.
- [21] P. Kovtun, Dan T. Son, and Andrei O. Starinets. "Viscosity in strongly interacting quantum field theories from black hole physics". In: *Phys. Rev. Lett.* 94 (2005), p. 111601. DOI: [10.1103/PhysRevLett.94.111601](https://doi.org/10.1103/PhysRevLett.94.111601).
- [22] Huichao Song and Ulrich W Heinz. "Interplay of shear and bulk viscosity in generating flow in heavy-ion collisions". In: *Phys. Rev. C* 81 (2010), p. 024905. DOI: [10.1103/PhysRevC.81.024905](https://doi.org/10.1103/PhysRevC.81.024905).
- [23] S. Ryu et al. "Importance of the Bulk Viscosity of QCD in Ultrarelativistic Heavy-Ion Collisions". In: *Phys. Rev. Lett.* 115.13 (2015), p. 132301. DOI: [10.1103/PhysRevLett.115.132301](https://doi.org/10.1103/PhysRevLett.115.132301).
- [24] Chun Shen et al. "The iEBE-VISHNU code package for relativistic heavy-ion collisions". In: *Comput. Phys. Commun.* 199 (2016), pp. 61–85. DOI: [10.1016/j.cpc.2015.08.039](https://doi.org/10.1016/j.cpc.2015.08.039).
- [25] Zi-Wei Lin et al. "A Multi-phase transport model for relativistic heavy ion collisions". In: *Phys. Rev. C* 72 (2005), p. 064901. DOI: [10.1103/PhysRevC.72.064901](https://doi.org/10.1103/PhysRevC.72.064901).
- [26] Rajeev S. Bhalerao, Amaresh Jaiswal, and Subrata Pal. "Collective flow in event-by-event partonic transport plus hydrodynamics hybrid approach". In: *Phys. Rev. C* 92 (1 July 2015), p. 014903. DOI: [10.1103/PhysRevC.92.014903](https://doi.org/10.1103/PhysRevC.92.014903).
- [27] Longgang Pang, Qun Wang, and Xin-Nian Wang. "Effects of initial flow velocity fluctuation in event-by-event (3+1)D hydrodynamics". In: *Phys. Rev. C* 86 (2 Aug. 2012), p. 024911. DOI: [10.1103/PhysRevC.86.024911](https://doi.org/10.1103/PhysRevC.86.024911).

- [28] Wenbin Zhao, Hao-jie Xu, and Huichao Song. “Collective flow in 2.76 A TeV and 5.02 A TeV Pb+Pb collisions”. In: *Eur. Phys. J. C* 77.9 (2017), p. 645. DOI: [10.1140/epjc/s10052-017-5186-x](https://doi.org/10.1140/epjc/s10052-017-5186-x).
- [29] J. Scott Moreland, Jonah E. Bernhard, and Steffen A. Bass. “Alternative ansatz to wounded nucleon and binary collision scaling in high-energy nuclear collisions”. In: *Phys. Rev. C* 92.1 (2015), p. 011901. DOI: [10.1103/PhysRevC.92.011901](https://doi.org/10.1103/PhysRevC.92.011901).
- [30] Jonah E. Bernhard et al. “Applying Bayesian parameter estimation to relativistic heavy-ion collisions: Simultaneous characterization of the initial state and quark-gluon plasma medium”. In: *Phys. Rev. C* 94 (2 Aug. 2016), p. 024907. DOI: [10.1103/PhysRevC.94.024907](https://doi.org/10.1103/PhysRevC.94.024907).
- [31] S. Voloshin and Y. Zhang. “Flow study in relativistic nuclear collisions by Fourier expansion of Azimuthal particle distributions”. In: *Z. Phys. C* 70 (1996), pp. 665–672. DOI: [10.1007/s002880050141](https://doi.org/10.1007/s002880050141).
- [32] ALICE, Jaroslav Adam et al. “Anisotropic flow of charged particles in Pb-Pb collisions at $\sqrt{s_{NN}} = 5.02$ TeV”. In: *Phys. Rev. Lett.* 116.13 (2016), p. 132302. DOI: [10.1103/PhysRevLett.116.132302](https://doi.org/10.1103/PhysRevLett.116.132302).
- [33] ALICE, K. Aamodt et al. “Higher harmonic anisotropic flow measurements of charged particles in Pb-Pb collisions at $\sqrt{s_{NN}}=2.76$ TeV”. In: *Phys. Rev. Lett.* 107 (2011), p. 032301. DOI: [10.1103/PhysRevLett.107.032301](https://doi.org/10.1103/PhysRevLett.107.032301).
- [34] ALICE, Jaroslav Adam et al. “Pseudorapidity dependence of the anisotropic flow of charged particles in Pb-Pb collisions at $\sqrt{s_{NN}} = 2.76$ TeV”. In: *Phys. Lett. B* 762 (2016), pp. 376–388. DOI: [10.1016/j.physletb.2016.07.017](https://doi.org/10.1016/j.physletb.2016.07.017).
- [35] ALICE, K Aamodt et al. “Elliptic flow of charged particles in Pb-Pb collisions at 2.76 TeV”. In: *Phys. Rev. Lett.* 105 (2010), p. 252302. DOI: [10.1103/PhysRevLett.105.252302](https://doi.org/10.1103/PhysRevLett.105.252302).
- [36] Jonah E. Bernhard, J. Scott Moreland, and Steffen A. Bass. “Bayesian estimation of the specific shear and bulk viscosity of quark–gluon plasma”. In: *Nature Phys.* 15.11 (2019), pp. 1113–1117. DOI: [10.1038/s41567-019-0611-8](https://doi.org/10.1038/s41567-019-0611-8).
- [37] Yingru Xu et al. “Data-driven analysis for the temperature and momentum dependence of the heavy-quark diffusion coefficient in relativistic heavy-ion collisions”. In: *Phys. Rev. C* 97.1 (2018), p. 014907. DOI: [10.1103/PhysRevC.97.014907](https://doi.org/10.1103/PhysRevC.97.014907).
- [38] J. Scott Moreland, Jonah E. Bernhard, and Steffen A. Bass. “Bayesian calibration of a hybrid nuclear collision model using p-Pb and Pb-Pb data at energies available at the CERN Large Hadron Collider”. In: *Phys. Rev. C* 101.2 (2020), p. 024911. DOI: [10.1103/PhysRevC.101.024911](https://doi.org/10.1103/PhysRevC.101.024911).
- [39] Ante Bilandzic, Raimond Snellings, and Sergei Voloshin. “Flow analysis with cumulants: Direct calculations”. In: *Phys. Rev. C* 83 (2011), p. 044913. DOI: [10.1103/PhysRevC.83.044913](https://doi.org/10.1103/PhysRevC.83.044913).
- [40] Nicolas Borghini, Phuong Mai Dinh, and Jean-Yves Ollitrault. “A New method for measuring azimuthal distributions in nucleus-nucleus collisions”. In: *Phys. Rev. C* 63 (2001), p. 054906. DOI: [10.1103/PhysRevC.63.054906](https://doi.org/10.1103/PhysRevC.63.054906).
- [41] Ilya Selyuzhenkov and Sergei Voloshin. “Effects of nonuniform acceptance in anisotropic flow measurements”. In: *Phys. Rev. C* 77 (3 Mar. 2008), p. 034904. DOI: [10.1103/PhysRevC.77.034904](https://doi.org/10.1103/PhysRevC.77.034904).

- [42] R.S. Bhalerao, N. Borghini, and J.Y. Ollitrault. “Analysis of anisotropic flow with Lee-Yang zeroes”. In: *Nucl. Phys. A* 727 (2003), pp. 373–426. DOI: [10.1016/j.nuclphysa.2003.08.007](https://doi.org/10.1016/j.nuclphysa.2003.08.007).
- [43] Ante Bilandzic et al. “Generic framework for anisotropic flow analyses with multiparticle azimuthal correlations”. In: *Phys. Rev. C* 89.6 (2014), p. 064904. DOI: [10.1103/PhysRevC.89.064904](https://doi.org/10.1103/PhysRevC.89.064904).
- [44] Katarina Gajdosova. “Investigations on collectivity in small and large collision systems at the LHC with ALICE”. PhD thesis. Bohr Inst., 2018.
- [45] Nicolas Borghini, Phuong Mai Dinh, and Jean-Yves Ollitrault. “Flow analysis from multiparticle azimuthal correlations”. In: *Phys. Rev. C* 64 (2001), p. 054901. DOI: [10.1103/PhysRevC.64.054901](https://doi.org/10.1103/PhysRevC.64.054901).
- [46] Nicolas Borghini, Phuong Mai Dinh, and Jean-Yves Ollitrault. “Flow analysis from cumulants: A Practical guide”. In: *International Workshop on the Physics of the Quark Gluon Plasma*. Oct. 2001.
- [47] “LHC Machine”. In: *JINST* 3 (2008). Ed. by Lyndon Evans and Philip Bryant, S08001. DOI: [10.1088/1748-0221/3/08/S08001](https://doi.org/10.1088/1748-0221/3/08/S08001).
- [48] *Analyzing the LHC Magnet Quenches*. URL: <https://spectrum.ieee.org/computing/software/analyzing-the-lhc-magnet-quenches%7D> (visited on 09/07/2020).
- [49] “Radiofrequency cavities”. In: (Sept. 2012). URL: <https://cds.cern.ch/record/1997424>.
- [50] The ALICE Collaboration. “The ALICE experiment at the CERN LHC”. In: *Journal of Instrumentation* 3.08 (Aug. 2008), S08002–S08002. DOI: [10.1088/1748-0221/3/08/S08002](https://doi.org/10.1088/1748-0221/3/08/S08002).
- [51] J. Alme et al. “The ALICE TPC, a large 3-dimensional tracking device with fast readout for ultra-high multiplicity events”. In: *Nuclear Instruments and Methods in Physics Research Section A: Accelerators, Spectrometers, Detectors and Associated Equipment* 622.1 (2010), pp. 316–367. ISSN: 0168-9002. DOI: <https://doi.org/10.1016/j.nima.2010.04.042>.
- [52] G. RENAULT et al. “THE LASER OF THE ALICE TIME PROJECTION CHAMBER”. In: *International Journal of Modern Physics E* 16.07n08 (2007), pp. 2413–2418. DOI: [10.1142/S0218301307008021](https://doi.org/10.1142/S0218301307008021).
- [53] The ALICE collaboration. “Performance of the ALICE VZERO system”. In: *Journal of Instrumentation* 8.10 (Oct. 2013), P10016–P10016. DOI: [10.1088/1748-0221/8/10/p10016](https://doi.org/10.1088/1748-0221/8/10/p10016).
- [54] Michael L. Miller et al. “Glauber Modeling in High-Energy Nuclear Collisions”. In: *Annual Review of Nuclear and Particle Science* 57.1 (2007), pp. 205–243. DOI: [10.1146/annurev.nucl.57.090506.123020](https://doi.org/10.1146/annurev.nucl.57.090506.123020).
- [55] ALICE, Betty Bezverkhny Abelev et al. “Performance of the ALICE Experiment at the CERN LHC”. In: *Int. J. Mod. Phys. A* 29 (2014), p. 1430044. DOI: [10.1142/S0217751X14300440](https://doi.org/10.1142/S0217751X14300440).
- [56] Rudolph Emil Kalman et al. “A new approach to linear filtering and prediction problems”. In: *Journal of basic Engineering* 82.1 (1960), pp. 35–45.

- [57] ALICE, K. Aamodt et al. "The ALICE experiment at the CERN LHC". In: *JINST* 3 (2008), S08002. DOI: [10.1088/1748-0221/3/08/S08002](https://doi.org/10.1088/1748-0221/3/08/S08002).
- [58] M. Krivda et al. "The ALICE trigger system performance for p-p and Pb-Pb collisions". In: *JINST* 7 (2012), p. C01057. DOI: [10.1088/1748-0221/7/01/C01057](https://doi.org/10.1088/1748-0221/7/01/C01057).
- [59] Rene Brun and Fons Rademakers. "ROOT — An object oriented data analysis framework". In: *Nuclear Instruments and Methods in Physics Research Section A: Accelerators, Spectrometers, Detectors and Associated Equipment* 389.1 (1997). New Computing Techniques in Physics Research V, pp. 81–86. ISSN: 0168-9002. DOI: [https://doi.org/10.1016/S0168-9002\(97\)00048-X](https://doi.org/10.1016/S0168-9002(97)00048-X).
- [60] Markus Zimmermann. "The ALICE analysis train system". In: *Journal of Physics: Conference Series* 608 (Feb. 2015). DOI: [10.1088/1742-6596/608/1/012019](https://doi.org/10.1088/1742-6596/608/1/012019).
- [61] *AliPhysics*. URL: <https://github.com/alispw/AliRoot>.
- [62] *AliPhysics*. URL: <https://github.com/alispw/AliPhysics>.
- [63] *SLUO Lectures on Statistics and Numerical Methods in HEP*. URL: https://www-group.slac.stanford.edu/sluo/lectures/stat_lecture_files/sluolec5.pdf (visited on 09/11/2020).
- [64] B. Efron. *An Introduction to the Bootstrap*. CRC Press, 1994.
- [65] ATLAS, Georges Aad et al. "Measurement of the azimuthal anisotropy for charged particle production in $\sqrt{s_{NN}} = 2.76$ TeV lead-lead collisions with the ATLAS detector". In: *Phys. Rev. C* 86 (2012), p. 014907. DOI: [10.1103/PhysRevC.86.014907](https://doi.org/10.1103/PhysRevC.86.014907).
- [66] CMS, Serguei Chatrchyan et al. "Centrality dependence of dihadron correlations and azimuthal anisotropy harmonics in PbPb collisions at $\sqrt{s_{NN}} = 2.76$ TeV". In: *Eur. Phys. J. C* 72 (2012), p. 2012. DOI: [10.1140/epjc/s10052-012-2012-3](https://doi.org/10.1140/epjc/s10052-012-2012-3).
- [67] B. Alver and G. Roland. "Collision geometry fluctuations and triangular flow in heavy-ion collisions". In: *Phys. Rev. C* 81 (2010). [Erratum: *Phys.Rev.C* 82, 039903 (2010)], p. 054905. DOI: [10.1103/PhysRevC.82.039903](https://doi.org/10.1103/PhysRevC.82.039903).
- [68] Mike Miller and Raimond Snellings. "Eccentricity fluctuations and its possible effect on elliptic flow measurements". In: (Dec. 2003).
- [69] PHOBOS, B. Alver et al. "System size, energy, pseudorapidity, and centrality dependence of elliptic flow". In: *Phys. Rev. Lett.* 98 (2007), p. 242302. DOI: [10.1103/PhysRevLett.98.242302](https://doi.org/10.1103/PhysRevLett.98.242302).
- [70] Ulrich Heinz, Zhi Qiu, and Chun Shen. "Fluctuating flow angles and anisotropic flow measurements". In: *Phys. Rev. C* 87.3 (2013), p. 034913. DOI: [10.1103/PhysRevC.87.034913](https://doi.org/10.1103/PhysRevC.87.034913).
- [71] Fernando G. Gardim et al. "Breaking of factorization of two-particle correlations in hydrodynamics". In: *Phys. Rev. C* 87.3 (2013), p. 031901. DOI: [10.1103/PhysRevC.87.031901](https://doi.org/10.1103/PhysRevC.87.031901).
- [72] ALICE, Shreyasi Acharya et al. "Searches for transverse momentum dependent flow vector fluctuations in Pb-Pb and p-Pb collisions at the LHC". In: *JHEP* 09 (2017), p. 032. DOI: [10.1007/JHEP09\(2017\)032](https://doi.org/10.1007/JHEP09(2017)032).

- [73] CMS Collaboration, V. Khachatryan *et al.* “Evidence for transverse-momentum- and pseudorapidity-dependent event-plane fluctuations in PbPb and p Pb collisions”. In: *Phys. Rev. C* 92 (3 Sept. 2015), p. 034911. DOI: [10.1103/PhysRevC.92.034911](https://doi.org/10.1103/PhysRevC.92.034911).
- [74] ALICE, K. Aamodt *et al.* “Harmonic decomposition of two-particle angular correlations in Pb-Pb collisions at $\sqrt{s_{NN}} = 2.76$ TeV”. In: *Phys. Lett. B* 708 (2012), pp. 249–264. DOI: [10.1016/j.physletb.2012.01.060](https://doi.org/10.1016/j.physletb.2012.01.060).
- [75] ALICE, S. Acharya *et al.* “Anisotropic flow of identified particles in Pb-Pb collisions at $\sqrt{s_{NN}} = 5.02$ TeV”. In: *JHEP* 09 (2018), p. 006. DOI: [10.1007/JHEP09\(2018\)006](https://doi.org/10.1007/JHEP09(2018)006).
- [76] ALICE, Shreyasi Acharya *et al.* “Non-linear flow modes of identified particles in Pb-Pb collisions at $\sqrt{s_{NN}} = 5.02$ TeV”. In: *JHEP* 06 (2020), p. 147. DOI: [10.1007/JHEP06\(2020\)147](https://doi.org/10.1007/JHEP06(2020)147).
- [77] ATLAS, Georges Aad *et al.* “Longitudinal flow decorrelations in Xe+Xe collisions at $\sqrt{s_{NN}} = 5.44$ TeV with the ATLAS detector”. In: (Jan. 2020).
- [78] ALICE, Shreyasi Acharya *et al.* “Linear and non-linear flow modes in Pb-Pb collisions at $\sqrt{s_{NN}} = 2.76$ TeV”. In: *Phys. Lett. B* 773 (2017), pp. 68–80. DOI: [10.1016/j.physletb.2017.07.060](https://doi.org/10.1016/j.physletb.2017.07.060).
- [79] PHOBOS, B. Alver *et al.* “Non-flow correlations and elliptic flow fluctuations in gold-gold collisions at $\sqrt{s_{NN}} = 200$ GeV”. In: *Phys. Rev. C* 81 (2010), p. 034915. DOI: [10.1103/PhysRevC.81.034915](https://doi.org/10.1103/PhysRevC.81.034915).
- [80] Andrew Adare. “Triggered di-hadron correlations in Pb-Pb collisions from the ALICE experiment”. In: *J. Phys. G* 38 (2011). Ed. by Yves Schutz and Urs Achim Wiedemann, p. 124091. DOI: [10.1088/0954-3899/38/12/124091](https://doi.org/10.1088/0954-3899/38/12/124091).
- [81] ATLAS, Jiangyong Jia. “Measurement of elliptic and higher order flow from ATLAS experiment at the LHC”. In: *J. Phys. G* 38 (2011). Ed. by Yves Schutz and Urs Achim Wiedemann, p. 124012. DOI: [10.1088/0954-3899/38/12/124012](https://doi.org/10.1088/0954-3899/38/12/124012).
- [82] Daniel Kikola *et al.* “Nonflow ‘factorization’ and a novel method to disentangle anisotropic flow and nonflow”. In: *Phys. Rev. C* 86 (2012), p. 014901. DOI: [10.1103/PhysRevC.86.014901](https://doi.org/10.1103/PhysRevC.86.014901).
- [83] CMS, Vardan Khachatryan *et al.* “Observation of Long-Range Near-Side Angular Correlations in Proton-Proton Collisions at the LHC”. In: *JHEP* 09 (2010), p. 091. DOI: [10.1007/JHEP09\(2010\)091](https://doi.org/10.1007/JHEP09(2010)091).
- [84] CMS, Serguei Chatrchyan *et al.* “Observation of Long-Range Near-Side Angular Correlations in Proton-Lead Collisions at the LHC”. In: *Phys. Lett. B* 718 (2013), pp. 795–814. DOI: [10.1016/j.physletb.2012.11.025](https://doi.org/10.1016/j.physletb.2012.11.025).
- [85] ATLAS, Georges Aad *et al.* “Observation of Long-Range Elliptic Azimuthal Anisotropies in $\sqrt{s} = 13$ and 2.76 TeV pp Collisions with the ATLAS Detector”. In: *Phys. Rev. Lett.* 116.17 (2016), p. 172301. DOI: [10.1103/PhysRevLett.116.172301](https://doi.org/10.1103/PhysRevLett.116.172301).
- [86] CMS, Vardan Khachatryan *et al.* “Evidence for Collective Multiparticle Correlations in p -Pb Collisions”. In: *Phys. Rev. Lett.* 115.1 (2015), p. 012301. DOI: [10.1103/PhysRevLett.115.012301](https://doi.org/10.1103/PhysRevLett.115.012301).

- [87] ATLAS, Morad Aaboud et al. “Measurement of multi-particle azimuthal correlations in pp , $p+Pb$ and low-multiplicity $Pb+Pb$ collisions with the ATLAS detector”. In: *Eur. Phys. J. C* 77.6 (2017), p. 428. DOI: [10.1140/epjc/s10052-017-4988-1](https://doi.org/10.1140/epjc/s10052-017-4988-1).
- [88] ALICE, Betty Bezverkhny Abelev et al. “Multiparticle azimuthal correlations in $p-Pb$ and $Pb-Pb$ collisions at the CERN Large Hadron Collider”. In: *Phys. Rev. C* 90.5 (2014), p. 054901. DOI: [10.1103/PhysRevC.90.054901](https://doi.org/10.1103/PhysRevC.90.054901).
- [89] CMS, Vardan Khachatryan et al. “Evidence for collectivity in pp collisions at the LHC”. In: *Phys. Lett. B* 765 (2017), pp. 193–220. DOI: [10.1016/j.physletb.2016.12.009](https://doi.org/10.1016/j.physletb.2016.12.009).
- [90] Björn Schenke. “Origins of collectivity in small systems”. In: *Nucl. Phys. A* 967 (2017). Ed. by Ulrich Heinz, Olga Evdokimov, and Peter Jacobs, pp. 105–112. DOI: [10.1016/j.nuclphysa.2017.05.017](https://doi.org/10.1016/j.nuclphysa.2017.05.017).
- [91] Stefan Roesler, Ralph Engel, and Johannes Ranft. “The Monte Carlo event generator DPMJET-III”. In: *International Conference on Advanced Monte Carlo for Radiation Physics, Particle Transport Simulation and Applications (MC 2000)*. Dec. 2000, pp. 1033–1038. DOI: [10.1007/978-3-642-18211-2_166](https://doi.org/10.1007/978-3-642-18211-2_166).
- [92] Igor Kozlov et al. “Transverse momentum structure of pair correlations as a signature of collective behavior in small collision systems”. In: (May 2014).
- [93] ALICE, Jaroslav Adam et al. “Correlated event-by-event fluctuations of flow harmonics in $Pb-Pb$ collisions at $\sqrt{s_{NN}} = 2.76$ TeV”. In: *Phys. Rev. Lett.* 117 (2016), p. 182301. DOI: [10.1103/PhysRevLett.117.182301](https://doi.org/10.1103/PhysRevLett.117.182301).
- [94] ATLAS, Georges Aad et al. “Measurement of the correlation between flow harmonics of different order in lead-lead collisions at $\sqrt{s_{NN}}=2.76$ TeV with the ATLAS detector”. In: *Phys. Rev. C* 92.3 (2015), p. 034903. DOI: [10.1103/PhysRevC.92.034903](https://doi.org/10.1103/PhysRevC.92.034903).
- [95] Jurgen Schukraft, Anthony Timmins, and Sergei A. Voloshin. “Ultra-relativistic nuclear collisions: event shape engineering”. In: *Phys. Lett. B* 719 (2013), pp. 394–398. DOI: [10.1016/j.physletb.2013.01.045](https://doi.org/10.1016/j.physletb.2013.01.045).
- [96] Hannah Petersen and Berndt Muller. “Possibility of event shape selection in relativistic heavy ion collisions”. In: *Phys. Rev. C* 88.4 (2013), p. 044918. DOI: [10.1103/PhysRevC.88.044918](https://doi.org/10.1103/PhysRevC.88.044918).

A Run lists

HIR LHC15o									
246276	246275	246272	246271	246225	246222	246217	246185	246182	246181
246180	246178	246153	246152	246151	246148	246115	246113	246089	246087
246053	246052	246049	246048	246042	246037	246036	246012	246003	246001
245963	245954	245952	245949	245923	245833	245831	245829	245705	245702
245700	245692	245683	246994	246991	246989	246984	246982	246980	246948
246945	246928	246851	246847	246846	246845	246844	246810	246809	246808
246807	246805	246804	246766	246765	246763	246760	246759	246758	246757
246751	246750	246495	246493	246488	246487	246434	246431	246428	246424

Table 7: List of 2015 high intensity Pb–Pb runs at $\sqrt{s_{\text{NN}}}$ = 5.02 TeV used in this analysis

LHC18r									
297595	297590	297588	297558	297544	297542	297541	297540	297537	297512
297483	297481	297479	297452	297451	297450	297446	297442	297441	297415
297414	297413	297406	297405	297380	297379	297372	297367	297366	297363
297336	297335	297333	297332	297317	297311	297310	297278	297222	297221
297218	297196	297195	297193	297133	297132	297129	297128	297124	297123
297119	297118	297117	297085	297035	297031	296966	296941	296938	296935
296934	296932	296931	296930	296903	296900	296899	296894	296852	296851
296850	296848	296839	296838	296836	296835	296799	296794	296793	296790
296787	296786	296785	296784	296781	296752	296694	296693	296691	296690
297219	297194	297029	296890	296849	296750	296749			

LHC18q									
296623	296622	296621	296619	296618	296616	296615	296594	296553	296552
296551	296550	296549	296548	296547	296516	296512	296511	296510	296509
296472	296433	296424	296423	296420	296419	296415	296414	296383	296381
296380	296379	296378	296377	296376	296375	296312	296309	296304	296303
296280	296279	296273	296270	296269	296247	296246	296244	296243	296242
296241	296240	296198	296197	296196	296195	296194	296192	296191	296143
296142	296135	296134	296133	296132	296123	296074	296066	296065	296063
296062	296060	296016	295942	295941	295937	295936	295913	295910	295909
295861	295860	295859	295856	295855	295854	295853	295831	295829	295826
295825	295822	295819	295818	295816	295791	295788	295786	295763	295762
295759	295758	295755	295754	295725	295723	295721	295719	295718	295717
295714	295712	295676	295675	295673	295668	295667	295666	295615	295612
295611	295610	295589	295588	295586	295558				

Table 8: List of 2018 Pb–Pb runs at $\sqrt{s_{\text{NN}}}$ = 5.02 TeV used in this analysis

LHC17n	
280234	280235

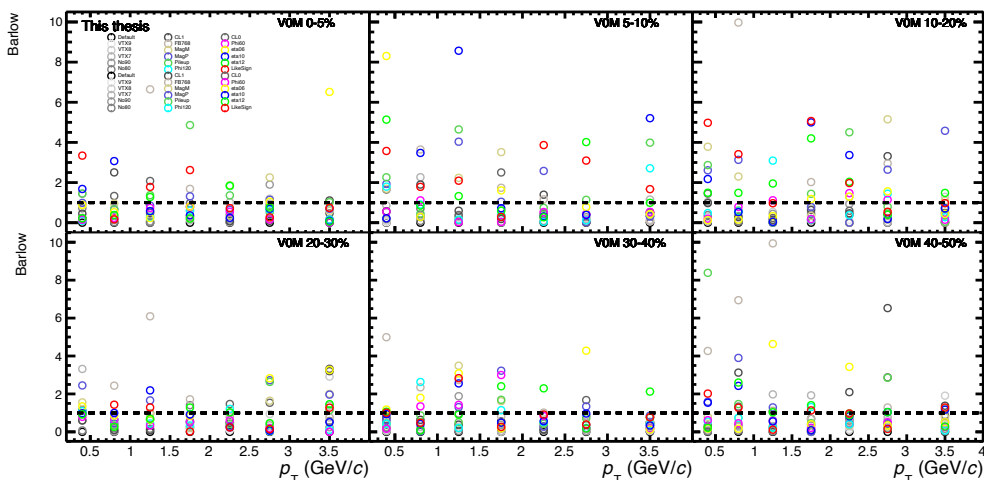
Table 9: List of 2017 Xe–Xe runs at $\sqrt{s_{\text{NN}}}=5.44$ TeV used in this analysis

B Systematics

The systematic uncertainties are obtained by estimating the statistical significance of the variation of event and track cuts via the Barlow test. If significant, the ratio of the observable with the variation cut to the observable with default cuts is fitted with either a constant or linear fit. From these fits, the systematic uncertainty is estimated. Figures of the values of the Barlow tests and of the ratio of the observables with variation cuts to default cuts are shown here. An example of the estimated systematic uncertainties are shown in tables [10](#) and [11](#) for $v_2\{2\}/v_2[2]$.

B.1 $v_n\{2\}/v_n[2]$

$v_2\{2\}/v_2[2]$	Systematic uncertainty					
	0-5%	5-10%	10-20%	20-30%	30-40%	40-50%
Vtx. z cuts	N/S	N/S	N/S	N/S	N/S	N/S
Centrality determination	0.05%	0.04%	N/S	N/S	N/S	0.03%
Pileup events	0.18%	0.04%	N/S	N/S	N/S	0.09%
Magnetic field polarities	N/S	N/S	N/S	N/S	0.06%	0.09%
Total	0.19%	0.05%	N/S	N/S	0.06%	0.13%

Table 10: Systematic uncertainties due to variations in the event selection cuts for $v_2\{2\}/v_2[2]$.Figure B.1: The values of the Barlow test compared against unity (dotted line) for each variation cut on $v_3\{2\}/v_3[2]$ in Pb–Pb collisions at $\sqrt{s_{\text{NN}}}=5.02$ TeV.

$v_2\{2\}/v_2[2]$ Uncertainty sources	p_T bin							
	1	2	3	4	5	6	7	8
TPC Ncls 0-5%	0.04%	0.04%	0.04%	0.04%	0.04%	0.04%	0.04%	0.04%
TPC Ncls 5-10%	N/S	N/S	N/S	N/S	N/S	N/S	N/S	N/S
TPC Ncls 10-20%	N/S	N/S	N/S	N/S	N/S	N/S	N/S	N/S
TPC Ncls 20-30%	N/S	N/S	N/S	N/S	N/S	N/S	N/S	N/S
TPC Ncls 30-40%	N/S	N/S	N/S	N/S	N/S	N/S	N/S	N/S
TPC Ncls 40-50%	N/S	N/S	N/S	N/S	N/S	N/S	N/S	N/S
FB768 0-5%	0.19%	0.19%	0.19%	0.19%	0.19%	0.19%	0.19%	0.19%
FB768 5-10%	0.21%	0.21%	0.21%	0.21%	0.21%	0.21%	0.21%	0.21%
FB768 10-20%	0.06%	0.06%	0.06%	0.06%	0.06%	0.06%	0.06%	0.06%
FB768 20-30%	0.04%	0.04%	0.04%	0.04%	0.04%	0.04%	0.04%	0.04%
FB768 30-40%	0.05%	0.05%	0.05%	0.05%	0.05%	0.05%	0.05%	0.05%
FB768 40-50%	0.03%	0.03%	0.03%	0.03%	0.03%	0.03%	0.03%	0.03%
NUA 0-5%	N/S	N/S	N/S	N/S	N/S	N/S	N/S	N/S
NUA 5-10%	N/S	N/S	N/S	N/S	N/S	N/S	N/S	N/S
NUA 10-20%	N/S	N/S	N/S	N/S	N/S	N/S	N/S	N/S
NUA 20-30%	N/S	N/S	N/S	N/S	N/S	N/S	N/S	N/S
NUA 30-40%	N/S	N/S	N/S	N/S	N/S	N/S	N/S	N/S
NUA 40-50%	N/S	0.02%	0.04%	0.06%	0.09%	0.11%	0.15%	0.20%
Non-flow 0-5%	0.64%	0.64%	0.64%	0.64%	0.64%	0.64%	0.64%	0.64%
Non-flow 5-10%	0.16%	0.16%	0.16%	0.16%	0.16%	0.16%	0.16%	0.16%
Non-flow 10-20%	0.04%	0.04%	0.04%	0.04%	0.04%	0.04%	0.04%	0.04%
Non-flow 20-30%	0.04%	0.04%	0.04%	0.04%	0.04%	0.04%	0.04%	0.04%
Non-flow 30-40%	0.06%	0.06%	0.06%	0.06%	0.06%	0.06%	0.06%	0.06%
Non-flow 40-50%	0.13%	0.13%	0.13%	0.13%	0.13%	0.13%	0.13%	0.13%

Table 11: Systematic uncertainty due to variations in the track selection cuts for $v_2\{2\}/v_2[2]$ in each p_T bin.

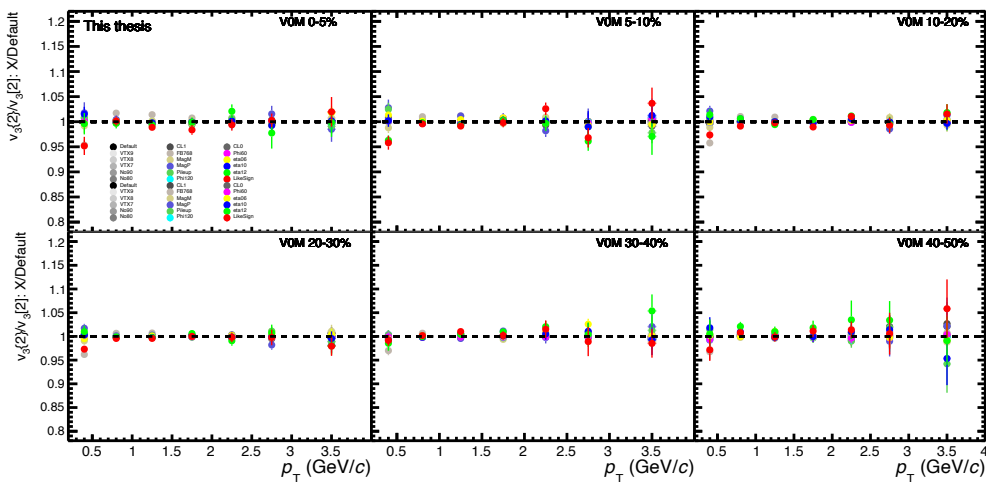


Figure B.2: The ratio of $v_3\{2\}/v_3[2]$ with different variations of the cuts to $v_3\{2\}/v_3[2]$ with default cuts in Pb–Pb collisions at $\sqrt{s_{NN}} = 5.02$ TeV.

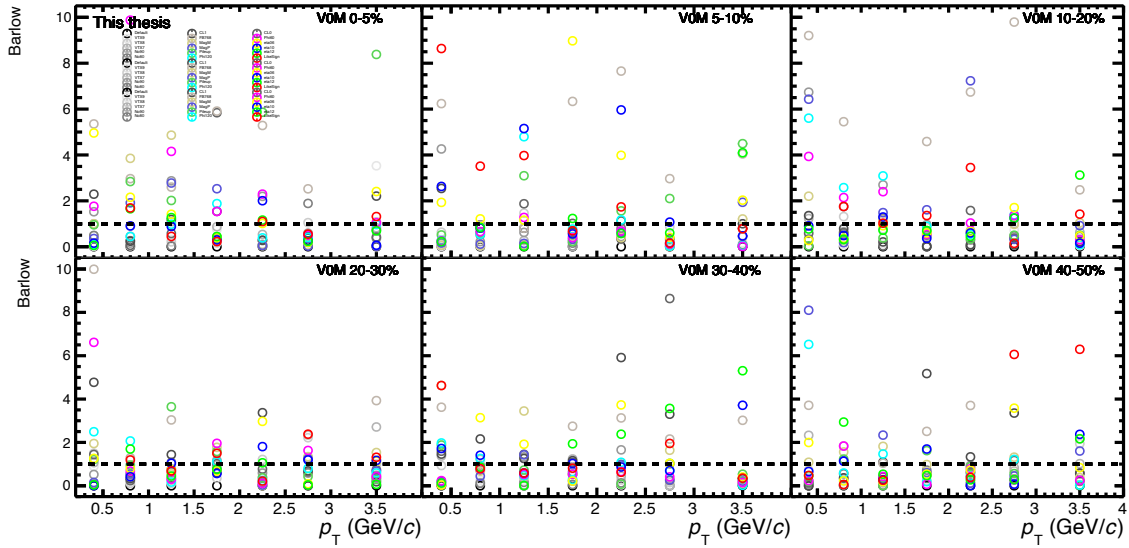


Figure B.3: The values of the Barlow test compared against unity (dotted line) for each variation cut on $v_4\{2\}/v_4[2]$ in Pb–Pb collisions at $\sqrt{s_{\text{NN}}}=5.02$ TeV.

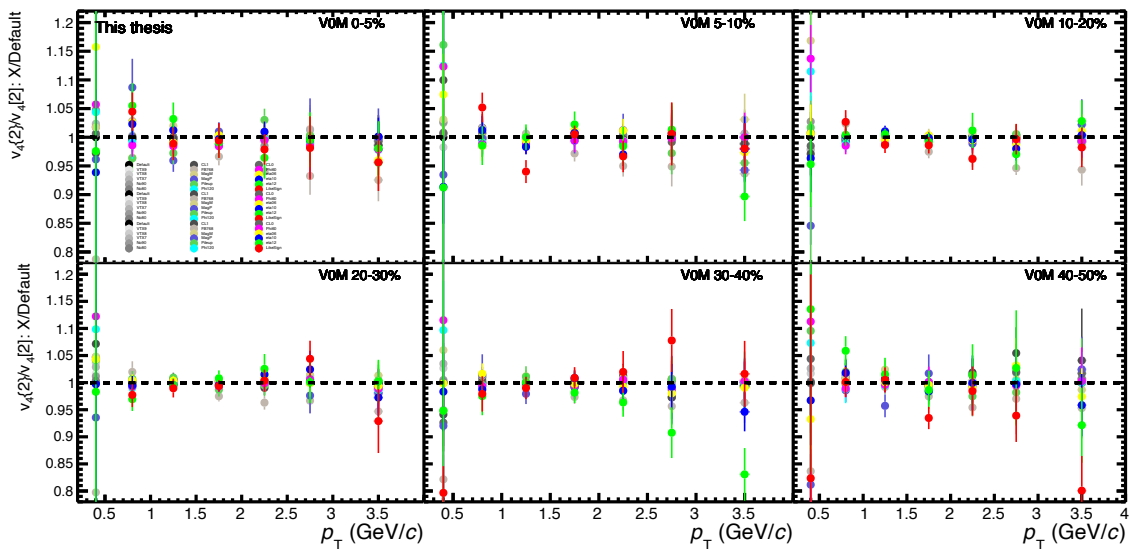


Figure B.4: The ratio of $v_4\{2\}/v_4[2]$ with different variations of the cuts to $v_4\{2\}/v_4[2]$ with default cuts in Pb–Pb collisions at $\sqrt{s_{\text{NN}}}=5.02$ TeV.

B.2 Factorization ratio r_n

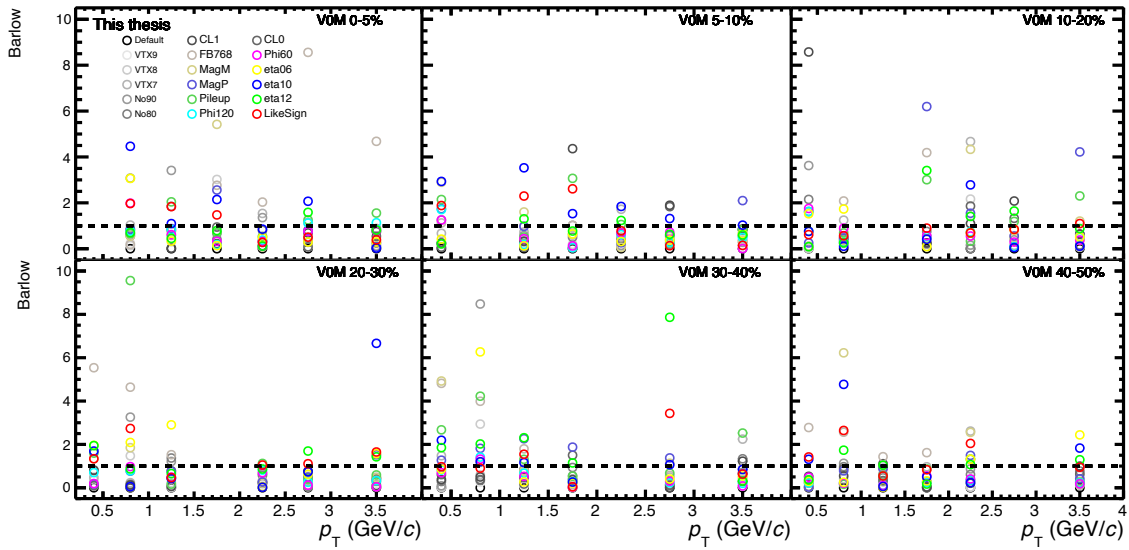


Figure B.5: The values of the Barlow test compared against unity (dotted line) for each variation cut on r_2 in Pb–Pb collisions at $\sqrt{s_{NN}} = 5.02$ TeV.

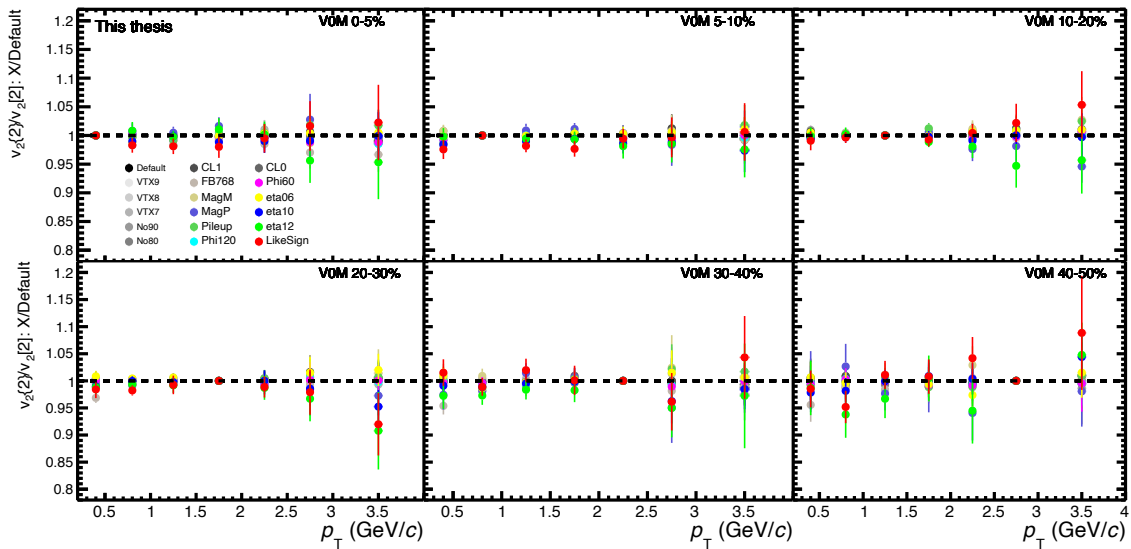


Figure B.6: The ratio of r_2 with different variations of the cuts to r_2 with default cuts in Pb–Pb collisions at $\sqrt{s_{NN}} = 5.02$ TeV.

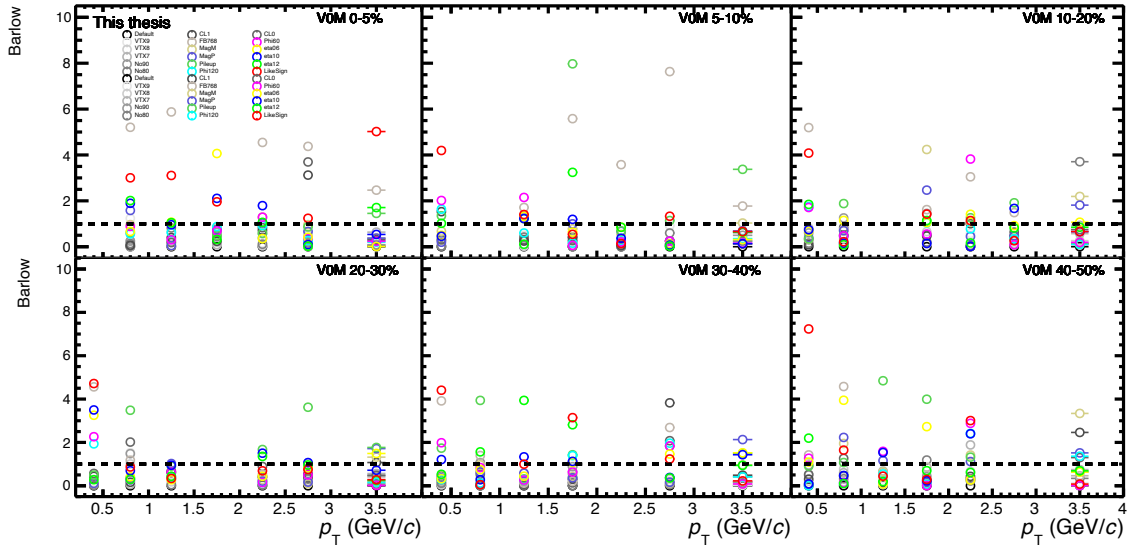


Figure B.7: The values of the Barlow test compared against unity (dotted line) for each variation cut on r_3 in Pb–Pb collisions at $\sqrt{s_{NN}} = 5.02$ TeV.

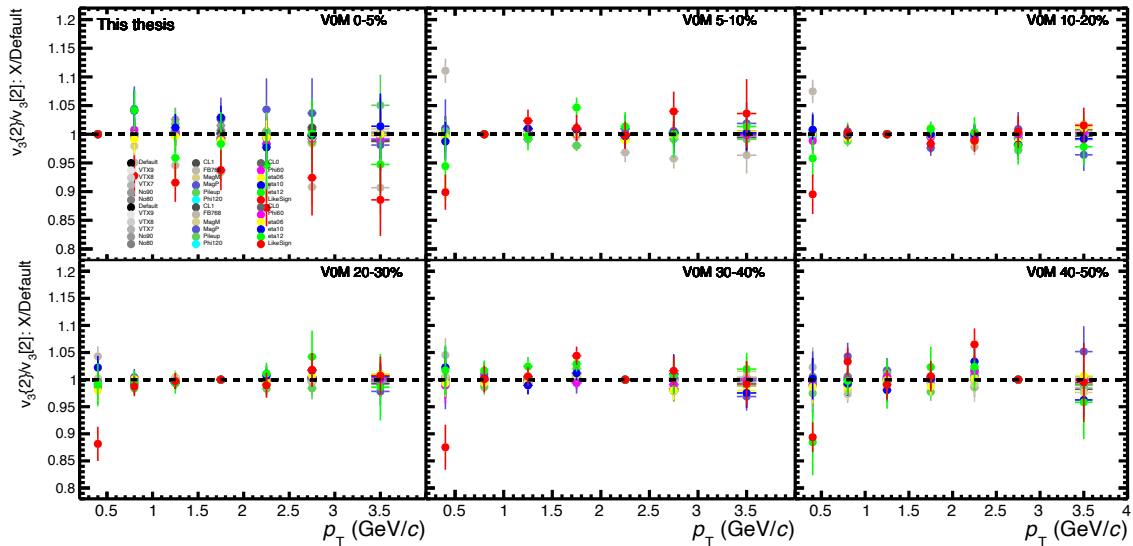


Figure B.8: The ratio of r_3 with different variations of the cuts to r_3 with default cuts in Pb–Pb collisions at $\sqrt{s_{NN}} = 5.02$ TeV.

B.3 Angle decorrelation

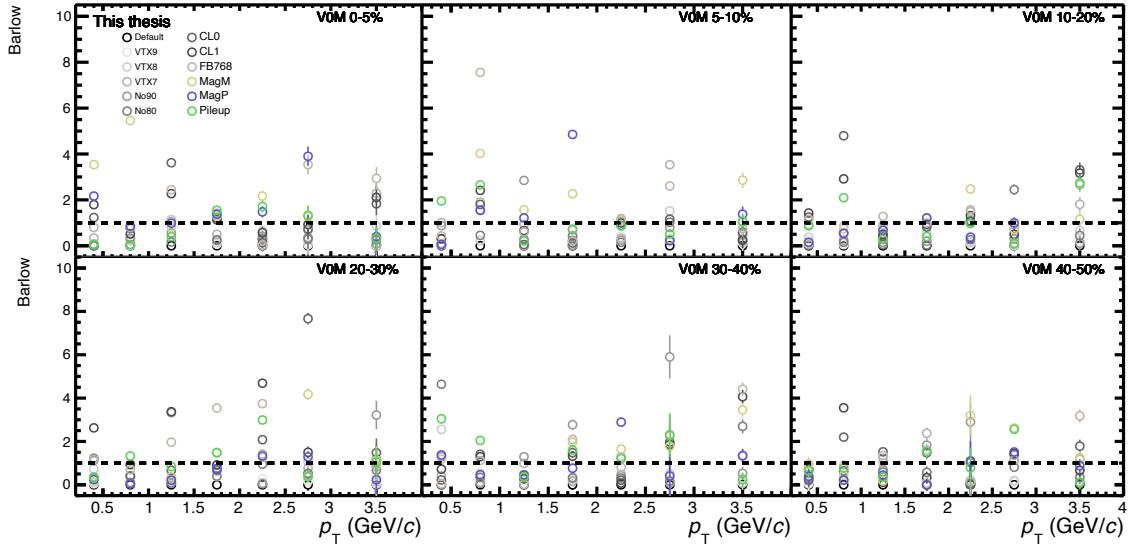


Figure B.9: The values of the Barlow test compared against unity (dotted line) for each variation cut on $\langle \cos 4[\Psi_2(p_T^a) - \Psi_2(p_T^t)] \rangle$ in Pb–Pb collisions at $\sqrt{s_{NN}} = 5.02$ TeV.

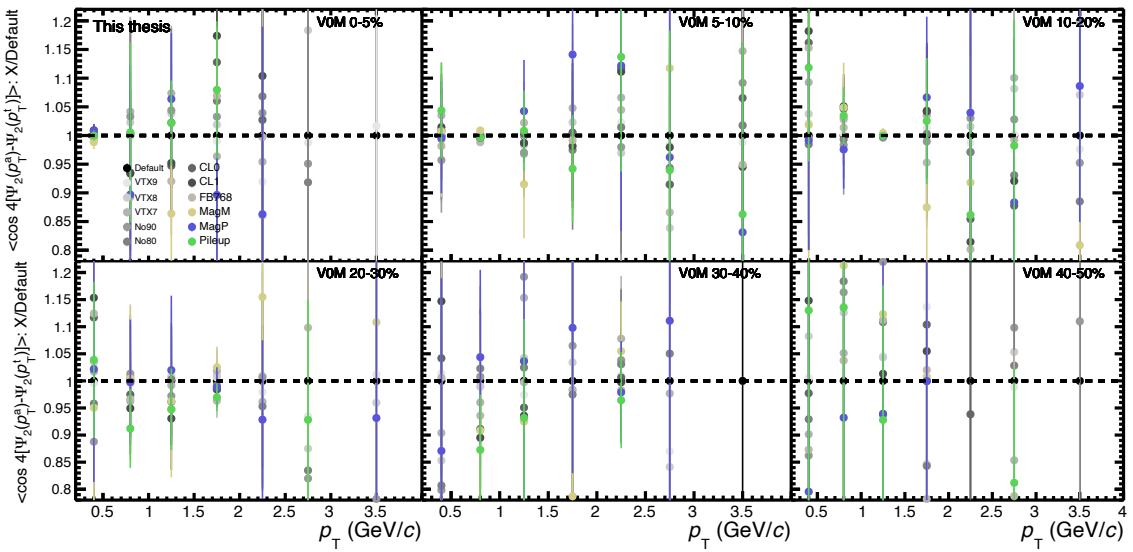


Figure B.10: The ratio of $\langle \cos 4[\Psi_2(p_T^a) - \Psi_2(p_T^t)] \rangle$ with different variations of the cuts to $\langle \cos 4[\Psi_2(p_T^a) - \Psi_2(p_T^t)] \rangle$ with default cuts in Pb–Pb collisions at $\sqrt{s_{NN}} = 5.02$ TeV.

B.4 p_T -differential normalized symmetric cumulant

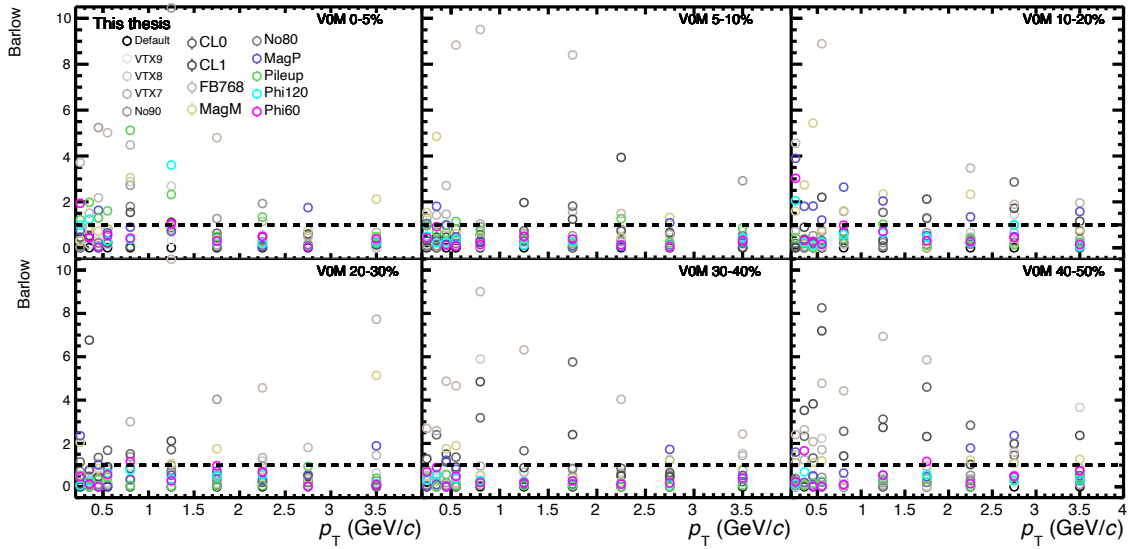


Figure B.11: The values of the Barlow test compared against unity (dotted line) for each variation cut on $\text{NSC}(3, 2_{p_T})$ in Pb–Pb collisions at $\sqrt{s_{\text{NN}}} = 5.02$ TeV.

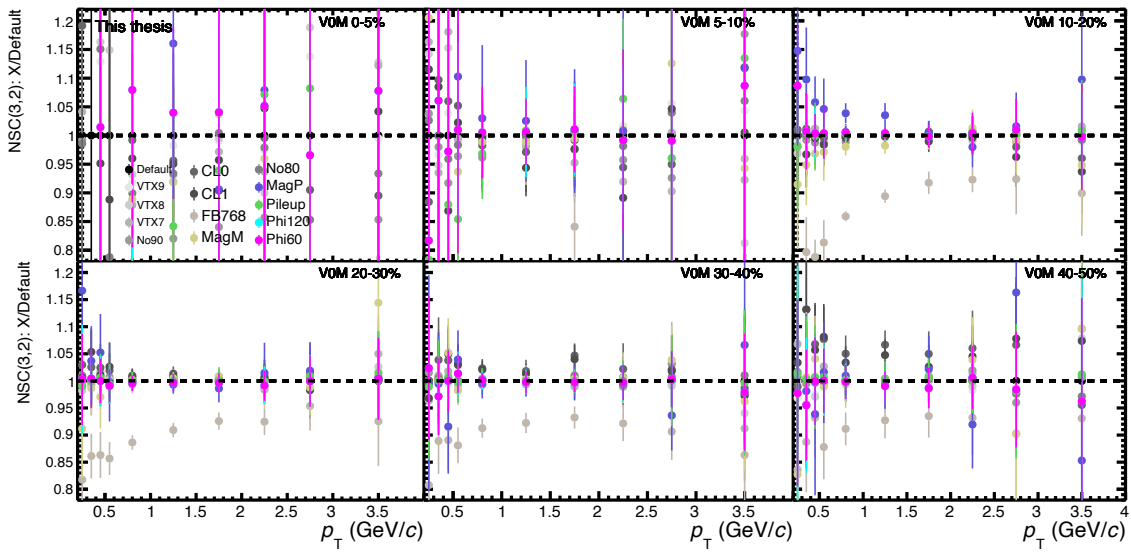


Figure B.12: The ratio of $\text{NSC}(3, 2_{p_T})$ with different variations of the cuts to $\text{NSC}(3, 2_{p_T})$ with default cuts in Pb–Pb collisions at $\sqrt{s_{\text{NN}}} = 5.02$ TeV.

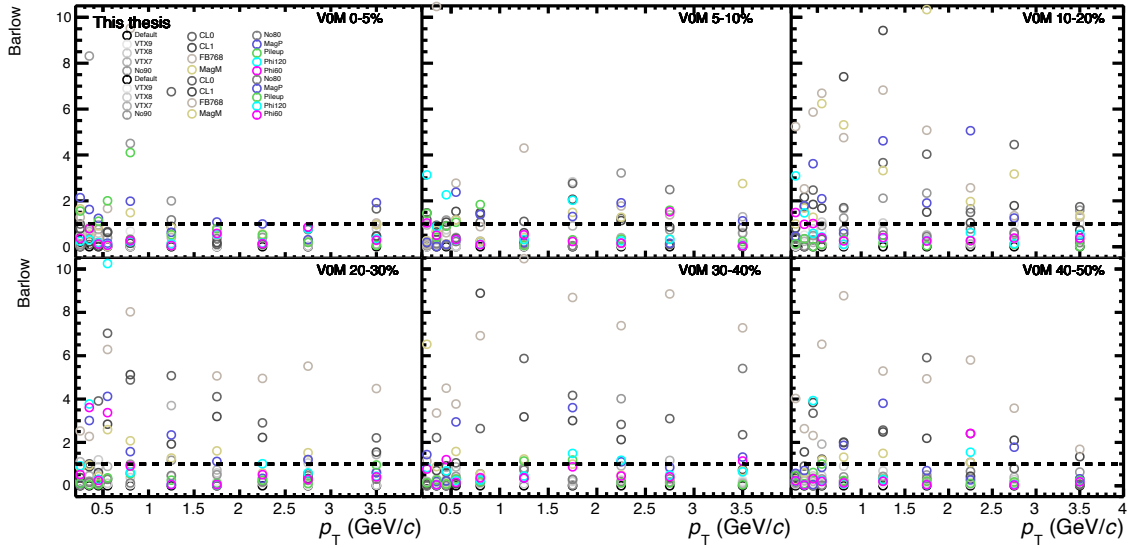


Figure B.13: The values of the Barlow test compared against unity (dotted line) for each variation cut on NSC(4, $2p_T$) in Pb–Pb collisions at $\sqrt{s_{NN}} = 5.02$ TeV.

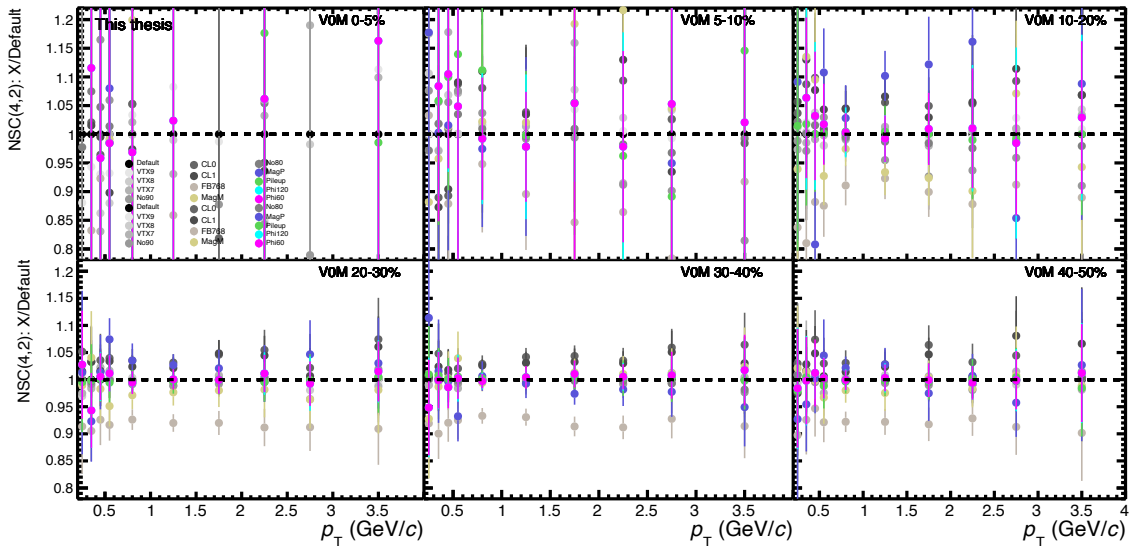


Figure B.14: The ratio of NSC(4, $2p_T$) with different variations of the cuts to NSC(4, $2p_T$) with default cuts in Pb–Pb collisions at $\sqrt{s_{NN}} = 5.02$ TeV.

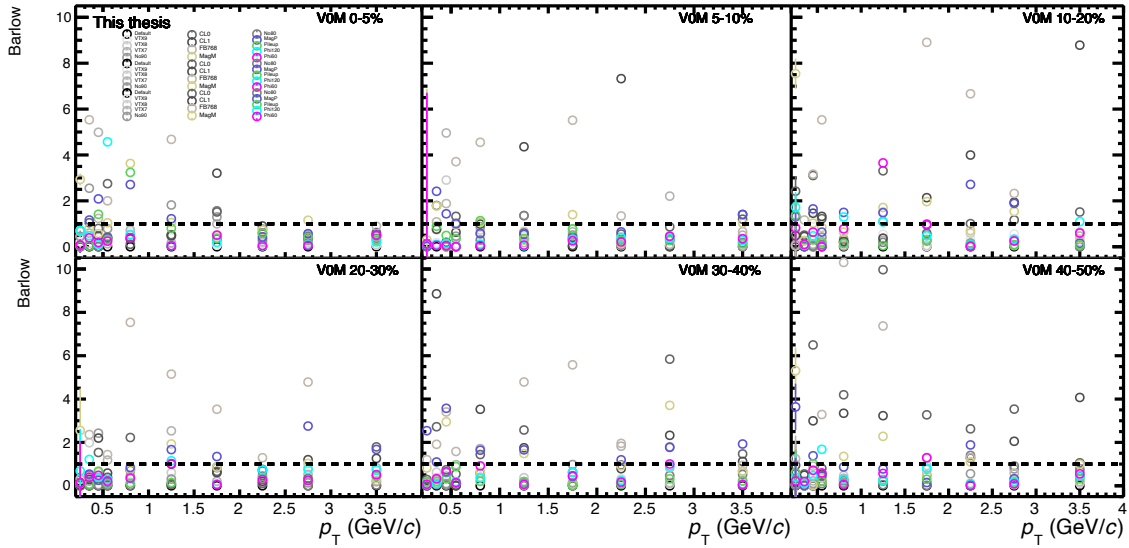


Figure B.15: The values of the Barlow test compared against unity (dotted line) for each variation cut on $\text{NSC}(2, 3_{p_T})$ in Pb–Pb collisions at $\sqrt{s_{\text{NN}}} = 5.02$ TeV.

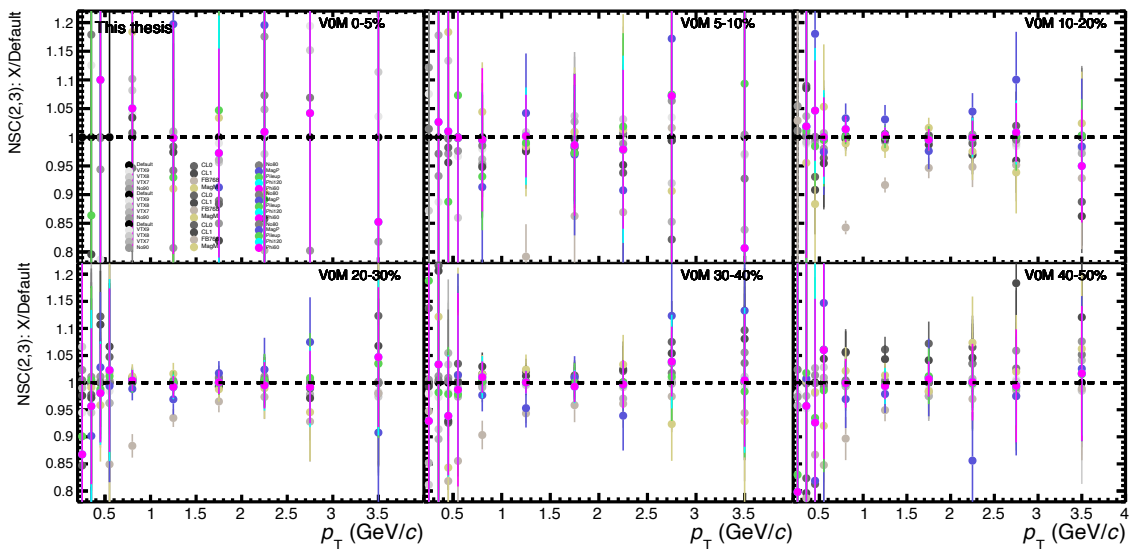


Figure B.16: The ratio of $\text{NSC}(2, 3_{p_T})$ with different variations of the cuts to $\text{NSC}(2, 3_{p_T})$ with default cuts in Pb–Pb collisions at $\sqrt{s_{\text{NN}}} = 5.02$ TeV.

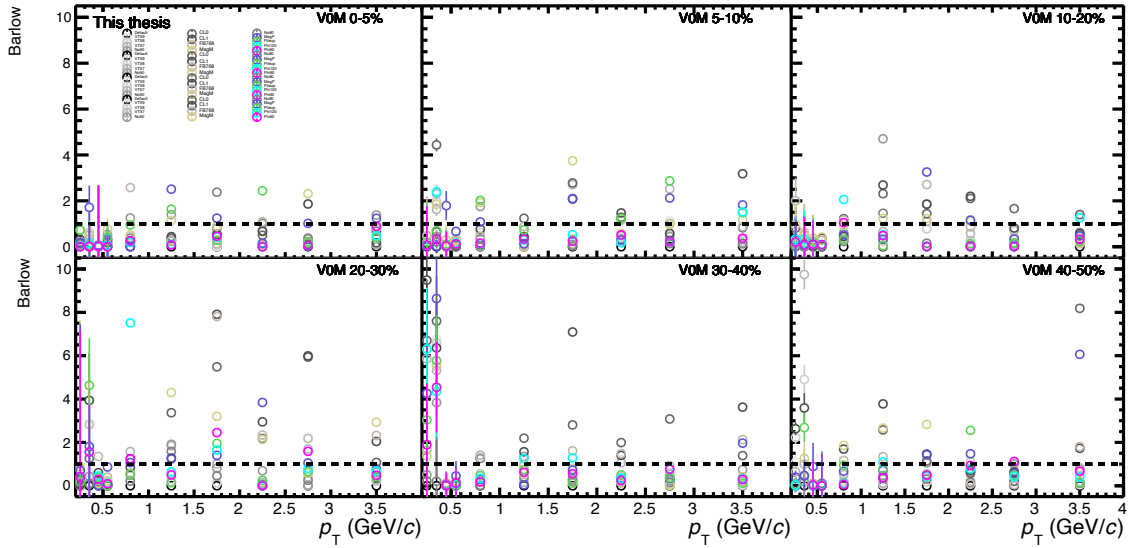


Figure B.17: The values of the Barlow test compared against unity (dotted line) for each variation cut on NSC(2, 4_{p_T}) in Pb–Pb collisions at $\sqrt{s_{NN}} = 5.02$ TeV.

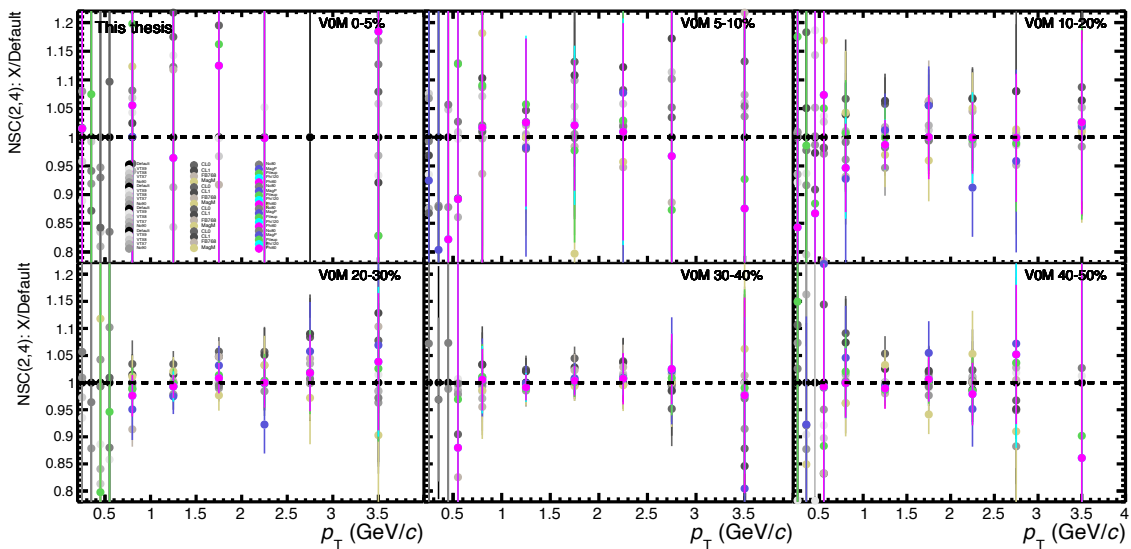


Figure B.18: The ratio of NSC(2, 4_{p_T}) with different variations of the cuts to NSC(2, 4_{p_T}) with default cuts in Pb–Pb collisions at $\sqrt{s_{NN}} = 5.02$ TeV.

C 2018 data measurements

The data from the 2018 periods LHC18q and LHC18r offer better statistics than the 2015 period LHC15o. The validity and accuracy of the reconstruction of the 2018 data is an ongoing discussion in the ALICE collaboration, and several passes over the data have been made in order to obtain the proper reconstruction. This appendix shows the comparison of some of the observables presented in the thesis for the different data sets.

C.1 $v_n\{2\}/v_n[2]$

In figure C.1, the ratio $v_2\{2\}/v_2[2]$ is shown for both 2015 and 2018 data. Both data sets show the same trend and figure C.2 shows that the data sets are compatible within 0.5%. However, as we move to higher-order $v_n\{2\}/v_n[2]$ the data sets start to deviate. Figure C.3 shows $v_3\{2\}/v_3[2]$ for 2015 and 2018 data, and while both data sets show $v_3\{2\}/v_3[2]$ consistent with unity, figure C.4 reveals deviations $> 3\%$. The same is observed for $v_4\{2\}/v_4[2]$ in figures C.5 and C.6. For all harmonics, the statistical uncertainty is significantly improved by the 2018 data.

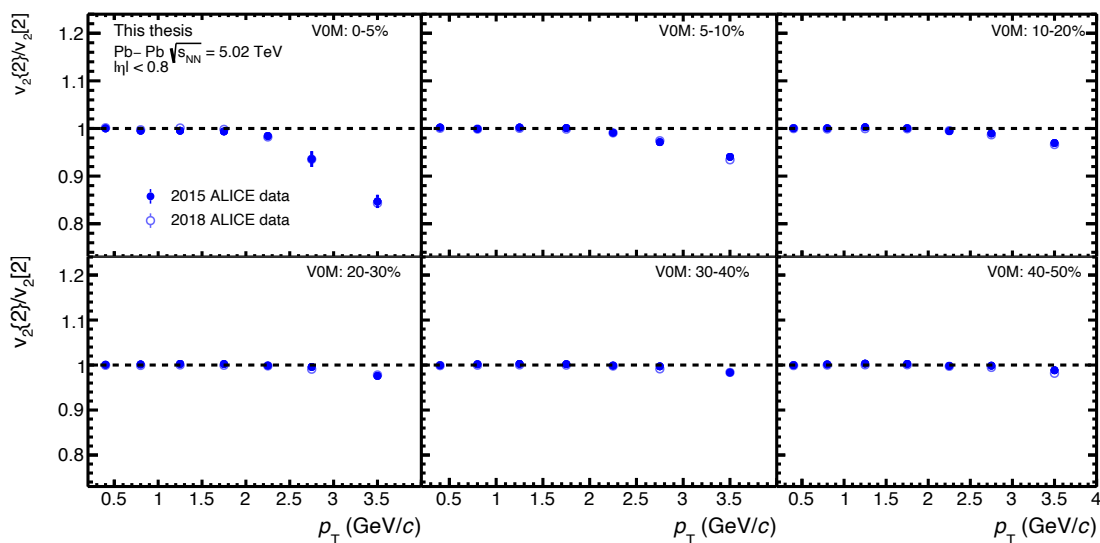


Figure C.1: Comparison of $v_2\{2\}/v_2[2]$ in Pb–Pb collisions from 2015 and 2018 data at $\sqrt{s_{\text{NN}}}=5.02$ TeV.

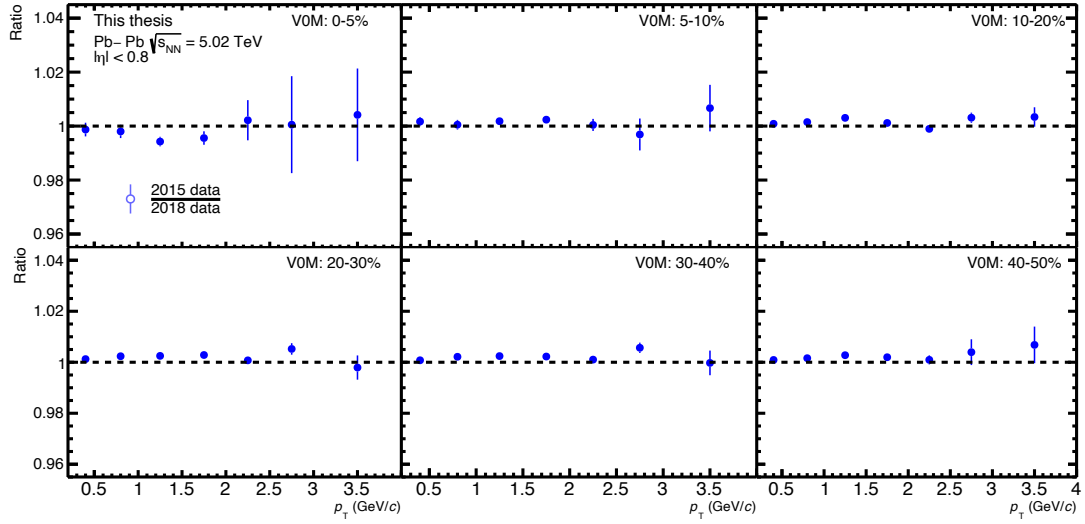


Figure C.2: The ratio of $v_2\{2\}/v_2[2]$ measured with 2015 data to $v_2\{2\}/v_2[2]$ measured with 2018 data.

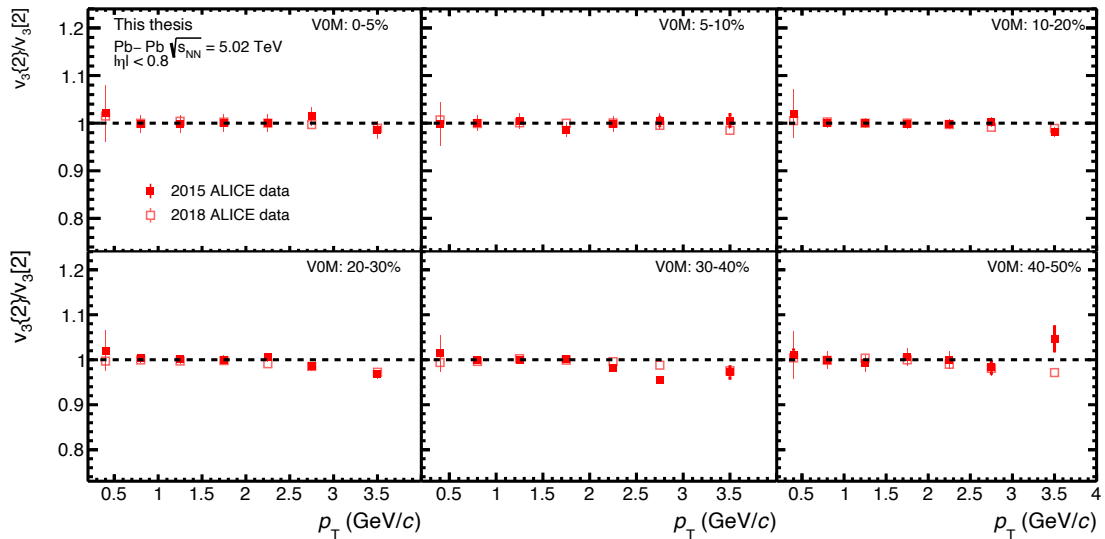


Figure C.3: Comparison of $v_3\{2\}/v_3[2]$ in Pb–Pb collisions from 2015 and 2018 data at $\sqrt{s_{\text{NN}}} = 5.02$ TeV.

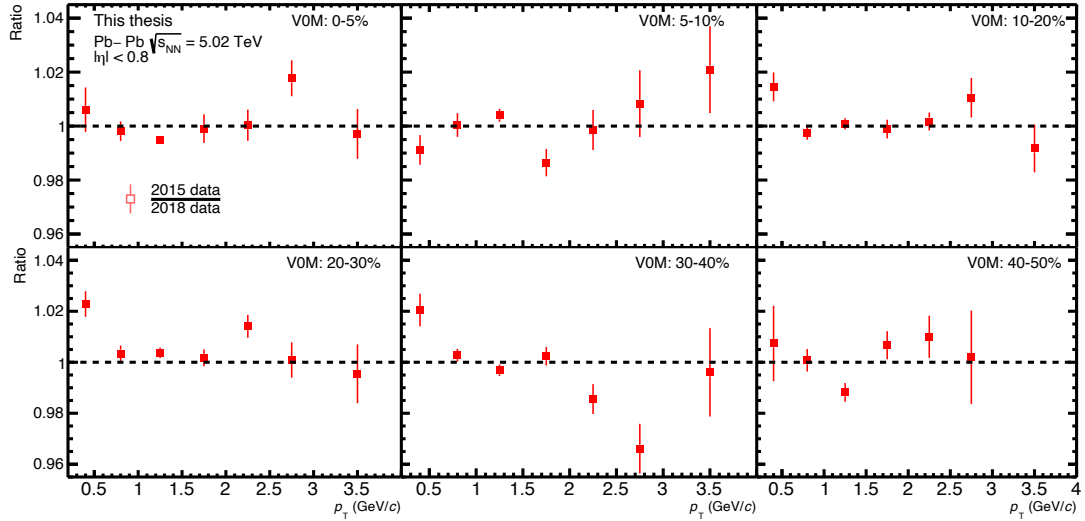


Figure C.4: The ratio of $v_3\{2\}/v_3[2]$ measured with 2015 data to $v_3\{2\}/v_3[2]$ measured with 2018 data.

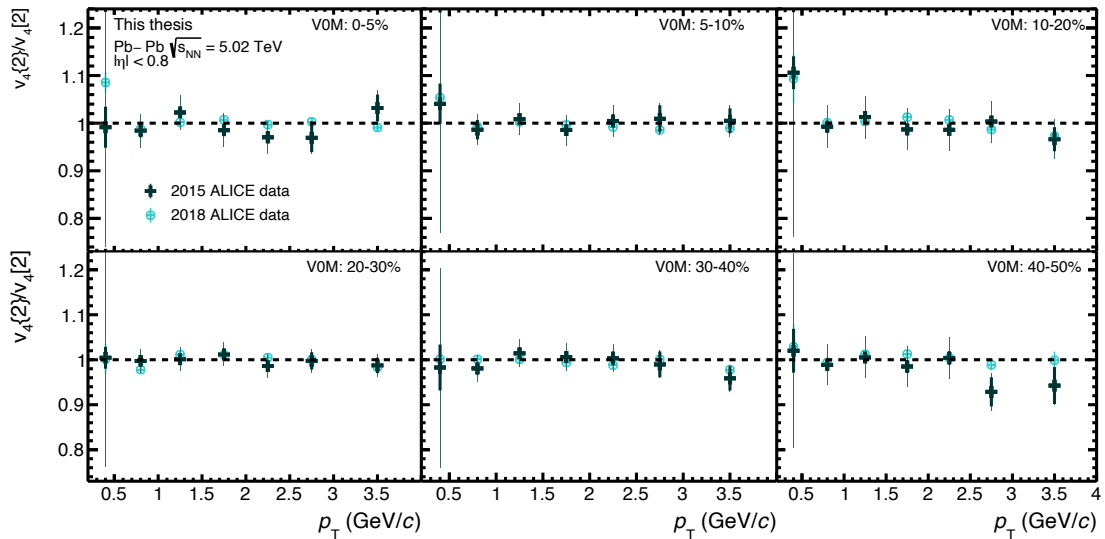


Figure C.5: Comparison of $v_4\{2\}/v_4[2]$ in Pb–Pb collisions from 2015 and 2018 data at $\sqrt{s_{\text{NN}}} = 5.02$ TeV.

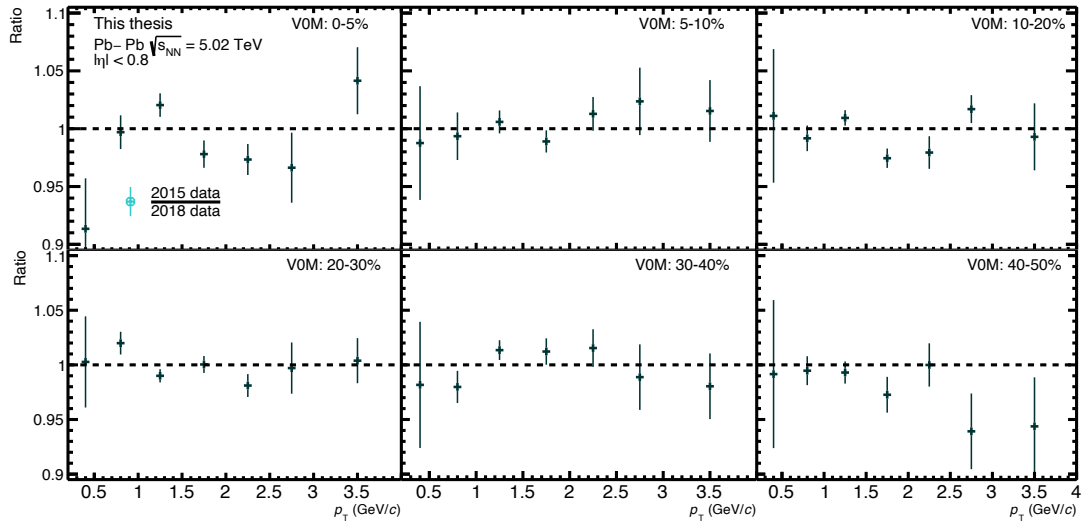


Figure C.6: The ratio of $v_4\{2\}/v_4[2]$ measured with 2015 data to $v_4\{2\}/v_4[2]$ measured with 2018 data.

C.2 Factorization ratio r_n

The factorization ratio r_2 is shown in figure C.7 for both 2015 and 2018 data. The measurements are qualitatively consistent with much smaller statistical uncertainty on the 2018 data. Quantitatively, figure C.8 shows deviations between the data sets up to $\sim 4\%$ in central collisions for r_2 and less in peripheral collisions. Figure C.9 shows the higher-order factorization ratio r_3 for the different data sets. Again, the 2018 data significantly improves the statistical uncertainty, although the ratio between the measurements show significant deviations in figure C.10.

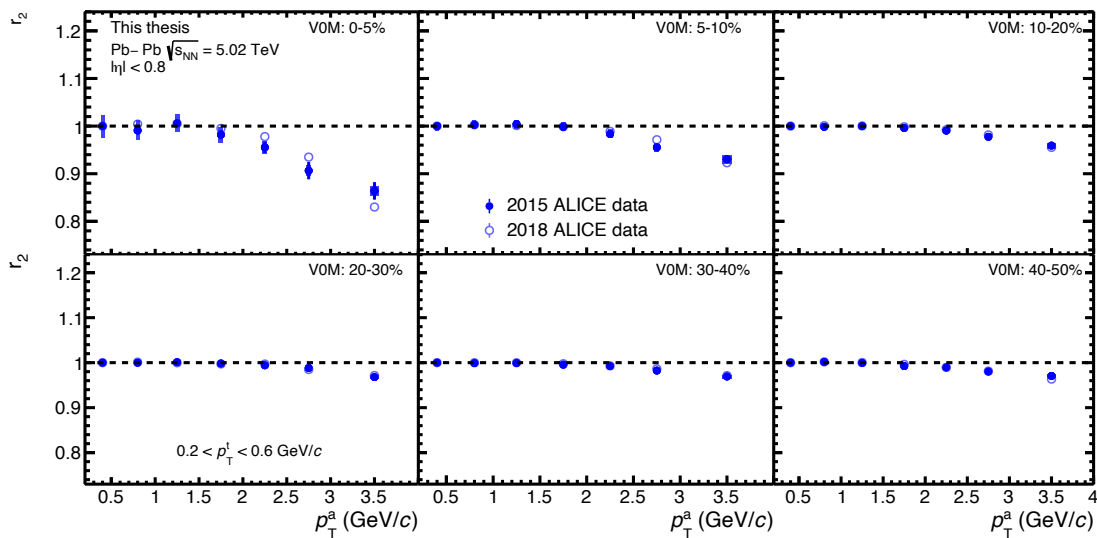


Figure C.7: Comparison of r_2 in Pb–Pb collisions from 2015 and 2018 data at $\sqrt{s_{NN}} = 5.02$ TeV.

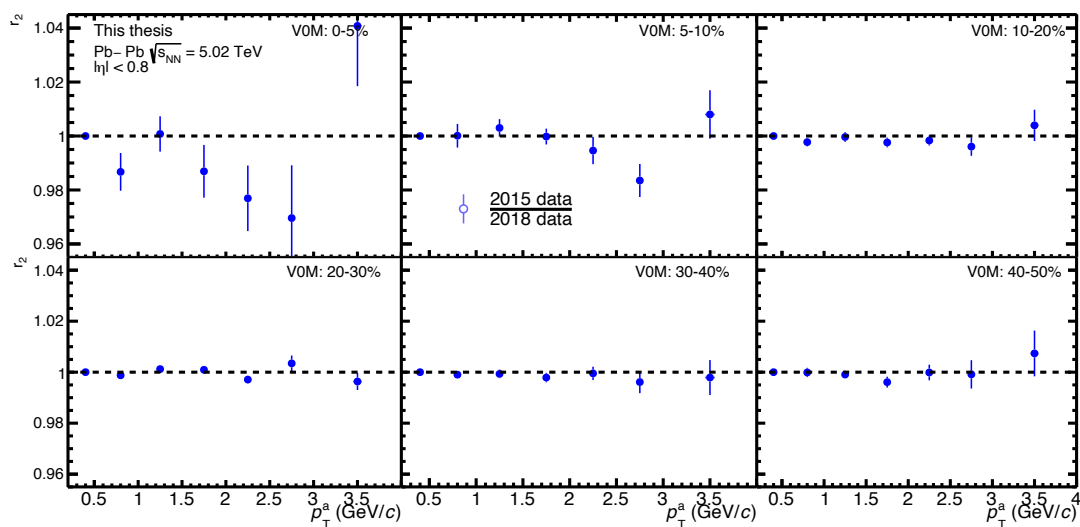


Figure C.8: The ratio of r_2 measured with 2015 data to r_2 measured with 2018 data.

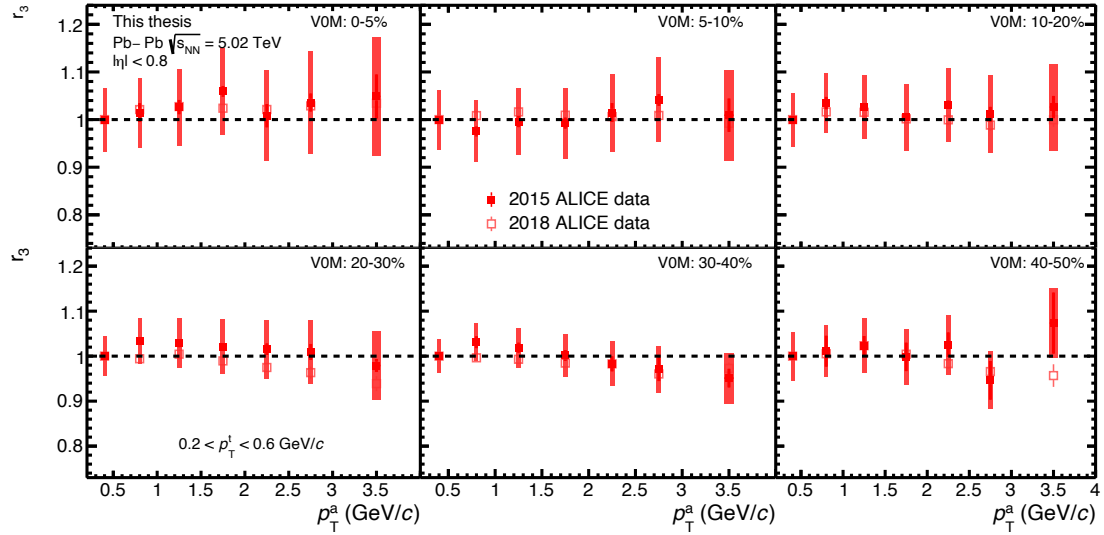


Figure C.9: Comparison of r_3 in Pb–Pb collisions from 2015 and 2018 data at $\sqrt{s_{NN}} = 5.02$ TeV.

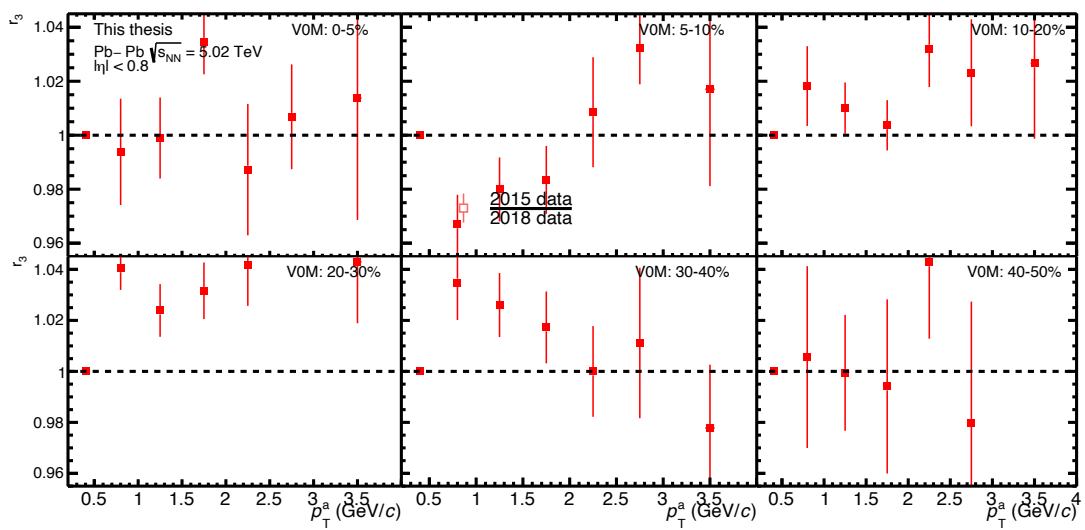


Figure C.10: The ratio of r_3 measured with 2015 data to r_3 measured with 2018 data.

C.3 Angle Decorrelation $C(\Psi_n)$

The double-differential angle decorrelation is shown in figure C.11 for both 2015 and 2018 data. The statistical uncertainty is much improved by the 2018 data. The ratio between the measurements are shown in C.12 and a significant deviation between the two data sets is observed, especially in central collisions, up to $\sim 10\%$. This needs further study to provide high-precision measurements of the double-differential flow angle fluctuations.

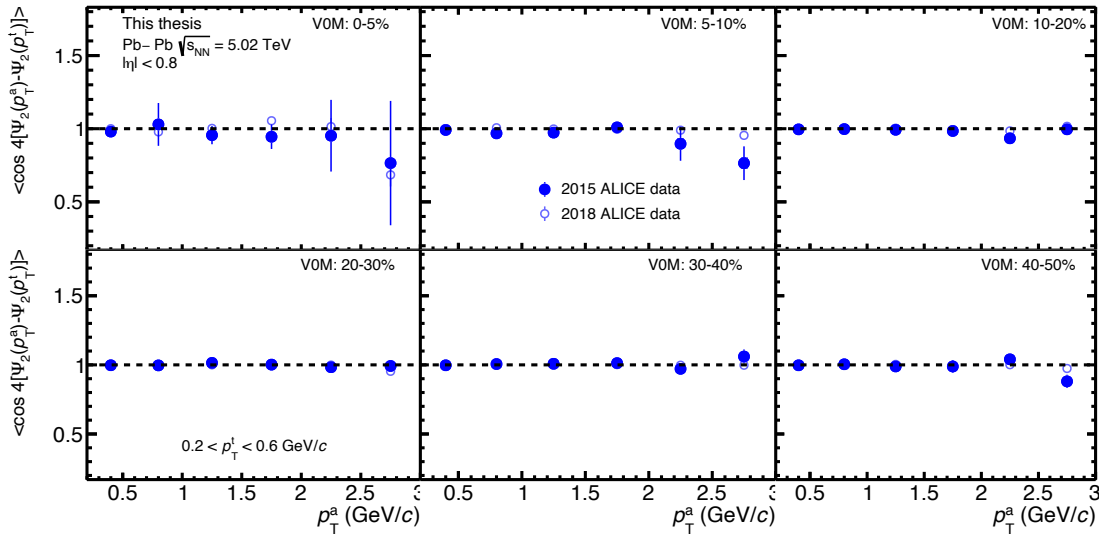


Figure C.11: Comparison of $C(\Psi_2^a, \Psi_2^t)$ with trigger particle $0.2 < p_T^t < 0.6$ GeV/c in Pb–Pb collisions from 2015 and 2018 data at $\sqrt{s_{NN}} = 5.02$ TeV.

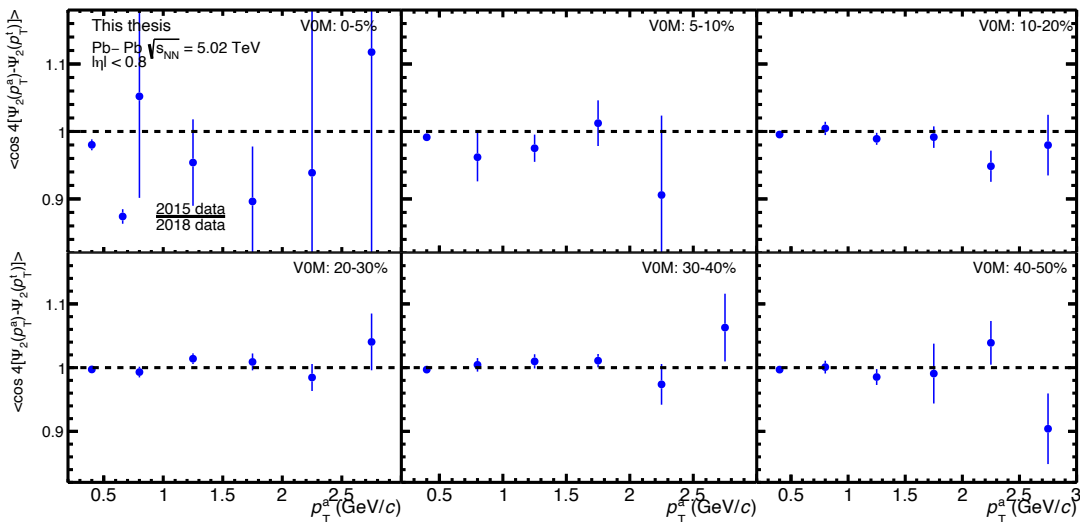


Figure C.12: The ratio of $C(\Psi_2^a, \Psi_2^t)$ measured with 2015 data to $C(\Psi_2^a, \Psi_2^t)$ measured with 2018 data.

C.4 p_T -differential normalized symmetric cumulant

Figure C.13 shows the measurements of $\text{NSC}(3, 2_{p_T})$ and $\text{NSC}(4, 2_{p_T})$ for both the 2015 and 2018 data sets. Qualitatively, the same trend is observed for both sets of data, i.e., $\text{NSC}(3, 2_{p_T})$ and $\text{NSC}(4, 2_{p_T})$ constant with p_T . In figure C.14 the comparison of $\text{NSC}(3, 2_{p_T})$ and $\text{NSC}(2, 3_{p_T})$ show that the difference observed in 2015 data is also observed with 2018 data. The 2018 data offers much more statistics, so this could suggest that the observed difference between $\text{NSC}(3, 2_{p_T})$ and $\text{NSC}(2, 3_{p_T})$ at low p_T is not due to statistics. The comparison of $\text{NSC}(4, 2_{p_T})$ and $\text{NSC}(2, 4_{p_T})$ is shown in figure C.15 for both 2015 and 2018 data. The statistical uncertainty of $\text{NSC}(2, 4_{p_T})$ is significantly improved with the 2018 data, and surprisingly seem to confirm the trend observed in 2015 data, where $\text{NSC}(2, 4_{p_T})$ changes sign and becomes negative at low and high p_T . A more thorough study on the differences between $\text{NSC}(n, m_{p_T})$ and $\text{NSC}(m, n_{p_T})$ with the 2018 data is needed to draw any firm conclusions.

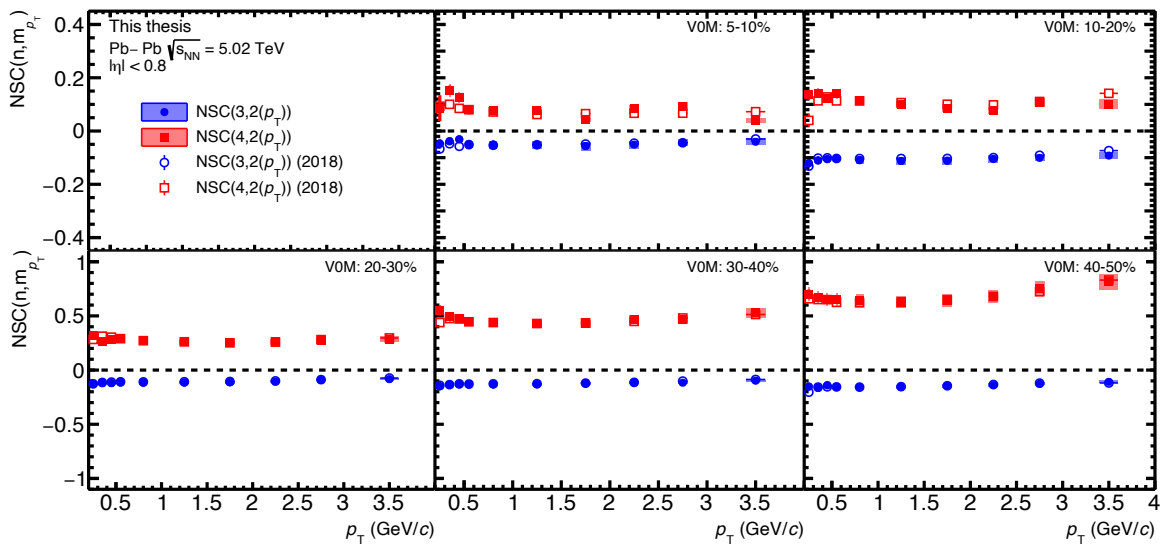


Figure C.13: $\text{NSC}(3, 2_{p_T})$ and $\text{NSC}(4, 2_{p_T})$ for 2015 and 2018 data sets in Pb–Pb collisions at $\sqrt{s_{NN}} = 5.02$ TeV.

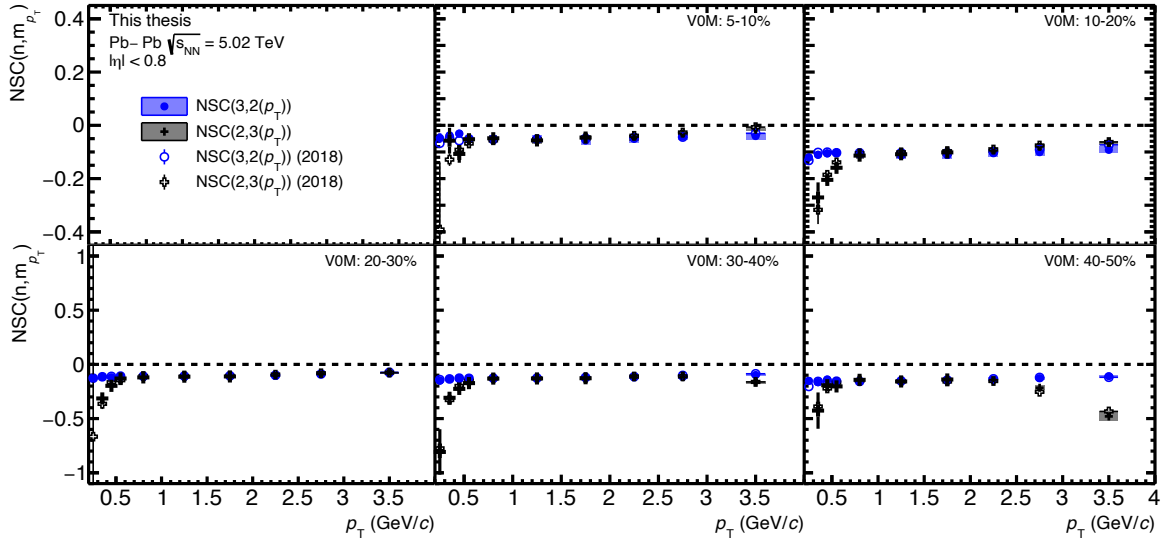


Figure C.14: $\text{NSC}(3, 2_{p_T})$ and $\text{NSC}(2, 3_{p_T})$ for 2015 and 2018 data sets in Pb–Pb collisions at $\sqrt{s_{\text{NN}}} = 5.02$ TeV.

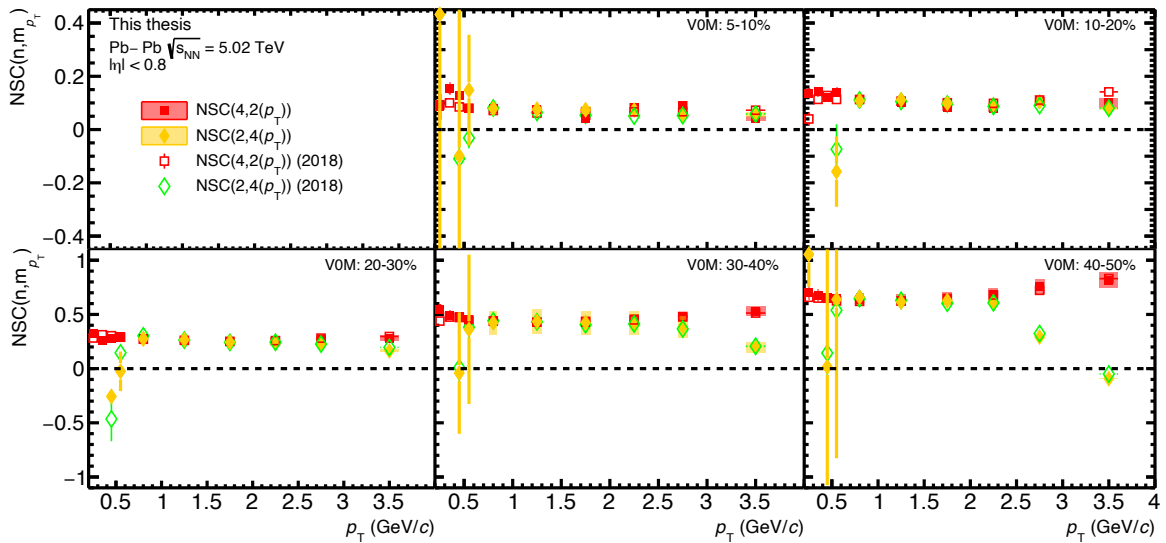


Figure C.15: $\text{NSC}(4, 2_{p_T})$ and $\text{NSC}(2, 4_{p_T})$ for 2015 and 2018 data sets in Pb–Pb collisions at $\sqrt{s_{\text{NN}}} = 5.02$ TeV.

List of Figures

1.1	The particles of the standard model with their mass, charge, and spin. Figure from [4]	2
1.2	Sketch of a central collision of two high energy nuclei in the center-of-mass frame [10].	3
1.3	Space-time evolution of a heavy-ion collision [11].	3
1.4	Diagram showing the QCD phase space. Figure is taken from [18].	5
1.5	Sketch of the geometry of a peripheral heavy-ion collision. The interaction region is marked by the cut-out almond shape and is horizontally cut by the reaction plane. Figure taken from [12].	7
1.6	Measurements of the anisotropic flow coefficient v_n as a function of centrality. The measurements are compared to hydrodynamic calculations. Figure from [32].	8
1.7	Measurements of the flow coefficient v_n as function of p_T (left) and η (right) in Pb–Pb collisions at $\sqrt{s_{NN}}= 2.76$ TeV. The left figure is taken from [35] and the right from [34].	9
1.8	Estimated temperature dependence of shear viscosity η/s and bulk viscosity ζ/s using Bayesian parameter estimation method. Figure taken from [36].	10
1.9	Comparison of model calculations using best-fit <i>maximum a posteriori</i> (MAP) parameters to experimental data for different observables as a function of centrality. Upper left: yields of charged particles, transverse energy, and identified particles. Lower left: mean transverse momenta $\langle p_T \rangle$. Upper right: Anisotropic flow cumulants $v_n\{k\}$. Lower right: mean transverse momentum fluctuations $\delta p_T / \langle p_T \rangle$	10
2.1	Sketch of side view of detector showing a two-particle correlation with no subevent.	16
2.2	Sketch of side view of detector showing a two-particle correlation with two subevents and a $ \Delta\eta $ gap separating them.	16
2.3	Sketch of the side view of the detector showing a four-particle correlation with two subevents and a $ \Delta\eta $ gap separating them.	17
2.4	Sketches of side view of the detector showing a two-particle correlation with two subevents and $ \Delta\eta $ gap separating them. The particles are selected from different subevents and p_T intervals.	20
3.1	Illustration of the location of the LHC tunnel at the border of France and Switzerland [48].	22
3.2	Schematic layout of the ALICE experiment.	24
3.3	Layout of the ITS	25
3.4	3D view of the TPC field cage [51].	25
3.5	Sketches of VZERO-A and VZERO-C arrays.	26
3.6	Distribution of the sum of amplitudes in the two VZERO arrays in Pb–Pb collisions at $\sqrt{s_{NN}}= 2.76$ TeV. The red line shows the fit with the Glauber model. The shaded areas define the different centrality classes of hadronic collisions. The inset shows the low amplitude part of the distribution [53].	27
3.7	Event reconstruction flow [55].	28
4.1	Diagram of the analysis workflow.	31
4.2	Correlation of centrality classes from centrality estimators V0M and CL0.	32

- 4.3 Selection of the primary $|V_z|$ vertex in 2015 Pb–Pb collisions at $\sqrt{s_{NN}}=5.02$ TeV before event cuts (left) and after event cuts (right). 32
- 4.4 Correlations between the number of ESD tracks and track using only TPC information used for the rejection of pileup events (left) and the correlation between TPC+ITS tracks and the same TPC+ITS+TOF tracks used for rejection of out-of-bunch crossing pileup events. 33
- 4.5 Distributions of η and p_T for Pb–Pb collisions at $\sqrt{s_{NN}}=5.02$ TeV from LHC15o period. 35
- 4.6 The three-dimensional distribution of φ, η and V_z without NUA corrections for Pb–Pb at $\sqrt{s_{NN}}=5.02$ TeV for run 246276 for tracks passing the selection cuts. 36
- 4.7 The two-dimensional distribution of φ and η without NUA correction for Pb–Pb run 246276 with $\sqrt{s_{NN}}=5.02$ TeV for tracks passing the selection cuts. 36
- 4.8 φ -distribution for run 246276 in LHC15o before and after NUA corrections are applied. 37
- 4.9 The values of the Barlow test compared against unity (dotted line) for each variation cut on $v_2\{2\}/v_2[2]$ in Pb–Pb collisions at $\sqrt{s_{NN}}=5.02$ TeV. . 39
- 4.10 The ratio of $v_2\{2\}/v_2[2]$ with different variations of the cuts to $v_2\{2\}/v_2[2]$ with default cuts in Pb–Pb collisions at $\sqrt{s_{NN}}=5.02$ TeV. 39
- 5.1 The ratio $v_2\{2, |\Delta\eta| > 0.8\}/v_2[2, |\Delta\eta| > 0.8]$ in Pb–Pb collisions at $\sqrt{s_{NN}}=2.76$ TeV. Hydrodynamic calculations with MC-Glauber [74], MC-KLN [74], TRENTo [28] and AMPT [28] initial conditions are shown with the coloured curves. Figure taken from [72]. 43
- 5.2 $v_2\{2\}$ in Pb–Pb collisions at $\sqrt{s_{NN}}=5.02$ TeV. Comparison with published Run1 measurements in Pb–Pb collisions at $\sqrt{s_{NN}}=2.76$ TeV shown with open triangles [32]. Comparison with iEBE-VISHNU hydrodynamic model with TRENTo initial conditions and temperature dependent $\eta/s(T)$ and $\zeta/s(T)$ [28], and with AMPT initial conditions and $\eta/s = 0.08$ [28] are shown in coloured bands. 44
- 5.3 $v_2[2]$ in Pb–Pb collisions at $\sqrt{s_{NN}}=5.02$ TeV. Comparison with iEBE-VISHNU hydrodynamic model with TRENTo initial conditions and temperature dependent $\eta/s(T)$ and $\zeta/s(T)$ [28], and with AMPT initial conditions and $\eta/s = 0.08$ [28] are shown in coloured bands. 44
- 5.4 The ratio $v_2\{2\}/v_2[2]$ in Pb–Pb collisions at $\sqrt{s_{NN}}=5.02$ TeV. Comparison with iEBE-VISHNU hydrodynamic model with TRENTo initial conditions and temperature dependent $\eta/s(T)$ and $\zeta/s(T)$ [28], and with AMPT initial conditions and $\eta/s = 0.08$ [28] are shown in coloured bands. 46
- 5.5 Comparison of the ratio $v_2\{2\}/v_2[2]$ in Pb–Pb collisions at $\sqrt{s_{NN}}=5.02$ TeV for the different data sets. The 2015 data (solid circles) are compared to the 2018 data (open circles). 46
- 5.6 The ratio $v_2\{2\}/v_2[2]$ in Xe–Xe collisions at $\sqrt{s_{NN}}=5.44$ TeV. Comparison with the Pb–Pb measurements is shown in open circles. 47

- 5.7 $v_3\{2\}$ for Pb–Pb collisions at $\sqrt{s_{\text{NN}}}= 5.02$ TeV. Comparison with published Run1 measurements in Pb–Pb collisions at $\sqrt{s_{\text{NN}}}= 2.76$ TeV shown with open triangles [32]. Comparison with iEBE-VISHNU hydrodynamic model with TRENTo initial conditions and temperature dependent $\eta/s(T)$ and $\zeta/s(T)$ [28], and with AMPT initial conditions and $\eta/s = 0.08$ [28] are shown in coloured bands. 47
- 5.8 $v_3[2]$ for Pb–Pb collisions at $\sqrt{s_{\text{NN}}}= 5.02$ TeV. Comparison with iEBE-VISHNU hydrodynamic model with TRENTo initial conditions and temperature dependent $\eta/s(T)$ and $\zeta/s(T)$ [28], and with AMPT initial conditions and $\eta/s = 0.08$ [28] are shown in coloured bands. 48
- 5.9 The ratio $v_3\{2\}/v_3[2]$ for Pb–Pb collisions at $\sqrt{s_{\text{NN}}}= 5.02$ TeV. Comparison with iEBE-VISHNU hydrodynamic model with TRENTo initial conditions and temperature dependent $\eta/s(T)$ and $\zeta/s(T)$ [28], and with AMPT initial conditions and $\eta/s = 0.08$ [28] are shown in coloured bands. 48
- 5.10 $v_4\{2\}$ for Pb–Pb collisions at $\sqrt{s_{\text{NN}}}= 5.02$ TeV. Comparison with published Run1 measurements in Pb–Pb collisions at $\sqrt{s_{\text{NN}}}= 2.76$ TeV shown with open triangles [32]. Comparison with iEBE-VISHNU hydrodynamic model with TRENTo initial conditions and temperature dependent $\eta/s(T)$ and $\zeta/s(T)$ [28], and with AMPT initial conditions and $\eta/s = 0.08$ [28] are shown in coloured bands. 49
- 5.11 $v_4[2]$ for Pb–Pb collisions at $\sqrt{s_{\text{NN}}}= 5.02$ TeV. Comparison with iEBE-VISHNU hydrodynamic model with TRENTo initial conditions and temperature dependent $\eta/s(T)$ and $\zeta/s(T)$ [28], and with AMPT initial conditions and $\eta/s = 0.08$ [28] are shown in coloured bands. 49
- 5.12 The ratio $v_4\{2\}/v_4[2]$ for Pb–Pb collisions at $\sqrt{s_{\text{NN}}}= 5.02$ TeV. Comparison with iEBE-VISHNU hydrodynamic model with TRENTo initial conditions and temperature dependent $\eta/s(T)$ and $\zeta/s(T)$ [28], and with AMPT initial conditions and $\eta/s = 0.08$ [28] are shown in coloured bands. 50
- 5.13 Examples of the global fit in 0–10% centrality events for $n = 2,3,4$ and 5. The measured $V_{n\Delta}$ coefficients are plotted on an interleaved $p_{\text{T}}^t, p_{\text{T}}^a$ axis in the upper panels, and the red curves denote the global fit function (Eq. (5.4)). The ratio of the data to the fit is shown in the lower section of each panel. Figure taken from [74]. 51
- 5.14 The ALICE measurements of the factorization ratio r_2 as function of p_{T}^a in bins of p_{T}^t for centrality classes 0-5%, 20-30% and 40-50% in Pb–Pb collisions at $\sqrt{s_{\text{NN}}}= 2.76$ TeV with comparison to hydrodynamic models with TRENTo initial conditions [28] and AMPT initial conditions [28] are shown in coloured curves. Figure taken from [72]. 53
- 5.15 The factorization ratio r_2 for Pb–Pb collisions at $\sqrt{s_{\text{NN}}}= 5.02$ TeV in different bins of p_{T}^t and centrality. Run1 ALICE measurements in Pb–Pb collisions at $\sqrt{s_{\text{NN}}}= 2.76$ GeV/c are presented as orange crosses [72]. 54
- 5.16 The factorization ratio r_2 for Pb–Pb collisions at $\sqrt{s_{\text{NN}}}= 5.02$ TeV. Comparison with iEBE-VISHNU hydrodynamic model with TRENTo initial conditions and temperature dependent $\eta/s(T)$ and $\zeta/s(T)$ [28], and with AMPT initial conditions and $\eta/s = 0.08$ [28] are shown in coloured bands. 55
- 5.17 The factorization ratio r_2 for Xe–Xe collisions at $\sqrt{s_{\text{NN}}}= 5.44$ TeV. Comparison with r_2 in Pb–Pb collisions at $\sqrt{s_{\text{NN}}}= 5.02$ TeV is shown in open circles. 55

- 5.18 The factorization ratio r_3 for Pb–Pb collisions at $\sqrt{s_{\text{NN}}}= 5.02$ TeV for different trigger particle p_{T}^t intervals. Run1 ALICE measurements in Pb–Pb collisions at $\sqrt{s_{\text{NN}}}= 2.76$ GeV/ c are presented as orange points [72]. 56
- 5.19 Sketches of side view of the detector showing a four-particle correlation with two subevents and $|\Delta\eta|$ gap separating them. The particles of interest are selected from the *same* subevent. 58
- 5.20 Sketches of side view of the detector showing a four-particle correlation with two subevents and $|\Delta\eta|$ gap separating them. The particles of interest are selected from *different* subevents. 58
- 5.21 The single p_{T} -differential flow angle decorrelation $C(\Psi_2^a, \Psi_2)$ in Pb–Pb collisions at $\sqrt{s_{\text{NN}}}= 5.02$ TeV for different gaps in pseudorapidity. 58
- 5.22 The the upper limit on the cosine term $\langle \cos 2[\Psi_2(p_{\text{T}}^a) - \Psi_2] \rangle$ in Pb–Pb collisions at $\sqrt{s_{\text{NN}}}= 5.02$ TeV for different pseudorapidity gaps. $v_2\{2\}/v_2[2]$ is shown for comparison with black crosses. 59
- 5.23 The ratio $R(v_2^a, v_2)$ for different pseudorapidity gaps in Pb–Pb collisions at $\sqrt{s_{\text{NN}}}= 5.02$ TeV. Comparison with $v_2\{2\}/v_2[2]$ is shown with black crosses. 60
- 5.24 The relative contribution of flow angle and flow magnitude fluctuations to the deviation of $v_2\{2\}/v_2[2]$ from unity in Pb–Pb collisions at $\sqrt{s_{\text{NN}}}= 5.02$ TeV for $3.0 < p_{\text{T}}^a < 4.0$ GeV/ c . The upper and lower limits are denoted by coloured arrows. 61
- 5.25 Sketches of side view of the detector showing a four-particle correlation with two subevents and $|\Delta\eta|$ gap separating them. The particles from the *same* p_{T} interval are selected from the *same* subevent. 63
- 5.26 Sketches of side view of the detector showing a four-particle correlation with two subevents and $|\Delta\eta|$ gap separating them. The particles from the *same* p_{T} interval are selected from *different* subevents. 63
- 5.27 The double p_{T} -differential flow angle decorrelation $C(\Psi_2^a, \Psi_2^t)$ for Pb–Pb collisions at $\sqrt{s_{\text{NN}}}= 5.02$ TeV in different bins of p_{T}^t and centrality. 63
- 5.28 The double p_{T} -differential flow angle decorrelation $C(\Psi_2^a, \Psi_2^t)$ for Pb–Pb collisions at $\sqrt{s_{\text{NN}}}= 5.02$ TeV for all centrality classes up to 40-50% with trigger particle $0.2 < p_{\text{T}}^t < 0.6$ GeV/ c 64
- 5.29 The double-differential flow angle decorrelation $\sqrt{\langle \cos^2 2[\Psi_2(p_{\text{T}}^a) - \Psi_2(p_{\text{T}}^t)] \rangle}$ and r_2 in different bins of p_{T}^t and centrality in Pb–Pb collisions at $\sqrt{s_{\text{NN}}}= 5.02$ TeV. 65
- 5.30 The double-differential flow angle decorrelation $\sqrt{\langle \cos^2 2[\Psi_2(p_{\text{T}}^a) - \Psi_2(p_{\text{T}}^t)] \rangle}$ and r_2 for trigger particle selected from $0.2 < p_{\text{T}}^t < 0.6$ GeV/ c in Pb–Pb collisions at $\sqrt{s_{\text{NN}}}= 5.02$ TeV. 66
- 5.31 The ratio $R(v_2^a, v_2^t)$ of r_n with $\sqrt{\langle \cos^2 2[\Psi_2(p_{\text{T}}^a) - \Psi_2(p_{\text{T}}^t)] \rangle}$ for trigger particle selected from $0.2 < p_{\text{T}}^t < 0.6$ GeV/ c in Pb–Pb collisions at $\sqrt{s_{\text{NN}}}= 5.02$ TeV. The comparison with r_2 is shown with solid circles. 66
- 5.32 The relative contribution of flow angle and flow magnitude fluctuations to the deviation of r_2 from unity in Pb–Pb collisions at $\sqrt{s_{\text{NN}}}= 5.02$ TeV for $3.0 < p_{\text{T}}^a < 4.0$ GeV/ c and $0.2 < p_{\text{T}}^t < 0.6$ GeV/ c . The upper and lower limits are denoted by coloured arrows. 67

- 5.33 Measurements of $v_2\{2\}/v_2[2]$ with $|\Delta\eta| > 0.8$ for various multiplicity classes in p–Pb collisions at $\sqrt{s_{\text{NN}}} = 5.02$ TeV. DPMJet calculations [91] are shown as green-shaded lines. Hydrodynamic calculations (MUSIC) [92] with modified MC-Glauber initial conditions and $\eta/s = 0.08$ are shown as blue lines. Figure taken from [72]. 68
- 5.34 The p_{T} -integrated symmetric cumulants $SC(4, 2)$ and $SC(3, 2)$ as function of centrality in Pb–Pb collisions at $\sqrt{s_{\text{NN}}} = 2.76$ TeV and hydrodynamic calculations (top). The normalized symmetric cumulants $NSC(4, 2)$ and $NSC(3, 2)$ as function of centrality in Pb–Pb collisions at $\sqrt{s_{\text{NN}}} = 2.76$ TeV and hydrodynamic calculations (bottom). Figure adapted from [93]. 70
- 5.35 The single p_{T} -differential symmetric cumulants $SC(4, 2_{p_{\text{T}}})$ and $SC(3, 2_{p_{\text{T}}})$ in Pb–Pb collisions at $\sqrt{s_{\text{NN}}} = 5.02$ TeV. 72
- 5.36 The single p_{T} -differential normalized symmetric cumulant $NSC(3, 2_{p_{\text{T}}})$ and $NSC(4, 2_{p_{\text{T}}})$ for Pb–Pb collisions at $\sqrt{s_{\text{NN}}} = 5.02$ TeV. Comparison with iEBE-VISHNU hydrodynamic model with TRENTo and AMPT initial conditions are shown in coloured bands. 72
- 5.37 The single p_{T} -differential normalized symmetric cumulant $NSC(3, 2_{p_{\text{T}}})$ and $NSC(2, 3_{p_{\text{T}}})$ for Pb–Pb collisions at $\sqrt{s_{\text{NN}}} = 5.02$ TeV. Comparison with iEBE-VISHNU hydrodynamic model with TRENTo and AMPT initial conditions are shown in coloured bands. 73
- 5.38 The single p_{T} -differential normalized symmetric cumulant $NSC(4, 2_{p_{\text{T}}})$ and $NSC(2, 4_{p_{\text{T}}})$ for Pb–Pb collisions at $\sqrt{s_{\text{NN}}} = 5.02$ TeV. Comparison with iEBE-VISHNU hydrodynamic model with TRENTo and AMPT initial conditions are shown in coloured bands. 73
- B.1 The values of the Barlow test compared against unity (dotted line) for each variation cut on $v_3\{2\}/v_3[2]$ in Pb–Pb collisions at $\sqrt{s_{\text{NN}}} = 5.02$ TeV. . 84
- B.2 The ratio of $v_3\{2\}/v_3[2]$ with different variations of the cuts to $v_3\{2\}/v_3[2]$ with default cuts in Pb–Pb collisions at $\sqrt{s_{\text{NN}}} = 5.02$ TeV. 85
- B.3 The values of the Barlow test compared against unity (dotted line) for each variation cut on $v_4\{2\}/v_4[2]$ in Pb–Pb collisions at $\sqrt{s_{\text{NN}}} = 5.02$ TeV. . 86
- B.4 The ratio of $v_4\{2\}/v_4[2]$ with different variations of the cuts to $v_4\{2\}/v_4[2]$ with default cuts in Pb–Pb collisions at $\sqrt{s_{\text{NN}}} = 5.02$ TeV. 86
- B.5 The values of the Barlow test compared against unity (dotted line) for each variation cut on r_2 in Pb–Pb collisions at $\sqrt{s_{\text{NN}}} = 5.02$ TeV. 87
- B.6 The ratio of r_2 with different variations of the cuts to r_2 with default cuts in Pb–Pb collisions at $\sqrt{s_{\text{NN}}} = 5.02$ TeV. 87
- B.7 The values of the Barlow test compared against unity (dotted line) for each variation cut on r_3 in Pb–Pb collisions at $\sqrt{s_{\text{NN}}} = 5.02$ TeV. 88
- B.8 The ratio of r_3 with different variations of the cuts to r_3 with default cuts in Pb–Pb collisions at $\sqrt{s_{\text{NN}}} = 5.02$ TeV. 88
- B.9 The values of the Barlow test compared against unity (dotted line) for each variation cut on $\langle \cos 4[\Psi_2(p_{\text{T}}^a) - \Psi_2(p_{\text{T}}^t)] \rangle$ in Pb–Pb collisions at $\sqrt{s_{\text{NN}}} = 5.02$ TeV. 89
- B.10 The ratio of $\langle \cos 4[\Psi_2(p_{\text{T}}^a) - \Psi_2(p_{\text{T}}^t)] \rangle$ with different variations of the cuts to $\langle \cos 4[\Psi_2(p_{\text{T}}^a) - \Psi_2(p_{\text{T}}^t)] \rangle$ with default cuts in Pb–Pb collisions at $\sqrt{s_{\text{NN}}} = 5.02$ TeV. 89
- B.11 The values of the Barlow test compared against unity (dotted line) for each variation cut on $NSC(3, 2_{p_{\text{T}}})$ in Pb–Pb collisions at $\sqrt{s_{\text{NN}}} = 5.02$ TeV. . 90

B.12	The ratio of $\text{NSC}(3, 2_{p_T})$ with different variations of the cuts to $\text{NSC}(3, 2_{p_T})$ with default cuts in Pb–Pb collisions at $\sqrt{s_{\text{NN}}}= 5.02$ TeV.	90
B.13	The values of the Barlow test compared against unity (dotted line) for each variation cut on $\text{NSC}(4, 2_{p_T})$ in Pb–Pb collisions at $\sqrt{s_{\text{NN}}}= 5.02$ TeV.	91
B.14	The ratio of $\text{NSC}(4, 2_{p_T})$ with different variations of the cuts to $\text{NSC}(4, 2_{p_T})$ with default cuts in Pb–Pb collisions at $\sqrt{s_{\text{NN}}}= 5.02$ TeV.	91
B.15	The values of the Barlow test compared against unity (dotted line) for each variation cut on $\text{NSC}(2, 3_{p_T})$ in Pb–Pb collisions at $\sqrt{s_{\text{NN}}}= 5.02$ TeV.	92
B.16	The ratio of $\text{NSC}(2, 3_{p_T})$ with different variations of the cuts to $\text{NSC}(2, 3_{p_T})$ with default cuts in Pb–Pb collisions at $\sqrt{s_{\text{NN}}}= 5.02$ TeV.	92
B.17	The values of the Barlow test compared against unity (dotted line) for each variation cut on $\text{NSC}(2, 4_{p_T})$ in Pb–Pb collisions at $\sqrt{s_{\text{NN}}}= 5.02$ TeV.	93
B.18	The ratio of $\text{NSC}(2, 4_{p_T})$ with different variations of the cuts to $\text{NSC}(2, 4_{p_T})$ with default cuts in Pb–Pb collisions at $\sqrt{s_{\text{NN}}}= 5.02$ TeV.	93
C.1	Comparison of $v_2\{2\}/v_2[2]$ in Pb–Pb collisions from 2015 and 2018 data at $\sqrt{s_{\text{NN}}}= 5.02$ TeV.	94
C.2	The ratio of $v_2\{2\}/v_2[2]$ measured with 2015 data to $v_2\{2\}/v_2[2]$ measured with 2018 data.	95
C.3	Comparison of $v_3\{2\}/v_3[2]$ in Pb–Pb collisions from 2015 and 2018 data at $\sqrt{s_{\text{NN}}}= 5.02$ TeV.	95
C.4	The ratio of $v_3\{2\}/v_3[2]$ measured with 2015 data to $v_3\{2\}/v_3[2]$ measured with 2018 data.	96
C.5	Comparison of $v_4\{2\}/v_4[2]$ in Pb–Pb collisions from 2015 and 2018 data at $\sqrt{s_{\text{NN}}}= 5.02$ TeV.	96
C.6	The ratio of $v_4\{2\}/v_4[2]$ measured with 2015 data to $v_4\{2\}/v_4[2]$ measured with 2018 data.	97
C.7	Comparison of r_2 in Pb–Pb collisions from 2015 and 2018 data at $\sqrt{s_{\text{NN}}}= 5.02$ TeV.	98
C.8	The ratio of r_2 measured with 2015 data to r_2 measured with 2018 data.	98
C.9	Comparison of r_3 in Pb–Pb collisions from 2015 and 2018 data at $\sqrt{s_{\text{NN}}}= 5.02$ TeV.	99
C.10	The ratio of r_3 measured with 2015 data to r_3 measured with 2018 data.	99
C.11	Comparison of $C(\Psi_2^a, \Psi_2^t)$ with trigger particle $0.2 < p_T^t < 0.6$ GeV/ c in Pb–Pb collisions from 2015 and 2018 data at $\sqrt{s_{\text{NN}}}= 5.02$ TeV.	100
C.12	The ratio of $C(\Psi_2^a, \Psi_2^t)$ measured with 2015 data to $C(\Psi_2^a, \Psi_2^t)$ measured with 2018 data.	100
C.13	$\text{NSC}(3, 2_{p_T})$ and $\text{NSC}(4, 2_{p_T})$ for 2015 and 2018 data sets in Pb–Pb collisions at $\sqrt{s_{\text{NN}}}= 5.02$ TeV.	101
C.14	$\text{NSC}(3, 2_{p_T})$ and $\text{NSC}(2, 3_{p_T})$ for 2015 and 2018 data sets in Pb–Pb collisions at $\sqrt{s_{\text{NN}}}= 5.02$ TeV.	102
C.15	$\text{NSC}(4, 2_{p_T})$ and $\text{NSC}(2, 4_{p_T})$ for 2015 and 2018 data sets in Pb–Pb collisions at $\sqrt{s_{\text{NN}}}= 5.02$ TeV.	102

List of Tables

1	Collision systems, energy and corresponding periods used in this thesis.	31
2	Event selection for candidate events. An explanation of the cuts are given in section 4.2 .	34
3	Track selection for candidate tracks. An explanation of the cuts are given in section 4.3 .	35
4	The cuts varied for the systematic study of p_T -dependent flow vector fluctuations in Pb–Pb collisions at $\sqrt{s_{NN}} = 5.02$ TeV in this analysis.	38
5	Deviations of $v_2\{2\}/v_2[2]$, $\sqrt{\langle \cos^2 2[\Psi_2(p_T^a) - \Psi_2] \rangle}$ and $R(v_2^a, v_2)$ from unity for $3.0 < p_T^a < 4.0$ GeV/ c along with the number of standard deviations from unity N_σ . Systematic uncertainties have not been considered, but should be smaller than the statistical uncertainty.	61
6	Deviations of r_2 , $\sqrt{\langle \cos^2 2[\Psi_2(p_T^a) - \Psi_2(p_T^t)] \rangle}$ and $R(v_2^a, v_2^t)$ from unity for $0.2 < p_T^t < 0.6$ GeV/ c and $3.0 < p_T^a < 4.0$ GeV/ c along with the number of standard deviations from unity N_σ . Systematic uncertainties have not been considered, but should be smaller than the statistical uncertainty.	67
7	List of 2015 high intensity Pb–Pb runs at $\sqrt{s_{NN}} = 5.02$ TeV used in this analysis	83
8	List of 2018 Pb–Pb runs at $\sqrt{s_{NN}} = 5.02$ TeV used in this analysis	83
9	List of 2017 Xe–Xe runs at $\sqrt{s_{NN}} = 5.44$ TeV used in this analysis	84
10	Systematic uncertainties due to variations in the event selection cuts for $v_2\{2\}/v_2[2]$.	84
11	Systematic uncertainty due to variations in the track selection cuts for $v_2\{2\}/v_2[2]$ in each p_T bin.	85